Contactless transfer of energy : 3D modeling and design of a position-independent inductive coupling integrated in a planar motor

Smeets, J.P.C.

Published: 01/01/2015

Document Version
Publisher's PDF, also known as Version of Record (includes final page, issue and volume numbers)

Contactless Transfer of Energy

3D Modeling and Design of a Position-Independent Inductive Coupling Integrated in a Planar Motor

PROEFSCHRIFT

ter verkrijging van de graad van doctor
aan de Technische Universiteit Eindhoven,
op gezag van de rector magnificus, prof.dr.ir. C.J. van Duijn,
voor een commissie aangewezen door het College voor Promoties
in het openbaar te verdedigen
op donderdag 19 maart 2015 om 16.00 uur

door

Johan Peter Christiaan Smeets

geboren te Eindhoven

Dit proefschrift is goedgekeurd door de promotoren en de samenstelling van de promotiecommissie is als volgt:

voorzitter:	prof.dr.ir. A.C.P.M. Backx
promotor:	prof.dr. E.A. Lomonova MSc
copromotor:	dr.ir. J.W. Jansen
leden:	univ.-prof.dr.-ing.habil.dr.h.c. K. Hameyer (RWTH Aachen)
	prof.dr. Y. Perriard MSc (EPFL)
	dr. J. Soulard (KTH Stockholm)
	prof.dr.ir. P.G.M. Baltus
adviseur:	dr.ir. J.P.M.B. Vermeulen MTD (ASML Research)

Contactless Transfer of Energy

3D Modeling and Design of a Position-Independent Inductive Coupling Integrated in a Planar Motor

This research is part of the IOP-EMVT program (Innovatiegerichte Onderzoeksprogramma's - Elektromagnetische Vermogenstechniek) under IOP-EMVT 08207. This program is funded by the Netherlands Enterprise Agency of the Dutch Ministry of Economical Affairs.

J.P.C. Smeets. Contactless Transfer of Energy: 3D Modeling and Design of a Position-Independent Inductive Coupling Integrated in a Planar Motor.
Eindhoven: Technische Universiteit Eindhoven, 2015

A catalogue record is available from the Eindhoven University of Technology Library.
ISBN: 978-90-386-3805-8

Summary

Contactless Transfer of Energy

3D Modeling and Design of a Position-Independent
Inductive Coupling Integrated in a Planar Motor

The power supply to the moving part of a linear or a planar motor is conventionally realized by moving cables which limit the performance of the system. To overcome these limitations, the cables can be replaced by a contactless energy transfer (CET) system in which energy is transferred by means of an inductive coupling, i.e. a transformer with an airgap between the primary and secondary coil. A CET system with a planar movement with one or multiple secondary coils, typically has an array of primary coils. Although energy can be transferred along the entire stroke of the moving secondary coil(s), the amount of transferred energy is extremely position dependent. Whereas, the variation in mutual inductance between the primary and secondary coil(s) is a measure for the position dependency of a CET system. This thesis concerns the three-dimensional modeling and analysis of position-independent CET systems. The derived knowledge has been applied in the design and realization of a magnetically suspended planar motor with integrated CET system.

A major contribution of this work is the extension of the harmonic modeling method by the formulation of the three-dimensional magnetic vector potential for both the static and quasi-static field analysis, which makes it possible to describe the magnetic fields of three-dimensional current-carrying coils. The current density distribution of a coil is modeled by four bars. Conducting and permeable material properties, and the eddy-current reaction field are included in the model. Furthermore, the mode-matching technique is extended towards three-dimensional structures such that slots and cavities can be taken into account. The flux density distribution, self-inductances and mutual inductances are obtained with the harmonic model, and they are validated with finite element analyses and measurements. Differences below 7% have been obtained among the different methods.

In addition, the magnetic model has been coupled with an electrical and thermal one in a modeling framework allowing to analyze a CET system in each of these domains. The developed modeling framework is adaptive to different ferromagnetic structures around a coil and various configurations of the primary coil array, such as numbers of energized primary coils and single or multi-layer coil arrays. Furthermore, both linear and planar displacements of the coils with respect to each other can be taken into account.

A second important contribution is the analysis of the position dependency of a CET system consisting out of a planar primary coil array and a single secondary coil. The analysis is conducted by comparing various topologies with respect to the variation in mutual inductance and average output power along the stroke of the moving secondary coil. A generic solution with a low variation in mutual inductance has been obtained in CET systems with a non-conducting and toothless structure around the coils, in which a secondary coil envelopes and receives energy from multiple adjacent primary coils located in a single-layer coil array. The desired output power can be reached by optimizing the electrical parameters of the inductive coupling, and can be maximized within the thermal constraints of the system.

The modeling framework and the obtained design considerations for a system with a low variation in mutual inductance have been taken into account in the design of a CET system entirely integrated in a novel type of planar motor in which the translator is magnetically suspended underneath the stator. The array of thin primary coils is located inside the airgap of the motor, and four secondary coils are located on the translator. Each of the secondary coils receives energy from three simultaneously-energized adjacent primary coils. The set of energized coils dynamically switches with respect to the movement of the secondary coils. A prototype of this unique system has been manufactured. The integrated CET system supplies an average power equal to 230 W to the moving part of the planar motor. Furthermore, a variation in output power equal to 32% and an efficiency of 71% has been obtained along the stroke of the moving secondary coils.

Overall, this thesis presents ready-to-use theory, a completed set of equations, and magnetic, electrical and thermal models, applicable for research and design of contactless energy transfer systems as the replacement of cabled connections, in, for example, linear or planar motors.

Contents

Nomenclature

Symbols

symbol	unit	description
A	m^2	geometrical area
$\vec{A}$	Wbm^{-1}	magnetic vector potential
a	ms^{-2}	accelaration
a	-	turn ratio in a tranformer
a	-	coefficients of a Fourier series
$\vec{B}$	T	magnetic flux density
b	-	coefficients of a Fourier series
C	F	capacitance
C	T	source term in magnetic field equations
C_{st}	$\mathrm{Wm}^{-3}\mathrm{Hz}^{-\gamma_{st}}\mathrm{T}^{-\zeta_{st}}$	constant in the Steinmetz equation
c	-	coefficients of the field equations
c_l	m	half length of a current-carrying bar
c_w	m	half outer width of a coil
c_{iw}	m	half inner width of a coil
D	m	diameter
D	-	number of calculation points in the xy-plane
$\vec{D}$	Cm^{-2}	electric flux density
$\vec{E}$	Vm^{-1}	electric field strength
F	N	force
f	Hz	frequency
$\vec{H}$	Am^{-1}	magnetic field strength
h	m	height
h_{con}	$\mathrm{Wm}^{-2}\mathrm{K}^{-1}$	convection heat transfer coefficient
h_r	$\mathrm{Wm}^{-2}\mathrm{K}^{-1}$	linearized radiation heat transfer coefficient
I	A	current
i	A	instantaneous current

symbol	unit	description
J	Am^{-2}	current density
$\vec{J}$	Am^{-2}	current density
j	-	geometrical coefficient of the current density distribution
K	-	number of energized primary coils
k	-	magnetic coupling factor
k	m^{-1}	propagation constant
k_f	-	packing factor
L	H	self-inductance
L_{lk}	H	leakage inductance
L_m	H	magnetizing inductance
l	m	length
l_s	m	length of a slot or cavity
M	H	mutual inductance
M	-	total number of harmonics y-direction periodic region
$\vec{M}$	Am^{-1}	magnetization
m	-	harmonic number y-direction periodic region
m	kg	mass
N	-	number of turns
N	-	total number of harmonics x-direction periodic region
n	-	harmonic number x-direction periodic region
n_l	-	number of layers of turns in a coil
P	W	power
P_{ave}	W	average output power of a CET system
P_{out}	W	instantaneous output power of a CET system
$\vec{P}$	Cm^{-2}	polarization
Q	-	quality factor of a resonant circuit
q	Wm^{-3}	volume power density
R	Ω	resistance
R_{load}	Ω	load resistance
R_{th}	$\mathrm{m}^2\mathrm{KW}^{-1}$	thermal resistance
$\vec{r}$	-	vector between two points
r	m	radius
r	m^{-1}	propagation constant slotted region
S	-	surface
T	°C	temperature
t	s	time
$\mathbb{T}$	T^2	Maxwell stress tensor
V	V	voltage
V	-	total number of harmonics x-direction non-periodic region

symbol	unit	description
v	-	harmonic number x-direction non-periodic region
v	V	instantaneous voltage
v	ms^{-1}	velocity
W	-	total number of harmonics y-direction non-periodic region
w	-	harmonic number y-direction non-periodic region
x, y, z	-	cartesian coordinates
α_l	-	constant linear description of the length of a trapezoidal bar
β	-	constant related to the current density description of a trapezoidal bar
β_r	-	constant in the calculate of the ac-resistance
γ	m^{-1}	propagation constant electrical conducting region
γ_{st}	-	exponent for frequency in Steinmetz equation
Δ	m	displacement
ΔM_{tot}	-	variation in mutual inductance
ΔP_{out}	-	variation in output power
ΔT	K	difference in temperature
δ	m	skin depth
ϵ	Fm^{-1}	electric permittivity coefficient
ϵ_0	Fm^{-1}	permittivity of free space
ε	-	thermal emissivity
ζ	-	periodical function
ζ_{st}	-	exponent for the magnetic flux density in Steinmetz equation
η	%	efficiency
θ	rad	angle
κ	$\mathrm{Wm}^{-1}\mathrm{K}^{-1}$	thermal conductivity
λ	Wb	flux linkage
μ	Hm^{-1}	permeability
μ_0	Hm^{-1}	permeability of vacuum
μ_r	-	relative permeability
ρ	$\Omega\mathrm{m}$	electrical resistivity
ρ	Cm^{-1}	electric charge density
σ	Sm^{-1}	electrical conductivity
σ_{SB}	$\mathrm{Wm}^{-2}\mathrm{K}^{-4}$	Stefan-Boltzman constant
τ	m	pitch
Φ	Wb	flux
φ	A	magnetic scalar potential
χ_m	-	suspectibility
ω	m^{-1}	spatial frequency
ω	$\mathrm{rad}s^{-1}$	radial frequency

Subscripts

subscript	description
0	initial value
ac	alternating current
acc	accelaration
amb	ambient
ave	average
bus	dc-bus
bw	bundle width
c	coil
cc	cosine-cosine
cs	cosine-sine
$cond$	conduction
$conv$	convection
dc	direct current
fsc	free surface charge
hm	harmonic model
$litz$	Litz wire
max	maximum
$mech$	mechanical
min	minimum
p	primary
o	operation point
res	resonance
rms	root mean square
s	secondary
ss	sine-sine
sc	sine-cosine
$susp$	suspension
tot	total
$torq$	torque

Abbreviations

abbreviation	explanation
3D	three-dimensional
ac	alternating current
CET	contactless energy transfer
dc	direct current
FEM	finite element method
MEC	magnetic Equivalent circuit
SQP	sequential quadratic programming
TEC	thermal equivalent circuit

1

Introduction

Contactless Energy Transfer (CET) systems are the solution to overcome the limitations of traditional methods for the supply of electrical energy to objects with a planar movement. Consider for example, industrial applications such as high-speed positioning systems or electrical vehicles. Traditionally, energy is supplied to a moving object by means of a physical connection, for example, a moving cable, or energy storage is established on a moving object by means of a battery. A cabled connection limits the movements to predefined tracks and increases the mechanical friction, the mass, and the stiffness. However, a constant and efficient flow of energy to the moving object is guaranteed by a cabled connection. Storage of energy on moving objects improves the freedom of movement, but also increases the weight of these objects, and the finite storage capacity requires regular recharging. A CET system installed along the entire stroke of a moving object overcomes the limitations of moving cables and energy storage.

Since the creation of the planet earth, energy has been transferred contactlessly from the sun to the earth. It lasted to end of the 19th century until the electromagnetic fields of the sun could be directly converted into electricity because of the invention of the photoelectric cell [41]. At the same time, Nikola Tesla demonstrated the ability to send energy, retrieved from an electrical source, contactlessly from one to another terminal over short distances [16, 100, 120]. The principles of a CET system with magnetic resonance, applied by Tesla, are similar to the techniques used nowadays. With the development of the semiconductors in the 20th century, the frequency of the alternating current was increased, which im-

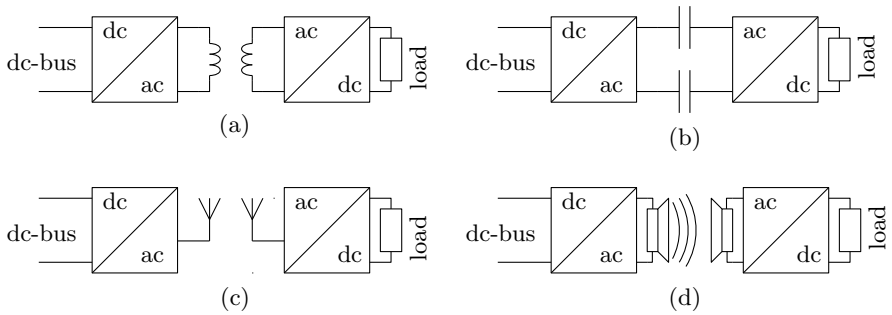

Figure 1.1: Block diagram of an (a) inductive, (b) capacitive, (c) far-field, and (d) acoustic CET system.

proved the energy transfer capability of CET systems. In the last decades, research has been conducted to CET technology for applications, varying from contactless charging platforms for mobile phones and laptops [118, 135] where a few watts are transferred across an airgap in the order of millimeters to electrical vehicles, in which kilowatts are transferred across an airgap of the order of 20 cm [18, 98, 99].

1.1 Contactless energy transfer principles

A CET system generally consists of four energy conversion steps. In the first step, a high frequency alternating current is created, usually from a dc-source. This high frequency alternating current produces either a magnetic field, electric field, electromagnetic field or an acoustic wave, which is used to transfer the energy contactlessly from the source to the receiver in an inductive, capacitive, far-field or acoustic coupling, respectively. The energy is recovered at the receiver, and, in a final step, the electrical energy is converted towards to requirements of the load. The different conversion principles are visualized in the four block diagrams in Fig. 1.1, where a CET system with a dc input and output is taken as an example.

Inductive coupling
In an inductive coupling, energy is transferred contactlessly between two coils by means of linked magnetic flux, as schematically shown by the block diagram in Fig. 1.1(a). Similar to a conventional transformer, an alternating current in a (primary) coil is the source of the magnetic flux. The time-varying magnetic field is linked with another (secondary) coil and induces a voltage across that coil. Comparable to a conventional transformer, a high magnetic coupling is desired to obtain an efficient transfer of energy in a CET system. However, because of the airgap between primary and secondary coils, the magnetic coupling in a CET

system is often low and resonance techniques have to be applied to improve the energy transfer capability [21]. In a resonant inductive coupling, the frequency of the alternating current is matched with the resonance frequency of a capacitor and the inductance of the coil. The capacitance in the resonant coupling can be either the parasitic capacitance of a coil or an additional capacitor in the electrical circuit. The resonant technique creates a path with a low impedance for the current alternating at the resonance frequency, and, thereby, energy can be efficiently transferred even in CET systems with a low magnetic coupling. A resonant inductive coupling typically operates in the order of tens or hundreds kilohertz.

The output voltage of a CET system is almost equal to the input voltage of the system and the turn ratio, if the resistance of the primary and secondary coils is negligible with respect to the impedance of the mutual inductance. The impedance of the mutual inductance linearly increases with the resonance frequency. Therefore, a resonance frequency in the order of hundred kilohertz does not only result in a resonance capacitor with a low value, but also reduces the volume of the primary and secondary coils while the transfer remains efficient.

A wide range of contactless energy transfer systems by means of an inductive coupling exits, varying from low-power systems with an airgap in the order of a meter between the coils to high-power systems with an airgap of several millimeters and cores of ferromagnetic material around the coils to guide the magnetic flux as presented in the overview given in [54]. A CET system is able to transfer energy through different kind of materials as long as these materials do not have an electrical conductivity. Examples of energy transfer systems by means of an inductive coupling is further explored in Section 1.2.

Capacitive coupling

In a capacitive coupling, energy is transferred contactlessly by means of electric fields between two sets of capacitive plates, as shown in Fig. 1.1(b) [54, 57, 121]. Two sets of capacitive plates are required to create a path for the current flow between the primary and secondary side of the capacitive coupling, compared to a single set of coils in an inductive coupling. The capacitance of a capacitive coupling is an important measure for the amount of energy which can be transferred. Since the capacitor value is inversely proportional to the airgap length, a capacitive coupling is only implemented in applications with small airgaps. Furthermore, the energy transfer is limited by the allowable voltage across the capacitive plates

$$v_c = \frac{i_c}{\omega C}, \tag{1.1}$$

where i_c is the current through the capacitive plates, ω the operating frequency, and the C capacitance of the plates. A higher output power can be obtained by increasing the capacity of the capacitive plates, i.e. enlarging the area of the

plates. This could be undesired in a capacitive coupling with a horizontal airgap between the primary and secondary side with respect to the involved volume. A capacitive coupling operates typically at high frequencies, $\omega \geq 10^6$ rads^{-1}, and an inductor could be placed in series with the capacitive plates to operate the system at resonance [54]. A CET system with a capacitive coupling can be optimized by making a trade-off between the frequency and the value of the capacitor, i.e. the switching losses, and the area of the capacitive plates. CET systems, that are realized by means of an capacitive coupling, have a maximum output power between 5-50 W and an efficiency of 50% [54]. Nevertheless, an advantage of the capacitive coupling is that it can operate nearby electrical conducting materials, which is not possible for an inductive coupling.

Far-field electromagnetic coupling
Far-field or microwave technology is another possible principle for a CET system, which applies radiative electromagnetic fields instead of the non-radiative near fields as used in the inductive and capacitive coupling. In a far-field electromagnetic coupling, a transmitter in combination with a beam control generates the electromagnetic waves which are received by a rectenna and transferred back to electrical energy, as shown in Fig. 1.1(c). These CET systems are able to transfer energy in the order of 30 kW across a distance of 1.5 km, and efficiencies between 80%-90% are achieved [16, 70]. However, when these systems are utilized over longer distances, their practical application becomes limited because of diffractive losses and the large dimensions of the antennas, respectively [23, 70].

Optical coupling
Optical systems operate with radiative electromagnetic fields [23, 54]. In an optical coupling, a beam of light, generated by a laser, is sent towards a photovoltaic diode. The photovoltaic diode converts the light back into electrical energy. An optical coupling is able to transfer up to 10 W with an efficiency varying between 20%-50% [90, 97]. A disadvantage of an optical coupling is the required line-of-sight.

Acoustic coupling
Energy could be transferred not only by means of electromagnetic fields, but also by acoustic waves. In an acoustic coupling a pressure wave is generated by a piezoelectric actuator, which can travel through different kinds of media such as, air, living tissue and metal. Along the path of the sound wave, a receiving transducer is positioned to transfer the motion of the wave back into electrical energy, as schematically shown in Fig. 1.1(d). Through air, an acoustic coupling is able to transfer power levels below 1 mW with a maximum efficiency of 17%, but through a solid medium, such as a metal wall, power levels up to a 1 kW with an efficiency of 84% can be reached [54, 93]. Contrary to the other methods, an acoustic coupling is able to transfer energy through electrical conducting materials.

Comparison
Considering a planar moving object with an unlimited stroke in which the energy, in the order or a few hundred watts, is provided by a CET system, the induc-

tive coupling is the most suitable technological solution. Firstly, an optical and far-field coupling require a line-of-sight, which cannot always be guaranteed in a system with a planar movement. Secondly, the maximum power levels, so far demonstrated in an acoustic and capacitive coupling, are low, 1 mW and 50 W, respectively [54, 93]. Thirdly, an inductive coupling gives a wide range of solutions in terms of the airgap length, the coil dimensions and the amount of energy which can be transferred.

1.2 Inductive contactless energy transfer systems

Most of the CET systems, by means of an inductive coupling, are designed for energy transfer in stationary applications, i.e. both the primary and secondary coils are not moving during the transfer of energy. These stationary systems have in common that they are designed for a specific distance between an aligned primary and secondary coil, at which the system is operating at magnetic resonance, and the maximum energy transfer is obtained. Such a stationary systems have an output power and efficiency which are extremely position dependent and drop significantly if the primary and secondary coils are not aligned [25, 27, 67].

Considering a planar moving object, the position dependency of a CET system results in a variation in the energy transfer. This is a disadvantage compared to an energy supply by means of a physical connection. To avoid a varying output power, electrical energy can be temporarily stored on the moving object and a continuous flow can be delivered to the embedded electronics. Another solution is to ensure that the system remains operating at resonance while the secondary coil is moving with respect to the primary coil. To establish resonance, the frequency of the alternating current should be matched with the resonance capacitance and leakage inductance of the inductive coupling. To establish this match during the movement of the secondary coil, the frequency of the alternating current can be modified by a self-tuning dc-ac converter [29]. Instead of a variable resonance frequency, the resonance capacitor can be implemented by means of a variable capacitor and the capacitance value can be modified as a function of position of the moving object. In the magnetic domain, a constant mutual inductance can be established along the trajectory of the secondary coil, such that the leakage inductance remains unchanged and operation at resonance is ensured along the trajectory of the moving object.

In the next sections various examples of CET systems designed for a secondary coil with a rotating, linear or planar movement are presented. Each system is designed for a different application, and, therefore, has a different output power.

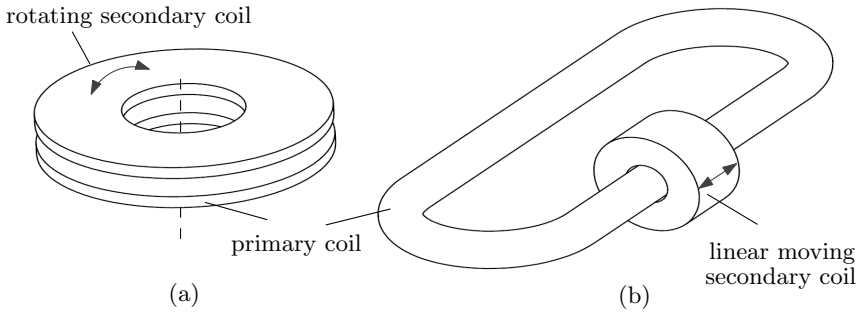

Figure 1.2: Schematic overview of: (a) a rotary transformer [7], and (b) a sliding transformer [8].

1.2.1 Systems with a rotating secondary coil

A CET system with a rotating secondary coils and a constant output power can be found in a rotary transformer. A rotary transformer consists of two axial or two radial symmetrical coils, from which one of them is rotating with respect to the other side, as illustrated for two axial coils in Fig. 1.2(a). Rotary transformers are, for example, applied to replace slip rings in a rotating motor [1, 77]. A rotary transformer exhibits a mutual inductance, which is independent of the rotation of the secondary coil because of the axisymmetry, and, therefore, provides constant flow of energy from the primary to the secondary side [96, 104].

1.2.2 Systems with a linearly moving secondary coil

A CET system with a linearly moving secondary coil and a constant output power can be found in a sliding transformer. A sliding transformer consists of a long primary coil, which forms a loop along the trajectory of a shorter secondary coil, as illustrated in Fig. 1.2(b). The secondary coil, which can freely move along the primary coil, envelopes the primary coil or is embedded in a structure, and closes a ferromagnetic path for the magnetic flux of the primary coil [8, 15]. The advantage of a sliding transformer is a constant magnetic coupling between the primary and secondary side since the magnetic geometry does not change as a function of position. Furthermore, multiple secondary coils can be applied to one long primary coil [88]. A major drawback is the fact that the long primary coil creates a large leakage field, which does not contribute to the energy transfer and may cause electromagnetic interference with electronic devices in the neighborhood of the primary coil [7]. An alternative to this large primary coil is to replace the coil by a long magnetic core, which guides the magnetic fields of a short primary coil to the moving secondary coil [61].

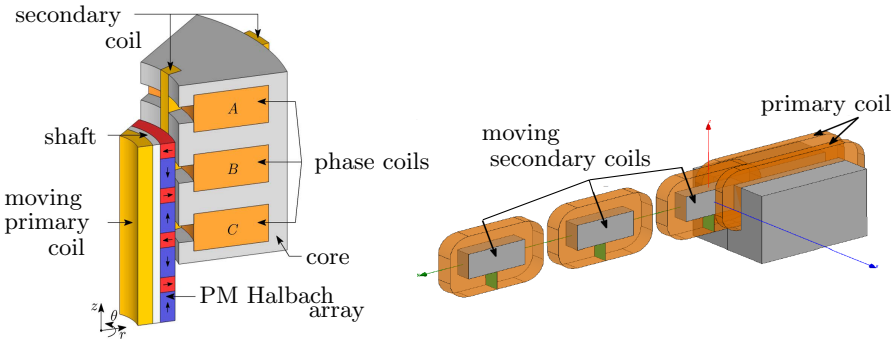

Figure 1.3: Schematic overview of: (a) a CET system integrated in a tubular linear synchronous permanent-magnet motor [58], and (b) a linear CET system with a segmented primary coil and multiple secondary coils [30].

Sliding transformers are, for example, used to replace the moving cables in a linear motor and are often not integrated but placed next to the linear motor [78, 101]. However, recently, the integration of CET systems is taken into account in the design of mechatronic systems. For example, primary coils are integrated in the design of the back-iron of a linear synchronous permanent-magnet motor [60, 62]. A second example is an electromagnetic bearing for an elevating system, in which the secondary coil is wound around the center leg of an omega-shaped core. In this system, the primary coil is embedded in the guide rail of the elevator and the system is able to transfer 200 W with an efficiency of 70% [5]. A final example is a tubular linear synchronous permanent-magnet motor, in which the primary coil is placed inside the hollow shaft and the secondary coil is wound around the core in the axial direction of the motor, as illustrated in Fig. 1.3(a) [58, 59]. This integrated system is able to transfer 800 W with an efficiency of 80%.

Although the CET systems are integrated in linear motors, the long primary coil remains present in all these examples. A solution to avoid this problem can be obtained by segmentation of the primary coil and active control of the primary segments [30]. A schematic overview of a segmented CET system for a linear movement is shown in Fig. 1.3(b), in which a segment of the primary side transfers energy to the three adjacent secondary coils. The dc output voltages of the secondary coils are connected in series, resulting in an output power of 1 kW, with a variation of 5% along one secondary coil segment with a system efficiency of 95%.

Linearly moving objects with a horizontal airgap between the primary and secondary coils can be, for example, found in on-road charging of electrical vehicles.

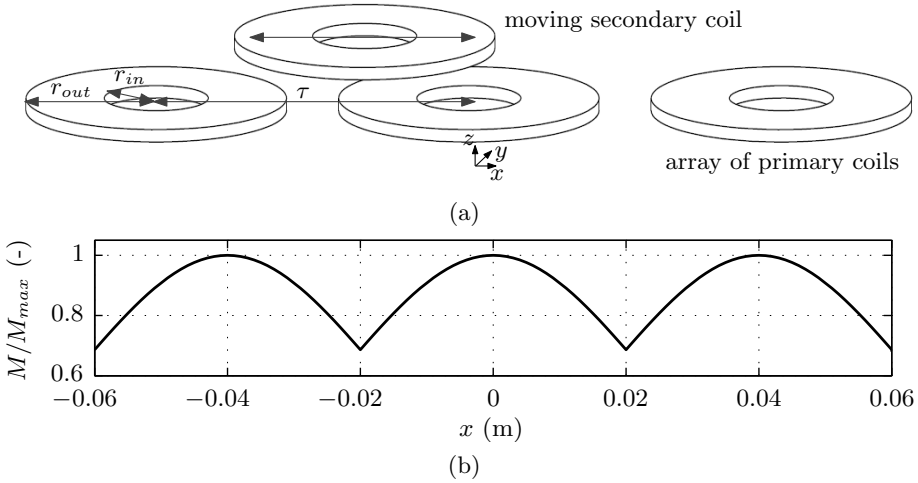

Figure 1.4: Mutual inductance of three primary coils with a single secondary coil: (a) schematic overview of the coils, and (b) mutual inductance with respect to its maximum value for the round coils with r_{in}=5 cm, r_{out}=15 cm, and τ=40 cm.

The energy transfer in these on-road charging system is extremely position dependent because of the segmented primary coil [42, 63]. Such a on-road charging system can be represented by multiple stationary CET system behind each other, as for example illustrated in Fig. 1.4(a). The figure shows three primary coils and a secondary coil with a linear movement along the primary coils. The mutual inductance seen by the secondary coil is shown in Fig. 1.4(b) and has a variation of 30% between the maximum and minimum value. This results in a varying energy transfer between the primary and secondary side. Therefore, energy has to be temporarily stored in the electrical vehicles which are on-road charged by a CET system. The combination of frequently contactless recharging of the batteries and storage of a small amount of energy in the batteries, does not only enlarge the range of the electrical vehicle, but it also reduces the required battery capacity and, thereby, the weight of the vehicle [50].

The replacement of a single-phase CET system by a three-phase one, is a way to remove the position dependency in a CET system for a linear movement with a horizontal airgap between the primary and secondary coils [56]. Although the output power becomes constant while the secondary coil is moving along the track, the efficiency of the system decreases dramatically towards 19% as concluded in [68].

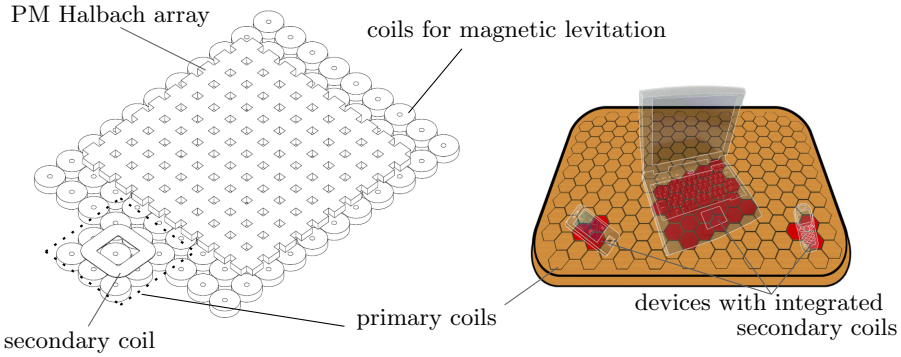

Figure 1.5: Schematic overview of (a) a CET system integrated in a planar motor [13], and (b) a CET-charging pad for mobile devices [118].

1.2.3 Systems with a secondary coil with a planar movement

A CET system, which transfers energy to a device with a planar movement, usually consists of an array of primary coils and one or multiple secondary coils. Similar to a CET system for a linear movement, the horizontal airgap between the primary and secondary side results in a position dependent magnetic coupling [2, 26, 99]. A solution to avoid this position dependency is to optimize the geometry of the secondary coil with respect to the primary coils [12].

In [13], a CET system is connected next to a planar motor, as illustrated in Fig. 1.5(a). The coil array at the stationary side of the planar motor embeds coils for both the magnetic levitation of the translator and the contactless energy transfer system. The coils underneath the permanent magnet array with quasi Halbach magnetization levitate and propel the translator of the planar motor. The nine coils underneath the secondary coil are able to transfer energy contactlessly to the secondary coil connected to the levitated translator. Since a single coil is able to fulfil only one of the two functions, the stroke of this planar motor is limited. The secondary coil overlaps four round primary coils, from which one of them is activated for the transfer of energy. The system energizes the next primary coil if symmetry is obtained with respect to the position of the secondary coil above the array of primary coils. The system has a variation in the magnetic coupling of 6% with respect to the center of the secondary coil moving along the surface of a single primary coil, and is able to transfer 150 W with an efficiency of 50%.

A constant transfer of energy is not only a beneficial property for planar motors. Similar properties are required for planar pads for charging mobile devices such as mobile phones or laptops, as shown in Fig. 1.5(b). In these applications the

secondary coil is not moving, however, because the secondary coil can be placed at any position of the planar charging pad, the system should be able to transfer an equal amount of energy at every position. Similar to the CET system integrated in the planar motor, as described in the previous section, in [118] the dimensions of the secondary coil are optimized for a constant mutual inductance at a number of different positions above three adjacent hexagonal primary coils. Instead of a single layer of primary coils, multiple layers of primary coils can be positioned on top of each other and shifted with respect to each other. With this topology an energy transfer is obtained with a variation of 17% above the middle of the charging path [43]. Instead of multiple layers, in [135], a variation in mutual inductance of 18% is found in a charging pad with a single layer of primary coils wound around a tooth and a secondary coil with a ferromagnetic plate behind the coil. The variation in output power as a function of position can be further reduced by transferring energy to multiple secondary coils [19]. A final solution to scale-down the position dependency of a CET system is to place multiple secondary coils orthogonally with respect to each other. On a system level it brings a lower variation in output power compared to a single secondary coil solution [69].

1.3 Research goal and objectives

Transferring energy contactlessly by means of an inductive coupling to an object with a planar movement can be realized by different approaches as presented in the previous section. None of the examples proposes a solution in which a position-independent CET system is integrated in a planar motor, and is able to transfer a similar amount of energy to the moving part along the entire stroke of the planar motor. This thesis concerns the three-dimensional modeling, analysis, design and realization of a position-independent contactless energy transfer system integrated in a planar motor, which is able to transfer energy along the infinite stroke of the motor. In particular, the following objectives are identified:

- **Extension of the three-dimensional harmonic modeling technique to describe the magnetic fields around coils**
  Discussed in Chapter 2
  The harmonic modeling technique is a modeling method which is used in two-dimensional periodical and axisymmetric structures to model the magnetic fields around coils and magnets. The method is able to take different kind of boundaries and materials into account, such as slots or conducting materials. For three-dimensional structures, this technique has only been applied to problems with permanent magnets as the sources of the magnetic fields in combination with a magnetic scalar potential formulation. The objective is to extend the harmonic modeling technique by formulating a solution for the three-dimensional magnetic vector potential and to obtain

the magnetic fields around a coil including different kind of boundaries such as slots, cavities, and electrical conducting materials.

- **Development of a multi-physical model for a contactless energy transfer system for a planar movement**
  Discussed in Chapters 3 and 4
  Generally, a contactless energy transfer system by means of an inductive coupling consists of one primary and one secondary coil. In case of a linear or planar movement, multiple primary and secondary coils can be used in the transfer of energy. The magnetic and an electrical equivalent circuit model for multiple primary and secondary coils are coupled with a thermal model, in such a way that the parameters and performances of a contactless energy transfer system can be accurately predicted.

- **Investigation of the position dependency of a contactless energy transfer system with flat coils for a linear and planar movement**
  Discussed in Chapter 4
  The literature suggests different solutions to reduce the position dependency of a contactless energy transfer system by means of an inductive coupling, such as the presence of ferromagnetic structures around the coils, modification of the geometry of the coils with respect to the primary and secondary side, and the transfer between multiple primary coils towards a single secondary coil. Different methods are analyzed with respect to the position-dependency of a contactless energy transfer system with a constant energy transfer along the linear or planar trajectory of the secondary coil. The objective is to obtain a set of design considerations for a position-independent contactless energy transfer system.

- **Design of an integrated and position-independent contactless energy transfer system for a magnetically suspended planar motor**
  Discussed in Chapter 5
  The obtained design considerations concerning the position dependency are taken into account in the design of a contactless energy transfer system integrated in a new type of planar motor. The planar motor consists of a wireless translator which is magnetically suspended and propelled underneath a stationary frame. The design of the planar motor with integrated CET system involves three challenges. Firstly, for the suspension and propulsion of the translator, a magnetically suspended planar motor needs to be researched [79]. Secondly, for a complete wireless operation of translator, a CET system has to be designed which transfers an equal amount of energy at every position of the translator. Thirdly, both the planar motor and the CET system need to be integrated into each other and should be able to operate simultaneously. The objective is to design a position-independent CET system for a secondary coil with a planar movement, which can be integrated in the planar motor such that the transferred energy can be applied to power the motor.

- **Realization and test of the contactless energy transfer system integrated in the planar motor**
  Discussed in Chapter 6
  A prototype of the planar motor with integrated CET system is designed and manufactured. The predicted performance of the realized contactless energy transfer system is experimentally verified, and the effects of the integration on the CET system into the planar motor are analyzed.

The research on the magnetically planar motor with integrated CET system is carried out by two PhD students. This thesis concerns the modeling, analysis and design of the CET system and the thesis of T.T. Overboom [79] focusses on the modeling, analysis and design of the planar motor.

1.4 Outline of the thesis

This thesis consists of seven chapters, including this introduction, and presents the modeling, design and integration of a contactless energy transfer system by means of an inductive coupling for a magnetically suspended planar motor. As emphasized in the introduction, the contactless energy transfer system should be position independent and supply a sufficient amount of output power to the load at the moving part of the system.

The modeling of the inductive coupling in the CET system is presented in Chapter 2 by describing the electromagnetic fields between the coil with the harmonic modeling method. To apply this method with three-dimensional current sources, the harmonic modeling method is extended by formulating the three-dimensional magnetic vector potential for both static and quasi-static field conditions. The magnetic vector potential is given for different type of materials and periodicities, such that the harmonic modeling method is able to consider ferromagnetic boundaries, cavities and electrical conducting materials including the eddy-current reaction field. To be able to incorporate a coil as the source of the magnetic fields in the harmonic model, the current density distribution is modeled by four current-carrying bars. To model a coil, three different combinations with four bars are presented in the chapter and the configurations are compared to each other with respect to the magnetic flux density distribution and the self-inductance of coils. Finally, the electromagnetic model is applied to obtain the electromagnetic quantities, such as the self- and mutual inductances, which are used as the input for the electrical model of the inductive coupling.

The electrical equivalent circuit of the CET system is presented in Chapter 3. The transformer T-model is extended for an energy transfer between multiple primary coils and a single secondary coil. Furthermore, resonance techniques are included

in the system to provide a magnetic resonance at the operating frequency of the system. The conduction losses limit the current flow in the CET system, and, thereby, reduce the energy transfer. To maximize the output power, a thermal model of the CET system is presented. The thermal model completes the modeling framework of the CET system, which predicts the system performances starting from the dimensions through estimation and analysis of the magnetic, electrical and thermal loading up to the output power of the system.

In Chapter 4, the position-dependency of the CET system is analyzed by using the modeling framework in terms of the variation in mutual inductance and average output power along the trajectory of the secondary coil. The influence of the different geometrical and electrical parameters is researched, and the results are incorporated in a design algorithm for a CET system with a secondary coil with a linear or planar movement. Furthermore, the design algorithm is applied to investigate the position dependency of the CET system for different aspects of the primary coil array, and different ferromagnetic structures around the coils.

The obtained design considerations for a position-independent CET system are applied in Chapter 5 for the design of a CET system with a low variation in output power integrated in a magnetically suspended planar motor. The design of the planar motor is described in [79]. The design of the CET system and its integration in the planar motor are intensively discussed in this chapter.

The manufactured prototype of the planar motor with integrated CET system is presented in Chapter 6, and the predicted performance indexes of the CET system are experimentally verified. Furthermore, the effects of the integration of the CET system in the planar motor with respect to the performance of the CET system and the planar motor are measured, analyzed, and discussed.

Finally, conclusions of the research and further recommendations are presented in Chapter 7.

2

Three-dimensional magnetic field modeling

Electromagnetic fields are figuratively the beating heart of a Contactless Energy Transfer (CET) system. These fields are generated by the time-varying current flowing through a primary coil and induce a time-varying voltage across a secondary coil. In other words, the energy transfer is related to the amount of magnetic flux which is generated by the primary coil and is linked with the secondary coil. To model this mutual flux, or the mutual inductance in the equivalent electrical circuit of a CET system, an accurate prediction of the magnetic fields needs to be obtained.

In the last decades, it has become a trend to model the (quasi-)static magnetic fields of periodical problems by means of the harmonic modeling method. The harmonic modeling method is a method which gives a direct solution of the Maxwell equations in terms of harmonic functions. The method is first introduced in the book of Hague [33] and has been further developed such that it can be applied to different types of two-dimensional problems, such as rotary, linear and tubular machines both for salient and non-salient structures [14, 31, 46, 83, 136]. In the past years, the harmonic modeling technique is extended for three-dimensional problems and is frequently applied to determine the magnetic fields for these kind of problems with permanent magnets as the sources of the magnetic fields [9, 22, 40, 46, 47, 72, 73]. Since no time-varying current source is present in these three-dimensional problems, an expression for the magnetic fields could be ob-

tained by the magnetic scalar potential. In case of a coil, a time-varying current source is present, and, therefore, a solution for the magnetic fields has to be found by means of the magnetic vector potential. In literature two examples can be found in which a time-varying current source is modeled with the three-dimensional magnetic vector potential. In [89] a line current is modeled and in [133] the magnetic vector potential is solved with the finite difference method.

This chapter presents the extension of the three-dimensional harmonic modeling method with coils as the source of the magnetic fields, including the incorporation of the eddy-current reaction fields and various salient and non-salient three-dimensional structures. The chapter starts with an overview of various three-dimensional modeling methods which can be applied to model the magnetic fields around a coil, and their advantages and limitations are listed. The following sections of this chapter introduce the three-dimensional magnetic vector potential and the developed three-dimensional current density distributions for the coils. The obtained expressions for the magnetic fields are applied to calculate the electromagnetic quantities, such as the self- and mutual inductances of a coil. Parameters which are crucial for the design of a contactless energy transfer system.

The contributions of this chapter are published in:

J. P. C. Smeets, T. T. Overboom, J. W. Jansen, and E. A. Lomonova [2011], 'Three-Dimensional Magnetic Field Modeling for Coupling Calculation Between Air-Cored Rectangular Coils', *IEEE Transactions on Magnetics* **47**(10), pp. 2935-2938.

J. P. C. Smeets, T. T. Overboom, J. W. Jansen, and E. A. Lomonova [2012], 'Mode-Matching Technique Applied to Three-Dimensional Magnetic Field Modeling', *IEEE Transactions on Magnetics* **48**(11), pp. 3383-3386.

J. P. C. Smeets, T. T. Overboom, J. W. Jansen, and E. A. Lomonova [2013], 'Three-Dimensional Analytical Modeling Technique of Electromagnetic Fields of Air-Cored Coils Surrounded by Different Ferromagnetic Boundaries', *IEEE Transactions on Magnetics* **49**(12), pp. 5698-5708.

J. P. C. Smeets, T. T. Overboom, J. W. Jansen, and E. A. Lomonova [2014], 'Inductance Calculation nearby Conducting Material', *IEEE Transactions on Magnetics* **50**(11), pp. 1-4.

2.1 Three-dimensional modeling methods

The calculation of the magnetic fields in a contactless energy transfer system starts from Maxwell's equations [28]. The Maxwell's equations are a set of four generalized equations which describe the electromagnetic field phenomena. In differential form they are given by

$$\nabla \times \vec{H} = \vec{J} + \frac{\partial \vec{D}}{\partial t}, \qquad \text{Ampère's circuit law} \tag{2.1}$$

$$\nabla \cdot \vec{B} = 0, \qquad \text{Gauss' law for magnetism} \tag{2.2}$$

$$\nabla \times \vec{E} = -\frac{\partial \vec{B}}{\partial t}, \qquad \text{Faraday's law} \tag{2.3}$$

$$\nabla \cdot \vec{D} = \rho. \qquad \text{Gauss' law} \tag{2.4}$$

In these equations $\vec{H}$ is the magnetic field strength, $\vec{B}$ is the magnetic flux density, $\vec{E}$ is the electric field strength, and $\vec{D}$ is the electric flux density. The current density is $\vec{J}$ and ρ is the electric charge density. The Maxwell equations (2.1)-(2.4) are not a complete set. The following three constitutive equations provide a relation between the field strength and the flux density in a given medium

$$\vec{B} = \mu_0 \left(\vec{H} + \vec{M} \right), \tag{2.5}$$

$$\vec{D} = \epsilon_0 \vec{E} + \vec{P}, \tag{2.6}$$

$$\vec{J} = \sigma \vec{E}, \tag{2.7}$$

where the natural physical constants μ_0 and ϵ_0 are the permeability and the permittivity of free space, respectively, and σ is the electrical conductivity of a medium. The magnetization, $\vec{M}$, and polarization, $\vec{P}$, are the net magnetic and net electric dipole moment per unit volume, respectively. The relation between the magnetic field strength and the magnetization is related to the properties of the medium and is given by

$$\vec{M} = \chi_m \vec{H}, \tag{2.8}$$

where χ_m is the susceptibility of the medium. Based on this relation, (2.5) is rewritten to

$$\vec{B} = \mu_0 (1 + \chi_m) \vec{H}, \tag{2.9}$$

$$\vec{B} = \mu \vec{H}. \tag{2.10}$$

The permeability, μ, consists of the permeability of free space and the relative permeability of the specific material, μ_r,

$$\mu = \mu_0 \mu_r. \tag{2.11}$$

Different modeling methods can be applied to solve the Maxwell equations and to obtain an expression for the magnetic fields around a coil or permanent magnet. Often the quasi-static field theory is applied in which the four coupled first-order differential Maxwell equations can be rewritten in terms of two uncoupled second-order differential equations by expressing the variables in terms of the magnetic vector potential, $\vec{A}$, or magnetic scalar potential, φ. The magnetic vector potential is defined by

$$\nabla \times \vec{A} = \vec{B}. \tag{2.12}$$

If no currents are modeled, the magnetic scalar potential can be introduced as well according

$$\vec{H} = -\nabla\varphi. \tag{2.13}$$

The second-order differential equations are written in as a Poisson or Laplace equation, a form of differential equations which can be solved by means of standard mathematical expressions. An overview of possible three-dimensional modeling methods which may be applied to model the magnetic fields around a coil is presented in the next sections.

The law of Biot-Savart

An often applied analytical modeling method to obtain the magnetic fields of a coil is the law of Biot-Savart, which gives a direct solution to the magnetic flux density. The law of Biot-Savart is a specific solution of the free-space Green's function, which may be applied to solve the Poisson equation in free space, $\mu = \mu_0$, [28]. The law calculates the magnetic flux density at a specific point with respect to a current flowing in a segment of a wire,

$$\vec{B} = \frac{\mu_0}{4\pi} \oint_c \frac{I d\vec{l} \times \vec{r}}{|r|^3}, \tag{2.14}$$

where I the current flowing through the wire, r the distance between the line segment $d\vec{l}$ and the point of interest, and c is the closed contour.

In case of a coil, the turns can be represented by segments or current-carrying bars [123–126]. To obtain the total amount of flux density, the law of Biot-Savart must

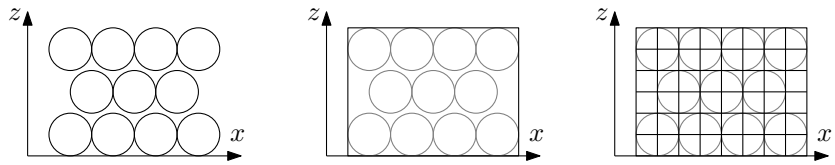

Figure 2.1: Schematic overview of the filament method for a cross-section of a part of a coil: (a) cross-section of a coil, (b) enclosed area by the windings of the coil, and (c) filament distribution in the enclosed area.

be applied to each segment and the separate contributions should be summed. In case of a relative thick turn with respect to the distance between the coil and the point of interest, this calculation may be rough and can be refined by applying the filament method [3, 6, 95, 117]. The filament method does not approach a coil as a number of individual turns, but as an enclosed volume in which the total current is equally distributed. The turns of a coil, as shown in the cross-section in Fig. 2.1(a), can be enclosed by a square area, Fig. 2.1(b), which can be divided into an imaginary number of filaments as shown in Fig. 2.1(c). Assuming a uniform current density distribution, the law of Biot-Savart can be applied to each filament instead of each turn.

The law of Biot-Savart can only be applied for coils surrounded by air. If a medium with a permeability is existing in the neighborhood of a coil, the imaging method has to be applied to replace the boundary by an imaginary source such that the distribution of the magnetic fields around the boundary remains identical without the physical presence of the boundary [45]. After applying the imaging method, the law of Biot-Savart can be applied to the real and imaginary sources to obtain an expression of the magnetic fields.

Harmonic modeling method

The harmonic modeling method is a second method which can be applied to solve the Poisson and Laplace equations. In this method, the Poisson and Laplace equations are solved by means of separation of variables, which leads to a solution for each harmonic as a product of the independent variables written as a Fourier series [31, 33]. The expression of the magnetic vector potential in terms of periodic functions reduces the geometry of the problem to a single period with periodic boundaries. The harmonic modeling method divides the geometry into horizontal regions, perpendicular to the direction of the periodicity. The regions distinguish from each other with respect to the properties of the medium, the existence of magnetic field sources, such as coils and magnets, and the spatial periodicity of the region. Each region has uniform properties, or consists of a combination of media with different properties, such as slots or cavities, which must be entirely enclosed in the direction of the spatial periodicity by infinitely-permeable ferromagnetic

material. This requirement limits the set of geometries which can be solved by the harmonic modeling method. For example, the magnetic fields around an iron tooth enclosed by air cannot be described by this method. To obtain a solution of the magnetic flux density, an expression for the magnetic vector potential is written for each region. These expressions are linked together by applying the boundary conditions around and between the regions, such that a unique expression for the magnetic fields is obtained.

The harmonic modeling technique is able to calculate the magnetic fields inside regions with materials with an electrical conductivity and/or a permeability and the eddy-current reaction field can be included in the model. Unfortunately non-linear materials properties cannot be taken into account. Finally, a large number of harmonics needs to be taken into account to model a relative small object in a large period which can be problematic for the numerical stability of this method.

Magnetic equivalent circuit method
The Magnetic Equivalent Circuit (MEC) method models a magnetic circuit analog to an electric circuit and follows from the integral form of Ampère's circuit law (2.1) and Gauss' law for magnetism (2.2). Compared to the law of Biot-Savart and the harmonic modeling method, the magnetic equivalent circuit method is able to model the flux density distribution inside ferromagnetic material and to take non-linear material properties into account. In the magnetic equivalent circuit, the flux paths are modeled by reluctances, and the sources of the magnetic fields are modeled as sources of magnetomotive force [94]. By solving Hopkinson's law, the magnetic flux flowing through the circuit can be obtained. Because of the discretization of the magnetic flux paths, prior knowledge of these paths is required, as, for example, shown in examples of a three-dimensional MEC models [4, 49, 52]. Therefore, this method is only suited for geometries with a small airgap, and is usually applied in geometries with coils wound around a core [104].

Finite element method
The Finite Element Method (FEM) is the most used numerical method to model the magnetic fields of complex three-dimensional structures. The method discretizes the magnetic problem into meshed elements, which are sufficiently small, such that a linear or quadratic variation may be assumed between two mesh points. Similar to the MEC method, this method requires prior knowledge of the magnetic fields to make a suitable mesh, i.e. a dens mesh in a volume with a strongly varying magnetic flux and a coarse mesh elsewhere. An expression of the magnetic fields is obtained by minimizing the total energy of the problem, which takes the boundaries between different types of medium and borders of the problem into account [91].

The advantage of the FEM in the modeling of three-dimensional problems is the ability to include non-linear material properties, irregular geometrical shapes and anisotropic materials. However, depending on the complexity of the structure, a large number of mesh elements needs to be taken into account to obtain an

accurate solution for the magnetic fields. For example, in case of conducting materials, several mesh layers per skin-depth need to be used to accurately model the eddy-currents.

Finite difference method
One of the oldest numerical methods is the finite difference method. This method discretizes an electromagnetic problem into a grid of lines, for example, parallel to the coordinate system. The nodal points are located at the intersection of two lines, for which a finite difference expression is obtained with the adjacent nodal points [10]. This set of equations is solved to obtain the magnetic fields. A disadvantage of this method is the constant grid, which does not guarantee a nodal point at all boundaries between the different media.

Comparison
A comparison is made among the different methods with respect to the ability to model the three-dimensional magnetic fields of a coil which may be surrounded by different type of structures and materials. The harmonic modeling method is a method which should be able to include different kind of materials and different types of boundaries, as shown by the two-dimensional electromagnetic problems which have been solved with this method [32]. Compared to the law of Biot-Savart, the harmonic modeling method is able to take a larger range of boundaries into account. The MEC method is only suited for problems with small airgaps and a ferromagnetic structure around the coils, which limits the possibility to calculate the magnetic fields around a coil located in air. The numerical FEM method could be applied, but, because of the required meshing of the problem after any geometrical modification, this method is not flexible in terms of a parametric search compared to an analytical method. Because of the flexibility and geometrical options of the harmonic modeling method it is chosen to extend this method by including the ability of coils as the source of the electromagnetic fields.

2.2 General solution of the three-dimensional magnetic vector potential

The harmonic modeling method is applied to obtain a solution of the magnetic fields in a periodic structure which is divided into regions. For each region, an expression of the magnetic vector potential is formulated, from which in combination with the boundary conditions a solution for the magnetic fields within the problem is obtained. In literature, only two-dimensional problems with a time-varying current source can be found, in which the magnetic fields are solved by applying the harmonic modeling method in combination with the one-dimensional magnetic vector potential, such as, for example, rotating or linear electrical machines [83, 136]. In these cases, the two-dimensional harmonic model is sufficient

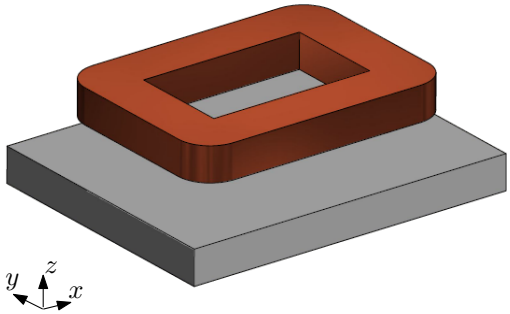

Figure 2.2: Schematic overview of an example of single period of a geometry which is solved by the harmonic modeling method.

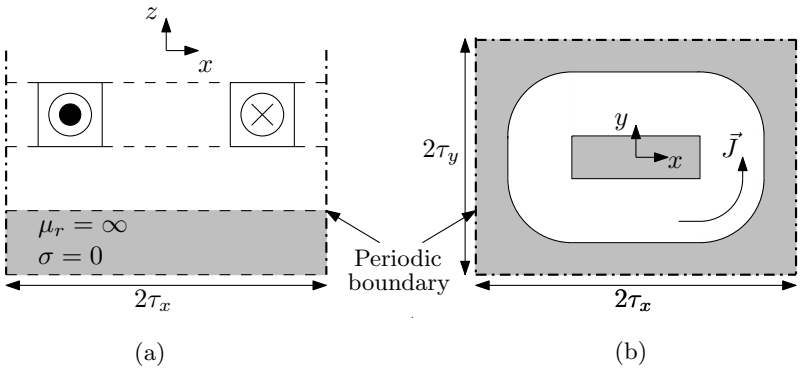

Figure 2.3: Example of a periodic geometry which is solved by the harmonic modeling method, a coil above an infinitely permeable ferromagnetic plate: (a) cross-section along y=0, and (b) top view.

since the part of the winding orthogonal to the direction of movement provides the major contribution to the interaction of the magnetic fields, and the influence of the end-windings may be ignored. In case of a planar movement, the complete coil contributes to the interaction of the magnetic fields and two-dimensional magnetic vector potential is not suitable, and, therefore, the problem needs to be solved by means of the three-dimensional magnetic vector potential.

An array of coils above a ferromagnetic plate is a typical geometry of a periodic problem which is solved by the three-dimensional harmonic modeling method. A single period of such a problem is shown in Fig. 2.2. Figure 2.3(a) shows the cross-section of the geometry along the y-axis. In the normal (z) direction, regions with different material properties and current sources can be identified. The periodicity in the tangential (x, y) direction can be visualized by the periodic boundaries as shown in the top view in Fig. 2.3(b).

In this next section the three-dimensional magnetic vector potential is formulated and solutions of the magnetic vector potential are given for different kind of regions.

2.2.1 Three-dimensional magnetic vector potential

The formulation of the magnetic vector potential starts with a set of assumptions. Firstly, the wave-length of the applied frequencies is assumed to be relative large compared to the region of interest. Therefore, any change in the magnetic fields is instantaneous across the whole region, and the quasi-static field theory may be applied. The quasi-static field theory ignores the variation of the electric flux density as a function of time

$$\frac{\partial D}{\partial t} = 0, \tag{2.15}$$

which reduces (2.1)-(2.4) to

$$\begin{aligned} \nabla \times \vec{H} &= \vec{J}, & (2.16)\\ \nabla \cdot \vec{B} &= 0, & (2.17)\\ \nabla \times \vec{E} &= -\frac{\partial \vec{B}}{\partial t}, & (2.18)\\ \nabla \cdot \vec{D} &= \rho. & (2.19) \end{aligned}$$

In the quasi-static field theory no time derivatives are present in (2.16) and (2.17). Even when the current source $\vec{J}$ is time dependent, $\vec{B}$ and $\vec{H}$ are calculated as if the system is static [28]. Furthermore, (2.16) implies that

$$\nabla \cdot \vec{J} = 0. \tag{2.20}$$

Secondly, it is assumed that the current in the coils and eddy-currents in electrical conducting materials are only flowing in the xy-plane,

$$J_z = 0. \tag{2.21}$$

Thirdly, the material properties of a medium are assumed to be linear, homogeneous and isotropic. Fourthly, in case of soft-magnetic materials, such as ferromagnetic plates and structures around non-periodic regions, the permeability is

assumed to be infinite, $\mu_r = \infty$. Finally, the solution of the magnetic vector potential must fulfil the Coulomb Gauge condition

$$\nabla \cdot \vec{A} = 0. \tag{2.22}$$

The magnetic vector potential is related to the magnetic flux density by

$$\nabla \times \vec{A} = \vec{B}, \tag{2.23}$$

and can be expressed as a function of the current density, by substituting (2.23) into (2.1), while taking the quasi-static field theory (2.15) and the constitutive relation (2.11) into account

$$\nabla \times \vec{H} = \vec{J}, \tag{2.24}$$

$$\frac{1}{\mu}\left(\nabla \times \vec{B}\right) = \vec{J}, \tag{2.25}$$

$$\frac{1}{\mu}\left(\nabla\left(\nabla \cdot \vec{A}\right) - \nabla^2 \vec{A}\right) = \vec{J}. \tag{2.26}$$

By applying the Coulomb Gauge condition, (2.26) reduces to

$$-\frac{1}{\mu}\nabla^2 \vec{A} = \vec{J}, \tag{2.27}$$

which is known as Poisson's equation. A solution of the magnetic vector potential can be obtained by solving this second order differential equation.

The current density is defined as the current flowing through an area and consists of one of the two components

$$\vec{J} = \vec{J}_{coil} + \vec{J}_{eddy}. \tag{2.28}$$

The first component, $\vec{J}_{coil}$, is related to the current density distribution of a coil in a region of air, which is further explored in Section 2.4. The second component, $\vec{J}_{eddy}$, is the current density distribution of the induced eddy-currents flowing in a region with an electrical conductive material, which are induced by time varying magnetic fields. An expression for the current density distribution related to the eddy currents in a conducting medium can be obtained by Faraday's law (2.3) in

combination with one of the constitutive relations (2.10), and can be written as a function of the material properties of a medium and the magnetic vector potential

$$\nabla \times \vec{E} + \frac{\partial \left(\nabla \times \vec{A} \right)}{\partial t} = \nabla \times \left(\vec{E} + \frac{\partial \vec{A}}{\partial t} \right) = 0, \tag{2.29}$$

$$\vec{J}_{eddy} = \sigma \vec{E} = -\sigma \frac{\partial \vec{A}}{\partial t}. \tag{2.30}$$

Taking the relation of the eddy currents and the magnetic vector potential into account, (2.27) can be rewritten as

$$\nabla^2 \vec{A} = -\mu \left(\vec{J}_{coil} - \sigma \frac{\partial \vec{A}}{\partial t} \right). \tag{2.31}$$

A mathematical expression of (2.31) in matrix form is given by

$$\nabla^2 \vec{A} = \begin{bmatrix} \frac{\partial^2 A_x}{\partial x^2} + \frac{\partial^2 A_x}{\partial y^2} + \frac{\partial^2 A_x}{\partial z^2} \\ \frac{\partial^2 A_y}{\partial x^2} + \frac{\partial^2 A_y}{\partial y^2} + \frac{\partial^2 A_y}{\partial z^2} \\ \frac{\partial^2 A_z}{\partial x^2} + \frac{\partial^2 A_z}{\partial y^2} + \frac{\partial^2 A_z}{\partial z^2} \end{bmatrix} = -\mu \begin{bmatrix} J_{coil_x} - \sigma \frac{\partial Ax}{\partial t} \\ J_{coil_y} - \sigma \frac{\partial Ay}{\partial t} \\ J_{coil_z} - \sigma \frac{\partial Az}{\partial t} \end{bmatrix}. \tag{2.32}$$

Since there is no current density in the z-direction, the magnetic vector potential in this direction is set equal to zero

$$A_z = 0. \tag{2.33}$$

This choice automatically defines the relation between the two remaining components of the magnetic vector potential in the x- and y-direction

$$A_y = -\int \frac{\partial A_x}{\partial x} dy. \tag{2.34}$$

The above presented assumptions reduce (2.32) into the following two differential equations which need to solved to obtain an expression for the magnetic fields

$$\frac{\partial^2 A_x}{\partial x^2} + \frac{\partial^2 A_x}{\partial y^2} + \frac{\partial^2 A_x}{\partial z^2} - \mu\sigma \frac{\partial Ax}{\partial t} = -\mu J_{coil_x}, \tag{2.35}$$

$$\frac{\partial^2 A_y}{\partial x^2} + \frac{\partial^2 A_y}{\partial y^2} + \frac{\partial^2 A_y}{\partial z^2} - \mu\sigma \frac{\partial Ay}{\partial t} = -\mu J_{coil_y}. \tag{2.36}$$

The differential equations are solved by applying the method of separation of variables, which results in a multiplication of four functions, each depending on x, y, z or t. The functions in the x- and y-direction are expressed as a Fourier series because of the periodicity in those directions. The time variation is described as the real part of a complex Fourier series such that the field quantities in the steady-state have a constant amplitude and a variation identical to that of the source component [10, 116]. The function in the z-direction is modeled by exponential function. The current density distribution of a coil is independent of the z-direction and modeled as a constant C_{coil}. Summarized, the x- and y-components of the magnetic vector potential are formulated in the form of

$$\begin{aligned} A &= \left(c_{1z}e^{\gamma z} + c_{2z}e^{-\gamma z} + C_{coil}\right)\left(a_{0x} + \sum_{n=1}^{N}\left(b_{1x}\sin(\omega_n x) + b_{2x}\cos(\omega_n x)\right)\right) \\ &\quad \times \left(a_{0y} + \sum_{m=1}^{M}\left(b_{1y}\sin(\omega_m y) + b_{2y}\cos(\omega_m y)\right)\right)e^{j\omega t}. \end{aligned} \tag{2.37}$$

The Fourier series are obtained for N and M harmonics, and have a periodicity with a length equal to $2\tau_x$ and $2\tau_y$ in the x- and y-direction respectively, as shown in Fig. 2.3. The spatial harmonics for both Fourier series are given by

$$\omega_n = \frac{n\pi}{\tau_x}, \tag{2.38}$$

$$\omega_m = \frac{m\pi}{\tau_y}. \tag{2.39}$$

The exponential function in the z-direction has a propagation constant equal to

$$\gamma = \sqrt{\omega_n^2 + \omega_m^2 + j\omega\mu\sigma}. \tag{2.40}$$

In the next sections the solution for the magnetic vector potential is presented for different type of regions. The solutions are written in the form of (2.37) and are found by fulfilling the Coulomb Gauge condition and (2.34) with respect to source terms.

2.2.2 Magnetic vector potential in a conducting medium

In a solid conducting medium, such as iron, aluminum or copper, the magnetic fields induce eddy currents, and, therefore, a solution is given in the form of the complex double Fourier series (2.37). Since such a region consists of a solid conducting medium, it is assumed that only eddy-currents in the region appear

and no external current source, such as a coil, is present, i.e. $\vec{J}_{coil}$ is equal to zero. In regions with a conducting medium, the magnetic vector potential can be expressed as

$$\begin{aligned} A_x &= \sum_{m=0}^{M}\sum_{n=0}^{N}\frac{\omega_m}{\gamma}\Big[\left(c_1e^{\gamma z}+c_2e^{-\gamma z}\right)\cos(\omega_n x)\sin(\omega_m y) \\ &\quad +\left(c_3e^{\gamma z}+c_4e^{-\gamma z}\right)\sin(\omega_n x)\cos(\omega_m y) \\ &\quad +\left(c_5e^{\gamma z}+c_6e^{-\gamma z}\right)\cos(\omega_n x)\cos(\omega_m y) \\ &\quad +\left(c_7e^{\gamma z}+c_8e^{-\gamma z}\right)\sin(\omega_n x)\sin(\omega_m y)\Big]e^{j\omega t}, \end{aligned} \tag{2.41}$$

$$\begin{aligned} A_y &= \sum_{m=0}^{M}\sum_{n=0}^{N}\frac{\omega_n}{\gamma}\Big[\left(-c_1e^{\gamma z}-c_2e^{-\gamma z}\right)\sin(\omega_n x)\cos(\omega_m y) \\ &\quad +\left(-c_3e^{\gamma z}-c_4e^{-\gamma z}\right)\cos(\omega_n x)\sin(\omega_m y) \\ &\quad +\left(c_5e^{\gamma z}+c_6e^{-\gamma z}\right)\sin(\omega_n x)\sin(\omega_m y) \\ &\quad +\left(c_7e^{\gamma z}+c_8e^{-\gamma z}\right)\cos(\omega_n x)\cos(\omega_m y)\Big]e^{j\omega t}, \end{aligned} \tag{2.42}$$

$$A_z = 0. \tag{2.43}$$

The coefficients c_1-c_8 are unknown constants which are solved by applying the boundary conditions.

Based on the magnetic vector potential, the expression of the flux density distribution is equal to

$$\begin{aligned} B_x &= \sum_{m=0}^{M}\sum_{n=0}^{N}\omega_n\Big[\left(c_1e^{\gamma z}-c_2e^{-\gamma z}\right)\sin(\omega_n x)\cos(\omega_m y) \\ &\quad +\left(c_3e^{\gamma z}-c_4e^{-\gamma z}\right)\cos(\omega_n x)\sin(\omega_m y) \\ &\quad +\left(-c_5e^{\gamma z}+c_6e^{-\gamma z}\right)\sin(\omega_n x)\sin(\omega_m y) \\ &\quad +\left(-c_7e^{\gamma z}+c_8e^{-\gamma z}\right)\cos(\omega_n x)\cos(\omega_m y)\Big]e^{j\omega t}, \end{aligned} \tag{2.44}$$

$$
\begin{aligned}
B_y &= \sum_{m=0}^{M}\sum_{n=0}^{N}\omega_m\Big[\left(c_1e^{\gamma z}-c_2e^{-\gamma z}\right)\cos(\omega_n x)\sin(\omega_m y)\\
&+\left(c_3e^{\gamma z}-c_4e^{-\gamma z}\right)\sin(\omega_n x)\cos(\omega_m y)\\
&+\left(c_5e^{\gamma z}-c_6e^{-\gamma z}\right)\cos(\omega_n x)\cos(\omega_m y)\\
&+\left(c_7e^{\gamma z}-c_8e^{-\gamma z}\right)\sin(\omega_n x)\sin(\omega_m y)\Big]e^{j\omega t}, \qquad (2.45)\\
B_z &= \sum_{m=0}^{M}\sum_{n=0}^{N}\frac{\omega_m^2+\omega_n^2}{\gamma}\Big[\left(-c_1e^{\gamma z}-c_2e^{-\gamma z}\right)\cos(\omega_n x)\cos(\omega_m y)\\
&+\left(c_3e^{\gamma z}+c_4e^{-\gamma z}\right)\sin(\omega_n x)\sin(\omega_m y)\\
&+\left(c_5e^{\gamma z}+c_6e^{-\gamma z}\right)\cos(\omega_n x)\sin(\omega_m y)\\
&+\left(-c_7e^{\gamma z}-c_8e^{-\gamma z}\right)\sin(\omega_n x)\cos(\omega_m y)\Big]e^{j\omega t}. \qquad (2.46)
\end{aligned}
$$

2.2.3 Magnetic vector potential in air

For regions with a non-conductive material, for example air or vacuum, the solution for the magnetic field becomes time independent, since $\vec{J}_{eddy}$ is equal to zero. Therefore, γ is equal to

$$k = \sqrt{\omega_n^2+\omega_m^2}. \qquad (2.47)$$

Furthermore, if a coil is present in the region, the current density distribution of the coil should be taken into account in the solution of the magnetic vector potential. Therefore, beside a homogeneous solution, which is similar to the solution presented in Section 2.2.2, a particular solution for the differential equations is obtained in the expression of the magnetic vector potential.

The magnetic vector potential for a region of air is equal to

$$
\begin{aligned}
A_x &= \sum_{m=0}^{M}\sum_{n=0}^{N}\Big[\left(\frac{\omega_m}{k}\left(c_1e^{kz}+c_2e^{-kz}\right)+C_{x_{cs}}\right)\cos(\omega_n x)\sin(\omega_m y)\\
&+\left(\frac{\omega_m}{k}\left(c_3e^{kz}+c_4e^{-kz}\right)+C_{x_{sc}}\right)\sin(\omega_n x)\cos(\omega_m y)\\
&+\left(\frac{\omega_m}{k}\left(c_5e^{kz}+c_6e^{-kz}\right)+C_{x_{cc}}\right)\cos(\omega_n x)\cos(\omega_m y)\\
&+\left(\frac{\omega_m}{k}\left(c_7e^{kz}+c_8e^{-kz}\right)+C_{x_{ss}}\right)\sin(\omega_n x)\sin(\omega_m y)\Big], \qquad (2.48)
\end{aligned}
$$

$$
\begin{aligned}
A_y &= \sum_{m=0}^{M}\sum_{n=0}^{N}\Bigg[\Big(\frac{-\omega_n}{k}\left(c_1e^{kz}+c_2e^{-kz}\right)+C_{y_{sc}}\Big)\sin(\omega_n x)\cos(\omega_m y) \\
&\quad +\Big(\frac{-\omega_n}{k}\left(c_3e^{kz}+c_4e^{-kz}\right)+C_{y_{cs}}\Big)\cos(\omega_n x)\sin(\omega_m y) \\
&\quad +\Big(\frac{\omega_n}{k}\left(c_5e^{kz}+c_6e^{-kz}\right)+C_{y_{ss}}\Big)\sin(\omega_n x)\sin(\omega_m y) \\
&\quad +\Big(\frac{\omega_n}{k}\left(c_7e^{kz}+c_8e^{-kz}\right)+C_{y_{cc}}\Big)\cos(\omega_n x)\cos(\omega_m y)\Bigg], \qquad (2.49)\\
A_z &= 0. \qquad (2.50)
\end{aligned}
$$

The constants $C_{x_{cs}}$-$C_{y_{cc}}$ in the particular solution of the differential equations are related to the current density distribution and are equal to

$$C_{x_{cs}} = \frac{-\mu j_{x_{cs}}}{\omega_n^2+\omega_m^2}, \qquad (2.51)$$

$$C_{x_{sc}} = \frac{-\mu j_{x_{sc}}}{\omega_n^2+\omega_m^2}, \qquad (2.52)$$

$$C_{x_{cc}} = \frac{-\mu j_{x_{cc}}}{\omega_n^2+\omega_m^2}, \qquad (2.53)$$

$$C_{x_{ss}} = \frac{-\mu j_{x_{ss}}}{\omega_n^2+\omega_m^2}, \qquad (2.54)$$

$$C_{y_{sc}} = \frac{-\mu j_{y_{sc}}}{\omega_n^2+\omega_m^2}, \qquad (2.55)$$

$$C_{y_{cs}} = \frac{-\mu j_{y_{cs}}}{\omega_n^2+\omega_m^2}, \qquad (2.56)$$

$$C_{y_{ss}} = \frac{-\mu j_{y_{ss}}}{\omega_n^2+\omega_m^2}, \qquad (2.57)$$

$$C_{y_{cc}} = \frac{-\mu j_{y_{cc}}}{\omega_n^2+\omega_m^2}, \qquad (2.58)$$

The current density distribution, $j_{x_{cs}}$-$j_{y_{cc}}$, is formulated in Section 2.4. Since the current density of a coil is modeled by four finite bars, the Coulomb Gauge condition is not satisfied in the particular solution of the magnetic vector potential, since

$$-\omega_n C_x - \omega_m C_y \neq 0. \qquad (2.59)$$

This is caused by the fact that the conservation of free charge is not continuous, and, as is shown in Section 2.4.5, may be ignored.

The flux density distribution for a region of air with a current-carrying coil inside is given by

$$
\begin{aligned}
B_x &= \sum_{m=0}^{M}\sum_{n=0}^{N}\omega_n\Bigg[\left(c_1e^{kz}-c_2e^{-kz}\right)\sin(\omega_n x)\cos(\omega_m y) \\
&\quad +\left(c_3e^{kz}-c_4e^{-kz}\right)\cos(\omega_n x)\sin(\omega_m y) \\
&\quad +\left(-c_5e^{kz}+c_6e^{-kz}\right)\sin(\omega_n x)\sin(\omega_m y) \\
&\quad +\left(-c_7e^{kz}+c_8e^{-kz}\right)\cos(\omega_n x)\cos(\omega_m y)\Bigg], \qquad (2.60)
\end{aligned}
$$

$$
\begin{aligned}
B_y \;=\; & \sum_{m=0}^{M}\sum_{n=0}^{N}\omega_m\Big[\left(c_1e^{kz}-c_2e^{-kz}\right)\cos(\omega_n x)\sin(\omega_m y)\\
& +\left(c_3e^{kz}-c_4e^{-kz}\right)\sin(\omega_n x)\cos(\omega_m y)\\
& +\left(c_5e^{kz}-c_6e^{-kz}\right)\cos(\omega_n x)\cos(\omega_m y)\\
& +\left(c_7e^{kz}-c_8e^{-kz}\right)\sin(\omega_n x)\sin(\omega_m y)\Big],
\end{aligned}
\tag{2.61}
$$

$$
\begin{aligned}
B_z = \sum_{m=0}^{M}\sum_{n=0}^{N}\Bigg[& \\
& -\left(\frac{\omega_m^2+\omega_n^2}{k}\left(c_1e^{kz}+c_2e^{-kz}\right)+C_{x_{cs}}\omega_m-C_{y_{sc}}\omega_n\right)\cos(\omega_n x)\cos(\omega_m y)\\
& +\left(\frac{\omega_m^2+\omega_n^2}{k}\left(c_3e^{kz}+c_4e^{-kz}\right)+C_{x_{sc}}\omega_m-C_{y_{cs}}\omega_n\right)\sin(\omega_n x)\sin(\omega_m y)\\
& +\left(\frac{\omega_m^2+\omega_n^2}{k}\left(c_5e^{kz}+c_6e^{-kz}\right)+C_{x_{cc}}\omega_m+C_{y_{ss}}\omega_n\right)\cos(\omega_n x)\sin(\omega_m y)\\
& -\left(\frac{\omega_m^2+\omega_n^2}{k}\left(c_7e^{kz}+c_8e^{-kz}\right)+C_{x_{ss}}\omega_m+C_{y_{cc}}\omega_n\right)\sin(\omega_n x)\cos(\omega_m y)\Bigg].
\end{aligned}
\tag{2.62}
$$

Notice that the contribution of the current density distribution only appears in the normal component of the flux density distribution. As a result, the expression of the flux density distribution in the x- and y-direction, obtained by the magnetic vector potential, similar to the one obtained by the magnetic scalar potential, as is shown in the next section.

2.2.4 Magnetic scalar potential

Regions with non-conductive material and without a current-carrying coil can either be modeled by the magnetic vector potential or by the magnetic scalar potential

$$\vec{H} = -\nabla\varphi. \tag{2.63}$$

Similarly to the magnetic vector potential, the solution of the magnetic scalar potential is formulated using the method of separation of variables, and is equal

to

$$\begin{aligned}\varphi &= \sum_{m=0}^{M}\sum_{n=0}^{N}\Big[\big(c_1e^{kz}+c_2e^{-kz}\big))\cos(\omega_n x)\cos(\omega_m y)\\ &\quad+\big(c_3e^{kz}+c_4e^{-kz}\big)\sin(\omega_n x)\sin(\omega_m y)\\ &\quad+\big(c_5e^{kz}+c_6e^{-kz}\big)\cos(\omega_n x)\sin(\omega_m y)\\ &\quad+\big(c_7e^{kz}+c_8e^{-kz}\big)\sin(\omega_n x)\cos(\omega_m y)\Big].\end{aligned} \tag{2.64}$$

The flux density distribution is equal to

$$\begin{aligned}B_x &= \sum_{m=0}^{M}\sum_{n=0}^{N}\mu_0\omega_n\Big[\big(c_1e^{kz}+c_2e^{-kz}\big)\sin(\omega_n x)\cos(\omega_m y)\\ &\quad+\big(-c_3e^{kz}-c_4e^{-kz}\big)\cos(\omega_n x)\sin(\omega_m y)\\ &\quad+\big(c_5e^{kz}+c_6e^{-kz}\big)\sin(\omega_n x)\sin(\omega_m y)\\ &\quad+\big(-c_7e^{kz}-c_8e^{-kz}\big)\cos(\omega_n x)\cos(\omega_m y)\Big],\end{aligned} \tag{2.65}$$

$$\begin{aligned}B_y &= \sum_{m=0}^{M}\sum_{n=0}^{N}\mu_0\omega_m\Big[\big(c_1e^{kz}+c_2e^{-kz}\big)\cos(\omega_n x)\sin(\omega_m y)\\ &\quad+\big(-c_3e^{kz}-c_4e^{-kz}\big)\sin(\omega_n x)\cos(\omega_m y)\\ &\quad+\big(-c_5e^{kz}-c_6e^{-kz}\big)\cos(\omega_n x)\cos(\omega_m y)\\ &\quad+\big(c_7e^{kz}+c_8e^{-kz}\big)\sin(\omega_n x)\sin(\omega_m y)\Big],\end{aligned} \tag{2.66}$$

$$\begin{aligned}B_z &= \sum_{m=0}^{M}\sum_{n=0}^{N}\mu_0 k\Big[\big(-c_1e^{kz}+c_2e^{-kz}\big)\cos(\omega_n x)\cos(\omega_m y)\\ &\quad+\big(-c_3e^{kz}+c_4e^{-kz}\big)\sin(\omega_n x)\sin(\omega_m y)\\ &\quad+\big(-c_5e^{kz}+c_6e^{-kz}\big)\cos(\omega_n x)\sin(\omega_m y)\\ &\quad+\big(-c_7e^{kz}+c_8e^{-kz}\big)\sin(\omega_n x)\cos(\omega_m y)\Big].\end{aligned} \tag{2.67}$$

Both the magnetic vector potential, (2.60)-(2.62), and the magnetic scalar potential, (2.65)-(2.67), result in similar expressions for the flux density distribution

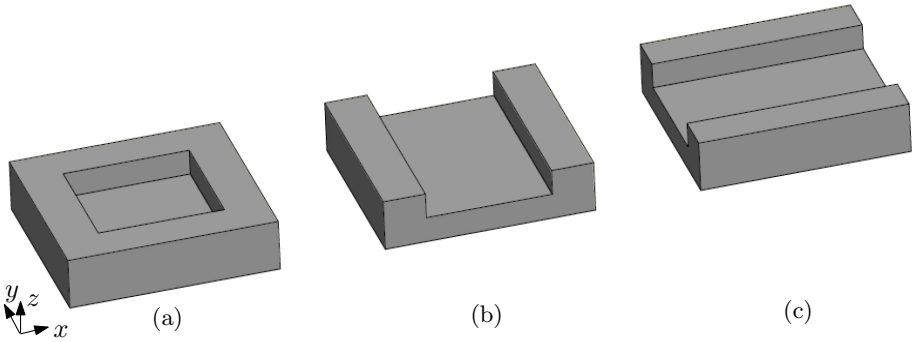

Figure 2.4: Schematic overview of a single period in x- and y-direction of a (a) cavity, (b) slot in the y-direction, and (c) slot in the x-direction.

in the x- and y-direction. The flux density distribution in the z-direction differs with respect to both methods, where the flux density distribution obtained from the magnetic vector potential, (2.62), includes constants related to the current density distribution. Because of the similarity, both the magnetic vector potential and the magnetic scalar potential can be used next to each other in a problem which is solved by the harmonic modeling method. Furthermore, the tangential components of the magnetic vector potential need to be rewritten towards an expression similar to the magnetic scalar potential to fulfil the tangential boundary conditions of the magnetic field strength, as is shown in Section 2.3.

2.2.5 Magnetic vector potential in a cavity

In the previous sections the magnetic vector potential is presented for regions with a length equal to the periodicity of the problem, i.e. continuous regions. In case of a slotted structure, the length of the region is smaller as the periodic length of the problem, and, therefore, the region inside the slot is called a discontinuous or a non-periodic region. Examples of discontinuous regions, i.e. slots or cavities, are shown in Fig. 2.4. A cavity is defined as a gap in a plate constructed of material with an infinitely permeability, and is both in the x- and y-direction bounded within a single period of the adjacent continuous region by the plate, as shown in Fig. 2.4(a). Multiple cavities can be modeled in a plate with the length equal to single period of a continuous region, as long as each cavity is surrounded by a layer of infinitely permeable material. A slot is defined as a region with a continuous gap in the x- or y-direction in which the length of the gap is equal to the periodic length and the width of the gap is smaller as the periodic length, and bounded by ferromagnetic material in that direction, as shown in Fig. 2.4(b). Other structures, such as a tooth surrounded by air cannot be modeled.

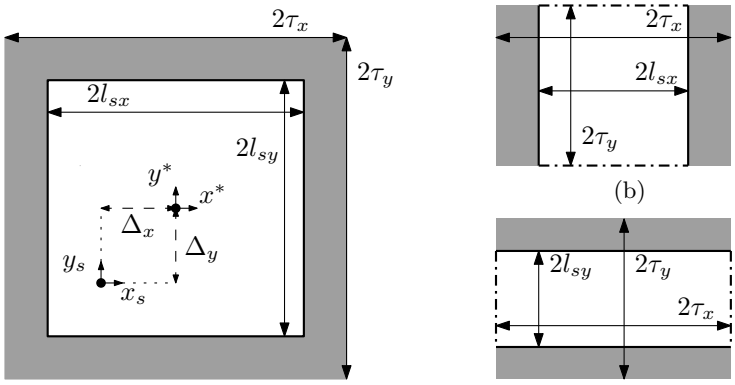

Figure 2.5: Top view of a single period of a (a) cavity, (b) slot in the y-direction, and (c) slot in the x-direction.

The presence of the infinitely permeable material introduces a Neumann boundary condition at the borders of the cavity, indicated by the solid black line in Fig. 2.5. The appearance of this boundary condition implies that the components of the magnetic field strength perpendicular to the direction of the boundary are equal to zero at the boundary.

In the cavity shown in Fig. 2.5(a), the origin of the coordinate system is located in the middle of the cavity. A description of the magnetic flux density in the normal direction, containing a cosine function in the x- and y-direction, fulfils the Neumann boundary condition at the borders of the cavity. Because of this boundary condition, the imaging method needs to be applied to describe the magnetic field sources in the cavity, as is presented in Section 2.4.6. The Neumann boundary condition at the border of the cavity results in a periodicity of the magnetic fields inside the cavity ($4l_{s_x}$, $4l_{sy}$) which is equal to twice the length of the cavity ($2l_{s_x}$, $2l_{sy}$). The spatial harmonics in a cavity are equal to

$$\omega_v = \frac{v\pi}{2l_{sx}}, \tag{2.68}$$

$$\omega_w = \frac{w\pi}{2l_{sy}}, \tag{2.69}$$

where v and w are the harmonics in the x- and y-direction, respectively. To fulfil the Neumann boundary condition, only odd-numbered harmonics need to be taken into account.

If the center of a coil, located inside the cavity, is shifted with respect to the

origin of the coordinate system of the cavity, the imaging method results in a source description containing both cosine and sine components in the x- and y-direction. To solve the Poisson equation within this non-periodic region, the center of the coordinate system of the cavity needs to be shifted as well, such that both descriptions have equal trigonometric functions. Therefore, a local coordinate system (x_s,y_s) is introduced according to

$$x_s = x^* + \Delta_x, \tag{2.70}$$
$$y_s = y^* + \Delta_y, \tag{2.71}$$

where x^* and y^* are the coordinate system with the origin in the center of the cavity and Δ_x and Δ_y are the displacement of the center of the coil with respect to the coordinate system (x^*,y^*), as illustrated in Fig. 2.5(a). With respect to the local coordinate system, the magnetic vector potential in a cavity becomes equal to

$$\begin{aligned} A_x = \sum_{w=1,3,5,..}^{W} \sum_{v=1,3,5,..}^{V} \Bigg[& \\ & (\frac{\omega_w}{r}\left(c_1 e^{rz} + c_2 e^{-rz}\right) + C_{x_{cs}}) \cos(\omega_v \Delta_x) \cos(\omega_w \Delta_y) \cos(\omega_v x^*) \sin(\omega_w y^*) \\ & + (\frac{\omega_w}{r}\left(c_3 e^{rz} + c_4 e^{-rz}\right) + C_{x_{sc}}) \sin(\omega_v \Delta_x) \sin(\omega_w \Delta_y) \sin(\omega_v x^*) \cos(\omega_w y^*) \\ & + (\frac{\omega_w}{r}\left(c_5 e^{rz} + c_6 e^{-rz}\right) + C_{x_{cc}}) \cos(\omega_v \Delta_x) \sin(\omega_w \Delta_y) \cos(\omega_v x^*) \cos(\omega_w y^*) \\ & + (\frac{\omega_w}{r}\left(c_7 e^{rz} + c_8 e^{-rz}\right) + C_{x_{ss}}) \sin(\omega_v \Delta_x) \cos(\omega_w \Delta_y) \sin(\omega_v x^*) \sin(\omega_w y^*) \Bigg], \end{aligned} \tag{2.72}$$

$$\begin{aligned} A_y = \sum_{w=1,3,5,..}^{W} \sum_{v=1,3,5,..}^{V} \Bigg[& \\ & (\frac{-\omega_v}{r}\left(c_1 e^{rz} + c_2 e^{-rz}\right) + C_{y_{sc}}) \cos(\omega_v \Delta_x) \cos(\omega_w \Delta_y) \sin(\omega_v x^*) \cos(\omega_w y^*) \\ & + (\frac{-\omega_v}{r}\left(c_3 e^{rz} + c_4 e^{-rz}\right) + C_{y_{cs}}) \sin(\omega_v \Delta_x) \sin(\omega_w \Delta_y) \cos(\omega_v x^*) \sin(\omega_w y^*) \\ & + (\frac{\omega_v}{r}\left(c_5 e^{rz} + c_6 e^{-rz}\right) + C_{y_{ss}}) \cos(\omega_v \Delta_x) \sin(\omega_w \Delta_y) \sin(\omega_v x^*) \sin(\omega_w y^*) \\ & + (\frac{\omega_v}{r}\left(c_7 e^{rz} + c_8 e^{-rz}\right) + C_{y_{cc}}) \sin(\omega_v \Delta_x) \cos(\omega_w \Delta_y) \cos(\omega_v x^*) \cos(\omega_w y^*) \Bigg], \end{aligned} \tag{2.73}$$

$$A_z = 0. \tag{2.74}$$

This results in the following expression for the flux density distribution in a cavity

$$
\begin{aligned}
B_x = \sum_{w=1,3,5,..}^{W} \sum_{v=1,3,5,..}^{V} \omega_v \Big[& \\
& \left(c_1 e^{rz} - c_2 e^{-rz}\right) \cos(\omega_v \Delta_x) \cos(\omega_w \Delta_y) \sin(\omega_v x^*) \cos(\omega_w y^*) \\
& + \left(c_3 e^{rz} - c_4 e^{-rz}\right) \sin(\omega_v \Delta_x) \sin(\omega_w \Delta_y) \cos(\omega_v x^*) \sin(\omega_w y^*) \\
& - \left(c_5 e^{rz} - c_6 e^{-rz}\right) \cos(\omega_v \Delta_x) \sin(\omega_w \Delta_y) \sin(\omega_v x^*) \sin(\omega_w y^*) \\
& - \left(c_7 e^{rz} - c_8 e^{-rz}\right) \sin(\omega_v \Delta_x) \sin(\omega_w \Delta_y) \cos(\omega_v x^*) \cos(\omega_w y^*) \Big],
\end{aligned}
\tag{2.75}
$$

$$
\begin{aligned}
B_y = \sum_{w=1,3,5,..}^{W} \sum_{v=1,3,5,..}^{V} \omega_w \Big[& \\
& \left(c_1 e^{rz} - c_2 e^{-rz}\right) \cos(\omega_v \Delta_x) \cos(\omega_w \Delta_y) \cos(\omega_v x^*) \sin(\omega_w y^*) \\
& + \left(c_3 e^{rz} - c_4 e^{-rz}\right) \sin(\omega_v \Delta_x) \sin(\omega_w \Delta_y) \sin(\omega_v x^*) \cos(\omega_w y^*) \\
& + \left(c_5 e^{rz} - c_6 e^{-rz}\right) \cos(\omega_v \Delta_x) \sin(\omega_w \Delta_y) \cos(\omega_v x^*) \cos(\omega_w y^*) \\
& + \left(c_7 e^{rz} - c_8 e^{-rz}\right) \sin(\omega_v \Delta_x) \cos(\omega_w \Delta_y) \sin(\omega_v x^*) \sin(\omega_w y^*) \Big],
\end{aligned}
\tag{2.76}
$$

$$
\begin{aligned}
B_z \;=\; & \sum_{w=1,3,5,..}^{W} \sum_{v=1,3,5,..}^{V} \Bigg[\Bigg(\frac{\omega_w^2 + \omega_v^2}{r} \left(-c_1 e^{rz} - c_2 e^{-rz}\right) - C_{x_{cs}} \omega_w \\
& \qquad + C_{y_{sc}} \omega_v \Bigg) \cos(\omega_v \Delta_x) \cos(\omega_w \Delta_y) \cos(\omega_v x^*) \cos(\omega_w y^*) \\
& + \Bigg(\frac{\omega_w^2 + \omega_v^2}{r} \left(c_3 e^{rz} + c_4 e^{-rz}\right) + C_{x_{sc}} \omega_w \\
& \qquad - C_{y_{cs}} \omega_v \Bigg) \sin(\omega_v \Delta_x) \sin(\omega_w \Delta_y) \sin(\omega_v x^*) \sin(\omega_w y^*) \\
& + \Bigg(\frac{\omega_w^2 + \omega_v^2}{r} \left(c_5 e^{rz} + c_6 e^{-rz}\right) + C_{x_{cc}} \omega_w \\
& \qquad + C_{y_{ss}} \omega_v \Bigg) \cos(\omega_v \Delta_x) \sin(\omega_w \Delta_y) \cos(\omega_v x^*) \sin(\omega_w y^*) \\
& + \Bigg(\frac{\omega_w^2 + \omega_v^2}{r} \left(-c_7 e^{rz} - c_8 e^{-rz}\right) - C_{x_{ss}} \omega_w \\
& \qquad - C_{y_{cc}} \omega_v \Bigg) \sin(\omega_v \Delta_x) \cos(\omega_w \Delta_y) \sin(\omega_v x^*) \cos(\omega_w y^*) \Bigg].
\end{aligned}
\tag{2.77}
$$

The constants related to the current density distribution in the slot are equal to

$$C_{x_{cs}} = C_{x_{ss}} = \mu_0 \frac{j_{x_{slot}}}{\omega_w^2 + \omega_v^2}, \tag{2.78}$$

$$C_{x_{sc}} = C_{x_{cc}} = -\mu_0 \frac{j_{x_{slot}}}{\omega_w^2 + \omega_v^2}, \tag{2.79}$$

$$C_{y_{sc}} = C_{y_{ss}} = \mu_0 \frac{j_{y_{slot}}}{\omega_w^2 + \omega_v^2}, \tag{2.80}$$

$$C_{y_{cs}} = C_{y_{cc}} = -\mu_0 \frac{j_{y_{slot}}}{\omega_w^2 + \omega_v^2}, \tag{2.81}$$

where the components of the description of the current density distribution in the slot, $j_{x_{slot}}$, and $j_{y_{slot}}$, are introduced in Section 2.4.6. The propagation constant r is equal to

$$r = \sqrt{\omega_v^2 + \omega_w^2}. \tag{2.82}$$

Not only cavities can be modeled, but also slots along one of the periodic directions can be modeled with the harmonic modeling method. Two examples are shown in Figs. 2.5(b) and (c). The dashed-dotted line in the figure indicates a periodic boundary condition, and the solid line a Neumann boundary condition. For a slot along the y-direction, shown in Fig. 2.5(b), the following set of spatial harmonics is obtained

$$\omega_v = \frac{v\pi}{2l_{sx}}, \tag{2.83}$$

$$\omega_m = \frac{m\pi}{\tau_y}, \tag{2.84}$$

and for a slot along the x-direction, shown in Fig. 2.5(c), the spatial harmonics are equal to

$$\omega_n = \frac{n\pi}{\tau_x}, \tag{2.85}$$

$$\omega_w = \frac{w\pi}{2l_{sy}}. \tag{2.86}$$

A description for the magnetic vector potential for a slot along the x- or y-direction can be obtained by a combination of the magnetic vector potential in air, Section 2.2.3, and the magnetic vector potential in a cavity (2.72). Because of the separation of variables, the independent spatial harmonics in the x- and y-direction can be multiplied with each other.

2.2.6 Two-dimensional magnetic vector potential

From the three-dimensional magnetic vector potential, the two-dimensional one can be written by an additional set of assumptions. If it is assumed that the current in the two-dimensional model is only flowing in the infinite y-direction, the current density and the magnetic vector potential in the x-direction may be set to zero, similar as applied to the magnetic vector potential in the z-direction in the three-dimensional case

$$J_x = 0, \tag{2.87}$$
$$A_x = 0. \tag{2.88}$$

This assumption automatically satisfies the Coulomb-Gauge condition, $\nabla \cdot \vec{A} = 0$. Finally, the partial derivative of the magnetic vector potential in the y-direction is equal to zero because of the infinite length

$$\frac{\partial A_y}{\partial y} = 0. \tag{2.89}$$

These assumptions reduce the differential equations (2.35) and (2.36) to

$$\frac{\partial^2 A_y}{\partial x^2} + \frac{\partial^2 A_y}{\partial z^2} - \mu\sigma \frac{\partial Ay}{\partial t} = -\mu J_{coil_y}. \tag{2.90}$$

Similar solutions of the magnetic vector potential and current density distributions can be obtained as presented in Section 2.2 and 2.4. Because of the finite length in the y-direction no harmonics in the y-direction are taken into account, and the two-dimensional magnetic vector potential is equal to

$$A_x = 0, \tag{2.91}$$
$$A_y = \left(c_{1z} e^{\gamma z} + c_{2z} e^{-\gamma z}\right) \times \left(a_{0x} + \sum_{n=1}^{N} \left(b_{1x} \sin(\omega_n x) + b_{2x} \cos(\omega_n x)\right)\right) e^{j\omega t}, \tag{2.92}$$
$$A_z = 0. \tag{2.93}$$

2.3 Boundary conditions

The descriptions of the magnetic vector potential of the different regions in a single electromagnetic problem are coupled to each other by the boundary conditions. The boundary conditions at the tangential borders of a region are satisfied by the choice of the harmonic description for the components in the x- and y-direction of the magnetic vector potential, as shown in Section 2.2. The unknown coefficients in the z-component of the magnetic vector potential are found by applying one the following three boundary conditions:

- Dirichlet boundary condition,
- Neumann boundary condition,
- continuous boundary condition,

at the boundaries in the normal (z-) direction of a region.

At the boundary of a region with infinitely-permeable ferromagnetic material or at the border of a region with infinite height the Neumann and Dirichlet boundary condition must be fulfilled, respectively. The Dirichlet condition defines that the magnetic vector or magnetic scalar potential is equal to zero. The Neumann boundary condition, defines that the tangential components of the magnetic field strength with respect to the boundary are equal to zero [45]. A schematic overview of the Neumann boundary condition is shown in Fig. 2.6, where

$$H_x = 0\Big|_{z=h_R}, \tag{2.94}$$

$$H_y = 0\Big|_{z=h_R}, \tag{2.95}$$

at the top of region R. The Neumann boundary condition gives no restriction for the normal component of the magnetic field strength at the boundary. The Dirichlet and the Neumann boundary condition can both be applied for periodic and non-periodic regions.

The continuous boundary condition defines that the magnetic flux density in the normal direction and the magnetic field strength in the tangential direction should be equal at both sides of a border between two regions. This implies the following

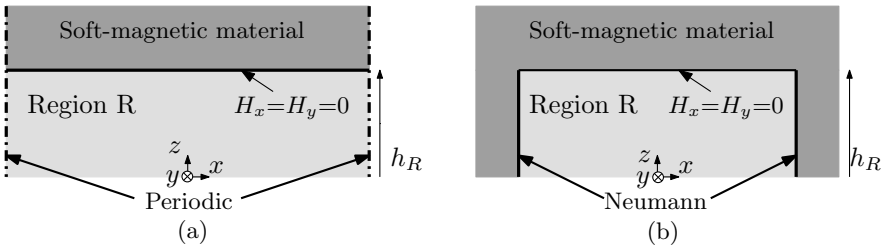

Figure 2.6: Schematic overview of the Neumann boundary condition in (a) a periodic and (b) a non-periodic region.

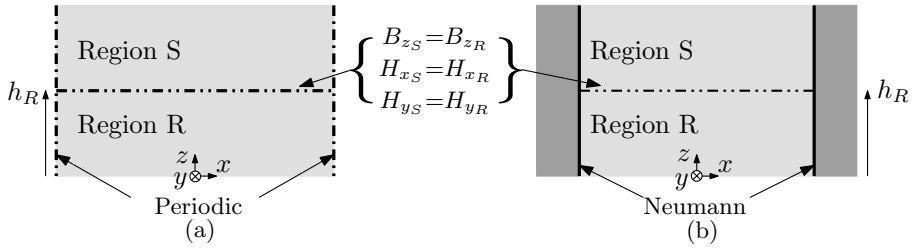

Figure 2.7: Schematic overview of the continuous boundary conditions between (a) two periodic and (b) two non-periodic regions.

set of constraints, for example, between regions R and S of Fig. 2.7,

$$H_{x_S} = H_{x_R}\Big|_{z=h_R}, \tag{2.96}$$

$$H_{y_S} = H_{y_R}\Big|_{z=h_R}, \tag{2.97}$$

$$B_{z_S} = B_{z_R}\Big|_{z=h_R}. \tag{2.98}$$

To match the periodicity of all regions, a distinction is made between boundaries of regions with a continuous periodicity and boundaries with a discontinuous periodicity, as is explained in the next sections.

2.3.1 Boundary conditions between continuous regions

The normal component of the magnetic flux density and the tangential components of the magnetic field strength between two continuous regions have a similar periodicity, and, therefore, only the functions in the z-direction have to be equalized. Furthermore, the summation of different terms in the expression of the magnetic fields allows that these boundary conditions can be separately solved for each combination of cosine and sine in the x- and y-direction. Nevertheless, the boundary conditions at the border of two continuous regions result in an overdetermined problem, in which the number of boundary conditions is higher compared to the number of unknown coefficients. Consider, for example, the two regions shown in Fig. 2.7(a), three boundary conditions are defined between the two regions, (2.96)-(2.98), and, another four conditions are introduced if the Neumann boundary condition is applied to the top of region S and the bottom of region R, (2.94)-(2.95). These seven conditions should be fulfilled to solve the four unknown coefficients per combination of sine and cosine functions in the x- and y-direction. This results in an overdetermined problem in which three boundary conditions remain unsolved. The solution to solve this problem, and thereby, obtain an expression for the magnetic vector potential is to reduce the number of boundary conditions.

If no current density distribution is present in the regions R and S, these regions can be modeled by the magnetic scalar potential instead of the magnetic vector potential. In this case, the two continuous boundary conditions of the magnetic field strength, (2.96) and (2.97), are replaced by a single boundary condition which defines that the magnetic scalar potential is equal on both sides of the boundary

$$\varphi_S = \varphi_R \Big|_{z=h_R}, \tag{2.99}$$

where

$$\varphi = -\int H_x dx = -\int H_y dy, \tag{2.100}$$

and, as a result, the problem is not over-constrained.

The boundary condition for the tangential components of the magnetic field strength is obtained from Ampere's law, and can be expressed for R and S as

$$\lim_{z \to h_R} \oint \vec{H} dl = \int H_{S_x} dx - \int H_{R_x} dx = \int_S \vec{J_{fsc}} dS, \tag{2.101}$$

where J_{fsc} is the free surface charge density at the boundary between the two regions. It is assumed that J_{fsc} is equal to zero, and, that no surface charge is

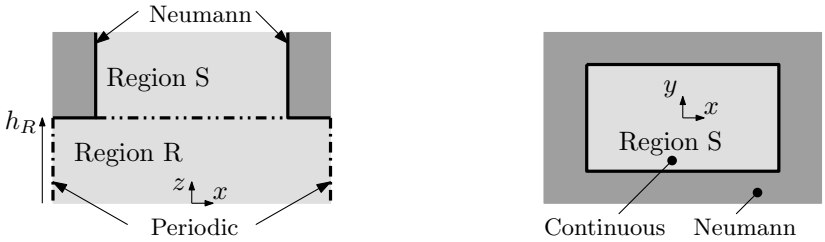

Figure 2.8: Schematic overview of the boundary conditions between a periodic and non-periodic region: (a) cross-section of the xz-plane, and (b) cross-section of the xy-plane.

present at the boundary between two regions. Furthermore, the two tangential components of the magnetic field strength retrieved from the magnetic vector potential (2.60)-(2.61), have no component related to the current density distribution of a coil, and are, therefore, similar to the tangential components obtained from the magnetic scalar potential, (2.65)-(2.66). Summarized, locally at the boundary, the magnetic vector potential may be expressed in the terms of the magnetic scalar potential by applying (2.100) to (2.60)-(2.61). This reduces the number of boundary conditions, and, thereby, the problem is not over-constrained.

2.3.2 Boundary conditions between discontinuous regions

The boundary conditions at the normal interface of a periodic and non-periodic region are position dependent. Figure 2.8(a) shows a cross-section of the boundary between a periodic and a non-periodic region in the xy-plane. The periodic region experiences a combination of boundary conditions at the interface between the two regions; the continuous boundary conditions between the overlapping area of the periodic and the non-periodic region, and, the Neumann boundary condition over the remaining area of the periodic region, as shown in Fig. 2.8(b),

$$\varphi_R = \begin{cases} \varphi_S\Big|_{z=h_R} & \text{for } x \leq \pm l_{s_x} \text{ and } y \leq \pm l_{s_y} \\ 0\Big|_{z=h_R} & \text{elsewhere} \end{cases}, \tag{2.102}$$

$$B_{z_S} = B_{z_R}. \tag{2.103}$$

Boundary condition (2.102) implies that the tangential components of the magnetic fields in the continuous region are equal to the tangential components of the magnetic fields inside the cavity across the common area of both regions, and are

equal to zero elsewhere. The boundary condition in the normal direction (2.103) implies that the normal component of the magnetic flux density distribution inside the cavity is equal to the sum of the normal components of the magnetic flux density in the continuous region over the area of the cavity. This boundary condition is evaluated across the overlapping area of the periodic and non-periodic region, since the normal component of the magnetic flux density is not defined in the periodic region outside the area of the cavity.

The magnetic fields in the periodic and non-periodic region are described with a different fundamental harmonic. Therefore, the boundary conditions cannot be solved directly since there is no relation in the position-depending trigonometric components of the field expression. The mode-matching technique is applied to correlate the magnetic fields at both sides of the boundary, and, thereby, obtain an expression which can be solved [31, 65, 87].

The mode-matching technique is based on fact that the periodic functions in the $x-$ and y-direction of the magnetic flux density distribution and magnetic field strength are written in terms of a Fourier series, and the fact that the boundary conditions imply that the fields are equal at both sides of the boundary. Consider for example, two general double Fourier series with different spatial frequencies

$$R(x,y,z) = \sum_{m=0}^{M}\sum_{n=0}^{N} C_r(z)\cos(\omega_m y)\cos(\omega_n x), \tag{2.104}$$

$$S(x,y,z) = \sum_{w=odd}^{W}\sum_{v=odd}^{V} C_s(z)\cos(\omega_w y)\cos(\omega_v x), \tag{2.105}$$

where C_r and C_s present the coefficients of the Fourier series, which may represent region R and S of Fig. 2.8. For illustration of the mode-matching technique, only the double cosine component is taken into account. The coefficient C_r is obtained by applying the Fourier transform to $R(x,y,z)$

$$C_r(z) = \frac{r_z(z)}{\tau_x\tau_y}\int_{-\tau_x}^{\tau_x}\left(\sum_{n=0}^{N}\cos(\omega_n x)\right)^2 \mathrm{d}x \int_{-\tau_y}^{\tau_y}\left(\sum_{m=0}^{M}\cos(\omega_m y)\right)^2 \mathrm{d}y. \tag{2.106}$$

At the boundary between regions R and S, the boundary condition implies that both expressions give a similar solution. In other words, the coefficient C_r can

also be obtained applying the Fourier transform to $S(x, y, z)$

$$C_r(z) = \frac{s_z(z)}{\tau_x \tau_y} \int_{-l_{sx}}^{l_{sx}} \left(\sum_{v=odd}^{V} \cos(\omega_v x) \cdot \sum_{n=0}^{N} \cos(\omega_n x) \right) \mathrm{d}x \times \int_{-l_{sy}}^{l_{sy}} \left(\sum_{w=odd}^{W} \cos(\omega_w y) \cdot \sum_{m=0}^{M} \cos(\omega_m y) \right) \mathrm{d}y. \quad (2.107)$$

By applying this technique to the components of the magnetic flux density and the magnetic field strength, the position dependency in the boundary conditions between the periodic and non-periodic regions is removed, and the boundary conditions can be solved.

2.4 Modeling of the current density distribution

The current-carrying coils are the sources of the magnetic fields in the CET system. Therefore, an accurate model of their current density distribution is important for a good prediction of the magnetic fields and the inductances of the coils in a contactless energy transfer system. A single coil, as shown in Fig. 2.9(a), can be decomposed into four straight segments and four round segments. The current density distribution of the straight segments can be modeled by a double Fourier series, resulting in expressions with similar position depending trigonometric components as the tangential components of the magnetic vector potential, (2.60)-(2.61). The current density distribution of the round segments, or corner parts of the coil, cannot be modeled since the $x-$ and y-components are related to each other, and the separation of variables cannot be applied. Therefore, the current density distribution of a single coil is modeled by four segments which all have a finite length in the direction of the current.

2.4.1 Geometry of a coil

Modeling of the magnetic fields around a coil by dividing the coil into segments and superposition of the individual parts is analogous to the procedure as applied by using the Biot-Savart law, in which the flux density distribution of a coil is also modeled by segments with a finite length. As the quasi-static field theory is applied, it is assumed that there is conservation of free charge over the global volume. However, locally, at the beginning and end of a finite segment, a negative and a positive charge appears, respectively. In [51], it is proven that the flux density distribution obtained from the charges at the end of a segment gives a

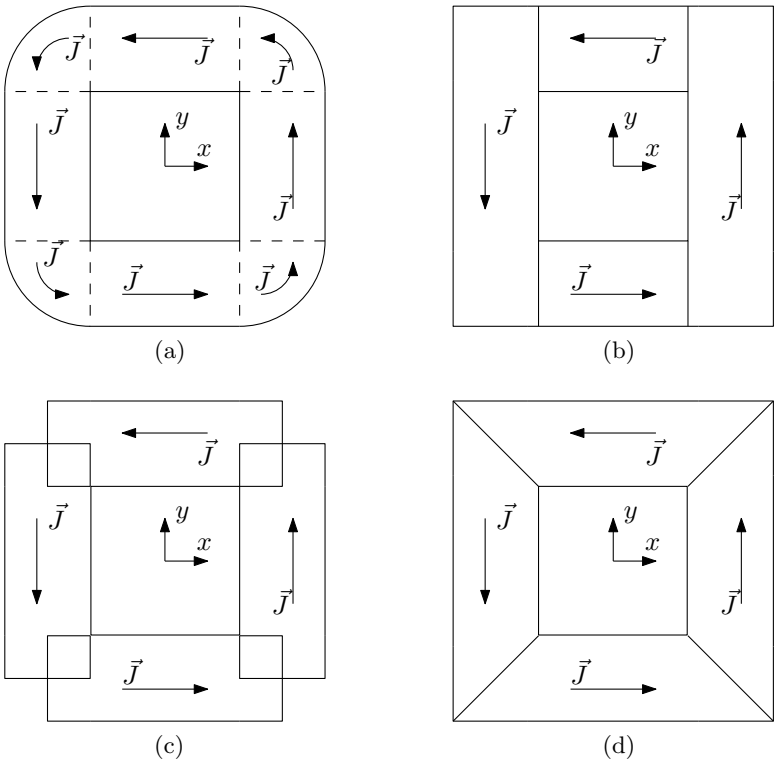

Figure 2.9: Top view of different modeling configurations of a coil: (a) original shape, (b) non-overlapping bars, (c) overlapping bars, and (d) trapezoidal bars.

similar expression of the flux density distribution obtained by the law of Biot-Savart. Therefore, the appearance of an electric charge may be ignored for a finite section of a single wire, since the end of one segment is the beginning of the next segment.

In practice, a current-carrying segment may consist of multiple wires. The magnetic fields around such a segment can be modeled by obtaining the flux density distribution around a single wire by applying the Biot-Savart law, and integrating the field of a single wire over the cross-section of the segment [122] or by using the filament method which is introduced in Section 2.1 [117]. One of the assumptions of the filament method is that there is a continuous current density distribution over the cross-section of the segment, i.e. the area which envelopes the multiple turns of a coil. With respect to the harmonic modeling technique, modeling of the magnetic fields around individual wires of a segment would require many harmonics in a geometry with a large pitch. Therefore, the same assumption as in the

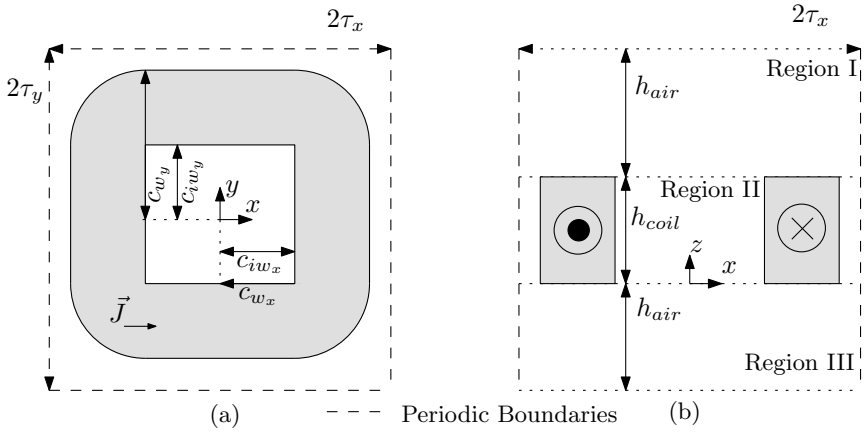

Figure 2.10: Harmonic model of a coil with a region of air above and below: (a) top view, and (b) side view.

filament method is assumed, while the wires inside the finite segments are ignored, and the segments are modeled as one volume with a constant current density. A segment of a coil including all turns is referred to as a current-carrying bar in the remaining part of this thesis.

To model the current density distribution of a coil in the harmonic modeling method, three configurations are compared, in which the four current-carrying bars are positioned in a different manner with respect to each other. The three configurations consist of a geometry in which: four rectangular bars are placed against each other, Fig. 2.9(b); four rectangular bars which overlap each other, Fig. 2.9(c); and four intersected trapezoidal bars, Fig. 2.9(d).

A single coil and the parameters, which define the dimensions of the coil, are shown in Fig. 2.10(a). As shown in the figure, the dimensions of a coil can be presented by five parameters with respect to the center of the coil. As seen from the origin of the coil, the half inner width is defined by parameter c_{iw}, the half outer width is defined by parameter c_w. All parameters, which define the dimensions of the coil, have a subscript x or y to indicate the width or length of a bar with respect to the coordinate system. In this case, the center of the coil is equal to the origin of the coordinate system. This is possible for a single coil, but is impossible if multiple coils are present in a single period of the periodical system. In the latest case, the position of a coil with respect to the center of the problem is indicated by Δ_x and Δ_y for displacements in the x- and y-direction, respectively.

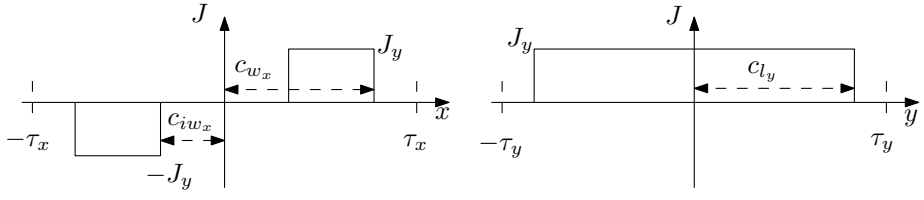

Figure 2.11: Finite rectangular bars in y-direction: (a) cross-section along y-axis, and (b) cross-section parallel to x-axis.

2.4.2 Rectangular non-overlapping bars

A coil surrounded by air and composed of four non-overlapping finite rectangular bars, as shown in Fig. 2.9(b), is modeled for the current flowing in the x- and y-direction. The current density in the y-direction is shown in Fig. 2.11, where c_l is the half length of a current-carrying bar. By expressing the current-carrying bars by a double Fourier series, the following description for the current density distribution J_y is obtained

$$\begin{aligned} J_y(x,y) = \quad & \sum_{n=1}^{N}\sum_{m=0}^{M} \left[j_{ycc}\cos(\omega_n x)\cos(\omega_m y) + j_{ycs}\cos(\omega_n x)\sin(\omega_m y) \right. \\ & \left. + j_{yss}\sin(\omega_n x)\sin(\omega_m y) + j_{ysc}\sin(\omega_n x)\cos(\omega_m y) \right], \end{aligned} \tag{2.108}$$

where

$$j_{ycc} = \begin{cases} \frac{-2Jc_{l_y}}{\tau_x\tau_y\omega_n}\left[\cos\left(c_{iw_x}\omega_n\right) - \cos\left(c_{w_x}\omega_n\right)\right]\sin\left(\Delta_x\omega_n\right) & \text{for } m = 0, \\ \frac{-4J}{\tau_x\tau_y\omega_n\omega_m}\sin\left(c_{l_y}\omega_m\right)\cos\left(\Delta_y\omega_m\right) & \\ \quad \times\left[\cos\left(c_{iw_x}\omega_n\right) - \cos\left(c_{w_x}\omega_n\right)\right]\sin\left(\Delta_x\omega_n\right) & \text{for } m \neq 0, \end{cases} \tag{2.109}$$

$$j_{ycs} = \begin{cases} \frac{-2Jc_{l_y}}{\tau_x\tau_y\omega_n}\left[\cos\left(c_{iw_x}\omega_n\right) - \cos\left(c_{w_x}\omega_n\right)\right]\sin\left(\Delta_x\omega_n\right) & \text{for } m = 0, \\ \frac{-4J}{\tau_x\tau_y\omega_n\omega_m}\sin\left(c_{l_y}\omega_m\right)\sin\left(\Delta_y\omega_m\right) & \\ \quad \times\left[\cos\left(c_{iw_x}\omega_n\right) - \cos\left(c_{w_x}\omega_n\right)\right]\sin\left(\Delta_x\omega_n\right) & \text{for } m \neq 0, \end{cases} \tag{2.110}$$

$$j_{yss} = \begin{cases} \frac{2Jc_{l_y}}{\tau_x \tau_y \omega_n} \left[\cos\left(c_{iw_x}\omega_n\right) - \cos\left(c_{w_x}\omega_n\right)\right] \cos\left(\Delta_x \omega_n\right) & \text{for } m = 0, \\ \frac{4J}{\tau_x \tau_y \omega_n \omega_m} \sin\left(c_{l_y}\omega_m\right) \sin\left(\Delta_y \omega_m\right) & \\ \quad \times \left[\cos\left(c_{iw_x}\omega_n\right) - \cos\left(c_{w_x}\omega_n\right)\right] \cos\left(\Delta_x \omega_n\right) & \text{for } m \neq 0, \end{cases} \tag{2.111}$$

$$j_{ysc} = \begin{cases} \frac{2Jc_{l_y}}{\tau_x \tau_y \omega_n} \left[\cos\left(c_{iw_x}\omega_n\right) - \cos\left(c_{w_x}\omega_n\right)\right] \cos\left(\Delta_x \omega_n\right) & \text{for } m = 0, \\ \frac{4J}{\tau_x \tau_y \omega_n \omega_m} \sin\left(c_{l_y}\omega_m\right) \cos\left(\Delta_y \omega_m\right) & \\ \quad \times \left[\cos\left(c_{iw_x}\omega_n\right) - \cos\left(c_{w_x}\omega_n\right)\right] \cos\left(\Delta_x \omega_n\right) & \text{for } m \neq 0, \end{cases} \tag{2.112}$$

and, J is the amplitude of the current density. Notice, that the finite length of the bars introduces a dc-term in the y-direction, because of the even symmetry around the z-axis, as shown in Fig. 2.11(b). To invoke the dc-term in the general expression, the summation over m starts at zero.

A similar expression is obtained for the current density in the x-direction J_x

$$\begin{aligned} J_x(x,y) \quad = \quad & \sum_{n=0}^{N} \sum_{m=1}^{M} \left[j_{xcc} \cos\left(\omega_n x\right) \cos\left(\omega_m y\right) + j_{xcs} \cos\left(\omega_n x\right) \sin\left(\omega_m y\right) \right. \\ & \left. + j_{xss} \sin\left(\omega_n x\right) \sin\left(\omega_m y\right) + j_{xsc} \sin\left(\omega_n x\right) \cos\left(\omega_m y\right) \right], \end{aligned} \tag{2.113}$$

where

$$j_{xcc} = \begin{cases} \frac{+2Jc_{l_x}}{\tau_x \tau_y \omega_m} \left[\cos\left(c_{iw_y}\omega_m\right) - \cos\left(c_{w_y}\omega_m\right)\right] \sin\left(\Delta_y \omega_m\right) & \text{for } n = 0, \\ \frac{+4J}{\tau_x \tau_y \omega_n \omega_m} \sin\left(c_{l_x}\omega_n\right) \cos\left(\Delta_x \omega_n\right) & \\ \quad \left[\cos\left(c_{iw_y}\omega_m\right) - \cos\left(c_{w_y}\omega_m\right)\right] \sin\left(\Delta_y \omega_m\right) & \text{for } n \neq 0, \end{cases} \tag{2.114}$$

$$j_{xsc} = \begin{cases} \frac{+2Jc_{l_x}}{\tau_x \tau_y \omega_m} \left[\cos\left(c_{iw_y}\omega_m\right) - \cos\left(c_{w_y}\omega_m\right)\right] \sin\left(\Delta_y \omega_m\right) & \text{for } n = 0, \\ \frac{+4J}{\tau_x \tau_y \omega_n \omega_m} \sin\left(c_{l_x}\omega_n\right) \sin\left(\Delta_x \omega_n\right) & \\ \quad \left[\cos\left(c_{iw_y}\omega_m\right) - \cos\left(c_{w_y}\omega_m\right)\right] \sin\left(\Delta_y \omega_m\right) & \text{for } n \neq 0, \end{cases} \tag{2.115}$$

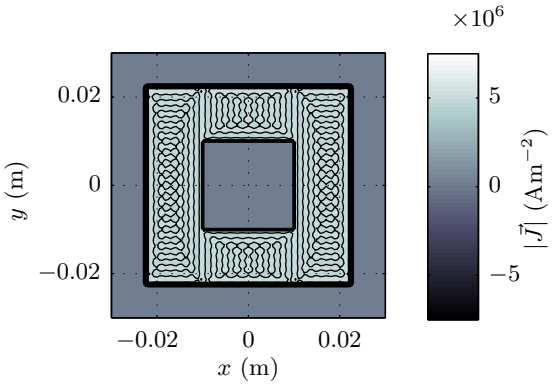

Figure 2.12: Top view of the current density distribution with four non-overlapping bars, $c_w = 22.5$ mm, $c_{iw} = 10.0$ mm, $\vec{J} = 5$ Amm^{-2}, N=M=15 harmonics.

$$j_{xss} = \begin{cases} \frac{-2Jc_{l_x}}{\tau_x \tau_y \omega_m} \left[\cos\left(c_{iw_y}\omega_m\right) - \cos\left(c_{w_y}\omega_m\right)\right] \cos\left(\Delta_y \omega_m\right) & \text{for } n = 0, \\ \frac{-4J}{\tau_x \tau_y \omega_n \omega_m} \sin\left(c_{l_x}\omega_n\right) \sin\left(\Delta_x \omega_n\right) & \\ \quad \left[\cos\left(c_{iw_y}\omega_m\right) - \cos\left(c_{w_y}\omega_m\right)\right] \cos\left(\Delta_y \omega_m\right) & \text{for } n \neq 0, \end{cases} \tag{2.116}$$

$$j_{xcs} = \begin{cases} \frac{-2Jc_{l_x}}{\tau_x \tau_y \omega_m} \left[\cos\left(c_{iw_y}\omega_m\right) - \cos\left(c_{w_y}\omega_m\right)\right] \cos\left(\Delta_y \omega_m\right) & \text{for } n = 0, \\ \frac{-4J}{\tau_x \tau_y \omega_n \omega_m} \sin\left(c_{l_x}\omega_n\right) \cos\left(\Delta_x \omega_n\right) & \\ \quad \left[\cos\left(c_{iw_y}\omega_m\right) - \cos\left(c_{w_y}\omega_m\right)\right] \cos\left(\Delta_y \omega_m\right) & \text{for } n \neq 0. \end{cases} \tag{2.117}$$

The finite lengths of the non-overlapping rectangular bars are equal to

$$2c_{l_x} = 2c_{iw_x}, \tag{2.118}$$

$$2c_{l_y} = 2c_{w_y}. \tag{2.119}$$

The resulting current density distribution for the configuration with four non-overlapping bars, Fig. 2.9(b), is shown in Fig. 2.12. The figure clearly shows the four bars with the different directions of the current flow. The current density distribution along the y-axis is shown in Fig. 2.13(a), with $M = N = 15$ harmonics. The maximum value of the current density should be equal to 5 Amm^{-2}, however peak values up to 6 Amm^{-2} are obtained. These peaks can be decreased

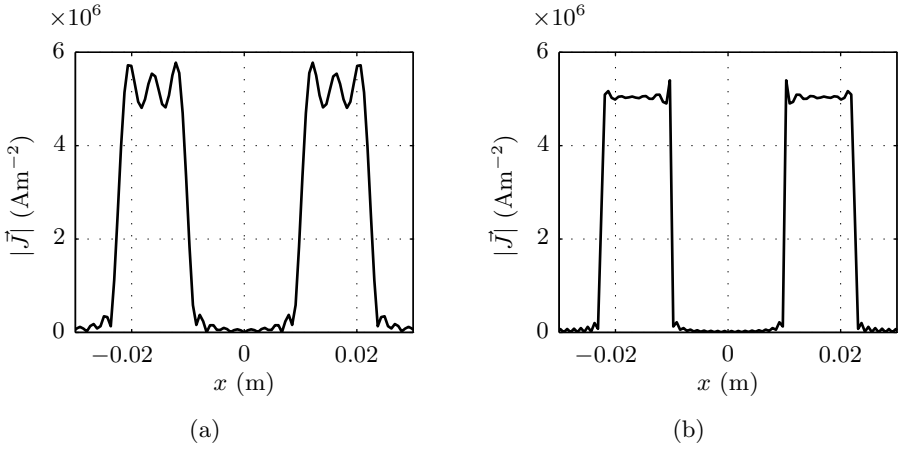

Figure 2.13: Cross-section of the current density distribution of Fig. 2.12(a) with (a) N=M=15 harmonics, and (b) N=M=75 harmonics.

by increasing the number of harmonics as shown by the current density distribution in Fig. 2.13(b), with $M = N = 75$ harmonics, five times more compared to Fig. 2.13(a). The remaining overshoot can be further reduced by increasing the number of harmonics. However, some overshoot is always present because of the Gibbs phenomenon [35].

2.4.3 Rectangular overlapping bars

The expressions for the current density distribution of the coil with overlapping bars are similar to (2.108) and (2.113). However, in this case the finite lengths are equal to

$$c_{l_x} = 0.5\left(c_{iw_x} + c_{w_x}\right), \tag{2.120}$$

$$c_{l_y} = 0.5\left(c_{iw_y} + c_{w_y}\right). \tag{2.121}$$

The modeled current density distribution of the four overlapping bars is shown in Fig. 2.14. Because of the overlapping bars, the absolute value of the current density at the inside part of each corner has a value of $\sqrt{2}J$, and is equal to zero at the outside part of each corner, respectively.

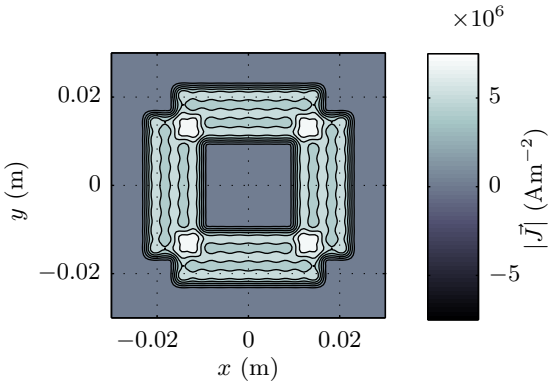

Figure 2.14: Top view of the current density distribution with four overlapping bars, $c_w = 22.5$ mm, $c_{iw} = 10.0$ mm, $\vec{J} = 5$ Amm^{-2}, N=M=15 harmonics.

2.4.4 Trapezoidal bars

Instead of rectangular current-carrying bars, the bars can be modeled by a trapezoidal shape as is applied for pieces of magnets in [22, 134]. The length of the trapezoidal bars is position dependent, and can be modeled by linear functions, as shown in Fig. 2.15(a) for the two trapezoidal bars with a current flowing in the y-direction. The trapezoidal shape introduces a dependency among the x- and y-components, which complicates the separation of variables. As it is shown in this section, such a dependency can be removed by applying a second Fourier transformation. Unfortunately, because of the required modeling parameters to obtain the trapezoidal shape, this configuration can only be applied for coils which have equal dimensions in the x- and y-direction.

The finite length of the trapezoidal bars can be modeled as a linear function

$$c_{l_x}(y) = \alpha_{l_x} y, \tag{2.122}$$

$$c_{l_y}(x) = \alpha_{l_y} x, \tag{2.123}$$

where

$$\alpha_{l_y} = \frac{c_{w_x} - c_{iw_x}}{c_{w_y} - c_{iw_y}}, \tag{2.124}$$

$$\alpha_{l_y} = \frac{c_{w_y} - c_{iw_y}}{c_{w_x} - c_{iw_x}}. \tag{2.125}$$

Normally, the modeling parameters, c_{l_x} and c_{l_y} should always be equal to one or

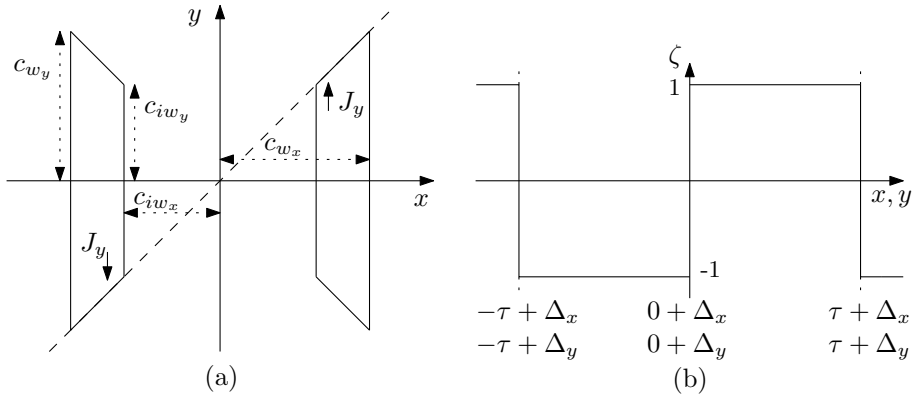

Figure 2.15: (a) Top view of two trapezoidal bars and (b) periodic function ζ.

zero, such that the amplitude of the current density distribution is not influenced by the shape of the current-carrying bar. However, because of the linear functions, in (2.122) and (2.123) this is not the case anymore. To correct for the negative part in the function describing the position dependent finite length, the current density description is multiplied with a periodic function

$$\begin{aligned}\zeta(x) &= \sum_{n_a=1}^{N_a} \frac{2(-1+\cos(\tau_x\omega_{n_a}))}{\tau_x\omega_{n_a}} \left(\sin(\Delta_x\omega_{n_a})\cos(\omega_{n_a}x)\right. \\ &\quad \left. -\cos(\Delta_x\omega_{n_a})\sin(\omega_{n_a}x)\right), \qquad (2.126)\\ \zeta(y) &= \sum_{m_a=1}^{M_a} \frac{2(-1+\cos(\tau_y\omega_{m_a}))}{\tau_y\omega_{m_a}} \left(\sin(\Delta_y\omega_{m_a})\cos(\omega_{m_a}y)\right. \\ &\quad \left. -\cos(\Delta_y\omega_{m_a})\sin(\omega_{m_a}y)\right), \qquad (2.127)\end{aligned}$$

This function, shown in Fig. 2.15(b), has an amplitude equal to one or to minus one and a similar pitch to the length of a period of the original problem.

The total current density distribution in the y-direction can be formulated by multiplying the periodic function (2.126) with the general expression of the current density in the y-direction (2.108), including the finite length of the trapezoidal

bars, $c_{l_y}(x)$ (2.123). This results for the double cosine component in

$$\begin{aligned} J_{y_{cc}} &= J\left(\frac{\alpha_{l_y}x}{\tau_y}+\sum_{m=1}^{M}\frac{2}{\tau_y\omega_m}\sin(\alpha_{l_y}x\omega_m)\cos(\Delta_y\omega_m)\cos(\omega_m y)\right) \\ &\quad\times\sum_{n_b=1}^{N_b}\frac{-2}{\tau_x\omega_{n_b}}\left(\cos(c_{iw_x}\omega_{n_b})-\cos(c_{w_x}\omega_{n_b})\right)\sin(\Delta_x\omega_n)\cos(\omega_{n_b}x) \\ &\quad\times\sum_{n_a=1}^{N_a}\frac{2(-1+\cos(\tau_x\omega_{n_a}))}{\tau_x\omega_{n_a}}\left(\sin(\Delta_x\omega_{n_a})\cos(\omega_{n_a}x)\right. \\ &\quad\left.-\cos(\Delta_x\omega_{n_a})\sin(\omega_{n_a}x)\right). \end{aligned} \tag{2.128}$$

Notice, that this function consists of three summations, where the spatial frequencies of harmonics n_a and n_b are equal to each other

$$\omega_{n_a}=\frac{n_a\pi}{\tau_x}, \tag{2.129}$$

$$\omega_{n_b}=\frac{n_b\pi}{\tau_x}. \tag{2.130}$$

Equation (2.128) consists of multiple terms depending on x, and not on a single term as preferred with respect to the method of separation of variables. Since the separated terms in the x-direction have a common periodicity, a Fourier transformation is applied to rewrite the function in a single x-term.

In case of a rectangular coil, the finite length of a bar is modeled with a linear function including an offset. To assure that the amplitude of the current density distribution is only depending on the direction of the current, the offset in the linear function needs to be multiplied with the periodic function, $\zeta(y)$. This additional multiplication introduces a component in the expression of the current density distribution in the form of $\sin(\alpha_{l_y}\omega_m x+b\sin(\omega_m y))$. This component cannot be separated by means of separation of variables, and, therefore, the current density description with trapezoidal bars can only be applied for square coils.

Applying the Fourier transformation on (2.128) gives the following expression for the current density distribution in the y-direction, for $n\neq 0$ and $m=0$

$$\begin{aligned} J_y(x,y) &= \sum_{n=1}^{N}\sum_{n_a=1}^{N_a}\sum_{n_b=1}^{N_b}\frac{2J\alpha_{l_y}}{\tau_x\tau_y\omega_{n_b}}\left(\frac{2(-1+\cos(\tau_x\omega_{n_a}))}{\tau_x\omega_{n_a}}\right) \\ &\quad\times\left(\cos(c_{iw_x}\omega_{n_b})-\cos(c_{w_x}\omega_{n_b})\right)\left(\beta_{sy1}\sin(\omega_n x)+\beta_{cy1}\cos(\omega_n x)\right), \end{aligned} \tag{2.131}$$

where

$$\begin{aligned}\beta_{sy1} &= \frac{1}{\tau_x}\int_{-\tau_x}^{\tau_x}\left[x\left(-\sin(\Delta_x\omega_{n_b})\cos(\omega_{n_b}x)+\cos(\Delta_x\omega_{n_b})\sin(\omega_{n_b}x)\right)\right.\\ &\quad\left.\times\left(\sin(\Delta_x\omega_{n_a})\cos(\omega_{n_a}x)-\cos(\Delta_x\omega_{n_a})\sin(\omega_{n_a}x)\right)\sin(\omega_n x)\right]dx,\end{aligned} \tag{2.132}$$

$$\begin{aligned}\beta_{cy1} &= \frac{1}{\tau_x}\int_{-\tau_x}^{\tau_x}\left[x\left(-\sin(\Delta_x\omega_{n_b})\cos(\omega_{n_b}x)+\cos(\Delta_x\omega_{n_b})\sin(\omega_{n_b}x)\right)\right.\\ &\quad\left.\times\left(\sin(\Delta_x\omega_{n_a})\cos(\omega_{n_a}x)-\cos(\Delta_x\omega_{n_a})\sin(\omega_{n_a}x)\right)\cos(\omega_n x)\right]dx,\end{aligned} \tag{2.133}$$

and for $n \neq 0$ and $m \neq 0$

$$\begin{aligned}J_y(x,y) &= \sum_{m=1}^{M}\sum_{n=1}^{N}\sum_{n_a=1}^{N_a}\sum_{n_b=1}^{N_b}\frac{4J}{\tau_x\tau_y\omega_{n_b}\omega_m}\left(\frac{2(-1+\cos(\tau_x\omega_{n_a})}{\tau_x\omega_{n_a}}\right)\\ &\quad\times\left(\cos(c_{iw_x}\omega_{n_b})-\cos(c_{w_x}\omega_{n_b})\right)\left(\cos(\Delta_y\omega_m)\cos(\omega_m y)\right.\\ &\quad\left.+\sin(\Delta_y\omega_m)\sin(\omega_m y)\right)\left(\beta_{sy2}\sin(\omega_n x)+\beta_{cy2}\cos(\omega_n x)\right),\end{aligned} \tag{2.134}$$

where

$$\begin{aligned}\beta_{sy2} &= \frac{1}{\tau_x}\int_{-\tau_x}^{\tau_x}\left[\sin(\alpha_{l_y}\omega_m x)\left(-\sin(\Delta_x\omega_{n_b})\cos(\omega_{n_b}x)+\cos(\Delta_x\omega_{n_b})\sin(\omega_{n_b}x)\right)\right.\\ &\quad\left.\times\left(\sin(\Delta_x\omega_{n_a})\cos(\omega_{n_a}x)-\cos(\Delta_x\omega_{n_a})\sin(\omega_{n_a}x)\right)\sin(\omega_n x)\right]dx,\end{aligned} \tag{2.135}$$

$$\begin{aligned}\beta_{cy2} &= \frac{1}{\tau_x}\int_{-\tau_x}^{\tau_x}\left[\sin(\alpha_{l_y}\omega_m x)\left(-\sin(\Delta_x\omega_{n_b})\cos(\omega_{n_b}x)+\cos(\Delta_x\omega_{n_b})\sin(\omega_{n_b}x)\right)\right.\\ &\quad\left.\times\left(\sin(\Delta_x\omega_{n_a})\cos(\omega_{n_a}x)-\cos(\Delta_x\omega_{n_a})\sin(\omega_{n_a}x)\right)\cos(\omega_n x)\right]dx.\end{aligned} \tag{2.136}$$

Similar, the current density distribution in the x-direction can be obtained, for $n = 0$ and $m \neq 0$

$$\begin{aligned}J_x(x,y) &= \sum_{m=1}^{M}\sum_{m_a=1}^{M_a}\sum_{m_b=1}^{M_b}\frac{2J\alpha_{l_x}}{\tau_x\tau_y\omega_{m_b}}\left(\frac{2(-1+\cos(\tau_y\omega_{m_a}))}{\tau_y\omega_{m_a}}\right)\\ &\quad\times\left(\cos(c_{iw_y}\omega_{m_b})-\cos(c_{w_y}\omega_{m_b})\right)\left(\beta_{sx1}\sin(\omega_m y)+\beta_{cx1}\cos(\omega_m y)\right),\end{aligned} \tag{2.137}$$

where

$$\begin{aligned}\beta_{sx1} &= \frac{1}{\tau_y}\int_{-\tau_y}^{\tau_y}\left[y\left(-\sin(\Delta_y\omega_{m_b})\cos(\omega_{m_b}y)+\cos(\Delta_y\omega_{m_b})\sin(\omega_{m_b}y)\right)\right.\\ &\left.\times\left(\sin(\Delta_y\omega_{m_a})\cos(\omega_{m_a}y)-\cos(\Delta_y\omega_{m_a})\sin(\omega_{m_a}y)\right)\sin(\omega_m y)\right]dy,\end{aligned} \tag{2.138}$$

$$\begin{aligned}\beta_{cx1} &= \frac{1}{\tau_y}\int_{-\tau_y}^{\tau_y}\left[y\left(-\sin(\Delta_y\omega_{m_b})\cos(\omega_{m_b}x)+\cos(\Delta_y\omega_{m_b})\sin(\omega_{m_b}x)\right)\right.\\ &\left.\times\left(\sin(\Delta_y\omega_{m_a})\cos(\omega_{m_a}y)-\cos(\Delta_y\omega_{m_a})\sin(\omega_{m_a}y)\right)\cos(\omega_m y)\right]dy,\end{aligned} \tag{2.139}$$

and for $n \neq 0$ and $m \neq 0$

$$\begin{aligned}J_x(x,y) &= \sum_{n=1}^{N}\sum_{m=1}^{M}\sum_{m_a=1}^{M_a}\sum_{m_b=1}^{M_b}\frac{4J}{\tau_x\tau_y\omega_n\omega_{m_b}}\left(\frac{2(-1+\cos(\tau_y\omega_{m_a})}{\tau_y\omega_{m_a}}\right)\\ &\times\left(\cos(c_{iw_y}\omega_{m_b})-\cos(c_{w_y}\omega_{m_b})\right)\left(\cos(\Delta_x\omega_n)\cos(\omega_n x)\right.\\ &\left.+\sin(\Delta_x\omega_n)\sin(\omega_n x)\right)\left(\beta_{sx2}\sin(\omega_m y)+\beta_{cx2}\cos(\omega_m y)\right),\end{aligned} \tag{2.140}$$

where

$$\begin{aligned}\beta_{sx2} &= \frac{1}{\tau_y}\int_{-\tau_y}^{\tau_y}\left[\sin(\alpha_{l_x}\omega_n y)\left(-\sin(\Delta_y\omega_{m_b})\cos(\omega_{m_b}x)+\cos(\Delta_y\omega_{m_b})\sin(\omega_{m_b}y)\right)\right.\\ &\left.\times\left(\sin(\Delta_y\omega_{m_a})\cos(\omega_{m_a}y)-\cos(\Delta_y\omega_{m_a})\sin(\omega_{m_a}y)\right)\sin(\omega_m y)\right]dy,\end{aligned} \tag{2.141}$$

$$\begin{aligned}\beta_{cx2} &= \frac{1}{\tau_y}\int_{-\tau_y}^{\tau_y}\left[\sin(\alpha_{l_x}\omega_n y)\left(-\sin(\Delta_y\omega_{m_b})\cos(\omega_{m_b}y)+\cos(\Delta_y\omega_{m_b})\sin(\omega_{m_b}y)\right)\right.\\ &\left.\times\left(\sin(\Delta_y\omega_{m_a})\cos(\omega_{m_a}y)-\cos(\Delta_y\omega_{m_a})\sin(\omega_{m_a}y)\right)\cos(\omega_m y)\right]dy,\end{aligned} \tag{2.142}$$

where spatial frequencies are equal to

$$\omega_{m_a} = \frac{m_a\pi}{\tau_y}, \tag{2.143}$$

$$\omega_{m_b} = \frac{m_b\pi}{\tau_y}. \tag{2.144}$$

The current density distribution of the four trapezoidal bars is shown in Fig. 2.16. The trapezoidal shape can be clearly seen in the figure.

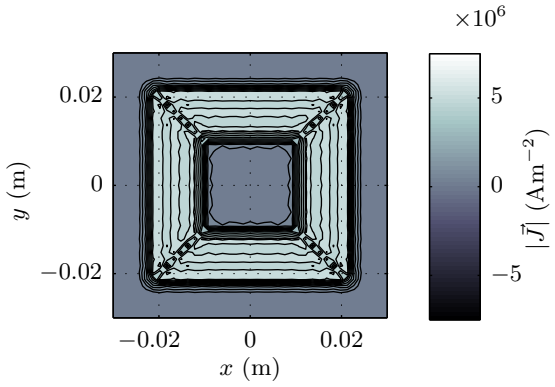

Figure 2.16: Top view of the current density distribution with four trapezoidal bars, $c_w = 22.5$ mm, $c_{iw} = 10.0$ mm, $\vec{J} = 5$ Amm^{-2}, N=M=15 harmonics.

2.4.5 Comparison of the coil configurations

To compare the three coil configurations, the magnetic fields above a coil surrounded by air are calculated by the three-dimensional harmonic model and compared to magneto-static FEM simulations using Flux 3D. A cross-section of the problem, solved by the harmonic model, is shown in Fig. 2.10 and consists of three regions. The coil is located in the middle region, and the regions above and below the coil are filled with air, and have an infinite height. The coils modeled in the FEM are meshed and have geometry similar to the coil presented in Fig. 2.9, including the round corners. The difference between the results obtained with the FEM model and the harmonic model is expressed as percentage of the value predicted in the FEM model. The average difference between the values from FEM model and the harmonic model is, for example, for the flux density distribution calculated as

$$\text{diff}_{ave} = \frac{1}{D_x D_y} \sum_{d_x=1}^{D_x} \sum_{d_y=1}^{D_y} \left| \frac{B_{FEM}(x_{d_x}, y_{d_y}) - B_{hm}(x_{d_x}, y_{d_y})}{B_{FEM}(x_{d_x}, y_{d_y})} \right|, \tag{2.145}$$

where D is the number of points in the xy-plane at which the values by both methods are obtained.

The magnetic flux density distribution simulated by the three-dimensional harmonic model using the current density distribution with four non-overlapping bars is shown in Fig. 2.17(a). The difference between the absolute values predicted by both methods is shown in Fig. 2.17(b), and an average difference of 18% is ob-

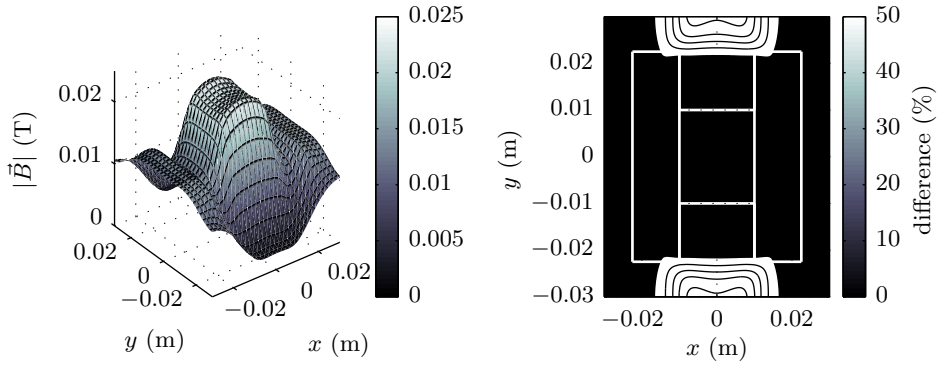

(a) (b)

Figure 2.17: Magnetic flux density distribution at 1 mm above a coil modeled by four rectangular non-overlapping bars with $c_w = 22.5$ mm, $c_{iw} = 10.0$ mm, $\vec{J} = 5$ Amm^{-2}, and N=M=15 harmonics: (a) absolute value obtained by the harmonic model, and (b) difference of the flux density distribution between the analytical and FEM results.

tained. The largest difference, approximately 50%, appears outside the coil along the positive and negative x-axis. This difference is caused by the relatively large distance between the end of the bars in the y-direction and the beginning of the bars in the x-direction.

Figure 2.18(a) shows the magnetic flux density above a coil modeled with four overlapping bars, and the difference with respect to the FEM model is shown in Fig. 2.18(b). In comparison with the large difference of the previous configuration, an average difference of only 1.7% between the analytical model and the FEM simulation is obtained. The largest difference, approximately 20%, can be found at the outside part of the corner, where the analytically calculated distribution of the current density has an amplitude equal to zero.

The magnetic flux density distribution above the configuration with four trapezoidal bars is shown in Fig. 2.19. Similar to the configuration with four overlapping-bars, an almost constant magnetic flux density is achieved in the area of the periodic region outside the coil, which is not obtained in the configuration with the non-overlapping bars. An average difference of 0.4% for the configuration with four trapezoidal bars is estimated compared to the FEM model. Furthermore, a maximum difference of approximately 20% occurs at the transition between the adjoining bars, as shown in Fig. 2.19(b).

From these simulations, it might be concluded that a topology, in which the end and the beginning of two adjoining bars are close to each other, results in a distribution of the magnetic flux density comparable to the flux density distribution

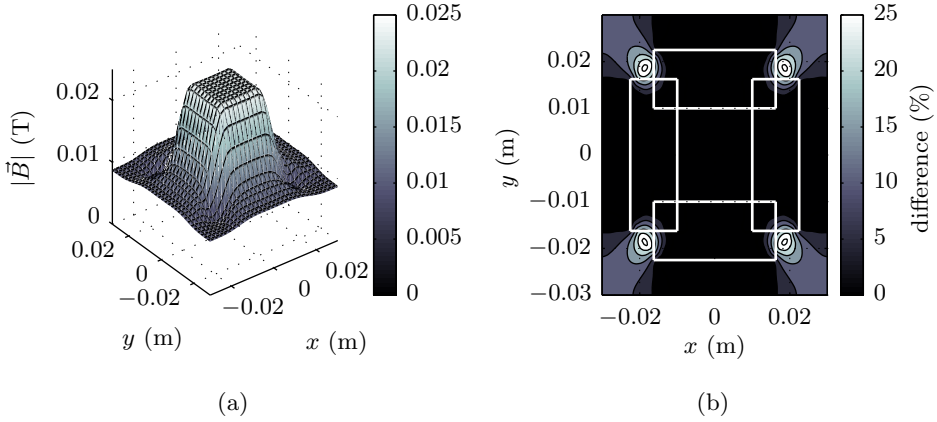

Figure 2.18: Magnetic flux density distribution at 1 mm above a coil modeled by four rectangular overlapping bars with $c_w = 22.5$ mm, $c_{iw} = 10.0$ mm, $\vec{J} = 5$ Amm^{-2}, and N=M=15 harmonics: (a) absolute value obtained by the harmonic model, and (b) difference of the flux density distribution between the analytical and FEM results.

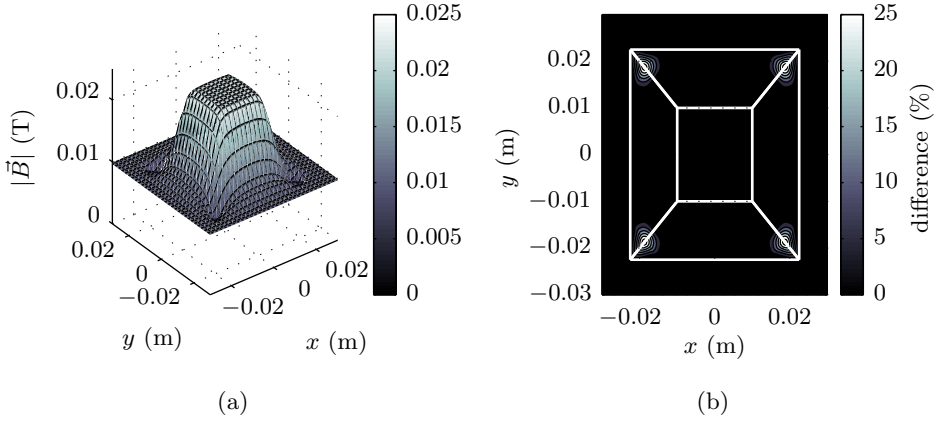

Figure 2.19: Magnetic flux density distribution at 1 mm above a coil modeled by four trapezoidal bars with $c_w = 22.5$ mm, $c_{iw} = 10.0$ mm, $\vec{J} = 5$ Amm^{-2}, and N=M=15 harmonics: (a) absolute value obtained by the harmonic model, and (b) difference of the flux density distribution between the analytical and FEM results.

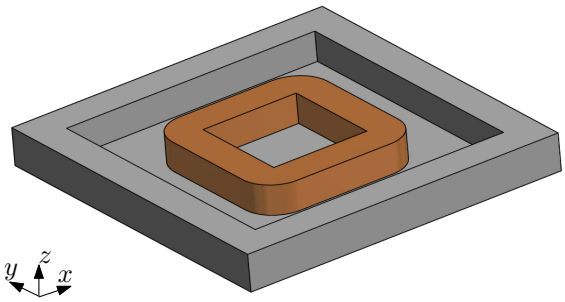

Figure 2.20: Schematic overview of a coil placed in a cavity for a single period of the harmonic model.

with a coil with round corners, as simulated by FEM. As the magnetic flux density distribution is only an initial step in the prediction of the electromagnetic quantities of the CET system, such as self- and mutual inductances, the comparison of the three configurations is continued in Section 2.5.1, in which measured self-inductances of coils with different dimensions are compared to the ones obtained with the three different configurations. Based on the conclusion drawn from the comparison of the flux density distribution, the topologies with overlapping and trapezoidal bars give the most accurate prediction of the flux density distribution. Since the configuration with overlapping bars allows to model square and rectangular coils, the current density distribution for a coil in a cavity is presented in the next section.

2.4.6 Coil in a cavity

The current density distribution of a coil in a cavity, as illustrated in Fig. 2.20, is different to the one outside a cavity because of the non-periodicity of the region. To satisfy the Neumann boundary condition in the tangential direction of the magnetic fields in the cavity, the magnetic field is modeled with a periodicity of the double length of the cavity (2.68). The imaging method is applied to obtain a current density description with similar periodicity. The imaging method replaces the Neumann boundary by an imaginary source, such that the magnetic field remains the same at the boundary [28, 45, 86]. The current-carrying bars parallel to the Neumann boundary are mirrored with respect to the boundary as shown in Fig. 2.21(a). The current-carrying bars orthogonal to the boundary are mirrored and, as a consequence, the current flows in opposite direction in the imaginary source, as shown in Fig. 2.21(c). Because of the opposite direction of the current, the amplitude of the imaginary source becomes negative with respect to the description of the current density distribution, as shown in Fig. 2.21(d).

Therefore, a finite bar including its image can be modeled by a complete sine or cosine function, and, as a result, the dc-term as required to model the finite length of a current-carrying bar in a continuous region, (2.108), disappears.

The current density distribution for a coil in a cavity, consisting of four overlapping bars, can be written as

$$\begin{aligned} J_x(x,y) &= \sum_{v=1,3,5,..}^{V} \sum_{w=1,3,5,..}^{W} j_{x_s lot} \\ &\times \Big[\cos(\omega_v \Delta_x) \cos(\omega_w \Delta_y) \cos(\omega_v x^*) \sin(\omega_w y^*) \\ &- \sin(\omega_v \Delta_x) \sin(\omega_w \Delta_y) \sin(\omega_v x^*) \cos(\omega_w y^*) \\ &- \cos(\omega_v \Delta_x) \sin(\omega_w \Delta_y) \cos(\omega_v x^*) \cos(\omega_w y^*) \\ &+ \sin(\omega_v \Delta_x) \cos(\omega_w \Delta_y) \sin(\omega_v x^*) \sin(\omega_w y^*) \Big], \end{aligned} \tag{2.146}$$

$$\begin{aligned} J_y(x,y) &= \sum_{v=1,3,5,..}^{V} \sum_{w=1,3,5,..}^{W} j_{y_{slot}} \\ &\times \Big[\cos(\omega_v \Delta_x) \cos(\omega_w \Delta_y) \sin(\omega_v x^*) \cos(\omega_w y^*) \\ &- \sin(\omega_v \Delta_x) \sin(\omega_w \Delta_y) \cos(\omega_v x^*) \sin(\omega_w y^*) \\ &+ \cos(\omega_v \Delta_x) \sin(\omega_w \Delta_y) \sin(\omega_v x^*) \sin(\omega_w y^*) \\ &- \sin(\omega_v \Delta_x) \cos(\omega_w \Delta_y) \cos(\omega_v x^*) \cos(\omega_w y^*) \Big], \end{aligned} \tag{2.147}$$

where

$$\begin{aligned} j_{x_{slot}} &= \frac{8J}{\tau_v \omega_v \tau_w \omega_w} \left(-\cos\left(c_{iw_y} \omega_w\right) + \cos\left(c_{w_y} \omega_w\right) \right) \\ &\times \left(\sin\left(\frac{\tau_w \omega_w}{2} \right) \right)^2 \left(-1 + \cos\left(\tau_v \omega_v\right) \right) \sin\left(c_{l_x} \omega_v\right) \end{aligned} \tag{2.148}$$

$$\begin{aligned} j_{y_{slot}} &= \frac{8J}{\tau_v \omega_v \tau_w \omega_w} \left(-\cos\left(c_{iw_x} \omega_v\right) + \cos\left(c_{w_x} \omega_v\right) \right) \\ &\times \left(\sin\left(\frac{\tau_v \omega_v}{2} \right) \right)^2 \left(-1 + \cos\left(\tau_w \omega_w\right) \right) \sin\left(c_{l_y} \omega_w\right). \end{aligned} \tag{2.149}$$

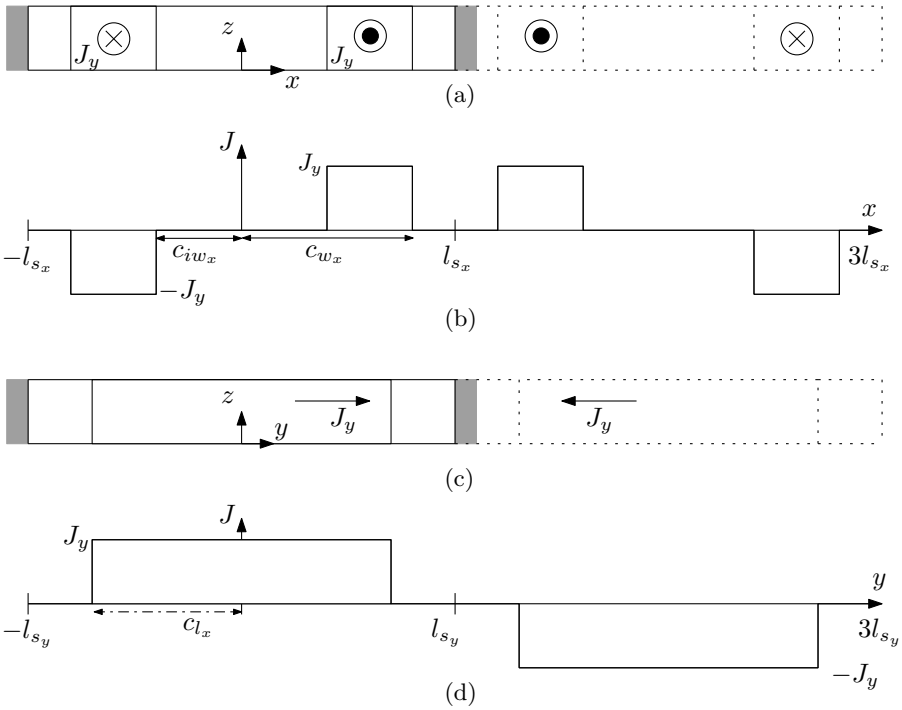

Figure 2.21: Source description for non-periodic regions using the imaging method: (a) current density perpendicular to the x-axis and (b) the corresponding model for the harmonic description, (c) current density parallel to the y-axis and (d) the corresponding model for the harmonic description.

$$c_{l_x} = 0.5\left(c_{iw_x} + c_{w_x}\right), \tag{2.150}$$

$$c_{l_y} = 0.5\left(c_{iw_y} + c_{w_y}\right). \tag{2.151}$$

The magnetic flux density distribution of a coil located in a cavity is calculated with the harmonic model and shown in Fig. 2.22(a) at 1 mm above the cavity. The calculated flux density distribution is compared to results achieved from FEM simulations, and the difference between the two methods has an average value of 6.8%, as shown in Fig. 2.22. Differences of 10% are obtained at the borders of the cavity and periodic in the x- and y-direction. They are caused by the correlation of the different spatial harmonics at the border of the cavity and the periodic region with the mode-matching technique.

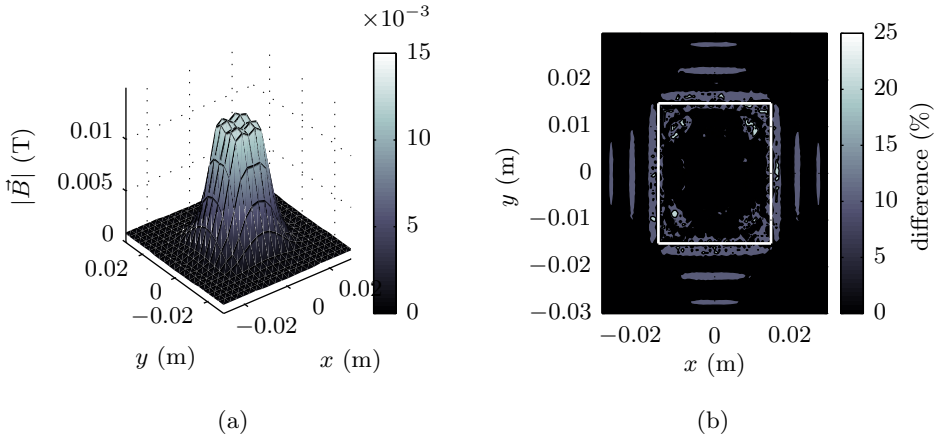

Figure 2.22: Magnetic flux density distribution at 1 mm above a cavity with a coil inside, with $2l_{sx} = 2l_{sy} = 30.0$ mm, $c_w = 13.0$ mm, $c_{iw} = 5.0$ mm, $\vec{J} = 5$ Amm^{-2}, N=M=10 harmonics, V=W=5 harmonics, and the coil is modeled by four overlapping bars: (a) absolute value obtained by the harmonic model, and (b) difference of the flux density distribution between the analytical and FEM results.

2.5 Electromagnetic quantities

The distribution of the magnetic fields is an important measure for the electromagnetic quantities, such as inductance and force. The inductances are a direct input for the lumped-parameter model of the contactless energy transfer system, which is presented in Chapter 3. In the next sections, the electromagnetic quantities are presented with respect to magnetic fields.

2.5.1 Self-inductance

The inductance of a coil is defined as the flux, λ, produced by a coil per ampere, i, flowing through that coil

$$L = \frac{\mathrm{d}\lambda(i)}{\mathrm{d}i}, \tag{2.152}$$

which is known as the incremental inductance and evaluated at the actual operation point of the λ-i curve of the media surrounded by the coil. In case of a coil surrounded by air, the coil is assumed to be a magnetic linear system and (2.152)

becomes equal to

$$L = \frac{\lambda}{i}, \tag{2.153}$$

which is known as the apparent inductance. With respect to the magnetic field parameters, the self-inductance of a coil can be obtained by either one of the two integrals

$$L = \frac{N^2}{I^2} \int_v \vec{J} \cdot \vec{A} dv_{domain}, \tag{2.154}$$

$$= \frac{N}{I} \int_s \vec{B} \cdot ds_{coil}, \tag{2.155}$$

where N is the number of turns of the coil, I the current through the coil, v is the volume of the coil, and s the area enclosed by the turns of the coil.

In case of a non-periodic region, where the height of a coil is equal to the height of the cavity, the magnetic vector potential contains an offset which is not included in the expression, and, therefore, not well defined at the boundary between the periodic and non-periodic region [92]. Because the flux density is obtained by differentiating the magnetic vector potential, this offset is not present in the flux density distribution, and, therefore, (2.155) should be used to calculate the self-inductance of a coil in a cavity. Since every turn of the coil is linked with a different amount of flux, (2.155) might lead to an inaccurate solution. A way to avoid this inaccurate solution, is to apply the filament method, as described in Section 2.1, and to calculate the average flux linkage per turn [3, 117].

To compare the three different configurations for the current density distribution of a coil, the self-inductance of various coils surrounded by air and of coils located above an aluminum plate are measured and calculated by means of the harmonic modeling method. A photo of the four coils is shown in Fig. 2.23 and the dimensions of the two round coils, A and B, and two square coils, C and D, are listed in Table 2.1. The parameters related to the harmonic modeling method are listed in Table 2.2, a similar model as shown in Fig. 2.10 is taken into account. For comparing, the self-inductance is also calculated by the law of Biot-Savart in combination with the filament method.

The self-inductances obtained by the different methods are listed in Table 2.3. It can be observed that the self-inductances calculated based on the coil configuration with the non-overlapping straight bars do not match with the measured self-inductances. For example, a difference above 100% is found for coil A and C. The inductances calculated with the current density distribution based on the configuration with the trapezoidal and the overlapping bars results in an average

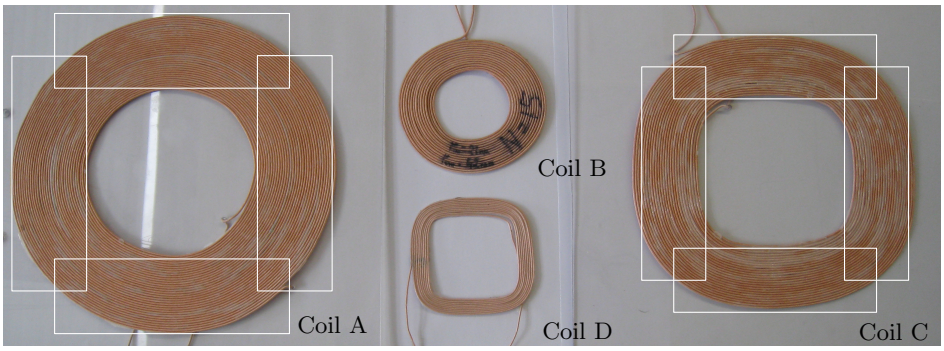

Figure 2.23: Photo of the sample coils, including the distribution of the four overlapping bars on top of a square and round coil.

Table 2.1: Dimensions of the sample coils

Coil	c_{w_x} (mm)	c_{iw_x} (mm)	c_{w_y} (mm)	c_{iw_y} (mm)	N (turns)
A	101	51	101	51	34
B	36	21	36	21	11
C	85	45	85	45	26
D	33	23	33	23	10

difference of 5.6% and 1.6% compared to the measured values for the two round coils, coils A and B, respectively. The calculated self-inductances for the square coils, coils C and D, are in better agreement with the current density description of the trapezoidal bars than with the overlapping bars. A difference of 6.0% and 17.4% is found between the two methods and the measured values, respectively. Since the self-inductance of a single coil surrounded by air is measured, the law of Biot-Savart gives with an average difference of 1.2% a good prediction of the self-inductance for all four coils.

To validate the harmonic model, which includes the eddy-current reaction field, the self-inductances of coil A and D positioned on top of an aluminum plate are calculated using the harmonic modeling method and are compared to measurements. In the harmonic model, the layer of air underneath the coil is replaced by a region with conduction material with the properties listed in Table 2.2, and the coil is modeled by four overlapping rectangular bars. Furthermore, the aluminum plate has a thickness of 10 mm, and, therefore, the amplitude of the magnetic field at the bottom of the plate is assumed to be equal to zero, and the Neumann boundary condition is applied at this boundary. The calculated and measured self-inductances for frequencies between 10 kHz and 150 kHz are shown in Fig. 2.24. In the frequency domain, an average difference of 2.2% and 2.4% is obtained between the calculated and measured self-inductances of Coil A and D, respectively. As shown in Fig. 2.24, the differences decrease with respect to an

Table 2.2: Obtained parameters for the harmonic model

par.	value
h_{coil}	1.5 mm
h_{air}	$h_{air} >> h_{coil}$
τ_x	$1.5c_{w_x}$
τ_y	$1.5c_{w_y}$
N	15 harmonics
M	15 harmonics
$\mu_{r_{AL}}$	1
σ_{AL}	$26{\cdot}10^6$ Sm^{-1}

Table 2.3: Self inductances of the sample coils

Method	L_A (μH)	L_B (μH)	L_C (μH)	L_D (μH)
Measured	220.30	9.70	124.90	10.6
3D FEM	219.43	9.42	118.60	10.7
Overlapping bars	202.45	9.37	104.40	8.65
Non-overlapping bars	533.73	13.6	242.81	12.8
Trapezoidal bars	218.88	9.93	121.72	9.60
Biot-Savart law	219.00	9.45	124.15	10.7

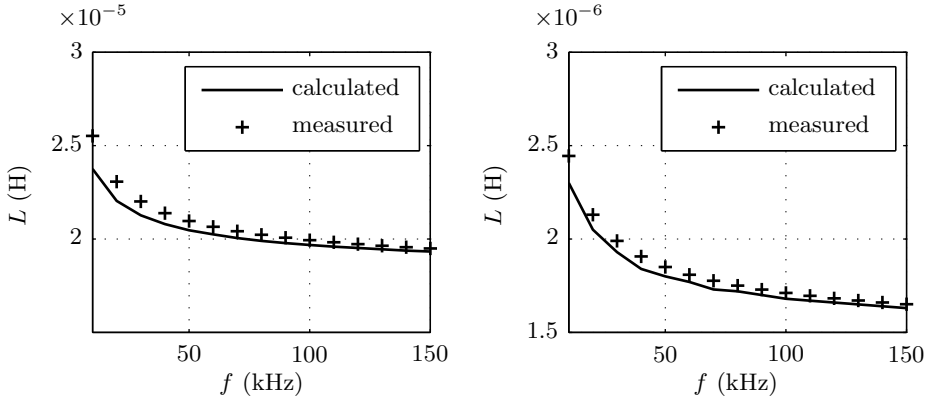

Figure 2.24: Calculated and measured self-inductance of (a) Coil A, and (b) Coil D on top of an aluminum plate for various frequencies.

increasing frequency, and they are also lower with respect to the differences found with the self-inductances of the coils surrounded by air. The eddy-current reaction field decreases the self-inductance of a coil compared to a coil surrounded by air. For example, at a frequency of 100 kHz the self-inductance of Coil A is equal to 19.9 μH, which is approximately 10 times lower compared to the self-inductance measured in air, as listed in Table 2.3.

Based on the comparison of the difference between the calculated and measured value of the self-inductance, both the current density descriptions with overlapping and trapezoidal bars give a result close to the measured values. Although, the current density description with the four trapezoidal bars gives a better prediction with respect to the measured values, the requirement of a square coil limits the geometric possibilities, and, therefore, the configuration of overlapping bars is taken into account.

2.5.2 Mutual inductance

The mutual inductance is defined by the ratio of the flux linked with the turns of a second coil with the current flowing through the first coil. Similar to the self-inductance, the mutual inductance between the primary and secondary coil can be calculated using two methods depending on the type of region in which the coil is positioned

$$M_{ps} = \frac{N_p N_s}{I_p I_s} \int_{v_s} \vec{J_s} \cdot \vec{A_p} dv_{domains}, \tag{2.156}$$

$$= \frac{N_s}{I_p} \int_{s_s} \vec{B_p} \cdot ds_{coil_s}, \tag{2.157}$$

where subscripts p and s present primary and secondary, respectively. Similar to the self-inductance, (2.156) can be evaluated over the entire volume of the region since the volume of the coil is embedded in the current density description. If a coil is located in a cavity, (2.157) should be applied. Similar to the self-inductance, the accuracy of (2.157) can be improved by applying the filament method to calculate an average flux linkage per turn.

2.5.3 Electromagnetic force

The time varying electromagnetic field generates an electromagnetic force between the primary and secondary coil of a contactless energy transfer system. Based on the magnetic field distribution, the attraction force can be calculated using the Maxwell stress tensor

$$\mathbb{T} = \begin{bmatrix} \frac{B_x^2 - B_y^2 - B_z^2}{2} & B_x B_y & B_x B_x \\ B_y B_x & \frac{B_y^2 - B_x^2 - B_z^2}{2} & B_y B_z \\ B_z B_x & B_z B_y & \frac{B_z^2 - B_x^2 - B_y^2}{2} \end{bmatrix}. \tag{2.158}$$

Integration of the stress tensor over an enclosed surface gives the force acting on the enclosed volume

$$\vec{F} = \frac{1}{\mu_0} \oint_s \mathbb{T} \cdot \vec{n} ds. \tag{2.159}$$

The use of ferromagnetic plates or cavities increases the magnetic flux density, and, thereby, the force between the coils. Therefore, the electromagnetic force may not be neglected in design of a contactless energy transfer system.

2.5.4 Eddy-current losses

The magnetic fields of the primary coils do not only introduce a voltage in the secondary coil, but also a circulating current in the nearby conducting materials. If the CET system is integrated into a linear or planar motor nearby volumes with conducting material are, for example, an array of permanent magnets or a stainless steel cooling plate. These induced eddy currents not only decrease the flux linkage between the primary and secondary coil, but also induce a magnetic flux which opposes to the magnetic flux of the primary coils. The eddy currents are modeled by taking the diffusion equation into account as presented in Section 2.2.2. The losses generated by the eddy currents can be obtained using Poynting's theorem [137]

$$P_{eddy} = \frac{1}{2} \oint_s \mathrm{Re}\left(\vec{E} \times \vec{H}\right) ds, \tag{2.160}$$

where the conducting is bounded by surface s.

The generated eddy-current losses cause a temperature increase in the conducting material. By segmentation of the conducting material or laminating of an iron-core, the width of the area with eddy currents is decreased, and hence, the enclosed variation in magnetic flux density. Moreover, the resistance of the path increases, and, as a result, the eddy-current losses are reduced.

If the conducting material is segmented, different approaches can be obtained to model the eddy-current losses with respect to the harmonic modeling method. A first approach takes the eddy-current reaction fields into account, by modeling the conducting material as a solid layer of conducting material in the harmonic model. However, this approach neglects the segmentation in the calculation of the magnetic fields and losses [55, 137]. A second approach neglects the reaction field of the eddy currents, but takes the segmentation into account during the determination of the magnetic fields by modeling the eddy-currents as an external

current source [75, 102]. This second approach is only valid in topologies with current with a fundamental frequency up to a few hundred Hertz, since the reaction fields have no signification effect on the magnetic field distribution in those cases. A third approach is to model the layer as a solid conducting material with an anisotropic equivalent conductivity and permeability, which are obtained with respect to the dimensions of the segments of conductive and non-conductive material in the region [34, 129].

A CET system operates usually at a frequency in the order of 100 kHz, and, therefore, the eddy-current reaction field may not be ignored in the determination of the magnetic field and inductances, as, for example, is shown in Section 2.5.1 for coils located above an aluminum plate. This requirement eliminates the second approach in which the segmentation is included in the geometry, and the eddy-current reaction field is neglected.

2.6 Summary and conclusions

The harmonic modeling method is presented in this chapter as an alternative for the law of Biot-Savart and numerical methods to obtain a description of the magnetic field around an air-cored coil. The harmonic modeling method divides the electromagnetic problem in horizontal regions, which differ from each other with respect to the presence of permanent magnets or coils as the source of the magnetic fields, different material properties and different periodicities. The three-dimensional magnetic vector potential is formulated for each different type of region. A mathematical description of the magnetic flux density distribution is obtained by solving the unknown coefficients in the description of the magnetic vector potential within the different regions in combination with the boundary conditions around and between the regions. The boundary conditions between the different regions are solved by expressing the tangential components of the magnetic field strength in terms of the magnetic scalar potential and extending the mode-matching technique to two dimensions. The extension of the mode-matching technique allows to obtain a solution for the magnetic fields in geometries with slots and cavities. Furthermore, the model is able to include regions with an electrical conductivity. Therefore, the eddy-current reaction fields are taken into account, which have a major influence on the inductances in a CET system with an operating frequency in the order of hundred kilohertz.

The current density distribution of a coil in the harmonic modeling method is represented by four straight bars. Three different configurations are presented: straight bars, which are placed against each other; straight bars, which are overlapping each other; and bars with a trapezoidal shape, which are positioned against each other. A mathematical description for each configuration is given, and they are compared to each other with respect to the magnetic flux density and self-

inductances of a coil. Both the configurations with overlapping and trapezoidal bars give a value of the inductance of a coil within 10% for various coil dimensions with respect to measurements and FEM simulations. The current density distribution of a coil is presented both for continuous and discontinuous regions.

The derivation of the magnetic fields is a first step in the design of a contactless energy transfer system. The electromagnetic quantities, such as self- and mutual inductances are used in the next chapters as input for the electrical model of a CET system.

3

Lumped parameter model of a contactless energy transfer system

The main component of a Contactless Energy Transfer (CET) system is a transformer with an airgap between the primary and secondary side, which can in the electric domain be represented by an electrical equivalent circuit. Two different electrical equivalent circuits for a CET system are presented in this chapter: the coupled inductance model, and the transformer T-model. The models are presented for a single primary and single secondary coil, and are extended for multiple primary coils. A CET system is often referred to as a loosely coupled inductive coupling, because the mutual inductance is usually a small percentage of the self-inductance of the coils [11, 130]. Although the magnetic coupling is low, resonance techniques can be applied to improve the energy transfer. The resonance technique is introduced and applied to formulate the transfer function of an inductive coupling with multiple primary coils and a single secondary coil. The energy transfer capability of a CET system is limited by the losses in the coils of the inductive coupling, or the temperature of the coils. To calculate the maximum energy that can be transferred, a thermal model of a contactless energy transfer system is presented.

The contributions of this chapter are published in:

J. P. C. Smeets, T. T. Overboom, J. W. Jansen, and E. A. Lomonova [2013], 'Modeling Framework for Contactless Energy Transfer Systems for Linear Actuators', *IEEE Transactions on Industrial Electronics*, **60**(1), pp. 391-399.

J. P. C. Smeets, T. T. Overboom, J. W. Jansen, and E. A. Lomonova [2013], 'Comparison of Position Independent Contactless Energy Transfer Systems', *IEEE Transactions on Power Electronics'*, **28**(4), pp. 2059-2067.

3.1 Electrical equivalent circuits

The transfer of magnetic energy in a transformer can be represented by two electrical equivalent circuit models: the coupled inductance model and the transformer T-model. The coupled inductance model can be directly obtained from Faraday's and Lenz's law and is rewritten in the more commonly used transformer T-model.

The coupled inductance model for a single primary and secondary coil is shown in Fig. 3.1. Each coil is represented by a self-inductance and a winding resistance. The voltage across the self-inductance of a coil, can be obtained by Faraday's law

$$v_{L_p} = N_p \frac{\mathrm{d}\Phi_p}{\mathrm{d}t} = \frac{\mathrm{d}\lambda}{\mathrm{d}t} = \frac{\mathrm{d}\left(Li_p\right)}{\mathrm{d}t} = L\frac{\mathrm{d}i_p}{\mathrm{d}t}, \tag{3.1}$$

where Φ_p is the flux produced by the primary coil. With respect to the coupling of the primary and secondary coil, the voltage across the mutual inductance at the secondary side is defined in opposite direction with respect to the primary side, since the magnetic fields of both coils are counteracting each other. Therefore, a combination of Faraday's and Lenz's law is applied to formulate the induced voltage across the mutual inductance

$$v_M = -N_p N_s \frac{\mathrm{d}\Phi_{sp}}{\mathrm{d}t} = -M\frac{\mathrm{d}i_s}{\mathrm{d}t}, \tag{3.2}$$

where Φ_{sp} is the flux linked by the primary coil produced by the secondary coil. In combination with the voltage drop across the resistance of the coil, Kirchhoff's voltage law describes the voltages at the input and output terminals of the inductive coupling, [20],

$$v_p = R_p i_p + L_p \frac{\mathrm{d}i_p}{\mathrm{d}t} - M\frac{\mathrm{d}i_s}{\mathrm{d}t}, \tag{3.3}$$

$$v_s = -R_s i_s - L_s \frac{\mathrm{d}i_s}{\mathrm{d}t} + M\frac{\mathrm{d}i_p}{\mathrm{d}t}, \tag{3.4}$$

where R_p and R_s are the resistance of the primary and secondary coil, respectively.

Another way to represent the transfer of energy in a transformer by an electrical equivalent circuit is given by the transformer T-model, as shown in Fig. 3.2. The electrical equivalent circuit embeds an ideal transformer in the circuit is defined as a transformer with an efficiency equal to 100%, and only modifies the amplitude of the voltages and currents with respect to the turn ratio. In the transformer

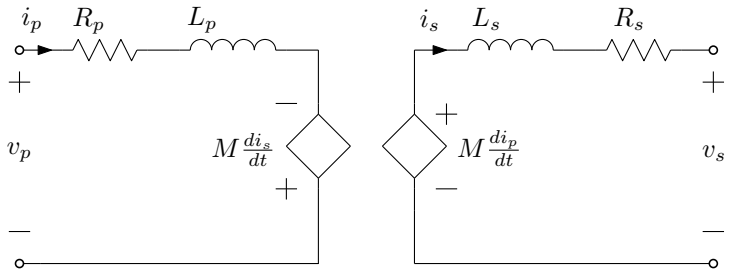

Figure 3.1: Electrical equivalent circuit of a transformer: coupled inductance model.

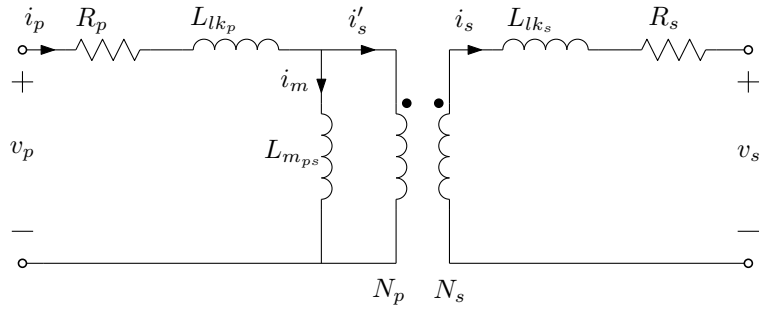

Figure 3.2: Electrical equivalent circuit of a transformer: T-model.

T-model, the self- and mutual inductance are rewritten into a leakage and magnetizing inductance, L_{lk} and L_m, respectively. The magnetizing inductance is a fraction of the self-inductance which is coupled with the secondary coil. The current through this inductance is required to establish a coupled magnetic field. The leakage inductance represents the uncoupled flux. Furthermore, the sum of the magnetizing and leakage inductance is always equal to the self-inductance of a coil.

The leakage and magnetizing inductances depend on the turn ratio, ($a = N_p / N_s$),

and the self- and mutual inductances, and are defined as

$$L_{lk_p} = L_p - aM, \tag{3.5}$$

$$L_{lk_s} = L_s - \frac{M}{a}, \tag{3.6}$$

$$L_{m_{ps}} = aM, \tag{3.7}$$

$$L_{m_{sp}} = \frac{M}{a}. \tag{3.8}$$

An expression for the primary and secondary voltages of the T-model is obtained by rewriting (3.3) and (3.4), using (3.5)-(3.8)

$$v_p = R_p i_p + (L_p - aM)\frac{\mathrm{d}i_p}{\mathrm{d}t} + aM\frac{\mathrm{d}\left(i_p - \frac{i_s}{a}\right)}{\mathrm{d}t}, \tag{3.9}$$

$$v_s = -R_s i_s - \left(L_s - \frac{M}{a}\right)\frac{\mathrm{d}i_s}{\mathrm{d}t} + \frac{M}{a}\frac{\mathrm{d}\left(ai_p - i_s\right)}{\mathrm{d}t}, \tag{3.10}$$

and is further simplified to

$$v_p = R_p i_p + L_{lk_p}\frac{\mathrm{d}i_p}{\mathrm{d}t} + L_{m_{ps}}\frac{\mathrm{d}i_m}{\mathrm{d}t}, \tag{3.11}$$

$$v_s = -R_s i_s - L_{lk_s}\frac{\mathrm{d}i_s}{\mathrm{d}t} + L_{m_{sp}}\frac{\mathrm{d}\left(ai_m\right)}{\mathrm{d}t}, \tag{3.12}$$

where i_m is the current through the magnetizing inductance.

A contactless energy transfer system may not be limited to a single primary coil, but multiple primary coils can transfer simultaneously energy towards a secondary coil. The induced voltage across the secondary coil, when the mutual inductances between the primary coils are assumed to be negligible, is given by

$$v_M = \sum_{k=1}^{K} M_{p_k s}\frac{\mathrm{d}i_{p_k}}{\mathrm{d}t}, \tag{3.13}$$

where K is the number of primary coils [1, 118]. The total mutual inductance between the primary and secondary coils is equal to the sum of the individual contributions of each primary coil to the secondary coil

$$M_{tot} = \sum_{k=1}^{K} M_{p_k s}. \tag{3.14}$$

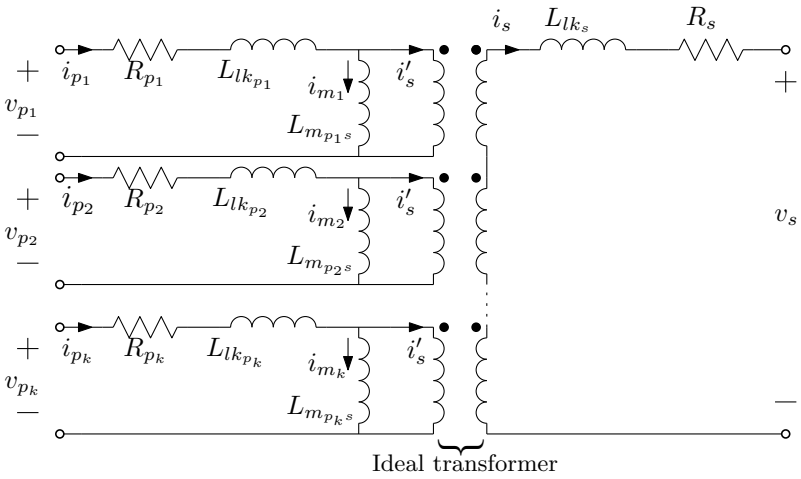

Figure 3.3: Transformer T-model for multiple primary coils and a single secondary coil.

Based on (3.13) and (3.14), an equivalent circuit based on the transformer T-model, as shown in Fig. 3.3, can be obtained. The voltage across each primary coil can be modeled similarly to (3.11), and the voltage across the secondary coil is equal to

$$v_s = -i_s R_s - L_{lk_s} \frac{\mathrm{d}i_s}{\mathrm{d}t} + \sum_{k=1}^{K} \frac{L_{m_{p_k s}}}{a_k} \frac{\mathrm{d}i_{m_k}}{\mathrm{d}t}. \tag{3.15}$$

As can be observed in the figure, the circuit embeds an ideal transformer in which each primary side is connected to the same secondary side. For illustration the secondary side of the ideal transformer is split in an equivalent amount of segments as there are primary coils. From this ideal transformer, two properties of a contactless energy transfer system between multiple primary and a single secondary coil can be obtained. Firstly, in an ideal transformer the currents on the primary and secondary side are equal to each other with respect to the turn ratio. Therefore, the reflected secondary current, i'_s, on the primary side of each ideal transformer is similar, with respect to the turn ratio, in all primary coils. Secondly, the voltage across the secondary side of the ideal transformer is equal to the sum of the voltages across the primary sides

$$\frac{v_p}{v_s} = \frac{N_p}{K N_s}, \tag{3.16}$$

in case of a primary voltage of same amplitude and phase.

3.2 Resonant circuits

An ideal inductive coupling has a high magnetizing inductance and a low leakage inductance, which results in an efficient system with an almost unity power factor. However in practice, the leakage inductance of the inductive coupling in a contactless energy transfer system is not negligible, and causes a voltage drop and a phase shift between the voltages and currents in the circuit. A voltage drop across the primary leakage inductance decreases the voltage across the magnetizing inductance, i.e. the voltage transferred from the primary to the secondary side, as can be observed in Fig. 3.2. Furthermore, on the secondary side, the output voltage is lower because of a voltage drop across the secondary leakage inductance. Finally, a large leakage inductance decreases the power factor and, thereby, the efficiency is reduced.

Based on the fundamental principle that resonant objects exchange energy more efficiently then non-resonant objects, both the primary and secondary side are made resonant by using an additional resonance capacitance [36, 107]. This resonance capacitance can be tuned such that the imaginary part of the transfer function, caused by the impedance of the leakage inductance, is reduced to zero [130, 131]. The resonance technique reduces the phase angle between the voltage and the current, and, thereby, improves the efficiency and boosts the energy transfer capability of the CET system [76, 98]. Furthermore, since the resonance technique reduces the imaginary part of the transfer function, the quality factor of the inductive coupling is improved as well. The quality factor Q of a series and parallel resonance circuit is defined by

$$Q_{series} = \frac{\omega_{res} L}{R}, \tag{3.17}$$

$$Q_{parallel} = \frac{R}{\omega_{res} L}, \tag{3.18}$$

where R is the resistance of the tuned circuit, and ω_{res} the resonance frequency. The quality factor determines the bandwidth of the impedance of the resonant circuit. A high quality factor results in a low resistance and a small bandwidth, and vice versa. The resonance capacitance can be placed in series or in parallel with respect to the leakage inductance, which results in four combinations for an inductive coupling with a single primary and secondary coil which are shown in Fig. 3.4

A series resonance capacitor on the secondary side results in a stable output voltage with the characteristics of a voltage source output. The impedance of the series resonance capacitance completely compensates the impedance of the leakage inductance. Therefore, the primary side exhibits a purely resistive reflected impedance from the secondary side which allows the primary capacitance to be

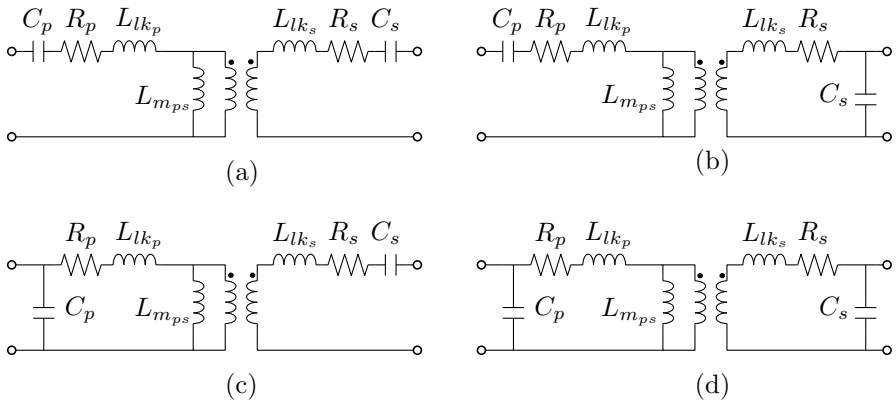

Figure 3.4: Resonance topologies: (a) series - series, (b) series - parallel, (c) parallel-series, and (d) parallel - parallel.

tuned independently of the magnetic coupling and the load.

A resonance capacitor parallel to the secondary coil, results in a circuit with the characteristics of a current source and has a stable output current. The secondary side reflects a capacitive load to the primary side, which means that the imaginary part of the reflected impedance is not equal to zero as realized by a series resonance capacitance on the secondary side. Consequently, the primary resonance capacitor has to be chosen such that it compensates for both the imaginary impedance of the leakage inductances.

On the primary side, the resonance capacitance can be placed in series or parallel, as well. A capacitance in series with the primary coil increases the voltage across the magnetizing inductance, by compensating the voltage drop across the leakage inductance. A capacitance placed in parallel with the primary coil results in a large primary current. To limit this current, an additional inductor should be placed between the voltage source and the parallel resonance capacitance. Furthermore, a parallel primary capacitor is dependent on the equivalent load of the CET system, and should, therefore, be tuned for the required power of the system [130]. In case of a series primary capacitor, the capacitance should be tuned such that in case of a series resonance capacitance on the secondary side, the value of the primary resonance capacitance is only compensating for the primary leakage inductance. If the secondary side contains a parallel resonance capacitor, the primary capacitor should compensate the impedance of both leakage inductances.

In a CET system with multiple primary coils and a moving secondary coil, both the mutual and leakage inductances are position dependent, and a trade-off can be made among the different resonance topologies. In case of a series-parallel,

a parallel-parallel, or a series-parallel resonance topology, the primary capacitor is not only tuned with respect to the primary leakage inductance, but also with the mutual inductance and secondary leakage inductance [76, 130]. In case of a series-series resonance topology, both the primary and secondary leakage inductance are independently compensated by the resonance capacitors at the primary and secondary side, respectively. With respect to a position dependent primary and secondary leakage inductance, both sides of the inductive coupling should be compensated individually, which can be realized by the series-series resonance topology. The resonance frequency of a series resonance capacitor in combination with the leakage inductance is defined as

$$\omega_{res} = \sqrt{\frac{1}{L_{lk_{min}} C_{res}}}. \tag{3.19}$$

The resonance frequency decreases for an increasing leakage inductance, a property which is also advantageous for the power converters in a CET system, as is shown in Section 5.3.2.

Although the magnetic coupling factor

$$k = \frac{M_{ps}}{\sqrt{L_p L_s}}, \tag{3.20}$$

is a measure for the ratio of the mutual inductance and the self-inductances, it does not give an indication of the efficiency of an inductive coupling. To illustrate this statement, the output power and efficiency of an inductive coupling with and without resonance capacitors are shown in Fig. 3.5. In the simulation, the self-inductances are kept constant and the mutual inductance between the primary and secondary coil is increased. Furthermore, the values of the resonance capacitors are modified with respect to leakage inductance during the simulation. The figure shows that in an inductive coupling without magnetic resonance, the output power increases quadratically with the coupling factor. In the given example, the output power of an inductive coupling with magnetic resonance reaches 90% of its maximum value at a coupling factor of 25%, as shown in Fig. 3.5(a). The output power remains increasing for a larger coupling factor, which is a result of the voltage division between the coil resistance and impedance of the magnetizing inductance, where an increasing magnetic coupling increases the mutual inductance, and, thereby, the impedance of the magnetizing inductance. The efficiency of an inductive coupling with resonance reaches a value above 90% for a coupling factor above 5% since the leakage inductance is compensated and, as a consequence, a circuit with a high power factor is obtained. The inductive coupling without magnetic resonance reaches an efficiency of 90% for a magnetic coupling above 55%.

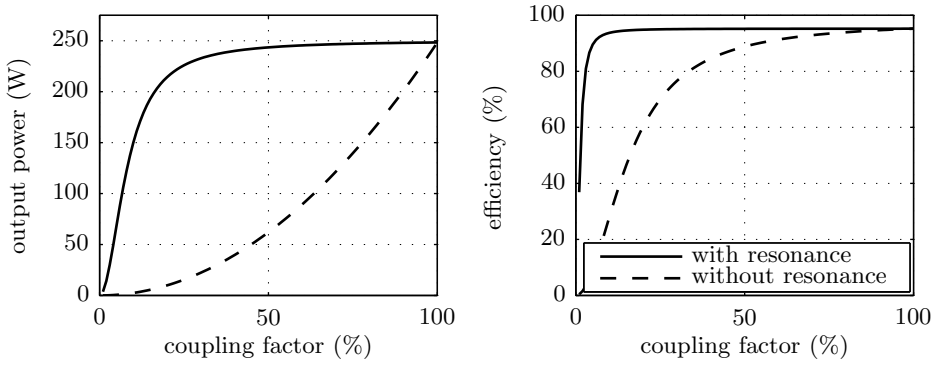

(a) (b)

Figure 3.5: (a) Output power and (b) efficiency as a function of the coupling factor for a CET system with L_p=L_s=20·10^{-5} H, R_p=R_s=0.25 Ω, i_p=5 A, R_{load}=10 Ω and ω_{res}=100 kHz.

3.3 Coil resistance and packing factor

The coils in an inductive coupling are typically made of Litz wire. This type of wire consists of multiple isolated strands to reduce the skin effect of the high-frequency current. The individual strands are combined into a single wire, woven in a pattern such that the proximity effect is reduced [66]. Nevertheless, because of the high-frequency currents in a CET system, the ac-part of the coil resistance should also be taken into account. The ac-part can be obtained by scaling the dc-part of the coil resistance. The dc-part is calculated by

$$R_{dc} = \rho \frac{N_p^2 l_{turn}}{A_{winding} k_f}, \tag{3.21}$$

where l_{turn} is the average turn length of a coil, $A_{winding}$ is the cross-section of the coil, and k_f is the copper packing factor of the cross-section, i.e. the total area of copper compared to the total cross-section. The ac-part of the coil resistance can be obtained as a function of the dc-part by [103, 119]

$$R_{ac} = R_{dc} \left(\frac{1}{k_s} \right) \left(1 + \frac{\beta_R^4}{192 + \beta_R^4} \right), \tag{3.22}$$

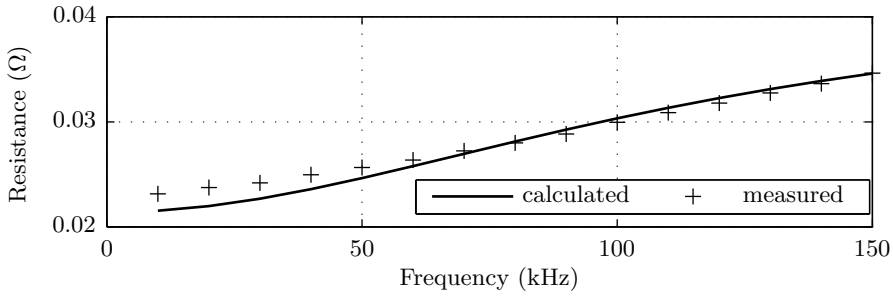

Figure 3.6: Comparison of the calculated and measured resistance of 1 m Litz wire, with 100 strands, each with a diameter of 0.10 mm, as a function of the frequency.

where k_s is the correction factor for the skin-depth, δ, equal to

$$k_s = \begin{cases} 1 & \text{for } \delta \geq r_s, \\ \frac{r_s^2-(r_s-\delta)^2}{r_s^2} & \text{for } \delta < r_s, \end{cases} \tag{3.23}$$

$$\delta = \sqrt{\frac{\rho}{\pi f_{res} \mu_0 \mu_r}}, \tag{3.24}$$

$$\beta_R^2 = \frac{8\pi f_{res} \cdot 10^{-7}}{R_{dc}}. \tag{3.25}$$

Finally, the temperature dependency of the resistance of a copper coil is modeled by

$$R_{dc_T} = (1 + 0.004\Delta T)\, R_{dc}, \tag{3.26}$$

where ΔT is the increase in temperature.

The resistance of 1 m Litz wire is calculated and measured for a frequency range between 10 and 150 kHz. As shown in Fig. 3.6, the calculated and measured values differ at maximum 7.5% with respect to each other.

To increase the effective copper area of a coil, and, thereby, the packing factor, the primary and secondary coils are wound with the orthocyclic winding method [64], as illustrated in Fig. 3.7. The number of turns in a coil can be obtained based on the number of layers of turns

$$N = \sum_{l=odd}^{n_l} N_{l_o} + \sum_{l=even}^{n_l} N_{l_e}, \tag{3.27}$$

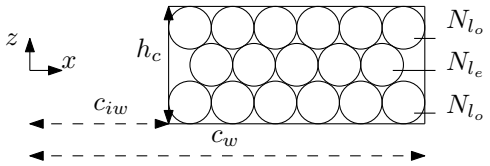

Figure 3.7: Cross-section of a coil in the xz-plane illustrating the orthocyclic winding.

where

$$N_{l_o} = \left\lfloor \frac{h_c}{D_{wire}} \right\rfloor, \tag{3.28}$$

$$N_{l_e} = \left\lfloor \frac{h_c - \sqrt{3}D_{wire}}{D_{wire}} \right\rfloor + 1, \tag{3.29}$$

$$D_{wire} = \frac{c_w - c_{iw}}{0.5\sqrt{3}(n_l - 1) + 1}. \tag{3.30}$$

N_{l_o} and N_{l_e} are the number of turns in an odd and even layer, and D_{wire} is the related wire diameter. The coil dimensions c_w and c_{iw} are defined in Fig. 2.10.

3.4 Transfer function

The energy transfer of an inductive coupling including the resonance capacitors can be defined and optimized by the transfer function of the circuit. In this section the transfer function is first defined for a single primary and single secondary coil, and extended later for multiple primary coils.

The current through the load is a measure for the output power in a contactless energy transfer system. In case of a single primary and secondary coil, as shown in Fig. 3.8, this current, expressed as a complex number, is equal to

$$i'_s = \frac{j\omega L_{m_{ps}}}{R'_{load} + R'_s + j(\omega^2 C'_s L'_{lk_s} - 1) + j\omega L_{m_{ps}}} i_p. \tag{3.31}$$

In the figure, the ideal transformer is removed and the circuit components of the secondary side are reflected to the primary side with respect to the winding ratio

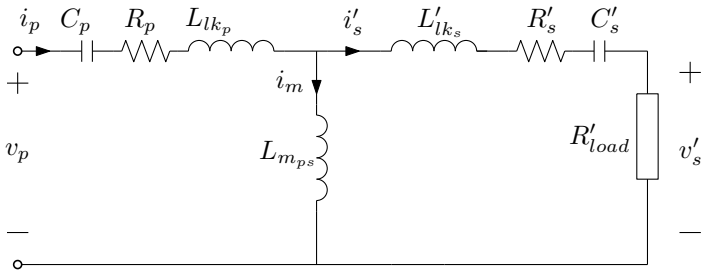

Figure 3.8: Equivalent circuit of a CET system with a single primary and secondary coil and series resonance.

by

$$i'_s = i_s N_p^{-1} N_s, \tag{3.32}$$

$$Z' = Z N_p^2 N_s^{-2}. \tag{3.33}$$

The voltage at the terminals of the primary side of the contactless energy transfer system, expressed as a complex number, is equal to

$$v_p = \left(R_p + j(\omega^2 C_p L_{lk_p} - 1) + \frac{j\omega L_{m_{ps}} \left(R'_{load} + R'_s + j(\omega^2 C'_s L'_{lk_s} - 1) \right)}{R'_{load} + R'_s + j(\omega^2 C'_s L'_{lk_s} - 1) + j\omega L_{m_{ps}}} \right) i_p. \tag{3.34}$$

If the circuit is operating at the resonance frequency, the resonance capacitors compensate the leakage inductance and their impedance may be ignored.

Similar to an inductive coupling with a single primary and secondary coil, a transfer function can be obtained for a coupling with multiple identical primary coils towards a single secondary coil

$$i'_s = \frac{j\omega \left(\sum_{k=1}^{K} L_{mp_k s} i_{p_k} \right)}{R'_{load} + R'_s + j \left(\omega L'_{lks} - \frac{1}{\omega C'_s} \right) + j\omega \left(\sum_{k=1}^{K} L_{mp_k s} \right)}, \tag{3.35}$$

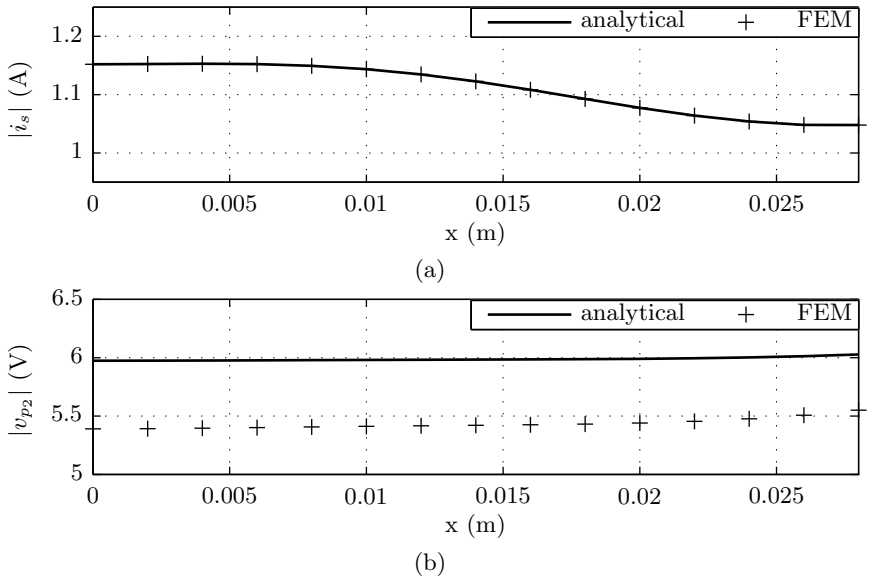

Figure 3.9: Comparison of analytically and numerically (FEM) obtained (a) secondary current and (b) primary voltage for an inductive coupling with three primary coils and a single secondary coil with $c_{pw} = 20$ mm, $c_{piw} = 5$ mm, $\tau_p = 35$ mm, $c_{sw} = 95$ mm, $c_{siw} = 50$ mm, $h_p = h_s = 5$ mm, $h_{gap} = 2$ mm, N_p=N_s=20 turns, $R_p = R_s = 0.25\ \Omega$, $i_p = 5$ A, $R_{load} = 10\ \Omega$, and $\omega_{res} = 100$ kHz.

$$v_{p_k} = i_{p_k}\left(R_{p_k} + j\left(\omega^2 C_{p_k} L_{llk_{p_k}} - 1\right) + \frac{j\omega L_{mp_k s}\left(R'_s + R'_{load} + j\left(\omega^2 C'_s L'_{lks} - 1\right)\right)}{j\omega\left(\sum_{k=1}^{K} L_{mp_k s}\right) + R'_s + R'_{load} + j\left(\omega^2 C'_s L'_{lks} - 1\right)}\right). \tag{3.36}$$

The mathematical transfer function is validated with a two-dimensional steady-state FEM simulation for different positions of a single secondary coil above an array of three adjacent primary coils. The secondary current is shown in Fig. 3.9(a). The calculated values are identical to the ones obtained from the FEM simulation. The corresponding input voltage of the middle primary coil is shown in Fig. 3.9(b). In this example, the calculate voltage is 9.3% higher compared to the one obtained from the FEM simulation, because of the neglected interaction between the primary coils. Since the secondary voltage and current are the most important parameters with respect to the output of a CET system, and can be directly obtained from the primary currents in the CET system, the difference in

input voltage has no influence in the prediction of the output power and position dependency of the CET system.

3.5 Thermal model

A three-dimensional thermal model is derived to estimate the temperature rise in the system. The temperature rise is caused by the conduction losses (I^2R) in the coils, and is limited by the wire of the coils and the materials in the environment of the coils. Therefore, the maximum output power of a CET system is a trade-off between the thermal constraints and current flowing through the coils.

The steady-state temperature distribution in a medium with temperature independent properties can by obtained by solving the heat equation, which is given by

$$\nabla^2 T = \frac{q}{\kappa}, \tag{3.37}$$

where T is the temperature, q is the volume power density, and κ the thermal conductivity of the medium [37]. The heat transfer rate can be obtained from the thermal conduction inside a medium and thermal convection and radiation from the surface of a medium.

Heat transfer by means of thermal conduction can be expressed by Fourier's law of heat conduction. The law gives an expression for the heat flow in x-, y-, and z-direction, which for the x-direction is equal to

$$q_x = -\kappa A_x \frac{\partial T}{\partial x}, \tag{3.38}$$

where A_x is the area to which the heat if flowing in the x-direction. A similar expression as (3.38) can be obtained for the heat flow in the other two directions. The heat transfer from the surface of a medium towards a moving fluid or air is called convection, and it is described by Newton's law of cooling

$$q_x = h_{con} A_x \left(T - T_\infty\right), \tag{3.39}$$

where h_{con} is the convection heat-transfer coefficient which typically has a value between 6 and 10 $\mathrm{Wm^{-2}K^{-1}}$ in case of natural convection.

Heat transfer between two surfaces through a transparent medium is called radiation and occurs by means of emission and absorption of electromagnetic waves.

The Stefan-Boltzmann equation describes the heat transfer by means of radiation

$$q_x = \varepsilon \sigma_{SB} (T_1^4 - T_2^4), \tag{3.40}$$

where ε is the emissivity, σ_{SB} is the Stefan-Boltzmann constant ($\sigma_{SB} = 5.67{\cdot}10^8$ $\mathrm{Wm^{-2}K^{-4}}$), and T_1 and T_2 are the temperatures of the surfaces between which the radiation occurs. If the temperature difference is small, (3.41) can be linearized and expressed as

$$q_x = h_r A_1 (T_1 - T_2), \tag{3.41}$$

where h_r is the radiation heat transfer coefficient equal to 6ε for T = 273 K, and A_1 the surface from which the radiation occurs. The heat transfer by radiation and convection can be combined to a single transfer heat-coefficient equal to 12 and 16 $\mathrm{Wm^{-2}K^{-1}}$.

The heat equation (3.37) can be analytically solved by means of a Thermal Equivalent Circuit (TEC), a model which is comparable to the MEC method, as introduced in Section 2.1. In a TEC, the heat transfer is described as a function of the temperature distribution between two points and the thermal resistance, R_{th}, between two points

$$q = \frac{\Delta T}{R_{th}}. \tag{3.42}$$

where

$$R_{th_{cond}} = \frac{1}{\kappa A}, \tag{3.43}$$

$$R_{th_{conv}} = \frac{1}{hA}, \tag{3.44}$$

in case of thermal conduction and convection, respectively.

A three-dimensional TEC is formulated for a CET system with multiple primary and secondary coils. The model consists of a nodal three-dimensional grid, where the temperature can be obtained at each node, and the heat transfer between the adjacent nodes is modeled by a thermal resistance [39, 74, 115]. In a CET system with different layers of solid media around the coils, each different type of media is modeled as a layer in the three-dimensional grid of the TEC model. For example, the TEC model in the xy-plane for a layer with three primary coils next to each other is shown in Fig. 3.10(a). The losses in the coils are the heat sources of the

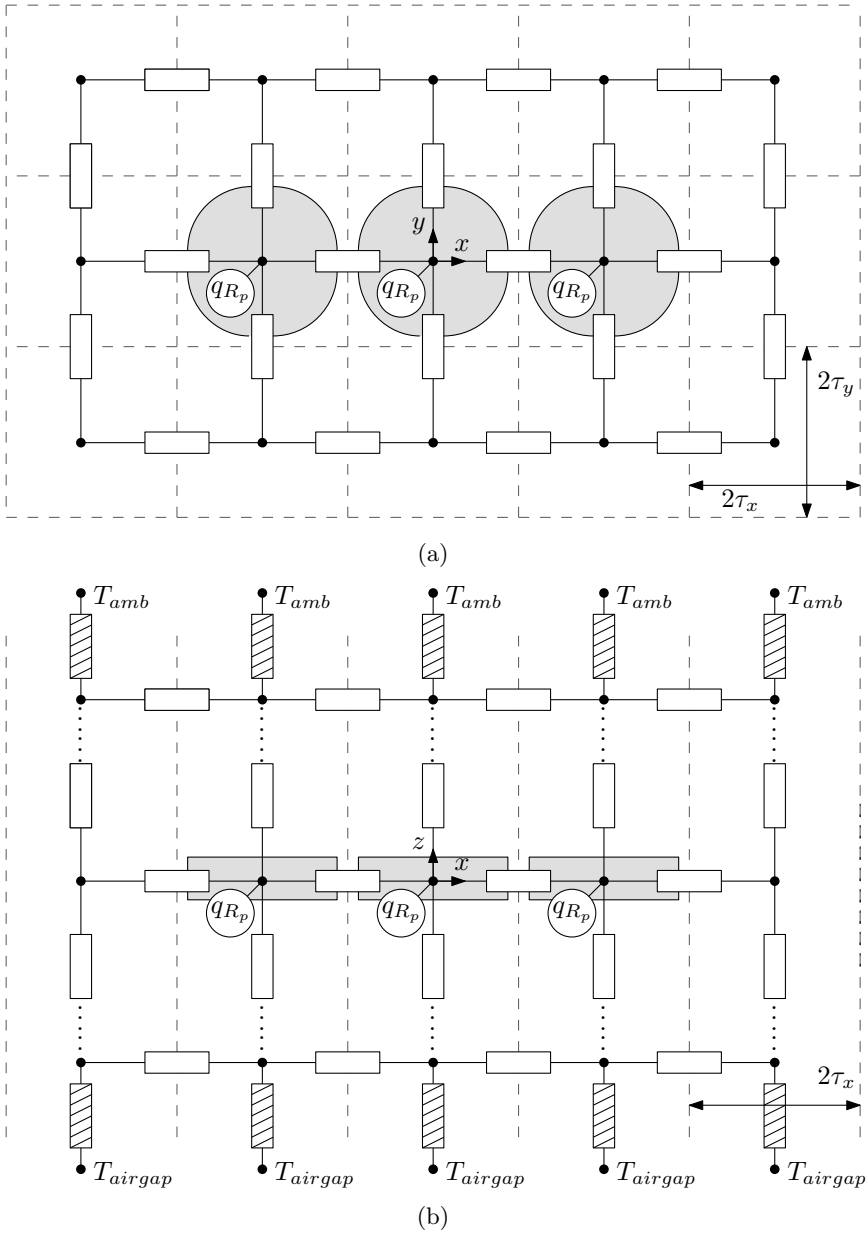

Figure 3.10: Cross-section of the thermal equivalent circuit: (a) a single layer in the xy-plane in the middle of the primary coils at z=0, and (b) a single layer and boundaries in the xz-plane for y=0.

Table 3.1: Thermal properties of the media in the TEC model

Layer	Description	height (mm)	κ ($\mathrm{Wm^{-1}K^{-1}}$)
1	non-magnetic material	5.0	0.7
2	magnetic material	5.0	10
3	non-magnetic material	0.3	0.4
4	coils	1.5	1
5	non-magnetic material	0.3	0.4

thermal model, q_{R_p}, which insert a heat flow at the node in the center of the coil. From the center of the coil, the heat flow is modeled in the x-, y- and z-direction. The main heat flow in the coil array is assumed in positive or negative z-direction, and therefore, no heat transfer is assumed in the x- and y-direction outside the area enveloped by the set of nodes outside the coil, as shown in Fig. 3.10(a).

The cross-section of the TEC model in the xy-plane, shown in Fig. 3.10(a), is representative for different layers of media above or underneath the coils. The nodes of these layer are connected in the z-direction to each other by means of thermal resistances, as for the presented example shown in Fig. 3.10(b). The figure show a cross-section of the TEC model in the xz-plane, again through the middle of the coils. Above and below the solid media around the coils, the heat flow is modeled by means of convection.

The presented TEC model, presented in Fig. 3.10, is verified by means of a three-dimensional steady-state thermal finite element simulation. The model consists of three primary coils and different layers of magnetic material and non-magnetic material above and below the coil, as listed in Table 3.1. The ambient and airgap temperature are equal to 20°C. A part of the cross-section of the xz-plane of the CET system and its environment in shown in Fig. 3.11(a). The figure shows the geometry from the middle of the first coil towards the middle of the second coil. A symmetrical distribution is obtained for the positive x-axis. The black dots in the cross-section indicate the points where the thermal model is compared to a three-dimensional steady-state thermal FEM simulation. The obtained temperature distribution along the similar cross-section from the FEM model is shown in Fig. 3.11(b). The obtained temperatures are listed in Table 3.2. The thermal model has temperatures up to 1.2 degree Celsius higher compared to the FEM model, which is equal to an deviation of 9.2% with respect to the temperature rise above the ambient temperature. The thermal model is applied to maximize the currents in the CET system reaching the thermal constraints, and, thereby, maximize the output power of the CET system.

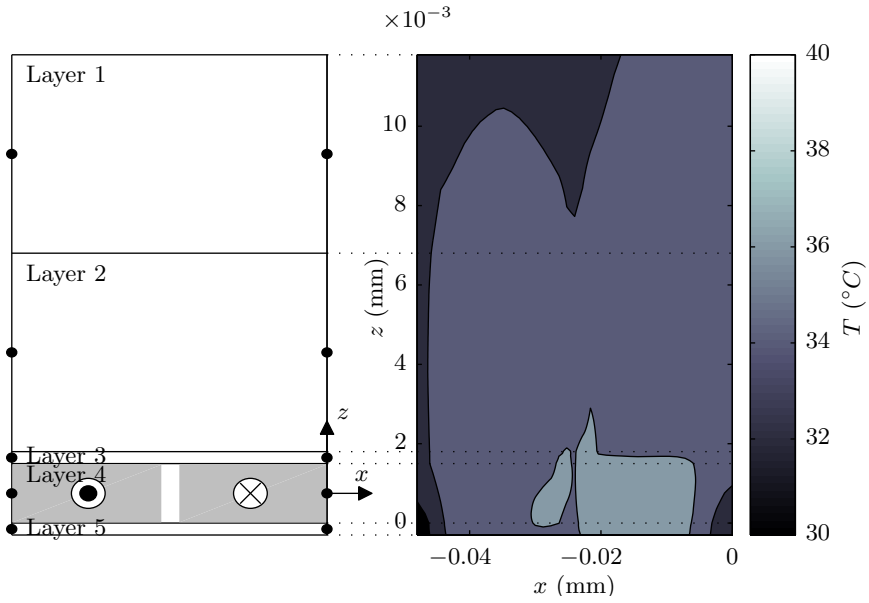

Figure 3.11: Model for verification of the TEC: (a) schematic overview of the different layers of the model on a part of the cross-section in the xz-plane for y=0, and (b) simulated temperature distribution in the cross-section, $T_{amb} = 20\ ^{\circ}C$.

Table 3.2: Temperature obtained in the TEC model and FEM simulation (Fig. 3.11), $T_{amb} = 20\ ^{\circ}C$.

$T_{TEC}(^{\circ}C)$	$T_{FEM}(^{\circ}C)$	$T_{TEC}(^{\circ}C)$	$T_{FEM}(^{\circ}C)$
(left dots)		(right dots)	
33.2	32.7	34.3	34.7
34.2	33.0	36.9	35.7
36.2	35.6	37.2	36.4
36.6	35.8	37.6	36.5
36.6	35.7	37.5	36.3

3.6 Summary and conclusions

An electrical and a thermal model of the inductive coupling in a contactless energy transfer system are presented in this chapter. The electrical T-model is formulated for multiple primary coils in combination with a single secondary coil. Resonance techniques are introduced and integrated in the electrical circuit of the inductive coupling to avoid the voltage drop across the leakage inductances in the system.

The conduction losses in combination with the thermal properties limit the energy transfer of the CET system. To estimate the temperature distribution as a function of the losses in the coil resistances, a three-dimensional thermal model is presented. The thermal model is verified with steady-state thermal FEM simulations and gives a prediction of the temperature rise with at maximum difference of 9% with to the ambient temperature.

In the next chapter, the magnetic, electrical, and thermal model are combined in a modeling framework for a CET system with a secondary coils with a linear or planar movement. The magnetic model, which is presented in Chapter 2, is applied to define the inductances of a CET system, which are the input of the electrical model. Based on a given geometry, the currents in the electrical model can be maximized to the thermal constraints of a CET system.

4

Position-independent contactless energy transfer systems

A Contactless Energy Transfer (CET) system replaces a physical cable connection between the stationary and the moving part of a system. Similar to a cabled connection, a CET system should provide a constant energy transfer, or practically an output power with a low variation at every position of the moving part with respect to the stationary part. This required low variation in output power can be electronically obtained by temporarily storing the transferred energy at the secondary side of the system and regulating the output power. This electronic solution actively controls the output power, whereas a passive solution can be obtained in the magnetic domain of the CET system. A low variation in output power is obtained by an almost constant secondary current, or from a magnetic point of view, it requires a position-independent mutual inductance. In other words, the flux linked with the secondary coils must be almost constant at every position of the moving part relative to the stationary part of the system.

In this chapter, a design method for a position-independent CET system is presented based on the magnetic, electrical and thermal model, which are discussed in the previous two chapters. The method is applied to analyze the influence of the different geometrical and electrical parameters of a CET system with a horizontal airgap between an array of primary coils and a single secondary coil, which is moving in a linear or planar stroke over the primary coil array. With respect to the integration of the CET system in a moving object, the coil height and airgap

length are limited to several millimeters. The chapter focusses on the energy transfer to a single secondary coil. Multiple secondary coils, i.e. multiple CET systems connected in series, can compensate the variation in mutual inductance of each other, and, as a result, the total variation in output power decreases. Multiple secondary coils are taken into account in the next chapter.

Besides the influence of the dimensions and the electrical parameters, there are several examples of CET systems in which the position dependency is reduced by modification of the coil configurations [17, 24, 26, 44, 71]. In this chapter, the following configurations are analyzed with respect to the position dependency of a CET system with secondary with a linear or planar movement:

- ferromagnetic structures around the coils,
- energy transfer from multiple primary coils,
- multi-layer primary coil array,
- different phase angles in the primary coils.

Finally, the analysis are summarized in a set of design considerations for a position-independent CET system.

The contributions of this chapter are published in:

J. P. C. Smeets, T. T. Overboom, J. W. Jansen, and E. A. Lomonova [2013], 'Modeling Framework for Contactless Energy Transfer Systems for Linear Actuators', *IEEE Transactions on Industrial Electronics*, **60**(1), pp. 391-399.

J. P. C. Smeets, T. T. Overboom, J. W. Jansen, and E. A. Lomonova [2013], 'Comparison of Position Independent Contactless Energy Transfer Systems', *IEEE Transactions on Power Electronics*, **28**(4), pp. 2059-2067.

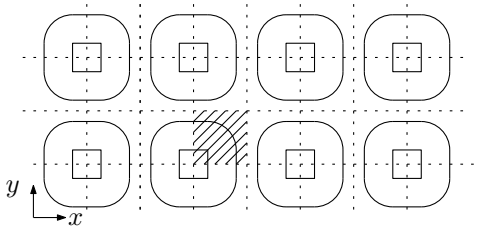

Figure 4.1: Part of a primary coil array with symmetry lines (dashed lines) and periodic area in which the variation in mutual inductance and average output power are investigated (dashed area).

4.1 Definition of position dependency

The CET systems considered in this thesis consist of a primary coil array, as shown in Fig. 4.1, and one or multiple secondary coils which move in a plane over the primary coil array. It is assumed that the primary coils have similar dimensions, and that the primary coil array has a symmetrical structure. Furthermore, to avoid a large leakage inductance only the primary coils which transfer energy to the secondary coil are energized. Switching between adjacent primary coils occurs when the center of the secondary coil is located at a symmetry line between the primary coils.

The position dependency of the CET systems in this chapter are defined by considering the variation in mutual inductance for a movement of the center of the secondary coil along a quarter of a single primary coil, i.e. the dashed area shown in the primary coil array of Fig. 4.1. The variation in mutual inductance is defined by

$$\Delta M_{tot} = \frac{\max\left(M_{tot}(x,y)\right) - \min\left(M_{tot}(x,y)\right)}{\max\left(M_{tot}(x,y)\right)}, \tag{4.1}$$

where M_{tot} in the total mutual inductance between all primary coils and the secondary coil. The average mutual inductance is calculated by

$$M_{ave} = \frac{1}{D_x D_y} \sum_{d_x=1}^{D_x} \sum_{d_y=1}^{D_y} M_{tot}(x_{d_x}, y_{d_y}), \tag{4.2}$$

where D_x and D_y are the number of positions taken into account in the $x-$, y-direction, respectively. The variation in mutual inductance is chosen as a figure of merit over the flux linkage and secondary current. Firstly, the mutual inductance

is independent of the primary current, which is not the case with the flux linkage, and only dependent on the dimensions of the primary and secondary coils and the relative position between the coils. Secondly, the number of primary and secondary turns only scale the amplitude of the mutual inductance, and, therefore, the variation can be obtained without knowledge of the number of turns and other electrical parameters of the CET system.

The average output power of the CET system is calculated for a movement of the secondary coil along the similar quarter of a single primary coil and obtained by

$$P_{ave} = \frac{1}{D_x D_y} \sum_{d_x=1}^{D_x} \sum_{d_y=1}^{D_y} P_{out}(x_{d_x}, y_{d_y}), \tag{4.3}$$

where

$$P_{out}(x,y) = |i_s(x,y)|^2 R_{load}, \tag{4.4}$$

Similar to the variation in mutual inductance, the variation in output power is defined by

$$\Delta P_{out} = \frac{\max\left(P_{out}(x,y)\right) - \min\left(P_{out}(x,y)\right)}{\max\left(P_{out}(x,y)\right)}. \tag{4.5}$$

The output power and the mutual inductance are related to each other with respect to the circuit parameters which are linked to the dimensions of the coil, the number of turns, the operating frequency, and the input current,

$$P_{out} = \frac{\gamma_p M_{tot}^2}{\alpha_p M_{tot}^2 + \beta_p M_{tot} + \zeta_p}, \tag{4.6}$$

where

$$\gamma_p = R'_{load}\omega^2 a^2 i_p^2, \tag{4.7}$$

$$\alpha_p = -\frac{\omega^2}{a^2}\left(a^2 - C'_s\omega\right)^2, \tag{4.8}$$

$$\beta_p = \frac{2\omega}{a}\left(a^2 - C'_s\omega\right)\left(1 - C'_s L'_s\omega^2 + j\left(R'_{load} + R'_s\right)\right), \tag{4.9}$$

$$\zeta_p = \left(R'_{load} + R'_s + j\left(\omega^2 C'_s L'_s - 1\right)\right)^2. \tag{4.10}$$

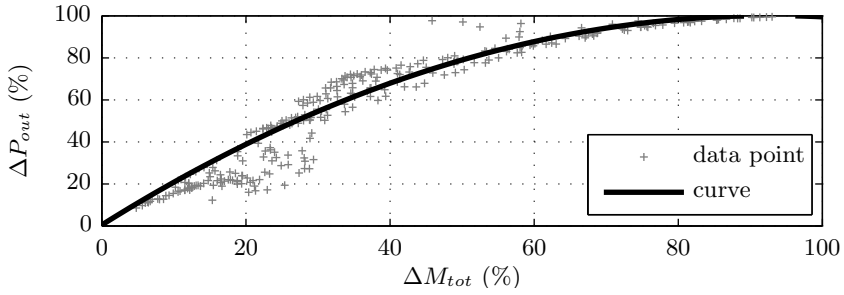

Figure 4.2: Variation in mutual inductance versus variation in output power, data points analysis Section 4.4.1, Fig. 4.12(c).

Equation (4.6) shows that output power has a second order relation with the mutual inductance depending on the remaining circuit components in the CET system. For the planar coil configurations taken into account in this thesis, the relation between the variation in mutual inductance and the variation in output power can be generalized by the curve shown in Fig. 4.2. The difference between the variation in mutual inductance and output power is related to the quality factor of the resonance circuit, which is determined by the electrical components and resonance frequency of the circuit. A variation in mutual inductance results in a variation in leakage inductance, which results in a shift of resonance frequency. Systems with a low quality factor have an impedance with a large bandwidth around the resonance frequency, which in a lower variation in output power compared to the variation in mutual inductance, and vice versa.

Although the overall goal is to obtain a CET system with a constant output power, the analysis in this chapter is mainly focused on the dimensions and layout of the primary coil array. Since the set of electrical variables and constraints is chosen and not defined for a specific system, the results in this chapter are presented in terms of the average output power of a CET system as a function of the variation in mutual inductance.

4.2 Design method

A position-independent CET system has a low variation in mutual inductance and a specified average output power, within the given geometrical, electrical and thermal constraints. The magnetic, electrical, and thermal lumped parameters models presented in the previous two chapters, are combined into a modeling framework which is used in the design algorithm of a position-independent CET system. Thirteen parameters; eight coil dimensions (c_{pw_x}, c_{pw_y}, c_{pbw}, h_p, c_{sw_x}, c_{sw_y}, c_{sbw}, and

Table 4.1: Parameters and initial values of the reference CET system of Section 4.2

Parameter		Value	
coil pitch	2τ	48.0	mm
outer width	$2c_w$	45.0	mm
inner width	$2c_{iw}$	20.0	mm
coil height	h_c	1.50	mm
number of turns	N	100	turns
airgap length	h_{gap}	1.00	mm
primary voltage	V_p	50.0	V
equivalent load	R_{load}	10.0	Ω
resonance frequency	f_{res}	100	kHz
variation mutual inductance	ΔM_{tot}	97.4	%
average output power	P_{ave}	15.8	W

h_s) and five electrical variables (N_p, N_s, $|V_p|$, f_{res}, and R_{load}), are the inputs of the modeling framework. In the design method, each set of possible combinations of coil dimensions is evaluated in the magnetic model to define the inductances and variation in mutual inductance. The calculated inductances together with the electrical variables are the input of the electrical model, in which the average output power is calculated along the trajectory of the moving secondary coil. The energy flow is limited by the losses in the system. The output of the electrical model is the input of the thermal model to predict the coil temperature. The electrical variables are modified during the optimization to obtain the maximum average output power within the electrical and thermal constraints. Finally, based on different sets of coil dimensions a design with a low variation in mutual inductance and the desired average output power can be selected.

In the next sections, the coil dimensions and the electrical parameters are separately investigated with respect to their influence on the position dependency and average output power of a CET system with one primary and one secondary coil. The CET system, referred to as the reference system and illustrated in Fig. 4.3, is surrounded by air, has an average output power of 16 W, and a variation in mutual inductance equal to 97% for a movement of the center of the secondary coil along quarter of the primary coil area in positive x- and y-direction, i.e. the dashed area in Fig. 4.3(a). It is chosen to start the investigation with a single primary and a single secondary coil with similar dimensions, which are listed in Table 4.1. The average output power for the initial dimensions is low because of the similar coil dimensions. During the investigation, single or multiple variables of the CET system are varied and normalized with respect to the initial values of the reference system. The influence of the different variables with respect to the variation in mutual inductance and output power is described in the following sections, resulting in a practical implementation of the design method.

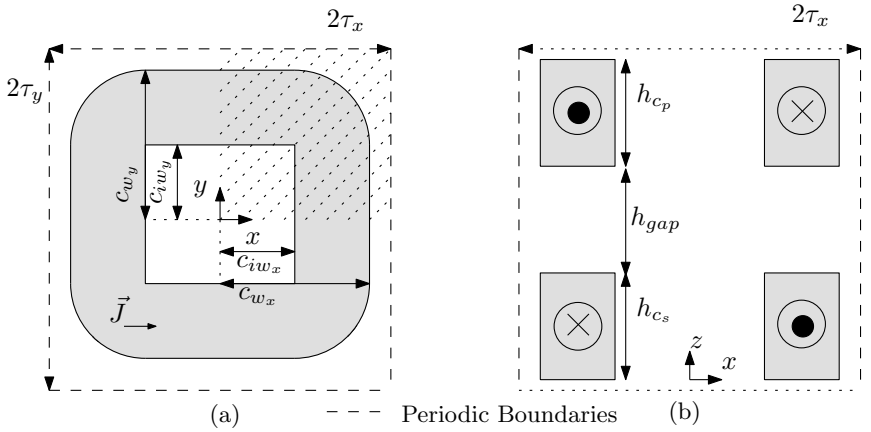

Figure 4.3: Geometry of the reference CET system with a similar primary and secondary coil aligned above each other: (a) top view of a single coil and (b) side view.

4.2.1 Analysis of the coil dimensions

In the magnetic model, the dimensions of a coil describe an enclosed volume with a constant current density. Therefore, the magnetic model defines the inductance of a coil as if the coil consists of a single turn. As shown in (2.154), the total inductance of a coil can be obtained by multiplication of the inductance of a coil with a single turn by the number of turns squared

$$L = N^2 L_0, \tag{4.11}$$

where L_0 represents the inductance of a coil with a single turn. Because the number of turns only scales the value of the inductance, this parameter has no influence on the variation in mutual inductance. Therefore, the variation in mutual inductance is only depending on the geometrical parameters of the CET system.

The dimensions of a coil can be divided into two sets; one set which defines the enclosed area of a coil in the xy-plane, and a next set which determines the height of a coil. With respect to a planar coil, the enclosed height is irrelevant for the variation in mutual inductance, as shown in Fig. 4.4(a), in which the variation in mutual inductance differs less than 1% with respect to the different combinations of primary and secondary coil heights. Fig. 4.4(b) shows that the output power increases for a higher coil. The increased height decreases the coil resistance with respect to a constant number of turns, and, therefore, a higher primary and secondary current can flow which results in a larger output power.

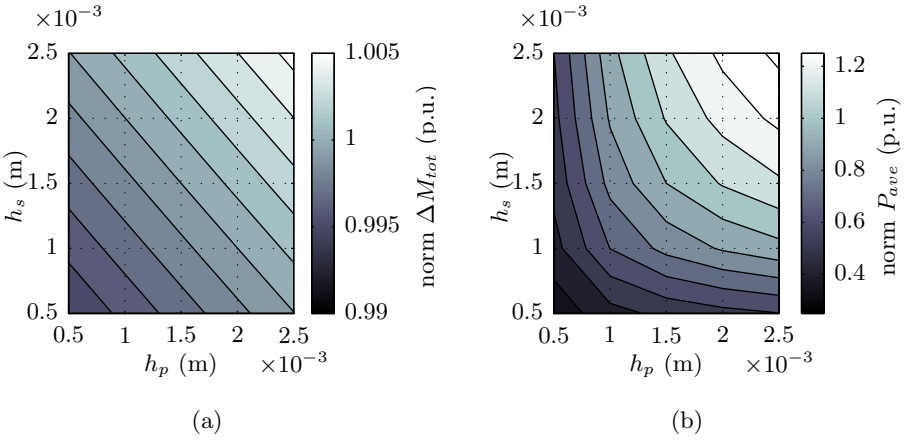

Figure 4.4: (a) Variation in mutual inductance and (b) normalized average output power for a varying height of the primary and secondary coil.

The enclosed area of a coil can be described by the inner and outer width, which together define the bundle width. The effect on the variation in mutual inductance and the average output power for a change of these parameters while one of them is kept constant is shown in Fig. 4.5. The bundle width is kept constant while the inner width of the primary and secondary coil is increasing. The figure shows that the variation in mutual inductance decreases for the geometries where the inner width of the secondary coil approaches or envelopes the outer width of the primary coil, and, consequently, the flux linkage becomes more uniform for a larger displacement of the secondary coil with respect to the primary coil.

A similar observation can be made in Fig. 4.5(c), where the inner width of the primary and secondary coil is kept constant, and the outer width of both coils is increasing. Also in this case, the variation in mutual inductance decreases if the secondary coil widely overlaps the primary coil. For the case with a constant outer width and a decreasing inner width, the variation in mutual inductance, as shown in Fig. 4.5(e), differs within 10% for the obtained coil dimensions, which is much lower than the difference of 60% which is found for a varying outer width. Based on Figs. 4.5(a) and (c), it can be concluded that a low variation in mutual inductance can be obtained if the secondary coil overlaps the primary coil.

For the case of a constant bundle width, the highest average output power is obtained for the situation in which the inner width of the secondary coil is larger than the outer width of the primary coil, as shown in Fig. 4.5(b). These coil dimensions result in a variation in mutual inductance which is approximately 60% lower compared to the reference value, and, therefore, the output power has a lower variation and a higher average value. With respect to a constant inner width

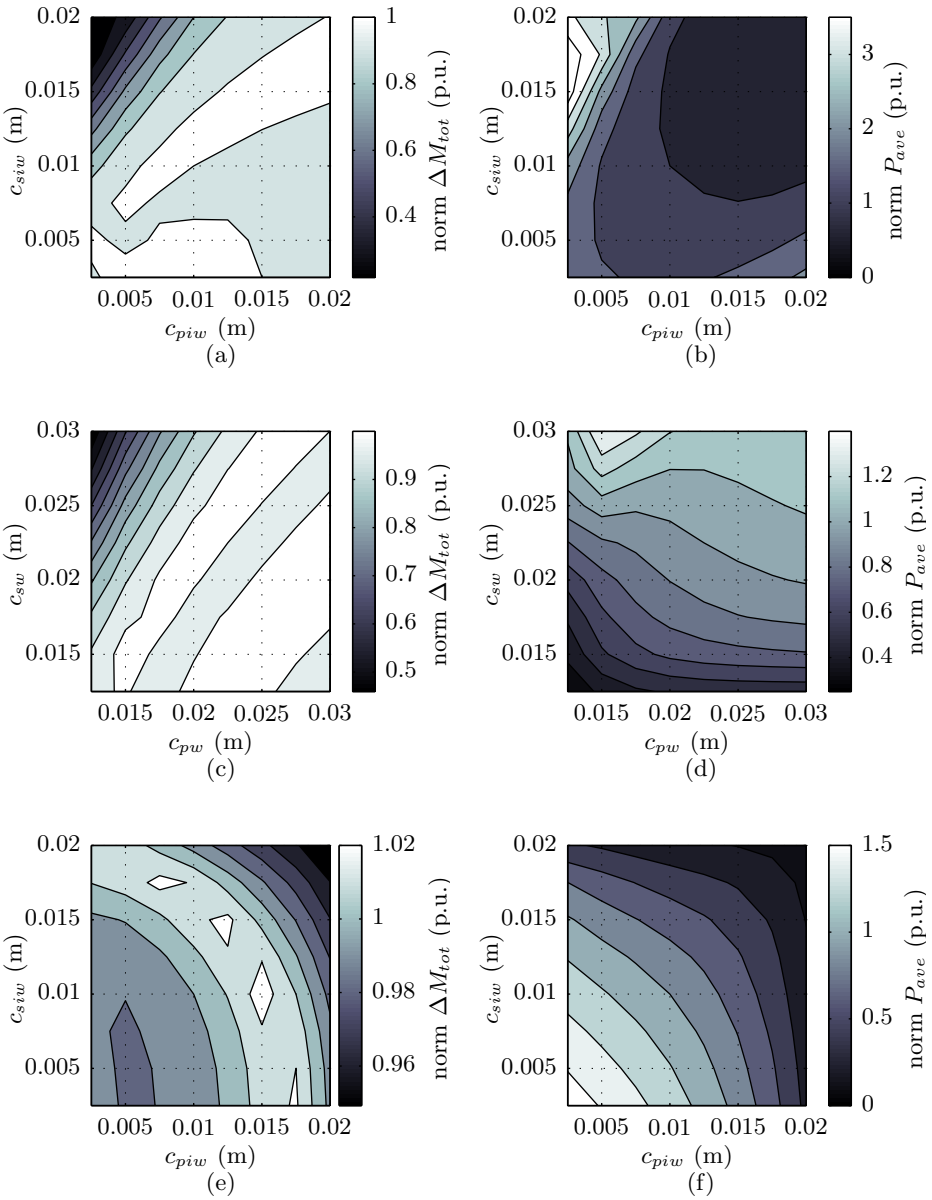

Figure 4.5: Normalized variation in mutual inductance and normalized average output power for: (a, b) a constant bundle width equal to 12.5 mm with an increasing inner and outer width, (c, d) constant inner width equal to 10 mm with an increasing bundle and outer width, and (e, f) a constant outer width equal to 22.5 mm with an increasing inner width and decreasing bundle width.

and an increasing outer width, the average output power increases for larger coil dimensions, as shown in Fig. 4.5(d). A similar observation can be made for the case of constant outer width and an increasing inner width, as shown in Fig. 4.5(f). Again the highest average output power is obtained if the maximum bundle width is reached, i.e. for the coil dimensions with the smallest inner width. Similar to the case of an increasing coil height, a higher average output power is obtained because of a lower coil resistance with respect to the constant number of turns.

4.2.2 Analysis of the electrical variables

The output power of a CET system can be obtained by the transfer function of a CET system and the input voltage of the primary coils. The electrical variables in the CET system, such as the number of turns, the equivalent load, and the resonance frequency have no influence on the variation in mutual inductance, and, therefore, only the output power is taken into account in this section.

The number of turns of the coils does not only define the ratio between the primary and secondary voltage and current, but also influences all other electronic components and, thereby, the energy transfer in a CET system. With respect to the electrical components, the inductances and the winding resistances scale with the number of turns squared. Furthermore, a growing number of turns in a constant coil volume increases the magnetizing inductance, and, as a result, the magnetizing and the primary current is decreased. Although a higher number of turns results in a lower primary current, the conduction losses in the coils,

$$\begin{aligned} P_{cond} &= I^2 R, \\ &= \left(\frac{J A k_f}{N}\right)^2 \left(\frac{\rho N^2 l_{turn}}{A k_f}\right), \\ &= \rho J^2 l_{turn} A k_f, \end{aligned} \tag{4.12}$$

are independent of the number of turns assuming a constant current density, an equal coil geometry, and a constant packing factor.

The resonance frequency defines the value of the resonance capacitances. At resonance the operating point with the lowest impedance of the total CET system is obtained. A high resonance frequency increases the impedances of the inductances, and, as a result, the magnetizing current decreases. The impedance of the primary coil and the magnetizing inductance can be seen as a voltage divider, where the voltage across the magnetizing inductance approaches the input voltage for an increasing resonance frequency. Consequently, both the induced voltage at the secondary side and the voltage across the load resistance also reach the input voltage with respect to the turn ratio and assuming a low impedance of the

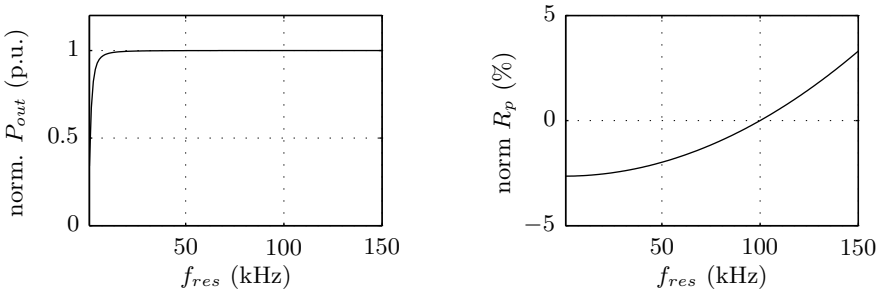

Figure 4.6: Normalized output power (a) and (b) primary coil resistance of the reference CET system for an increasing resonance frequency.

secondary coil. Finally, this results in a constant output power for an increasing resonance frequency as shown in Fig. 4.6(a). The figure shows that the reference CET system reaches its largest output power already at a frequency of 25 kHz. A higher frequency has neither a negative nor a positive effect on the output power, since the resistance of the primary coil remains almost constant for an increasing resonance frequency as shown in Fig. 4.6(b). The frequency, at which the highest output power is obtained, differs for each CET system and depends on the coil resistance and the impedance of the magnetizing inductance.

If the coils of a CET system are surrounded by air or non-conducting material, no eddy currents are induced by the high-frequency magnetic fields, and the frequency may be increased towards its maximum value with respect to the ac-resistance of the Litz wire. But if conducting materials are present in the neighborhood of the coils, the eddy-current reaction field influences the inductances of the coils as presented in Section 2.5.1 and [113]. Consequently, the frequency and amplitude of the primary current should be taken into account in the calculation of the inductances.

The output power of a CET system can be regulated by defining three of the following five parameters: primary voltage, primary current, secondary voltage, secondary current, and equivalent load resistance. With two of those parameters and the transfer function of the electrical equivalent circuit, the remaining parameters can be calculated. It is chosen to vary the primary voltage and the load resistance, and to specify the secondary voltage

$$\begin{aligned} v_s &= \frac{N_s}{N_p}\left[\left(\sum_{k=1}^{K} j\omega L_{mp_k s}\left(i_{p_k}(V_p) - i_s^*(R_{load})\right)\right)\right. \\ &\quad \left. - \left(R_s^* - j\left(\omega L_{lk_s} - \frac{1}{\omega C_s^*}\right)\right) i_s^*(R_{load})\right], \end{aligned} \tag{4.13}$$

Table 4.2: Geometrical constraints for the parametric sweep.

Primary coil	Secondary coil
$0 \leq c_{piw_x} < c_{pw_x}$	$0 \leq c_{siw_x} < c_{sw_x}$
$0 \leq c_{piw_y} < c_{pw_y}$	$0 \leq c_{siw_y} < c_{sw_y}$
$c_{pw_x} - c_{piw_x} = c_{pw_y} - c_{piw_y}$	$c_{sw_x} - c_{siw_x} = c_{sw_y} - c_{siw_y}$
$c_{pw_x} \leq \tau_{p_x}$	$c_{sw_x} \leq \tau_{s_x}$
$c_{pw_y} \leq \tau_{p_y}$	$c_{sw_y} \leq \tau_{s_y}$
$0 \leq h_p \leq h_{p_{max}}$	$0 \leq h_s \leq h_{s_{max}}$

where the primary and secondary current can be obtained as a function of the primary voltage and the load resistance, respectively. It is chosen to specify the secondary voltage, since the output of the CET system is generally connected to a dc-bus, similar to a cabled connection, and the current flow in the system is depending on the load. By varying the primary voltage and the load resistance, the currents in the system can be maximized based on the thermal constraints to obtain a maximum output power.

4.2.3 Implementation of the design method

The previous two sections have shown a clear separation between the geometrical and electrical parameters of a CET system, which in their turn are responsible for the variation in mutual inductance and output power, respectively. Practically, this means that the value of the inductances can be separately obtained without knowledge of the electrical parameters of the CET system. Therefore, the optimization of the dimensions and electrical parameters of a position-independent CET system is conducted in two steps.

In the first step, a parametric search is performed to obtain the values and variation of the inductances along the trajectory of the secondary coil related to all possible geometrical combinations. The constraints involved in the parametric search are listed in Table 4.2. The step size in the parametric search in this work is set equal to 0.5 mm for the coil height and to 5 mm for the widths of the coil. A large geometric domain results in many options which have to be evaluated in the parametric search. To reduce the number of options, the height of the coil can be set to its largest value instead of varied during the parametric sweep, since, as illustrated in Section 4.2.1, a maximum output power is obtained for the largest coil height, and the widths of a coil have more influence on the variation in mutual inductance compared to the height of a coil.

In the second step of the design method, the obtained data set of the parametric search is optimized for a maximum output power by using a Sequential Quadratic Programming (SQP) algorithm. The optimization is performed within the thermal constraints of the CET system, the voltage ratings, the minimum required

Table 4.3: Electrical constraints for SQP.

$N_{p_{min}}$	$\leq$	N_p	$\leq$	$N_{p_{max}}$
$N_{s_{min}}$	$\leq$	N_s	$\leq$	$N_{s_{max}}$
$V_{p_{min}}$	$\leq$	V_p	$\leq$	$V_{p_{max}}$
		f_{res}	$\leq$	$f_{res_{max}}$
$R_{load_{min}}$	$\leq$	R_{load}	$\leq$	$R_{load_{max}}$
		V_s	$\approx$	$V_{s_{rated}}$
		T_{coil}	$\leq$	$T_{coil_{max}}$
		η_{ave}	$\geq$	80 %.

efficiency, and the maximum allowable number of turns, as listed in Table 4.3, and results in an optimal set of electrical variables for each possible geometrical combination.

In the SQP the number of turns is constraint between a maximum and minimum value, which are depending on the dimensions of the coil. The minimum number of turns of a coil is defined by a single layer of turns filled for 70%

$$N_{min} = 0.7\frac{c_w - c_{iw}}{h_c}. \tag{4.14}$$

The maximum number of turns is defined by a predefined maximum number of layers in combination with the orthocyclic winding method (3.27). Furthermore, it is assumed that the wide range of available Litz wire diameters is able to result in a coil in which the entire volume is filled with turns.

The turn ratio in combination with the currents and the desired secondary voltage determine the input voltage, which is equal for each primary coil in case of an energy transfer between multiple primary coils towards a single secondary coil. The optimized input voltage is, therefore, a trade-off between the coil resistances, mainly defined by the number of turns, and the primary and secondary currents. The resonance frequency is be maximized, which is advantageous with respect to a decrease in magnetizing current and, as a result, a larger fraction of the primary current is transferred to the secondary side. The maximum frequency can only be obtained if it is assumed that the Litz wire has a strand diameter which is smaller as the skin-depth of the conductor for the related frequency. The minimum required efficiency for the inductive coupling is set equal to 80%.

Finally, based on the variation in mutual inductance and the output power, a design is selected from the different optimized solutions. The separation of the two steps in the optimization method, allows the method to optimize the geometrical structures for different sets of electrical variables without repeating the analysis in the magnetic domain.

The separation of the design method in two steps becomes invalid with the presence

of conducting materials in the neighborhood of the primary and or secondary coils. In these cases, the inductances are influenced by the eddy-current reaction field which is related to the amplitude of the current and the frequency of the time varying current [113]. This should be taken into account in the design of a position-independent CET system, and the two design steps should be combined into one, in which the geometrical parameters are also optimized with the SQP algorithm. This combination makes the design method more sensitive for a local optima. To guarantee convergence of the SQP programming algorithm, the optimization is conducted multiple times starting with different initial values, and afterwards the different sets of optimized CET systems can be compared to each other.

4.3 Ferromagnetic structures around the coils

The output power of a CET system in which a single primary coil is transferring energy towards a similar secondary coil is extremely position dependent, as demonstrated in the previous section and as is shown for the CET system with a linear moving secondary coil in Section 1.2.2. A method to reduce the position dependency is to modify the geometry of the secondary coil and to transfer energy from multiple simultaneously activated primary coils towards a single secondary coil. An example of this principle is shown in Fig. 4.7, where the secondary coil overlaps a set of three adjacent primary coils. Figures 4.7(a)-(c) illustrate the transition between the three activated sets of primary coils with respect to the position of the secondary coil. A transition occurs when the center of the secondary coil is at a symmetry point between the middle energized primary coil and an adjacent coil in the direction of movement. For example, the transition between the set activated in Figs. 4.7(a) and (b) occurs at the dashed line shown in Fig. 4.7(a), and the transition towards the activated set of primary coils of Fig. 4.7(c) occurs at the dashed line in Fig. 4.7(b). The mutual inductance from each set of primary coils has a similar shape as a function the position of the center of the secondary coil. The mutual inductances overlap each other if symmetry is obtained between the different sets, i.e. the peak values in the mutual inductance as shown in Fig. 4.7(d). The solid line shows the total mutual inductance between the secondary coil and the activated set of primary coils along the movement of the secondary coil. In the example, the mutual inductance varies 6.3% during the movement of the secondary coil along the x-axis.

Up to now, all the analyzed CET systems are surrounded by air, but as observed in Section 2.5.1, the material around a coil could have a positive or negative effect on the inductance of a coils, and, therefore, influences the energy transfer capability of a CET system. Ferromagnetic material around the coils of a CET system guides the flux between the primary and secondary coil, and increases the mutual inductance [17, 24, 71]. In a planar structure, a ferromagnetic plate or a toothed structure of ferromagnetic material can be placed behind the coils. To

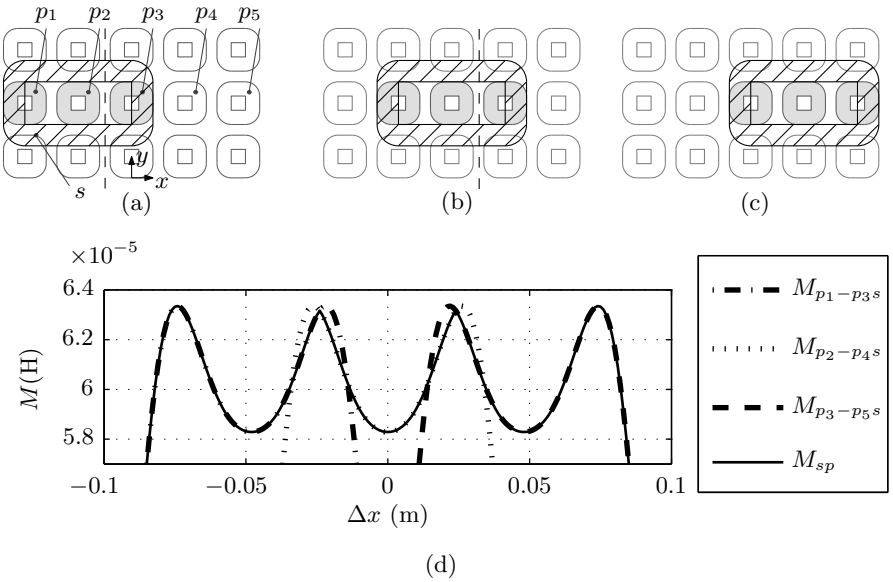

Figure 4.7: Displacement of the secondary coil and activation of three primary coils with respect to the position of the secondary coil: (a) primary coils p_1-p_3 activated, (b) primary coils p_2-p_4 activated, (c) primary coils p_3-p_5 activated, and (d) corresponding mutual inductances.

investigate the effect of these different ferromagnetic structures around the coils, six topologies, as shown in Fig. 4.8, are compared to each other with respect to the variation in mutual inductance and the average output power. For example, in topology A, the volume around the coils is filled with air or non-magnetic material. In topology C, the coils are placed against a ferromagnetic plate, and in topology E, the coils are located in a slotted structure. The different combinations are summarized in Table 4.4. On the secondary side of topologies E and F a small tooth is added at the beginning and end of the period for the ease of calculation of the magnetic flux density by using the harmonic modeling method. The three possible geometric boundaries on both sides of the CET system give nine unique combinations. Only the six presented combinations are compared, since the effect of a ferromagnetic plate versus a boundary of non-magnetic material can be compared based on topologies A - C. Furthermore, the effect of a ferromagnetic plate versus slots can be examined in topologies C - F.

The comparison of the different ferromagnetic structures around the primary and secondary coil is performed on a two-dimensional representation of a CET system, consisting of five primary coils and a single secondary coil. During the comparison, three adjacent primary coils are energized simultaneously, and the secondary coil moves in the x-direction above the primary coils. A two-dimensional geometry is chosen because of the fact that the three-dimensional magnetic model is not

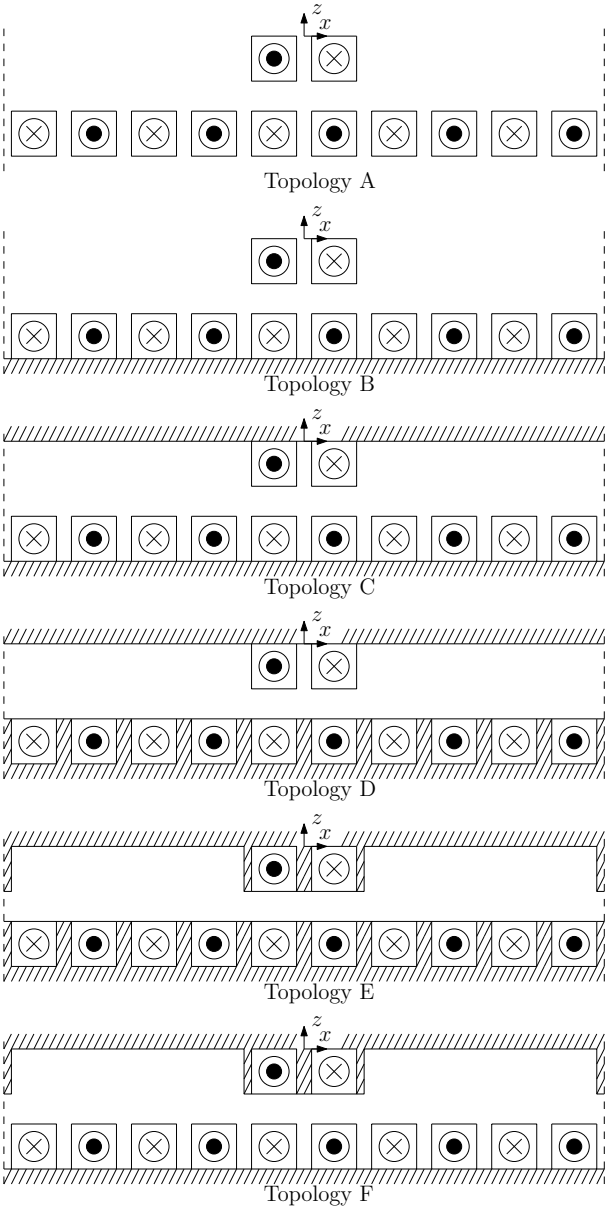

Figure 4.8: Schematic overview of the six CET systems with different ferromagnetic structures around the coils.

Table 4.4: Different combinations of ferromagnetic structures around the coils.

Topology	Primary side	Secondary side
A	non-magnetic material	non-magnetic material
B	ferromagnetic plate	non-magnetic material
C	ferromagnetic plate	ferromagnetic plate
D	ferromagnetic slots	ferromagnetic plate
E	ferromagnetic slots	ferromagnetic slots
F	ferromagnetic plate	ferromagnetic slots

Table 4.5: Parameters and constraints for the comparison of different ferromagnetic structures around the coils.

Parameters			Constraints				
τ_{p_x}	=	30 mm	10 mm	$\leq$	c_{pw_x}	$\leq$	30 mm
τ_{s_x}	=	105 mm	5 mm	$\leq$	c_{piw_x}	$\leq$	25 mm
depth_y	=	50 mm	20 mm	$\leq$	c_{sw_x}	$\leq$	105 mm
h_{gap}	=	1 mm	5 mm	$\leq$	c_{sw_x}	$\leq$	100 mm
$h_p = h_s$	=	2 mm	$c_{pw_x}+c_{piw_x}$	$\leq$	τ_{p_x}		(top. d, e)
f_{res}	=	100 kHz	$c_{sw_x}+c_{siw_x}$	$\leq$	τ_{s_x}		(top. e, f)
N_p	=	3 horizontal layers	$N_{s_{min}}$	$\leq$	N_s	$\leq$	$N_{s_{max}}$
V_s	=	100 V	10 V	$\leq$	V_p	$\leq$	500 V
			1 Ω	$\leq$	R_{load}	$\leq$	250 Ω
					T_{coil}	$\leq$	50 °C

able to model planar geometries with coils wound around a tooth. The different topologies are compared to each other with respect to variation in mutual inductance for different coil dimensions in which the average output power is maximized using the design method presented in Section 4.2.3. During the analysis the coil height, number of primary turns, and resonance frequency are kept constant. The remaining variables are optimized for a maximum output power subjected to the constraints listed in Table 4.5. The dimensions with respect to the different slotted and slottless structures are defined in Fig. 4.9. Furthermore, in the topologies with a ferromagnetic boundary at the primary or secondary side, the core losses are taken into account in the efficiency calculation of the CET system

$$\eta = \frac{P_{out}}{P_{out} + P_{core_p} + P_{core_s} + P_{cond_p} + P_{cond_s}}, \tag{4.15}$$

where the core losses, P_{core}, are obtained by the Steinmetz equation

$$P_{core} = C_{st} f_{res}^{\gamma_{st}} B^{\zeta_{st}} V_{core}. \tag{4.16}$$

Parameters C_{st}, γ_{st}, and, ζ_{st} are material depending parameters and are equal

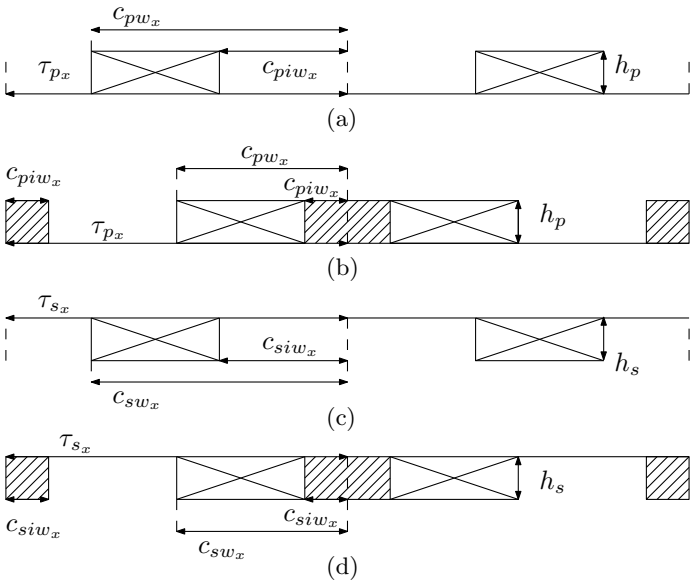

Figure 4.9: Schematic overview of the geometric parameters for a single coil pitch: (a) slottless primary side, (b) slotted primary side, (c) slotless secondary side, and (d) slotted secondary side.

to 0.25 $\mathrm{Wm^{-3}Hz^{-\gamma_{st}}T^{-\zeta_{st}}}$, 1.6, and, 2.5, respectively, assuming that 3F3 ferrite material is used [38].

The results of optimization are shown in Fig. 4.10. The figures show that the addition of ferromagnetic boundaries increases the average output power, but that the number of solutions which fulfill the constraints, mainly the required secondary output voltage, as listed in Table 4.5, decreases if either the primary or secondary coil(s) are embedded in a slotted structure. For topologies with similar dimensions, the mutual inductance is almost eight times larger if a ferromagnetic plate is located behind the coils compared to the case in which the coils are surrounded by air. A higher mutual inductance results in a larger magnetizing inductance, and, as a result, the voltage drop across the primary coil resistance decreases. This improved voltage balance is beneficial for the conduction losses in the primary coils, and, therefore, a higher average output power can be achieved. For the topologies with a slotted structure at the primary and/or secondary side, a lower number of solutions with a low variation in mutual inductance can be obtained because of the predefined flux paths through the teeth of the geometry. As a low variation in mutual inductance is obtained by a constant flux linkage, a slotted structure at the primary side, in this particular case at the side which is not moving, is more beneficial than a slotted structure at the secondary side. This occurs because the secondary side has no preferred flux paths, and the flux density distribution

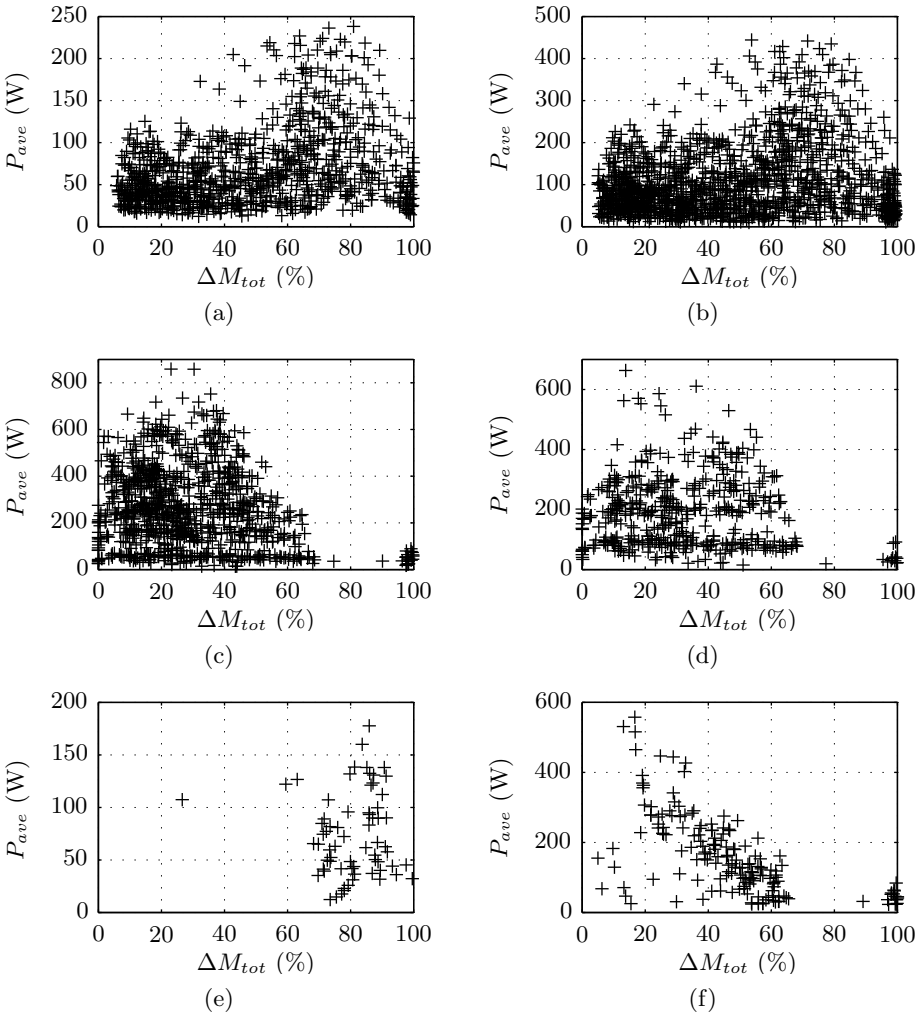

Figure 4.10: Average output power as a variation in mutual inductances for: (a) topology A, (b) topology B, (c) topology C, (d) topology D, (e) topology E, and (f) topology F.

from the primary towards the secondary coil remains the same for every position of the secondary coil. Furthermore, the self-inductance of a coil does not remain constant in case of a moving ferromagnetic slotted structure, and, therefore, the system does not remain operating at resonance.

The CET systems with the lowest variation in mutual inductance and the highest average output power are extracted from the set of possible solutions, and listed

Table 4.6: Minimum variation in mutual inductance for the topology comparison with different ferromagnetic boundaries around the coils.

Topology		A	B	C	D	E	F
c_{pw_x}	(mm)	30.0	30.0	15.0	15.0	15.0	20.0
c_{piw_x}	(mm)	5.00	5.00	10.0	10.0	5.00	15.0
c_{sw_x}	(mm)	80.0	80.0	65.0	65.0	75.0	75.0
c_{siw_x}	(mm)	15.0	15.0	5.00	5.00	30.0	30.0
ΔM_{tot}	(%)	5.70	5.06	0.01	0.02	26.6	4.99
P_{ave}	(W)	48.8	100	83.3	137	107	155
ΔP_{out}	(%)	30.4	30.3	29.0	32.1	98.9	99.6
N_p	(turns)	101	101	18.0	18.0	38.0	18.0
N_s	(turns)	120	60.0	30.0	21.0	36.0	18.0
V_p	(V)	163	316	116	188	194	152
R_{load}	(Ω)	163	75.5	144	109	66.4	31.1
$F_{z_{peak}}$	(N)	0.00	0.00	0.14	0.23	2.61	0.61
η_{ave}	(%)	86.1	92.7	95.1	48.3	47.6	67.3

in Table 4.6 and 4.7, respectively. Since a ferromagnetic plate does not only provide a low reluctance path for the magnetic fields, but also introduces a normal force between the primary and secondary side, the peak normal force, $F_{z_{peak}}$ is also included in the table. The normal force is dependent on the amplitude of the current flowing in the primary and secondary side. The secondary current has a phase-shift compared to the primary current, therefore, the normal force is calculated for different angles of primary current at each position of the secondary coil using (2.159).

The parameters for the CET systems with the lowest variation in mutual inductance are listed in Table 4.6. All solutions have a variation in mutual inductance below 6% except for topology E, in which a variation of 26.6 % is obtained. The highest average output power, equal to 137 W, is obtained in topology D, and the lowest average output power, equal to 48.8 W is obtained in topology A. Topologies A - D have a variation in the output power around 30%. In topologies E and F, the secondary coil is placed in a slotted structure which increases the variation in output power to almost 100%, because of the predefined flux path to the secondary coil. Efficiencies above 90% are obtained in topologies A, B, and C, and with the presence of a toothed structure at the primary and or the secondary side, the efficiency drops towards a value around 50% because of the increased core losses. The highest peak normal force is predicted for topology E, and is equal to 2.61 N.

The CET systems with the highest average output power for each topology are listed in Table 4.7. Among the selected solutions, the highest output power is obtained in topology C, and the lowest amount of energy is transferred with topol-

Table 4.7: Maximum average output power for the topology comparison with different ferromagnetic boundaries around the coils.

Topology		A	B	C	D	E	F
c_{pw_x}	(mm)	30.0	30.0	30.0	25.0	15.0	30.0
c_{piw_x}	(mm)	5.00	5.00	25.0	5.00	5.00	25.0
c_{sw_x}	(mm)	90.0	105	80.0	105	80.0	75.0
c_{siw_x}	(mm)	80.0	80.0	60.0	100	20.0	15.0
ΔM_{tot}	(%)	80.9	53.7	23.0	13.7	85.9	16.5
P_{ave}	(W)	238	444	858	663	178	602
ΔP_{out}	(%)	95.0	71.7	86.0	55.3	99.8	46.6
N_p	(turns)	101	101	18.0	80.0	38.0	18.0
N_s	(turns)	38.0	27.0	7.00	16.0	20.0	21.0
V_p	(V)	69.3	104	173	183	201	162
R_{load}	(Ω)	34.2	22.3	11.4	15.3	25.9	19.3
$F_{z_{peak}}$	(N)	0.00	0.03	0.63	1.39	2.94	0.28
η_{ave}	(%)	95.3	97.1	98.5	54.0	42.0	22.8

ogy E. The combination of a high output power does not benefit to the variation in mutual inductance, which is increased to a minimum value of 13% for topology D and a maximum value of 86% for topology E. The increased variation in mutual inductance results in a higher variation in output power, which varies between 47% for topology F and almost 100% for topology E. Although a high average output power is obtained in these designs, the high variation in output power makes the designs unrealistic for a CET system with a low position dependency. The peak normal forces in the topologies with a slotted structure at the primary and/or secondary side has increased, up to a peak value of 2.94 N for topology E, with slots on both sides. Similar efficiencies are reached as in Table 4.6.

The designs with the lowest variation in mutual inductance have an average output power which is by average five times lower compared to the designs with the highest average output power. Furthermore, the designs with the highest average output power have a high variation in output power which results in a position dependent CET system. To compare the six configuration for a realistic design of a CET system, the highest average output power with a variation in output power below 20% are listed in Table 4.8. Both for topologies E and F no results are obtained with a variation in output power below 20% within the given electrical constraints. The highest average output power is obtained in topology C, in which a ferromagnetic plate is present behind the primary and secondary coil.

Overall, the comparison of the six different (non)-ferromagnetic structures around the coils has shown that the toothless topologies result in many possible solutions for a CET system with a low variation in mutual inductance. Ferromagnetic structures around the coils increase the mutual inductance, which results in a

Table 4.8: Maximum average output power for $\Delta P_{ave} < 20\%$ for the topology comparison with different ferromagnetic boundaries around the coils.

Topology		A	B	C	D
c_{pw_x}	(mm)	30.0	30.0	25.0	20.0
c_{piw_x}	(mm)	5.00	5.00	20.0	10.0
c_{sw_x}	(mm)	105	105	70.0	100
c_{siw_x}	(mm)	90.0	90.0	5.00	15.0
ΔM_{tot}	(%)	32.0	32.3	4.67	21.7
P_{ave}	(W)	173	340	442	385
ΔP_{out}	(%)	17.5	19.6	15.1	18.0
N_p	(turns)	101	101	18.0	38.0
N_s	(turns)	59.0	30.0	22.0	29.0
V_p	(V)	44.1	85.2	188	193
R_{load}	(Ω)	54.3	27.2	29.3	32.0
$F_{z_{peak}}$	(N)	0.00	0.03	0.51	1.24
η_{ave}	(%)	93.2	96.5	98.0	39.1

larger energy transfer. Slotted structures are not preferable since they give a limited amount of geometrical solutions with a low variation in mutual inductance, and, meanwhile, these CET systems exhibit a normal force.

4.4 Primary coil array configurations

This section analyzes several properties of a primary coil array with a single secondary coil with a planar movement over the primary coil array, such as the simultaneously-active number of primary coils, the effect of multiple layers, and the phase angle of the current flowing through the activated primary coils. As shown in the previous section, a slotted ferromagnetic structure at either the primary or secondary side of the CET system does not result in a system with a low variation in mutual inductance, and, therefore, the primary and secondary coils are surrounded by air in this section.

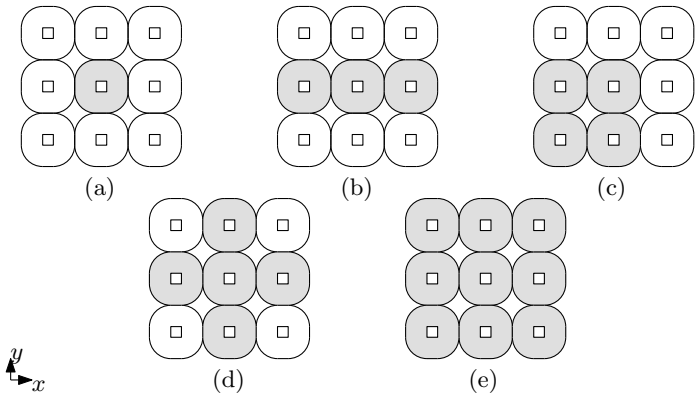

Figure 4.11: Schematic overview of the different sets of active coils in the 3x3 primary coil array with: (a) a single primary coil and (b) three, (c) four, (d) five, and (e) nine primary coils.

4.4.1 Number of active primary coils

In the analysis of the previous section a set of three primary coils is investigated to examen the variation in mutual inductance for various ferromagnetic structures around the coils of a CET system. If an array of 3x3 primary coils is considered, a single and sets of three, four, five, and nine coils can be used to transfer energy towards a secondary coil, as shown in Fig. 4.11. The variation in mutual inductance and the average output power of the different sets are analyzed for a fixed dimension of the primary coils and for various dimensions of the secondary coil. The analysis is conducted with the design method presented in Section 4.2. To reduce the number of variables, which are included in the optimization process, it is chosen to predefine the height of the primary and secondary coil, the number of turns of the primary coil, and the resonance frequency. The remaining variables are optimized for a maximum output power with respect to the constraints listed in Table 4.9. Based on the observation that a low variation in mutual inductance is obtained if the secondary coil tends to envelope the primary coils, the shape of the secondary coil is set similar to the contour of the set of active primary coils. Therefore, the possible secondary coil dimensions of the sets with one, four, five and nine active primary coils are limited to a square shape. A secondary coil with a rectangular shape is taken into account in the set with three primary coils.

The optimized average output power of the different sets of primary coils is shown in Fig. 4.12 as a function of the variation in mutual inductance. Common in Figs. 4.12(a)-(d) is the envelope of the possible solutions with respect to the variation in mutual inductance and output power. In these four topologies, Figs. 4.11(a)-(d), the highest average output power is obtained for a variation

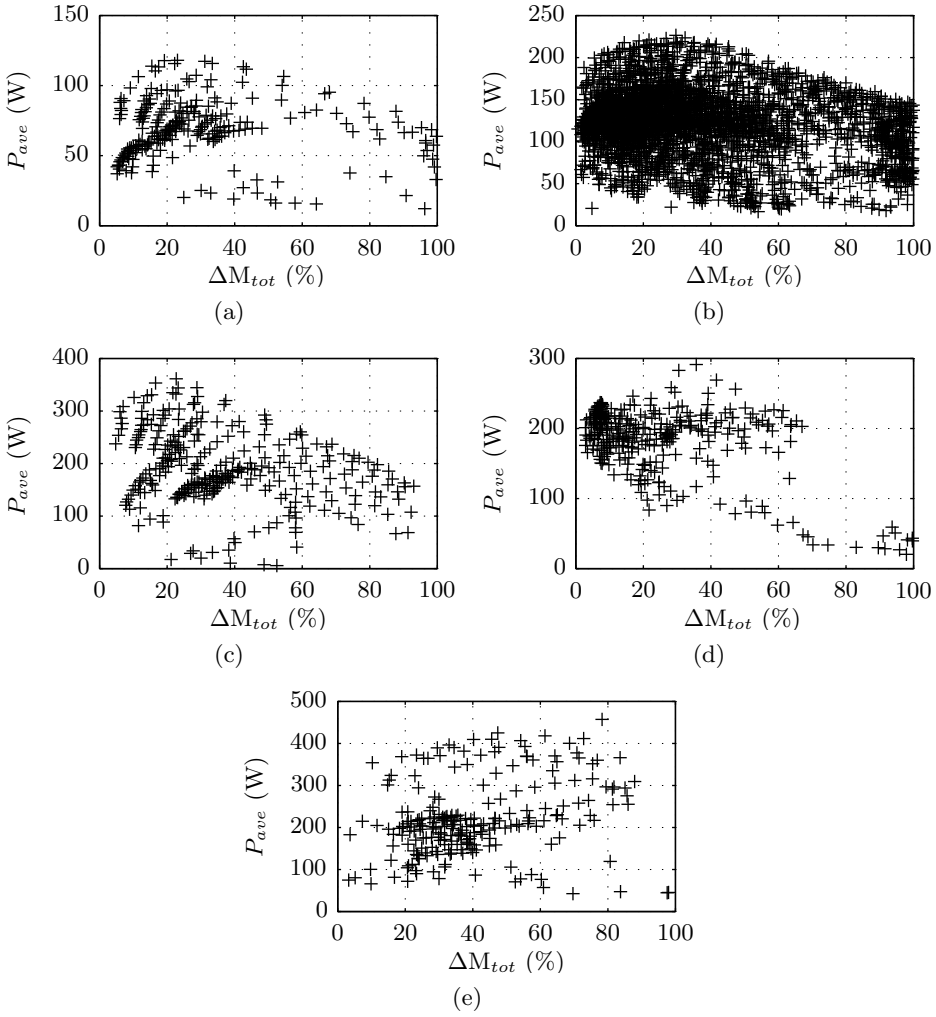

Figure 4.12: Average output power versus variation in mutual inductance for: (a) one, (b) three, (c) four, (d) five, and (e) nine activated primary coils.

Table 4.9: Parameters and constraints for the comparison of different number of active primary coils.

Parameters					Constraints				
τ_{p_x}	=	τ_{p_y}	=	30 mm	20 mm	$\leq$	c_{sw_x}	$\leq$	135 mm
c_{pw_x}	=	c_{pw_y}	=	30 mm	5 mm	$\leq$	c_{siw_x}	$\leq$	120 mm
c_{piw_x}	=	c_{piw_y}	=	10 mm	20 mm	$\leq$	c_{sw_y}	$\leq$	135 mm
h_p	=	h_s	=	1.5 mm	5 mm	$\leq$	c_{siw_y}	$\leq$	120 mm
		N_p	=	107 turns	$N_{s_{min}}$	$\leq$	N_s	$\leq$	$N_{s_{max}}$
		f_{res}	=	100 kHz	1 V	$\leq$	V_p	$\leq$	500 V
		h_{gap}	=	1 mm	1 Ω	$\leq$	R_{load}	$\leq$	250 Ω
							V_s	$\approx$	100 V
							T_{coil}	$\leq$	50°C
							η_{ave}	$\geq$	80 %

in mutual inductance between 20% and 40%, and decreases for a higher variation becomes larger than 40%. This is not the case for topology E, Figs. 4.11(e) and 4.12(e), where a high average output power is obtained for a variation in mutual inductance equal to 40% and 60%, ignoring the point with the highest average output power at a variation of mutual inductance equal to 80%.

The optimized results with the lowest variation in mutual inductance for the different sets are listed in Table 4.10. The different sets of active primary coils have a variation in mutual inductance varying between 0.66% and 5.22%, where the lowest variation is obtained in the set with three primary coils and the highest one for the set with one primary coil. The dimensions of the different secondary coils have an outer width close to the maximum constraint. Furthermore, in all cases the inner width of the secondary coil is larger than the outer width of the middle primary coil. The average output power varies between 42 W and 238 W, where the highest value is obtained in the set with four primary coils. With respect to the power density, P_{dens}, defined as the output power divided across the enveloped area of the secondary coil, the sets with three, four, five and nine primary coils all resulted in a value between 11 $\mathrm{kWm^{-2}}$ and 14 $\mathrm{kWm^{-2}}$. The configuration with a single active primary coil results in a power density equal to 3 $\mathrm{kWm^{-2}}$, approximately four times lower compared to the other sets.

The results with the highest average output power are listed in Table 4.11. The set with nine primary coils gives the overall highest average output power, which is equal to 457 W. The remaining sets have an output power varying between 118 W and 361 W. The accompanying variation in mutual inductance differs between 23% and 72% for the different sets along the trajectory of the secondary coil. The output power varies between 23% and 96% within the selected results. The corresponding secondary coils have an average bundle width of 24 mm, which is smaller compared to average bundle width of 63 mm for the results with the

Table 4.10: Lowest variation in mutual inductance for the comparison of different number of active primary coils.

Number of primary coils		1	3	4	5	9
c_{sw_x}	(mm)	120	90.0	130	135	80.0
c_{siw_x}	(mm)	85.0	20.0	60.0	40.0	35.0
c_{sw_y}	(mm)	120	115	130	135	80.0
c_{siw_y}	(mm)	85.0	45.0	60.0	40.0	35.0
ΔM_{tot}	(%)	5.22	0.66	4.21	2.86	3.27
P_{ave}	(W)	42.0	115	238	201	74.8
ΔP_{out}	(%)	8.69	23.3	8.56	9.89	7.45
N_p	(turns)	107	107	107	107	107
N_s	(turns)	180	75.0	34.0	44.0	25.0
V_p	(V)	65.1	108	81.1	68.0	143
R_{load}	(Ω)	219	77.6	42.9	56.0	123
P_{dens}	($\mathrm{kWm^{-2}}$)	2.92	11.1	14.1	11.0	11.7

Table 4.11: Maximum average output power for the comparison of different number of active primary coils.

Number of primary coils		1	3	4	5	9
c_{sw_x}	(mm)	55.0	105	80.0	70.0	90.0
c_{siw_x}	(mm)	35.0	90.0	65.0	15.0	80.0
c_{sw_y}	(mm)	55.0	90.0	80.0	70.0	90.0
c_{siw_y}	(mm)	35.0	50.0	65.0	15.0	80.0
ΔM_{tot}	(%)	23.0	29.6	22.7	35.6	78.2
P_{ave}	(W)	118	226	361	291	457
ΔP_{out}	(%)	23.2	46.7	35.7	47.7	95.5
N_p	(turns)	107	107	107	107	107
N_s	(turns)	71.0	30	23.0	76	12
V_p	(V)	149	110	120	161	82.8
R_{load}	(Ω)	83.8	41.5	29.9	42.6	13.8
P_{dens}	($\mathrm{kWm^{-2}}$)	39.0	43.2	56.5	59.5	56.4

Table 4.12: Maximum average output power for $\Delta P_{ave} < 20\%$ for the comparison of different number of active primary coils.

Number of primary coils		1	3	4	5	9
c_{sw_x}	(mm)	60.0	115	95.0	75.0	125
c_{siw_x}	(mm)	35.0	90.0	60.0	20.0	90.0
c_{sw_y}	(mm)	60.0	60.0	95.0	75.0	125
c_{siw_y}	(mm)	35.0	35.0	60.00	20.0	90.0
ΔM_{tot}	(%)	19.2	14.3	10.2	29.3	10.3
P_{ave}	(W)	118	218	326	252	354
ΔP_{out}	(%)	19.6	11.4	18.5	19.2	4.67
N_p	(turns)	107	107	107	107	107
N_s	(turns)	72.0	34.0	25.0	58.0	18.0
V_p	(V)	147	98.6	110	155	52.1
R_{load}	(Ω)	86.7	46.7	31.0	39.8	24.1
P_{dens}	($\mathrm{kWm^{-2}}$)	32.7	31.5	36.1	44.8	22.7

lowest variation in mutual inductance. The inner width of the secondary coil, c_{siw}, envelopes the outer width of the primary coil array in the set with one, three and four primary coils. The highest power density is obtained in the configurations with four, five and nine primary coils, and it has an average value of 57 $\mathrm{kWm^{-2}}$ for the three configurations. The power density in the configuration with a single primary coil and three primary coils is 32% and 24% lower, respectively.

It may be concluded that a topology with a low variation in mutual inductance has a secondary coil with a large outer width in combination with a large bundle width, and topologies with the highest average output power have a variation in mutual inductance between 20% - 40% in combination with a smaller bundle width. An ideal CET system should have a high output power with a low variation in output power. These requirements are translated to reduce the set of possible solutions with a variation in output power below 20%. From this limited set of solutions, the designs with the highest average output power are listed in Table 4.12. The average output power of the solutions presented in the table varies between 118 W and 354 W, in combination with a variation in output power between 5% and 20%. Again, the inner width of the secondary coil belonging to the topology with a single, three, four and nine active primary coils envelopes the outer dimensions of the entire set of active coils. The average bundle width of the secondary coils is equal to 35 mm. The highest power density is obtained the configuration with five active primary coils, and is approximately 30% higher compared to the average power density of the other configurations.

The comparison of the sets with different number of active primary coils has shown that it is possible to obtain a CET system with a low variation of mutual inductance for different number of active primary coils. The average output power is

dependent on the number of active primary coils, where sets of multiple primary coils have a higher output power compared to a single primary coil. Generally, for each design the allowable geometries for the secondary coil result in a trade-off between variation in mutual inductance and output power, while the average output power increases if a larger coil variation in mutual inductance is allowed.

4.4.2 Number of layers

In the previous section, different numbers of active primary coils in a single-layer coil array are compared to each other. The limitation of a single layer results in configurations in which coils are placed next to each other, while a multi-layer coil array allows arrangements of active primary coils in which coils are overlapping each other. This section starts with the comparison of a single- and a double-layer primary coil array, and later different configurations of double-layer coil arrays are compared to each other.

A single-layer primary coil array with three adjacent primary coils is compared to an array consisting of two layers in which three adjacent coils are activated per layer. In the coil array with two layers, the three adjacent activated coils are positioned on top of each other. Both coil arrays have an equal height, which means that the coil height of the double-layer array is half the coil height in the single layer. Both configurations are compared to each other with respect to the average output power and the variation in mutual inductance. For this comparison, both topologies are optimized for different secondary coil dimensions with respect to the parameters and constraints listed in Table 4.13, the dimensions in brackets are specific for the case of a single-layer primary coil array. The secondary coil envelopes the three activated primary coils, and, therefore, the dimensions of the secondary coil in the y-direction are limited with respect to the possible dimensions analyzed in the previous section. The resulted average output power as a function of variation in mutual inductance of the active sets of primary coils in the single- and the double-layer coil array is shown in Fig. 4.13. For a low variation in mutual inductance, designs with an average output power around 100 W and 50 W are obtained in the single- and double-layer primary coil array, respectively. The difference in output power is mainly caused by the difference in the coil resistances, as a larger coil height results in a lower resistance with respect to a lower coil height in case of an equal coil area, and a similar number of layers of primary turns.

As mentioned above, the activated coils in the first and second layer are located on top of each other. If the coils in the second layer are displaced with respect to the single layered coil array, configurations with overlapping active primary coils can be built to transfer energy towards the secondary coil. Four different configurations with a different distribution of the coils in the second layer of the primary coil array, configuration Da-Dd, are considered and compared to each other with respect to the variation in mutual inductance and the average output

Table 4.13: Parameters and constraints for the comparison of different layers of the primary coil array.

Parameters						Constraints				
τ_{p_x}	=	τ_{p_y}	=	24 mm		30 mm	$\leq$	c_{sw_x}	$\leq$	120 mm
c_{pw_x}	=	c_{pw_y}	=	22.5 mm		5 mm	$\leq$	c_{siw_x}	$\leq$	115 mm
c_{piw_x}	=	c_{piw_y}	=	5 mm		30 mm	$\leq$	c_{sw_y}	$\leq$	50 mm
h_p	=	h_s	=	0.75 (1.5) mm		0 mm	$\leq$	c_{siw_y}	$\leq$	45 mm
		N_p	=	87 (103) turns		$N_{s_{min}}$	$\leq$	N_s	$\leq$	$N_{s_{max}}$
		f_{res}	=	100 kHz		1 V	$\leq$	V_p	$\leq$	500 V
		h_{gap}	=	1 mm		1 Ω	$\leq$	R_{load}	$\leq$	250 Ω
								V_s	$\approx$	25 V
								T_{coil}	$\leq$	50°C
								η_{ave}	$\geq$	80 %

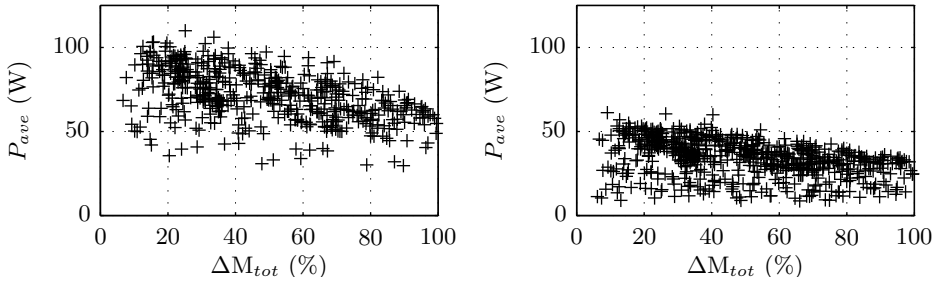

Figure 4.13: Average output power versus variation in mutual inductance for: (a) single-layer coil array with three activated primary coils, and (b) double-layer coil array with three primary coils activated per layer.

Table 4.14: Different configurations of active primary coils in the double-layer coil array.

configuration	coils 1^{st} layer	coils 2^{nd} layer	displacement 2^{nd} layer
Da	3	3	(0,0)
Db	3	2	(τ_x,0)
Dc	3	4	(τ_x,τ_y)
Dd	3	2	(τ_x,τ_y)

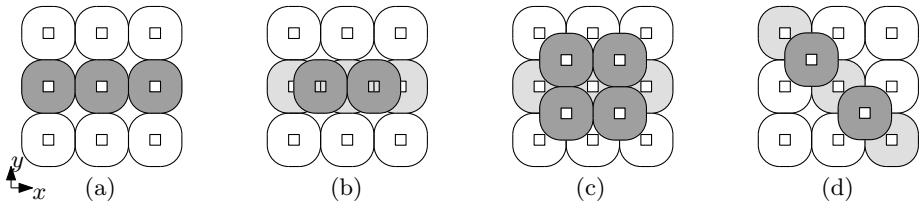

Figure 4.14: Schematic overview of the different configurations of active coils in the primary coil array divided across two layers: (a) configuration Da, (b) configuration Db, (c) configuration Dc and (d) configuration Dd of Table 4.14.

power. The different configurations are listed in Table 4.14 and shown in Fig. 4.14.

Among the four topologies, the highest average output power is found in configuration Da, in which the primary coils are located on top of each other. A displacement of the secondary layer reduces the output power because the current through the primary coils has a similar phase angle, which results in the cancelation of the magnetic fields with respect to each other. In configuration Dc, the enveloped area of the active set of primary coils is enlarged compared to topologies Da and Db. This results in a variation in mutual inductance between 20% and 60% for the given possible dimensions of the secondary coil. In configuration Dd the coil pitch is enlarged with respect to configuration Db. The large coil pitch results in a lower average output power and a higher variation in mutual inductance for the given dimensions of the secondary coil. Overall in case of a limited coil height, a primary coil array with a single layer of coils is preferable with respect to a higher average output power of the CET system compared to a double-layer coil array.

4.4.3 Phase angle of the primary current

In the previous two sections, the phase angle of the currents in the primary coils is used to be equal to each other. This section treats the effect of a different phase angle for the current in each activated coil of the primary coil array with respect to the average output power of a CET system. The variation in mutual inductance is independent of the amplitude and phase angle of the current, and, therefore, is not taken into account. Different combinations of phase angles are applied to a CET system in which three primary coils in a single layer are transferring energy towards a single secondary coil. The applied phase angles are listed in Table 4.15: in combination I a similar phase angle is applied to the primary coil; in combination II an 180-degrees alternating phase angle is applied to the adjacent coils; and in combination III the three primary coils are operating as a three-phase system.

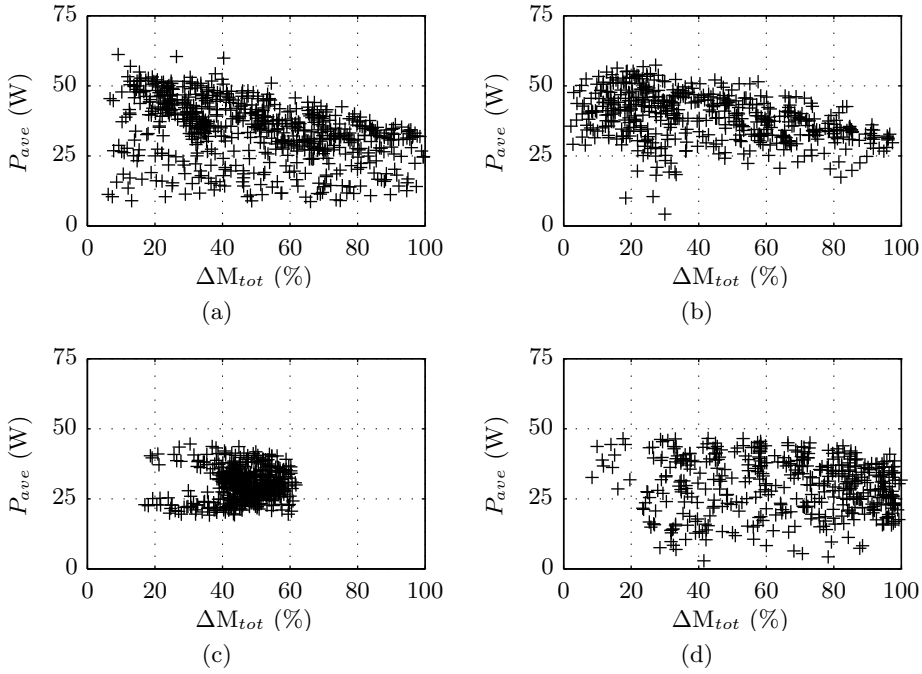

Figure 4.15: Average output power versus variation in mutual inductance for a double layers primary coil array with: (a) configuration Da, (b) configuration Db, (c) configuration Dc, and (d) configuration Dd.

The parameters of the CET system are similar to the CET system with the lowest variation in mutual inductance with three coils presented in Section 4.4.1, and listed in Table 4.10.

The linked flux between the three primary and the single secondary coil with respect to the different combinations of phase angles is shown in Fig. 4.16(a) for a single period of the resonance frequency, and is equal to the mutual inductance times the instantaneous value of the current through a primary coil. The related induced voltages in the secondary coil are shown in Fig. 4.16(b). The highest induced voltage in the secondary coil is obtained in combination I, in which the coils have a similar phase angle. The other two combinations, in which the phase angle of the primary coils differs with respect to each other, have a lower amplitude of the flux linkage which results in a lower induced voltage at the secondary side.

The output power as a function of the displacement of the secondary coil along the x-direction is shown in Fig. 4.17 for the different combinations of phase angles. The variation in output power is equal to 21.5%, 68.4% and 63.1% for combinations I, II and III, respectively. Again, the highest amplitude and lowest variation in output power is obtained with combination I, in which the primary coils have an

Table 4.15: Selected combinations of phase angles

Combination	Phase I_{coil_1} (rad)	Phase I_{coil_2} (rad)	Phase I_{coil_3} (rad)
I	0	0	0
II	0	π	0
III	$-\frac{2}{3}\pi$	0	$\frac{2}{3}\pi$

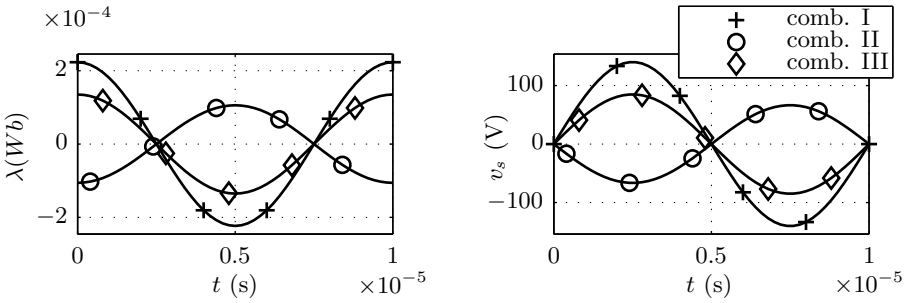

Figure 4.16: (a) Flux seen by the secondary coil and (b) induced voltage in the secondary coil, for different combinations of phase angles.

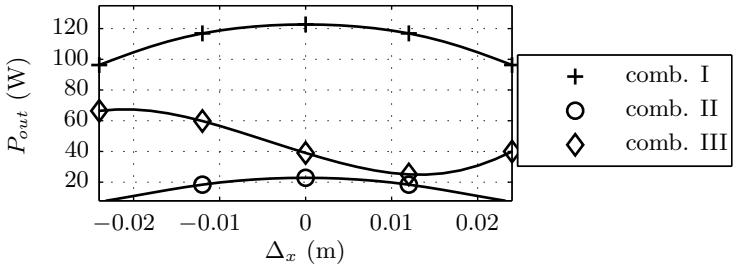

Figure 4.17: Output power of a CET system with of three primary coils and a single secondary coil as a function of the displacement for different combinations of phase angles of the primary coils.

equal phase angle.

Summarized, the phase angle of the primary coils in a CET system in which multiple primary coils transfer energy to a single secondary coil should be similar to each other to obtain the highest average output power.

4.5 Summary and conclusions

This chapter concerns the analysis of the position dependency of a CET system with flat coils and a single secondary coil with a linear or planar movement. A design method is presented in which the position dependency is minimized and the performance indexes (output power, efficiency, etc.) are maximized. By means of this method, the coil dimensions, the electrical parameters, and the layout of the primary coil array are synthesized taking into account the variation in mutual inductance and average output power. Summarizing, the results of the analysis yields to a set of design considerations for a position-independent CET system.

The dimensions of the coils have a major influence on the position-dependency and average output power of a CET system. A high average output power can be obtained with a primary coil with a small inner width and an outer width equal to the coil pitch. The dimensions of the secondary coil should match the ones of the primary coils to obtain a system with a low variation in mutual inductance. This can be reached if the inner width of the secondary coil envelopes the outer width of the set of active primary coils. The heights of the primary and secondary coil are irrelevant for the variation in mutual inductance, whereas an increased energy transfer can be obtained for a maximized coil height.

The electrical parameters of a CET system can be optimized for a maximum energy transfer, which is limited by the conduction losses in the coils. To minimize the conduction losses, i.e. the temperature of the coil, the number of turns, and resonance frequency can be optimized such that a low coil resistance and a magnetizing inductance with a high impedance are reached. In this way, the voltage drop across the coil resistances is low and the output voltage of the CET system approaches the input voltage of the CET system with respect to the turn ratio. The input voltage and load resistance can be defined such that the output power is maximized for a predefined output voltage and with respect to the allowable conduction losses.

Ferromagnetic plates behind the primary and secondary coils increase the mutual inductance and, thereby, improve the energy transfer of a CET system compared to coils surrounded by air. For these configurations a CET system with a low variation in mutual inductance can be obtained, which is not the case if one or two sides of the CET system have a salient ferromagnetic structure. The teeth around the coils provide a preferred path for the magnetic flux which varies with respect to a moving secondary side, and, therefore, the energy transfer of the CET system becomes more position-dependent.

Multiple active primary coils contribute to the decrease in variation of the mutual inductance. The output power is depending on the number of active primary coils, where the use of sets with multiple primary coils results in a higher average output power compared to a single primary coil. Generally, for each set of energized

adjacent primary coils it is possible to match the dimensions of the secondary coil such that a low variation in mutual inductance is gained.

In a multi-layer primary coil array, the height of the individual primary coils is decreased and, therefore, the use of a multi-layer array results in a lower average output power compared to a single-layer coil array. In a single-layer coil array a low variation in mutual inductance and the highest output power can be obtained if the set of active primary coils and a single secondary coil have a similar phase angle.

The results for a position-independent CET system obtained in this chapter, combined with the design method, are applied in the next chapter to design a position-independent CET system integrated in a magnetically suspended planar motor.

5

Design of a contactless energy transfer system in a planar motor

In this chapter a design of a position-dependent Contactless Energy Transfer (CET) system integrated in a planar motor is presented. In the planar motor, the translator is magnetically suspended underneath the stator. A CET system is integrated in the planar motor to transfer electrical energy to the translator, such that the four embedded linear motors on the translator can be used to suspend and propel the translator underneath a stationary frame. Theoretically, the translator of the planar motor has an unlimited stroke, and multiple translators can operate around each other underneath a similar stationary frame. Applications of the planar motor with integrated CET system can be found within the high-tech industry, for example, for visual inspection or as a part of a pick-and-place machine.

The design of the planar motor with integrated CET system involves three main challenges. First, a magnetically suspended planar motor needs to be designed. The planar motor combines the magnetic suspension and propulsion of translator, and, in case of a power failure, the translator should clamp itself to the stationary magnet array. Second, for a complete wireless operation of the translator, a cable connection between the stationary part and the translator should be avoided. Therefore, energy needs to be transferred contactlessly to the translator. Since the motor should be able to operate at every position in its planar stroke, the CET system should be able to transfer an equal amount of energy at every position of

the translator. Third, because of the planar stroke both the magnetically levitated planar motor and the CET system should be integrated into each other.

This chapter presents a solution to the three challenges involved in the design of the planar motor with integrated CET system. In the first section, the magnetically planar motor is described briefly, and the energy requirements of the CET system are discussed. A detailed design of the planar motor is presented in [79]. The second section treats the design of the CET system and discusses the limitations related to the integration. The final sections of this chapter deals with the two remaining conversions steps in the CET system, the dc-ac and ac-dc power converters, and the real-time control of the primary coil array is given.

5.1 The magnetically suspended planar motor

The magnetically suspended planar motor consists of a stationary checkerboard permanent magnet array and a magnetically suspended translator, which embeds four iron-cored linear permanent-magnets motors [80, 85]. The four linear motors are positioned in pairs along the x- and y-direction and are rotated 45 degrees with respect to the orientation of the alternating checkerboard magnet array. A schematic overview of the stationary magnet array and the four linear motors is given in Fig. 5.1.

The iron-cores of the linear permanent-magnet motors provide a passive attraction force larger than the weight of the translator for an airgap up to 4 mm. The passive attraction force clamps the translator against the ceiling if no currents are supplied to the coils of the linear motors and, therefore, avoids that the translator falls down in case of a power failure. Each linear motor is separately exited as a three-phase synchronous motor such that the planar motor can be controlled over the six degrees-of-freedom. In each linear motor, the normal and propulsion force components are decoupled by means of the $dq0$-decomposition of the three-phase currents [82–84]. The magnetic suspension is controlled by imposing a negative d-axis current in the coils of the four linear motors, which generates an active normal force which counteracts the passive attraction force and suspends the translator underneath the stationary ceiling. A positive or negative q-axis current in the coils of the linear motors produces the required propulsion force.

The design of the planar motor is optimized for minimum ohmic losses in combination with a total translator mass equal to 10 kg and an acceleration of 5 ms^{-2} [81, 85]. Furthermore, the primary coils of the CET system are located in the airgap of the planar motor, and, therefore, a clearance of 3 mm is obtained between the permanent magnets and the linear motors. The primary coils of the CET system have a maximum height of 2 mm, such that a mechanical clearance of 1 mm remains between the stationary and moving part of the planar motor. The planar motor uses a low magnetic loading which results in a balance between the passive attraction force, the active normal force and the ohmic losses. Furthermore, for an efficient CET system materials with a high electrical conductivity are minimized in the neighborhood of the primary coils. Both the low magnetic loading and a low electrical conductivity are reached by the use of plastic bonded magnets in the stationary permanent magnet array.

As concluded in Section 4.3, a ferrite plate behind the coils of the CET system increases the energy transfer capability. However, the motor requires a non-ferromagnetic plate behind the magnets to obtain a linear relation between the normal force and the d-axis current [84]. Furthermore, ferromagnetic structures at the translator create an additional passive force in combination with the permanent magnet array which are unwanted. Therefore, no ferromagnetic plates are

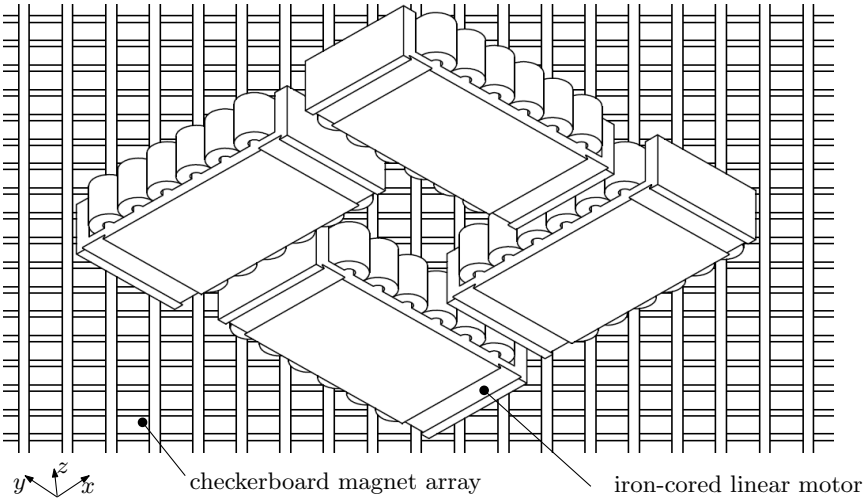

Figure 5.1: Schematic overview of the magnetically suspended planar motor.

located behind the coils of the CET system.

The supply of electrical energy to the translator in the planar motor is provided by the CET system. The required energy flow to the translator of the planar motor is determined with respect to a second-order motion profile and for various accelerations of the planar motor. The planar motor has a maximum stroke in x- and y-direction, x_{max}, y_{max}, of 0.2 m and the maximum velocity in both directions, v_{max}, is equal to 0.5 ms^{-1} which is limited by the position measurement system. Furthermore, the maximum acceleration of the translator along the x- and y-direction, a_{max}, is equal to 5 ms^{-2}. For a diagonal movement along the stroke of the translator, the average dissipated power can be obtained by

$$P_{avg} = \frac{(P_{acc} + P_{torq})\, t_{acc}}{t_{tot}} + P_{susp}, \tag{5.1}$$

where

$$P_{acc} + P_{torq} = \alpha_{acc} a^2 + \alpha_{torq} a^2 = (\alpha_{acc} + \alpha_{torq})\, a^2, \tag{5.2}$$

$$t_{tot} = \frac{x_{max} - 2x_{acc}}{a t_{acc}}, \tag{5.3}$$

$$t_{acc} = \sqrt{\frac{x_{acc}}{a}}, \tag{5.4}$$

$$x_{acc} = \begin{cases} \frac{v_{max}^2}{a} & \text{for } a \leq 2.5 \text{ ms}^{-2} \\ 0.5x_{max} & \text{elsewhere} \end{cases}, \tag{5.5}$$

where P_{susp} is the power required for the magnetic suspension, and is equal to a constant value of 15 W [85]. P_{acc} is the power dissipation during acceleration, and P_{torq} is the power dissipation related to the torque compensation during acceleration. The power dissipation, P_{acc} and P_{torq}, are quadratically depending on the acceleration with $(\alpha_{acc} + \alpha_{torq})$ equal to 13 Wm^{-2}s^4 [85]. The acceleration time, t_{acc}, depends on the acceleration and is limited by the stroke of the translator. The required peak power is obtained as

$$P_{peak} = P_{acc_{max}} + P_{torq_{max}} + P_{susp_{max}} + P_{mech_{max}}, \tag{5.6}$$

where the maximum mechanical power during acceleration is equal to

$$P_{mech_{max}} = F_{max} v_{max} = m t_{acc} a^2, \tag{5.7}$$

and is delivered by the source during acceleration. Because of the low magnetic loading and, hence, the low electromotive force, the total stored kinetic energy during acceleration is dissipated in the coils during deceleration. The required peak and average power as a function of the acceleration are shown in Fig. 5.2. For an acceleration below 2.5 ms^{-2} the maximum velocity is not reached within the stroke. At a maximum acceleration equal to 5 ms^{-2}, a peak power of 335 W is required, and an average power of approximately 170 W is needed along the trajectory. Based on this required power consumption, an assumed efficiency of 80% for the amplifiers of the linear motors and a maximum consumption of 33% of the total transferred energy for additional electronics on the translator, a total power of 340 W should be provided by the CET system. Furthermore, an output voltage of 100 V is required to match the voltage specifications of the three-phase amplifiers of the linear motors.

5.2 Design of the integrated contactless energy transfer system

A position-independent CET system is integrated in the planar motor to fulfil the required energy supply towards the magnetically suspended translator. Integration of the planar motor and the CET system requires a trade-off in dimensions

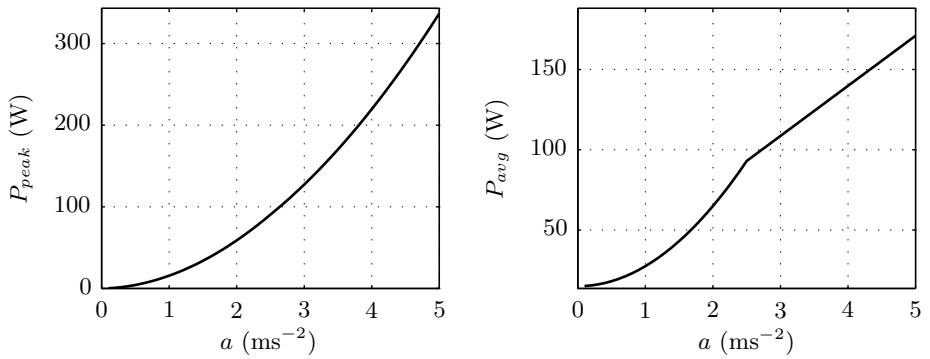

(a) (b)

Figure 5.2: Peak (a) and average (b) power dissipation of the planar motor as a function of the acceleration (a_x=a_y=a) for a diagonal movement of the translator.

and performance indexes, as is discussed for the design of the primary and the secondary coils in this section. As concluded in Chapter 4, the highest power density can be obtained in a system with an active set of multiple adjacent primary coils in a single-layer coil array and with an identical phase-angle in each activated primary coil.

5.2.1 Design of the primary coil array

The primary coil array of the CET system is integrated in the airgap of the planar motor, and is located directly underneath the checkerboard permanent magnet array. The planar motor operates at an airgap equal to 3 mm between the magnets and the linear motors. To keep a mechanical clearance of at least 1 mm, the height of the primary coil array is specified to be equal to 1.5 mm. Furthermore, for mechanical protection of the primary coils against impacts of the translator a non-magnetic and non-conducting plate with a thickness equal to 0.5 mm is placed underneath the coils.

The permanent magnet array of the planar motor has a pitch equal to 24 mm. For the ease of construction of the coil array on top of the magnet array and the guidance of the leads of every coil through the magnet array, the primary coils have a pitch equal to n-times the magnet pitch. In this way, a repetitive pattern is created at the stationary part of the planar motor. Theoretically, this pattern of magnets and coils can be enlarged towards an unlimited stroke.

Table 5.1: Maximal dimensions of a primary coil

Parameter		Value	
coil pitch	$2\tau_p$	48.0	mm
half outer width	c_{pw}	22.5	mm
half inner width	c_{piw}	5.00	mm
coil height	h_p	1.50	mm

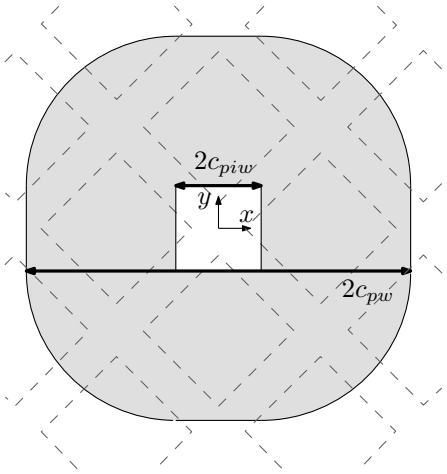

Figure 5.3: Top view of a single primary coil (the dashed-lines indicate the magnet array).

With respect to the primary coil dimensions, a large primary coil area increases the amount of transferred energy, as concluded in Section 4.2.1. Furthermore, a low variation in mutual inductance is obtained if the inner width of the secondary coil envelopes the outer width of the primary coil, as concluded in Section 4.4.1. For manufacturing reasons, the minimum inner width of a primary coil is set equal to 5 mm, and a clearance equal to 3 mm is chosen between two adjacent coils. Based on a coil pitch equal to one, two, and three times the magnet pitch, this results in a maximum bundle width of 5.5, 17.5 and 29.5 mm, respectively. To limit the dimensions of the secondary coil, which envelopes the active set of primary coils for a low variation in mutual inductance, and to have a large enough coil volume for the required output power, a primary coil pitch equal to two times the magnet pitch is selected. Furthermore, to obtain a similar variation in mutual inductance in the x- and y-direction the primary coil is considered to have a square shape. The maximum dimensions of a primary coil are listed in Table 5.1, and a single primary coil on top of the magnet array is schematically shown in Fig. 5.3.

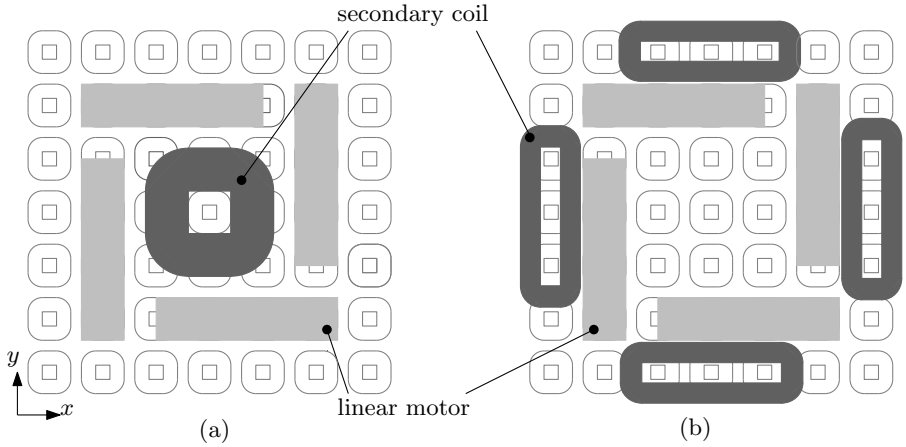

Figure 5.4: Two geometrical options for the secondary side of the CET system on top of the primary coil array: (a) a single secondary coil in between the four linear motors, and (b) four secondary coils, each one parallel to a linear motor.

5.2.2 Design of the secondary coil

The secondary coil of the CET system is located in the translator of the planar motor. The combination of the four linear motors on the translator leads to two possible geometrical options for the secondary side of the CET system. A first option is a single secondary coil in between the four linear motors, schematically shown in Fig. 5.4(a). In this combination, a single secondary coil receives energy transmitted from a set of four active primary coils. The dimensions of the secondary coil in this set are limited by the available area between the four linear motors. A second option is shown in Fig. 5.4(b), and can be obtained with four secondary coils, one parallel to each linear motor. Four sets of three adjacent active primary coils are transferring energy to the secondary coils. In this option, the width of the secondary coil parallel to the translator is limited, aiming to reduce the overall size of the translator. The output of the rectifiers is connected in series, such that each combination of three primary and a secondary coils can contribute to the energy transfer, as is shown in Section 5.3.3.

The two geometrical options for the secondary side of the CET system are analyzed by means of the design method, presented in Section 4.2.3, for various dimensions of the secondary coils to obtain a position-independent system, in which the dimensions of the secondary coil are optimized with the one of the primary coils. During the design, the output power level of each considered set of dimensions is maximized with respect to the constraints specified in Tables 5.2 and 5.3 for the

Table 5.2: Constraints for the CET system with a single secondary coil.

40 mm	$\leq$	c_{sw}	$\leq$	80 mm
5 mm	$\leq$	c_{siw}	$\leq$	75 mm
$N_{s_{min}}$	$\leq$	N_s	$\leq$	$N_{s_{max}}$
1 V	$\leq$	V_p	$\leq$	500 V
1 Ω	$\leq$	R_{load}	$\leq$	250 Ω
		f_{res}	$=$	100 kHz
		T_{coil}	$\leq$	50°C
		η	$\geq$	80 %
		V_s	$\approx$	100 V

Table 5.3: Constraints for the CET system with four secondary coils.

30 mm	$\leq$	c_{sw_x}	$\leq$	120 mm
5 mm	$\leq$	c_{siw_x}	$\leq$	115 mm
30 mm	$\leq$	c_{sw_y}	$\leq$	50 mm
5 mm	$\leq$	c_{siw_y}	$\leq$	45 mm
$N_{s_{min}}$	$\leq$	N_s	$\leq$	$N_{s_{max}}$
1 V	$\leq$	V_p	$\leq$	500 V
1 Ω	$\leq$	R_{load}	$\leq$	250 Ω
		f_{res}	$=$	100 kHz
		T_{coil}	$\leq$	50°C
		η	$\geq$	80 %
		V_s	$\approx$	25 V

option with a single and four secondary coils, respectively. The major difference between the two sets of constraints are the possible dimensions for the secondary coil. The outer dimensions in case of a single secondary coil are limited to 160 mm ($2c_{sw}$), which is equal to the maximum distance between two linear motors on the translator. For the option with four secondary coils, the length parallel to a linear motor is bounded to 240 mm ($2c_{sw_x}$), and, the width perpendicular to a linear motor is bounded to 100 mm ($2c_{sw_y}$) to restrict the maximum area of the translator. Furthermore, the output voltage of the CET system is desired to be equal to 100 V, which means a secondary voltage equal to 100 V for the option with a single coil and a secondary voltage of 25 V per coil in the option with four secondary coils, consequently. In both cases the resonance frequency is set to 100 kHz. The value of the resonance frequency is finally matched with the resonance frequency obtained by the value of the resonance capacitors in combination with the leakage inductance. The maximum allowable coil temperature is set to 50 °C. The minimum and maximum number of secondary turns are related to the coil dimensions as discussed in Section 4.2.3.

The average output power as a function of the variation in output power for the

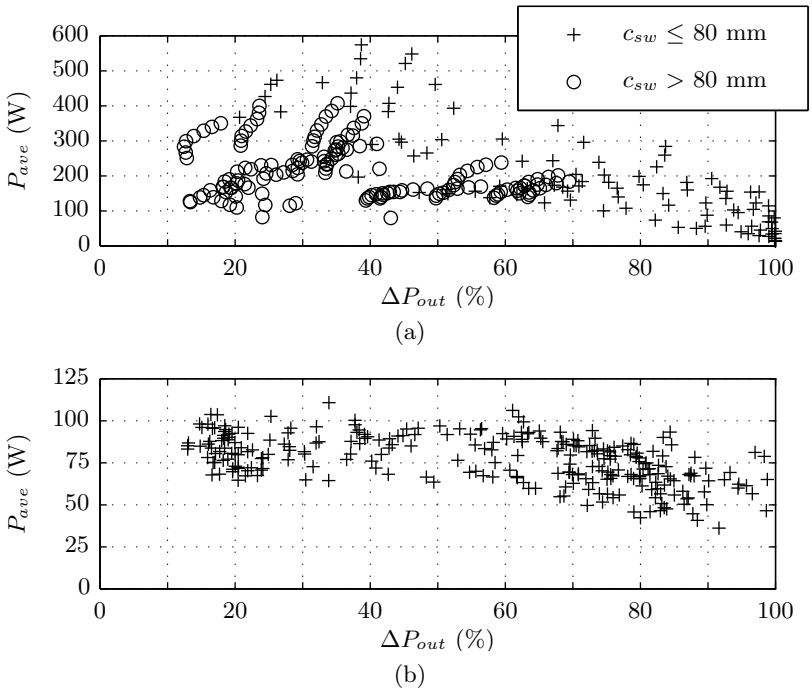

Figure 5.5: Output power as a function of the variation in mutual inductance for: (a) the option with a single square secondary coil and (b) for a single secondary coil in the option with four rectangular secondary coils.

option with a one secondary coil and for a single secondary coil in the option with four secondary coils are shown in Figs. 5.5(a) and (b), respectively. The geometrical option with a single secondary coil gives no solution with a variation in output power below 20% in combination with a maximum half outer width below or equal to 80 mm. Secondary coil dimensions with a half outer width larger than 80 mm are able to perform both a low variation in output power in combination with the requested output power of 340 W, as can be observed in Fig. 5.5(a). From this observation it be concluded that the area for a secondary coil in between the four linear motors is too small for a design with the desired output power in combination with a low variation in output power.

The geometrical option with four secondary coils gives various designs with an output power between 65 and 105 W per secondary coil in combination with a variation in output power below 20%, as shown in Fig. 5.5(b). The possible solutions are shown in more detail in Fig. 5.6, in which the designs are ordered with respect to the half coil width (c_{sw_y}) perpendicular to the linear motor. Among the different options, the design with the lowest variation in output power and an average output power above 85 W is chosen.

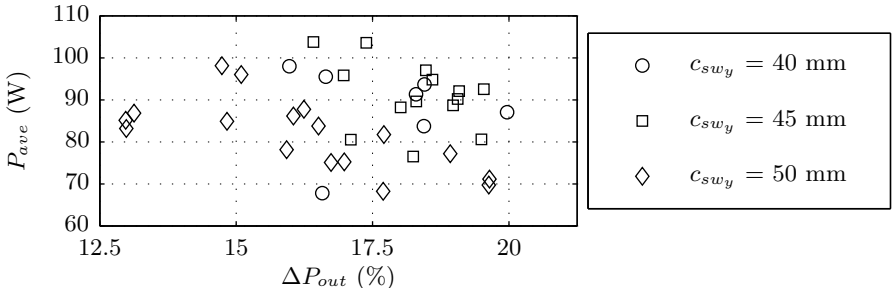

Figure 5.6: Output power of a single secondary coil for the second geometrical option for a variation in mutual inductance below 20% with respect to the length perpendicular to a linear motor, c_{sw_y}.

Table 5.4: Dimension of the primary and secondary coil

Parameter	Value			
	primary coil		secondary coil	
outer width x-direction	$2c_{pw_x}$	45.0 mm	$2c_{sw_x}$	190.0 mm
inner width x-direction	$2c_{piw_x}$	10.0 mm	$2c_{siw_x}$	150.0 mm
outer width y-direction	$2c_{pw_y}$	45.0 mm	$2c_{sw_y}$	100.0 mm
inner width y-direction	$2c_{piw_y}$	10.0 mm	$2c_{siw_y}$	60.0 mm
coil height	h_p	1.5 mm	h_s	1.0 mm
number of turns	N_p	130 turns	N_s	20 turns
diameter Litz wire	D_{litz_p}	0.50 mm	D_{litz_s}	1.00 mm
diameter single strand	D_{strand_p}	0.071 mm	D_{strand_s}	0.071 mm
number of strands		20 strands		80 strands

The optimization resulted in a secondary coil with a total length equal to 190 mm parallel to a linear motor and a width equal to 100 mm perpendicular to a linear motor, and a primary coil with dimensions equal to the maximum outer width and minimum inner width. An average output voltage of 26 V is obtained for a primary input voltage of 42.5 V in combination with three primary coils with 103 turns each and a secondary coil with 20 turns, as given by (3.16). The combination of a higher primary voltage and a higher number of primary turns results in a lower primary current compared to the secondary current, which reduces conduction losses in the primary coils. The 103 turns of the primary coil are wound in 41 vertical layers alternating between two and three turns per layer. The 20 turns of the secondary coil are wound in a single layer. The complete set of parameters of the secondary coil is presented in Table 5.4. The output power of a single set of three primary and a single secondary coil is equal to 87 W, and a variation in output power of 13% is obtained. A complete overview of the system parameters is given in Table 5.5.

Table 5.5: Electrical parameters of a single set of three primary coils and a single secondary coil.

Parameter	Value	
L_p	290	μH
L_s	95.2	μH
M_{ave}	73.1	μH
ΔM_{tot}	23.4	%
R_p	2.26	Ω
R_s	0.51	Ω
V_p	42.5	V
$V_{s_{ave}}$	25.9	V
R_{load}	7.44	Ω
T_{coil}	50.0	°C
P_{ave}	86.9	W
ΔP_{out}	13.1	%
η	91.0	%

In the previous section, the performances of a single secondary coil for the geometrical solution with four secondary coils are presented. The output power of a single set, equal to 87 W, can be multiplied by four to obtain a total output power of 348 W. Although the multiple sets increase the output power, the variation in output power remains to be equal to 13%. To reduce the position dependency of the system, the secondary coils can be shifted with respect to each other, and, thereby, become differently orientated above the primary coil array. The relative displacement of two parallel-orientated secondary coils with respect to the aligned position of a secondary coil above the three active primary coils is shown in Fig. 5.7. In the figure the secondary coil at the bottom of the figure, is shifted Δx_c and Δy_c in the x- and y-direction, respectively.

The average output power and variation in output power for two secondary coils, as a function of the displacement between them, is shown in Fig. 5.8. As demonstrated in Fig. 5.8(a), the amplitude of the output power of two secondary coils varies between 180 and 182 W for a relative displacement of a half coil pitch in the x- and y-direction between the coils. The variation in output power for a relative displacement between two secondary coils is shown in Fig. 5.8(b), and can be decreased from 13.1% to 6% if one of the secondary coils is shifted a quarter coil pitch in the y-direction. The highest output power is obtained when the distance between the coils in the x-direction is equal to a multiple of a half coil pitch.

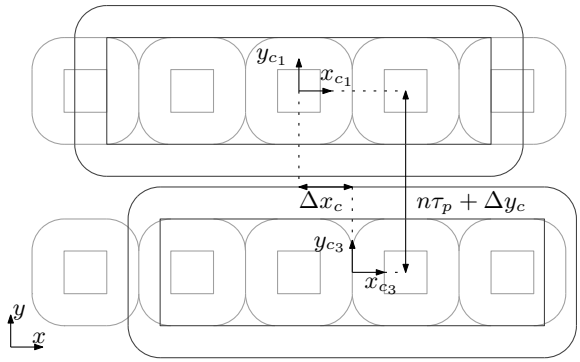

Figure 5.7: Schematic overview of the displacement of two parallel secondary coils with respect to each other.

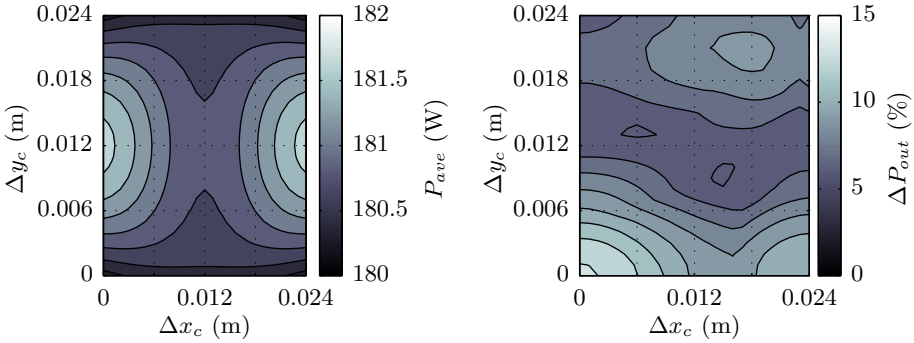

Figure 5.8: Average value (a) and variation (b) in the output power of two parallel-orientated secondary coils, displaced with respect to each other and the primary coil array.

5.2.3 Integrated design

A schematic overview of the design of the CET system integrated in the planar motor is presented in Fig. 5.9. The bottom view in Fig. 5.9(b) shows the four secondary coils above the array of primary coils. The primary coil array consists of an array of 13x13 coils, 169 in total, from which twelve coils are energized simultaneously to provide the energy transfer to the four secondary coils. The maximum output power of the CET system with four secondary coils varies between 349 W

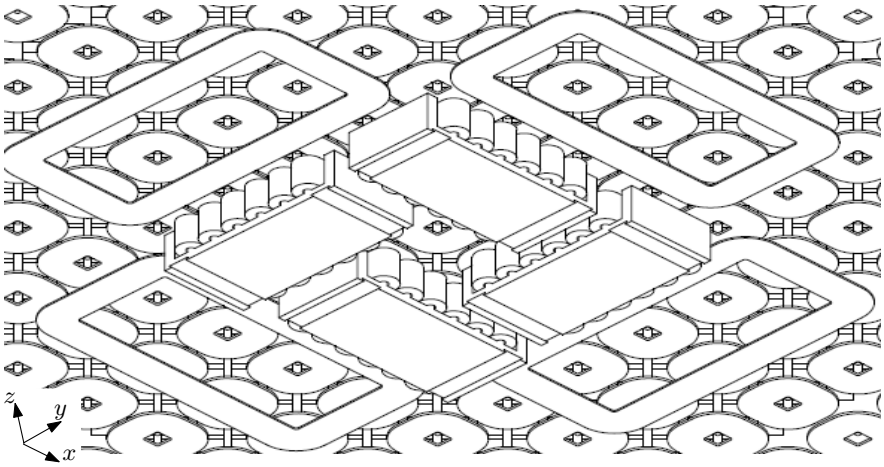

(a)

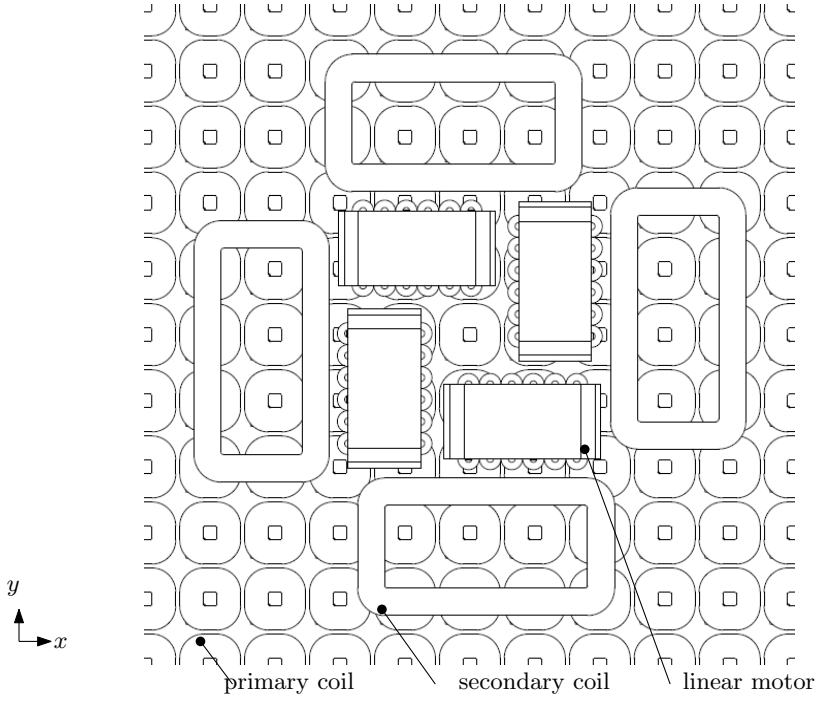

(b)

Figure 5.9: CET system integrated in the planar motor: (a) schematic overview, and (b) bottom view without checkerboard magnet array.

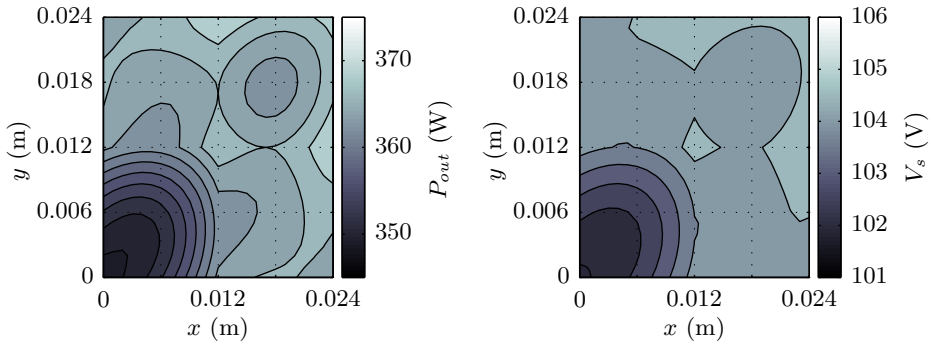

(a) (b)

Figure 5.10: Performance integrated CET system as a function of the displacement along a quarter primary coil pitch: (a) output power, and (b) output voltage.

and 370 W for a displacement of a quarter primary coil as shown in Fig. 5.10(a). This results in a variation in output power of 5.6% for the system with an average output power of 363 W. The output voltage of the CET system, shown in Fig. 5.10(b), has an average value of 104.1 V and varies ± 2.8 V along the stroke of the secondary coil.

5.3 Implementation

In this section the practical implementation of the CET system integrated in the magnetically suspended planar motor is presented, and concern about the presence of conducting materials in the construction, the two power converters in the CET system, and the control of the primary coils.

5.3.1 Materials in the integrated system

Conducting materials should be avoided in the neighborhood of the coils of the CET system, because the reaction field of the induced eddy-currents counteracts the magnetic fields of the coils which reduces the efficiency of the CET system. At the stationary side, the planar motor requires a non-ferromagnetic construction behind the permanent magnets. Furthermore, this plate should be able to handle the forces between the stationary and moving part of the motor. Therefore, the

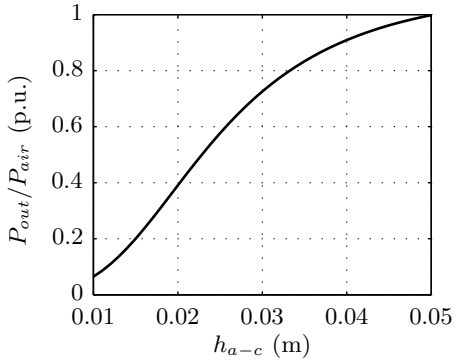

Figure 5.11: Output power a secondary coil as a function of the distance between an aluminum plate and the coil for a frequency equal to 90 kHz.

stationary side of the planar motor is constructed of an epoxy-resin glass-fabric plate (G11), which is both non-ferromagnetic and non-conductive.

The alternating permanent magnet array is constructed from plastic bonded Nd-FeB magnets, which provide a low magnetic loading for the planar motor and have a low electrical conductivity for the CET system. The plastic bonded permanent magnets have an electrical conductivity equal to 40 Sm^{-1} and a relative permeability equal to 1.26. A continuous plate with similar material properties is modeled above the array of primary coils. The self-inductance of primary coils increases by 5% with respect to the designed value, and the output power is decreased by 17% compared to the designed value. A FEM simulation is conducted with a segmented magnet array above the primary coils, which resulted in a decrease in output power by 6.3%.

At the translator, the secondary coils are placed parallel to the iron-cored linear motors, as shown in Fig. 5.9(b). The self-inductance of a secondary coil is measured for various distances between the coil and the iron core. A self-inductance between 98.0 and 99.0 μH is measured for a distance between 0 and 25 mm between the coil and the iron core. From these measurements, it can be concluded that the iron-cored linear motors have no influence on the inductances, and, thereby, on the power transfer.

The base-frame of the translator and the target plates for the position measurement system are constructed from aluminum. The base-frame is required to create stiffness to the construction of the translator, but because of the high electrical conductivity, $26{\cdot}10^6$ Sm^{-1}, the distance between the CET system and the aluminum frame should be maximized to avoid eddy-currents. The output power of the CET system is calculated for various distances between an aluminum plate and a sec-

ondary coil, h_{c-a}. During the calculation of the output power, the inductances of the CET system are calculated based on the harmonic model, as presented in Section 2.5.1. The calculated output power with respect to the output power of the CET system surrounded by air is shown in Fig. 5.11. The distance of the aluminum base-frame of the translator and a secondary coil varies between 25 mm at the border of the frame and 45 mm for the chamber underneath the secondary coil. With respect to the output power of a single secondary coil, this results in a decrease of 4% for a distance of 45 mm and 42% for a distance of 25 mm. Overall, the distance between the secondary coil and the aluminum base-frame should be maximized in the construction of the translator to avoid eddy-currents, and, thereby, a decrease in the output power.

5.3.2 Dc-ac converter

In the primary coil array four sets of thee adjacent coils are simultaneously providing the energy transfer towards the four secondary coils. These sets are dynamically reconfigured with respect to the movement of the secondary coil, and, therefore, every primary coil needs to be switched on and off individually. Two solutions are possible to supply the high-frequency voltage to the active primary coils. First, every individual primary coil can be connected to an individual dc-ac converter. Second, only twelve dc-ac converters can be connected towards a dc-bus and controlled switches connects the active primary coils towards the dc-ac converters. The first solution is chosen to be the most convenient and practical one for the integrated CET system, which does not only result in an similar converter for each primary coil, but makes the CET system also more flexible and not limited to operate simultaneously with only a restricted number of primary coils.

Three types of dc-ac converters can be considered to create the high-frequency input voltage: the half-bridge unipolar converter, the half-bridge bipolar converter, and the full-bridge converter [53]. The lowest number of required circuit components is obtained in the half-bridge unipolar converter, where the output power is switched between the bus voltage and zero voltage using two MOSFETs. The combination of the unipolar converter with the resonance capacitor connected in series, creates a bipolar voltage with an amplitude equal to the half bus voltage. Furthermore, the primary current becomes sinusoidal because of the magnetic resonance. The dc-bus voltage can be obtained by the rms-value of the required input voltage of each primary coil

$$V_{bus} = 2\frac{\sqrt{2}\pi}{4}v_p, \tag{5.8}$$

where the ratio, $\frac{\sqrt{2}\pi}{4}$, is the difference between the amplitude of the fundamental component of the square wave output and the dc-bus voltage. Furthermore, the

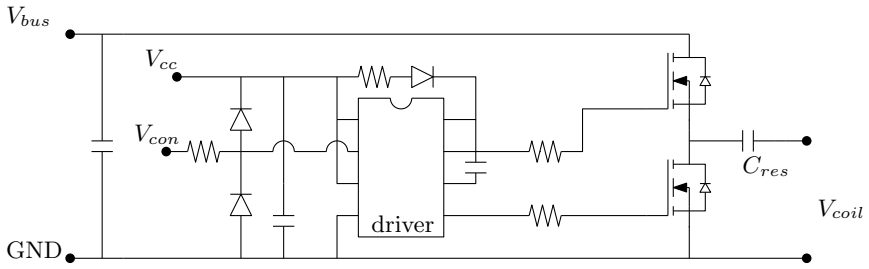

Figure 5.12: Electric circuit of the half-bridge unipolar converter including primary series resonance capacitor.

dc-bus voltage is doubled to compensate for the 50% decrease in amplitude because of the converter topology.

The circuit of the half-bridge unipolar converter including the primary series resonance capacitor is shown in Fig. 5.12, and the involved components are listed in Table A.1 in Appendix A. The resonance capacitors are represented by C_6 and C_7, and their value is chosen such that the leakage of each individual primary coil is compensated in aligned position with the secondary coil according to (3.19). With respect to the available capacitor values and number of required components, the resonance frequency is set to 90 kHz. The secondary coil is tuned at resonance with respect to the leakage inductance related to the mutual inductance between the secondary coil and the three primary coils. To decrease the losses in the dc-ac converter it is advantageous to switch the converter at a frequency slightly higher than the resonance frequency of the contactless energy transfer system [127, 128].

5.3.3 Ac-dc converter

The high-frequency output voltage of the four secondary coils is rectified by using four series-connected single-phase diode bridge rectifiers, as shown in Fig. 5.13(a) [30]. Each secondary coil has an individual rectifier, such that the phase difference with respect to four induced voltages is removed. The series connection ensures that the voltage across the equivalent load resistance is equal to the sum of contribution of each individual set of three primary and one secondary coils. The circuit diagram of a diode bridge rectifier is shown in detail in Fig. 5.13(b) and the components are listed in Table A.2 in Appendix A.

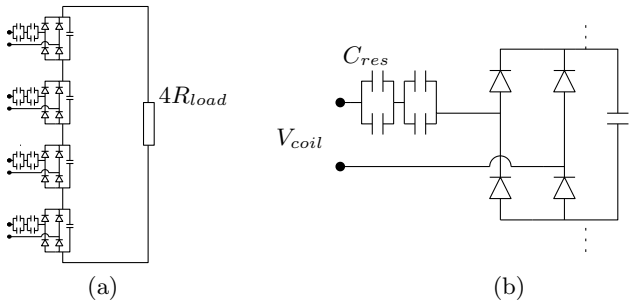

Figure 5.13: Electric circuit of the ac-dc converter: (a) complete circuit of the secondary side of the CET system, and (b) detailed diagram of a single rectifier circuit.

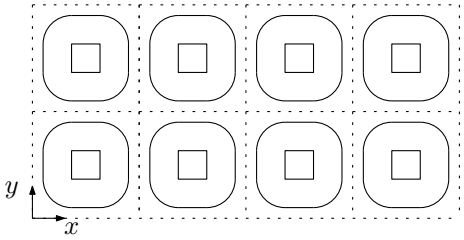

Figure 5.14: Schematically overview of a part of the primary coil array, switching of the active set of coils occurs if the center of the secondary coil passes a dashed line.

5.3.4 Control of the primary coils

The four sets of three adjacent energized primary coils are individually switched depending on the center of the related secondary coil. Switching of the active set of primary coils occurs if the center of the secondary coils moves from one primary coil to another primary coil, as schematically shown by the dashed lines in Fig. 5.14. The switching algorithm is implemented on an FPGA, Xilinx Spartan 2, and activates and deactivates the driver in the dc-ac converters of the primary coils, based on the received actual position of the translator, by supplying or stopping the supply of an alternating signal, with a frequency equal to the frequency of the primary current, to the MOSFET-driver of each H-bridge. The output of the switching algorithm is shown in Fig. 5.15, where the energized primary coils are highlighted for two positions of the translator.

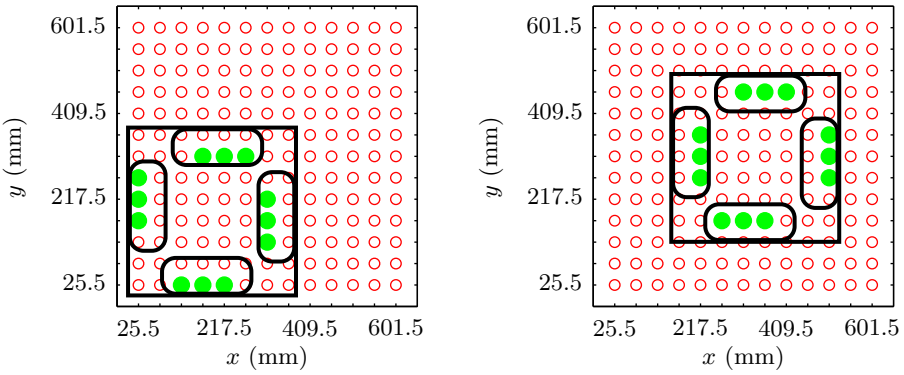

Figure 5.15: Schematic overview of the active primary coils as a function of the center position of the translator: (a) for (x_g,y_g) = (190, 190) mm, and (b) for (x_g,y_g) = (340, 310) mm.

5.4 Summary and conclusions

The design of a position-independent CET system integrated in a magnetically suspended planar motor is presented in this chapter. The magnetically suspended planar motor consists of a stationary checkerboard magnet array constructed from plastic bonded permanent magnets and a translator with four embedded linear motors. A CET system is integrated in the planar motor to transfer energy to the magnetically suspended translator. The planar motor requires an average power of 170 W, in combination with the assumed efficiency of the three-phase amplifiers and additional power electronics on the translator, a CET system with an output power equal to 340 W is considered.

The primary coils of the CET system are located underneath the magnet array in the airgap of the planar motor. Two geometrical configurations for the secondary coil are considered. A configuration in which a single secondary coil is located in between the four linear motors and an arrangement with four secondary coils, one placed next to each linear motor. Whereas the option with a single secondary coil is not able to transfer the required energy within the limited area. Therefore, the arrangement with four secondary coils is selected. The dimensions of the secondary coils are optimized with respect to the sizes of the primary coil, resulting in a system with an average output power of 363 W and a variation in output power of 5.6% along the stroke of the translator. Each primary coil in the CET system is connected to a dc-ac converter which can be dynamically energized, such that the three adjacent primary coils closest to each secondary coil are activated and

contribute to the energy transfer. The output of the four ac-dc converters at the secondary side is connected in series. which results in an average output voltage of the CET system equal to 104 V.

Integration of both the planar motor and CET system is obtained by locating the primary side of the CET system inside the airgap of the planar motor, and minimizing the presence of materials with a high electrical conductivity in the neighborhood of the CET system. Based on the predicted performance of the CET system in the neighborhood of the conducting materials, i.e. the plastic bonded magnets and the aluminum base-frame of the translator, a decrease in output power equal to 25% is expected. A prototype of the planar motor with integrated CET system was manufactured, and the performance indexes are measured and presented in the next chapter.

6

Experimental validation

A prototype of the magnetically suspended planar motor with integrated Contactless Energy Transfer (CET) system is manufactured based on the design presented in Chapter 5. The electromagnetic behavior and experimental verification of the CET system is presented in this chapter through sets of different experiments on the realized prototype. To identify the influence of the integration of the CET system in the planar motor on the output power of the CET system, three additional CET systems are manufactured in which successively parts of the planar motor are added with respect to a system with coils surrounded by air. The output power of the CET system integrated in the planar motor is measured for a single, two and four secondary coils for different velocities of the translator, respectively. Finally, the influence of the CET system on the planar motor is analyzed with respect to the position error of the planar motor.

6.1 Experimental setups

To verify the predicted performances of the CET system, three setups, consisting of a small primary coil array and a single secondary coil, are manufactured next to the prototype of the magnetically suspended planar motor with integrated CET system. This section briefly describes the setups.

6.1.1 Contactless energy transfer systems with a single secondary coil

To analyze the influence of the different parts of the planar motor on the magnetic quantities and the output power of the CET system, three CET systems are manufactured, in which parts of the planar motor are successive added. The first CET system consists of three primary coils and a single secondary coil which are surrounded by air. A photo of this setup is shown in Fig. 6.1(a), and is referred as System A. The second CET system is an extension of System A by means of mounting the primary coil array on top of a permanent magnet array, similar to the stationary side of the planar motor. This system is referred as System B, and a photo of the stationary side is shown in Fig. 6.1(b). The primary coils are numbered p_1-p_8. In the third CET system, a linear motor is placed next to the secondary coil, as shown in Fig. 6.1(c), and this setup is referred as System C. System C represents a quarter of the integrated CET system without the conducting materials used for the base-frame of the translator.

6.1.2 Planar motor with integrated contactless energy transfer system

A prototype of the magnetically suspended planar motor with integrated CET system is manufactured, and a photo of the prototype is shown in Fig. 6.2. The dc-ac converters are located on top of the G11-plate and provide an alternating current, which is fed to the primary coils mounted underneath the G11-plate. A photo of the 169 primary coils, glued on top of the permanent magnet array, is shown in Fig. 6.3.

An exploded view of the translator of the planar motor is shown in Fig. 6.4. The four secondary coils of the CET system are located on top of the translator. The four coils are glued on a hollow PVC cover, as shown in Fig. 6.5(a). The hollow chambers in the PVC cover and the aluminum base-frame do not only reduce the mass of the translator, but also provide space for the ac-dc converters at the secondary side of the CET system, as shown in Fig. 6.5(b). The three-phase power amplifiers of the linear motors do not fit within the translator and are located on

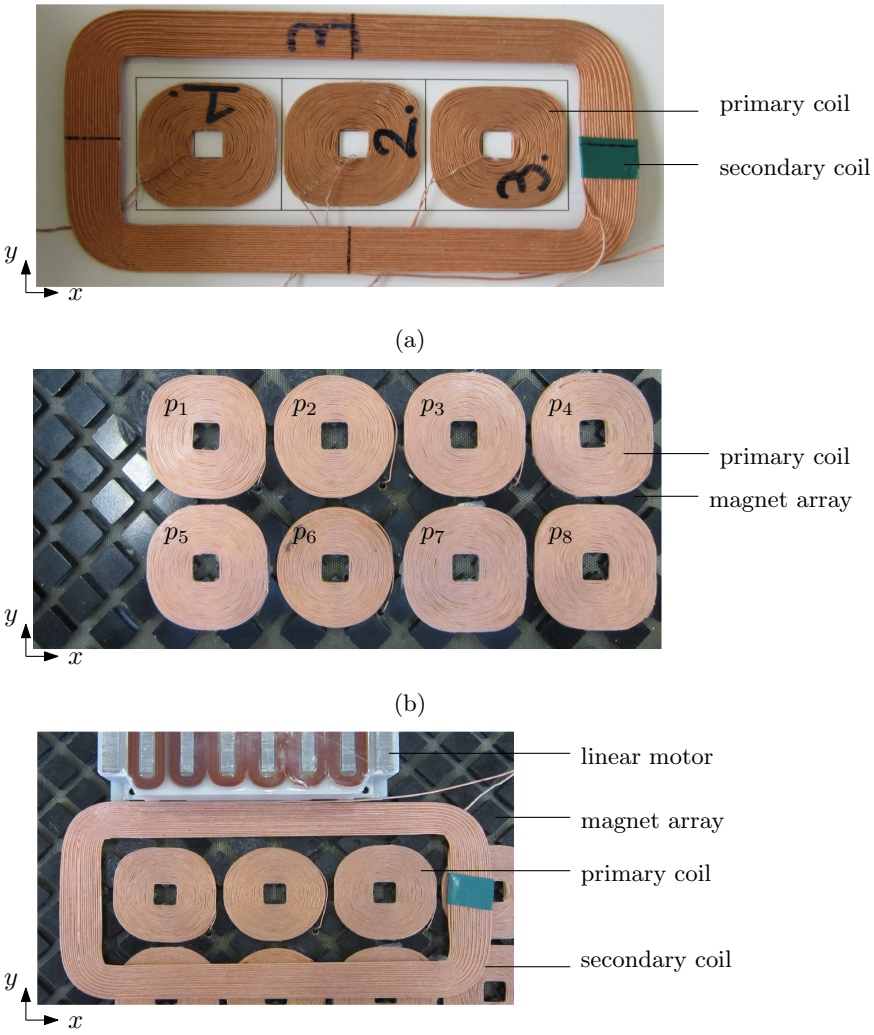

Figure 6.1: Photo of the three different CET systems with a small primary coil array and a single secondary coil: (a) System A with the coils surrounded by air, (b) System B with the primary coils mounted against the magnet array, and (c) System C with a linear motor next to the secondary coil.

the static world. Moving cables connect the power amplifiers to the linear motors. The aluminum plates at the bottom, left, and right sides of the translator are target plates for the eddy-current sensors, which measure the position of the translator.

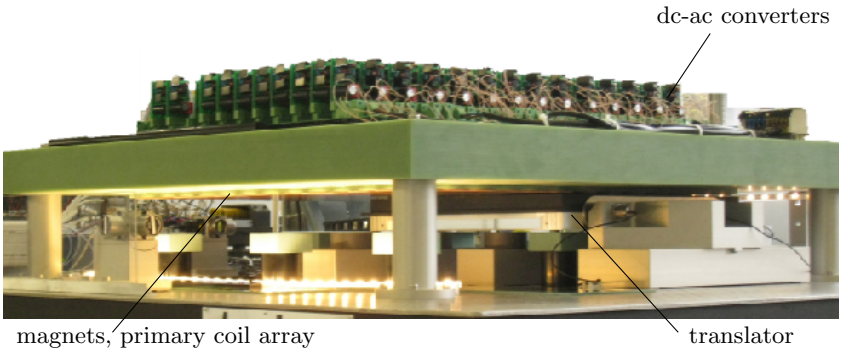

Figure 6.2: Photo of the magnetically suspended planar motor with integrated CET system.

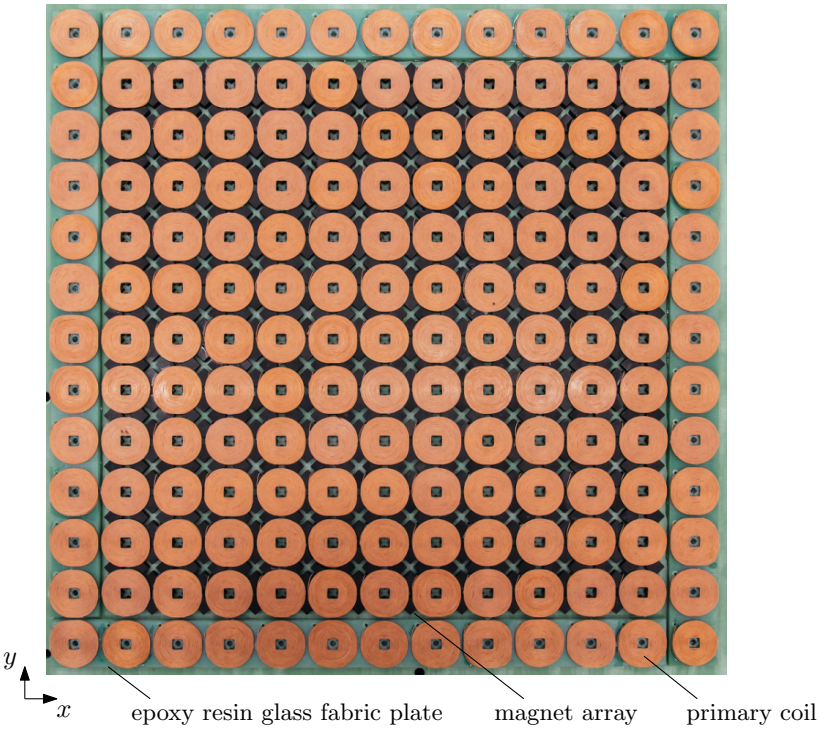

Figure 6.3: Photo of the stationary part of the planar motor with integrated CET system, 169 primary coils glued on top of a magnet array.

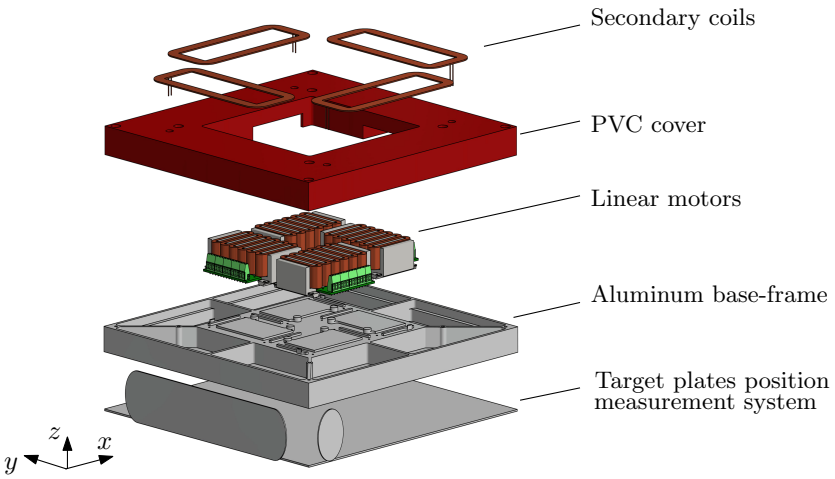

Figure 6.4: Exploded view of the translator.

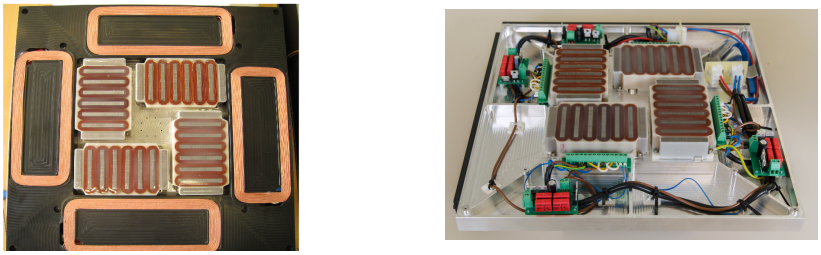

(a) (b)

Figure 6.5: Secondary side of the CET system: (a) secondary coils on top of the translator, and (b) power electronics inside the chambers of the translator.

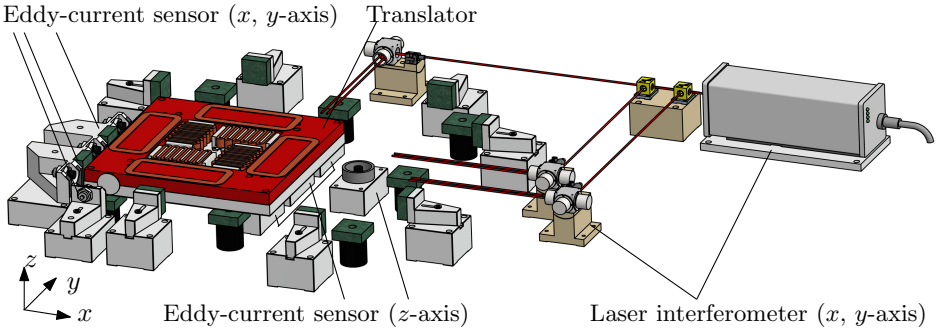

Figure 6.6: Position measurement system of the translator in the planar motor.

The position measurement system of the planar motor is located at the stationary side of the setup, and an overview of the complete position measurement system is shown in Fig. 6.6. The system consists of five eddy-current sensors located underneath the translator, from which three of them are simultaneously used to measure the position in the z-direction and the rotation around the x- and y-axis. A second set of eddy-current sensors, located at the left side of the figure, determines the x- and y-position of the translator and the rotation around the z-axis. The range of the eddy-current sensors is equal to 5 mm and these sensors measure the absolute position of the translator. Once the absolute position of the translator is determined, a laser interferometer system takes over x, y and rotation z measurements of the second set of eddy-current sensors.

6.2 Lumped circuit parameters

To ensure the position-independency of the integrated CET system, the coils are designed such that a low variation in mutual inductance is obtained along the entire stroke of the translator. In this section, the inductances and resistances of the manufactured coils are measured and compared to the values predicted during the design of the CET system.

6.2.1 Self-inductance and coil resistance

The self-inductances of the primary coils are measured with an impedance analyzer at a frequency of 90 kHz, and the measured values are shown in Fig. 6.7(a). The 169 primary coils of the integrated CET system have an average self-inductance equal to 271.42 μH. The self-inductance of each individual coil deviates within 3% of the average value, and the average value is 5.4% lower compared to the designed value of 289.90 μH. The difference between the predicted and average measured value is caused by the outer shape of the primary coils. The designed orthocyclic winding could not be realized during the construction of the primary coils because of the combination of the flexible Litz wire and the limited coil height. This resulted in 169 coils with a different outer shape. The self-inductances of coils with a square envelope are above the average value and coils with a round envelope have a self-inductance below the average value.

The resistances of the 169 primary coils are measured, and the results are shown in Fig. 6.7(b). The resistances of the primary coils have an average value equal to 2.55 Ω, and a variation within 10% is found with respect to all individual measured resistances. The average resistance is 11% higher compared to the designed primary coil resistance of 2.26 Ω.

The self-inductance and resistance of a single primary coil in System A and a

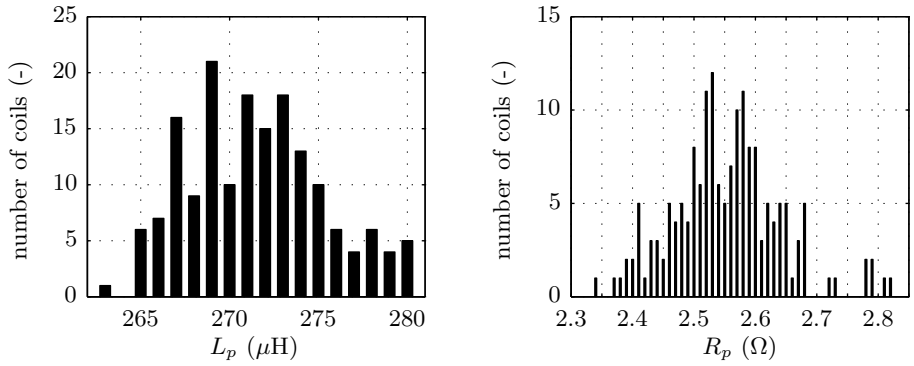

(a) (b)

Figure 6.7: (a) Self-inductances and (b) resistances of the coils in the primary coil array.

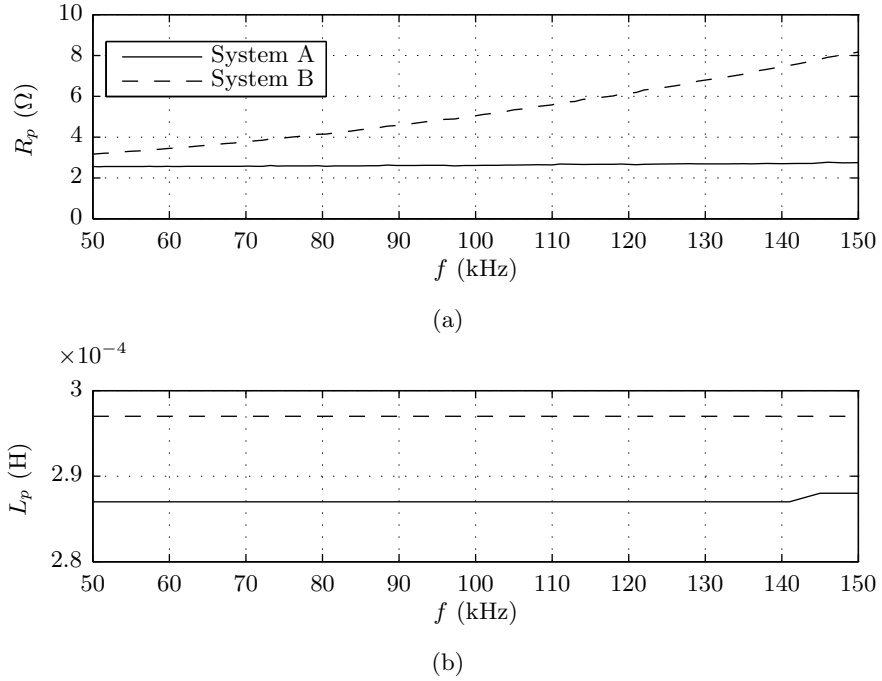

(a)

(b)

Figure 6.8: Primary coil: (a) resistance, and (b) inductance, for different frequency ranges measured for a coil surrounded by air and mounted on top of the plastic bonded permanent magnet array.

single primary coil in System B are measured as a function of the frequency of the alternating current through the coil. The measured values for both coils are shown in Fig. 6.8(a). The figure indicates that the resistance of a coil in System A remains constant along the entire frequency range. The resistance of a coil in System B becomes larger for an increasing frequency, and is equal to 4.62 Ω at a frequency of 90 kHz, an increase of 81%. The increase of the resistance for higher frequencies is caused by the eddy currents induced by the high-frequency magnetic field of the primary coils in the plastic bonded magnetic material. The measured self-inductance of a primary coil in System B is increased 3.6% compared to the self-inductance of a coil in System A, as shown in Fig. 6.8(b). The increase is lower than the 5% expected rise, as modeled for a solid layer of plastic bonded magnetic material in Section 5.3.1. The increase in self-inductance is caused by the relative permeability of the plastic bonded magnets.

The secondary coils have an average self-inductance of 98.43 μH with a variation below 0.5% with respect to all four coils. This average value differs by 3.4% with respect to the designed value of 95.18 μH. The average resistance of the secondary coils is equal to 608 mΩ, with a variation of maximum 3% among the four coils. The measured resistance is 19.4% higher than the designed resistance. The increase in resistance is caused by the leads of the secondary coils which are not taken into account in the model and enlarge the total length of a secondary coil with approximately two turns.

6.2.2 Mutual inductance

The mutual inductance is obtained by measuring the open-circuit voltage at the secondary side of the inductive coupling while a sinusoidal primary voltage is applied at the terminals of three adjacent primary coils. Based on the measured values, the mutual inductance is obtained by

$$M = \frac{V_s}{\omega I_p}, \tag{6.1}$$

where I_p is the primary current, ω is the frequency of the applied sinusoidal primary voltage, and V_s is the open circuit voltage. The mutual inductance is measured in System B at a frequency of 1 kHz such that the losses related to the permanent magnets can be neglected.

The mutual inductance is measured between a single secondary coil and primary coils, $p_1 - p_3$, in System B for a displacement of the center of the secondary coil along a quarter of primary coil p_2, i.e. the dashed area illustrated in Fig. 6.9. The measured values are shown in Fig. 6.10(a), and the difference with respect to the mutual inductances obtained with the magnetic model is shown in Fig. 6.10(b).

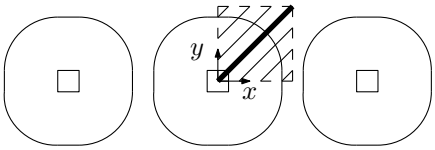

Figure 6.9: Illustration of three adjacent primary coils, indicating the measurement area on the middle coil.

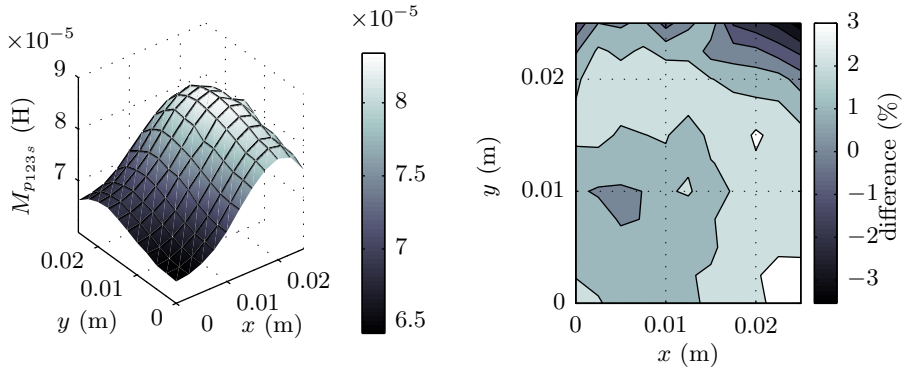

(a) (b)

Figure 6.10: Mutual inductance three primary coils, $p_1 - p_3$, and a single secondary coil in system B: (a) measured values, and (b) difference between the designed and the measured values.

An average difference of 1.9% is obtained between the predicted and measured values with a maximum difference of 3.5% when the center of the secondary coil is located in the corner of the primary coil. The measured mutual inductance has a variation of 23% which is similar to the predicted variation.

6.2.3 Impedance of the inductive coupling

The impedance of the inductive coupling seen from a single secondary coil is shown in Fig. 6.11 for a secondary coil aligned with the center of a set of three adjacent primary coils. The figure shows that magnetic resonance is obtained at a frequency of 87.3 kHz, which is lower than the designed resonance frequency of 90 kHz. This lower frequency is caused by a variation of the capacitance of the resonance capacitors and the inductances of the coils with respect to the ideal values obtained in the design. At resonance, the inductive coupling has an impedance of 2.1 Ω and a phase shift of 0 rad.

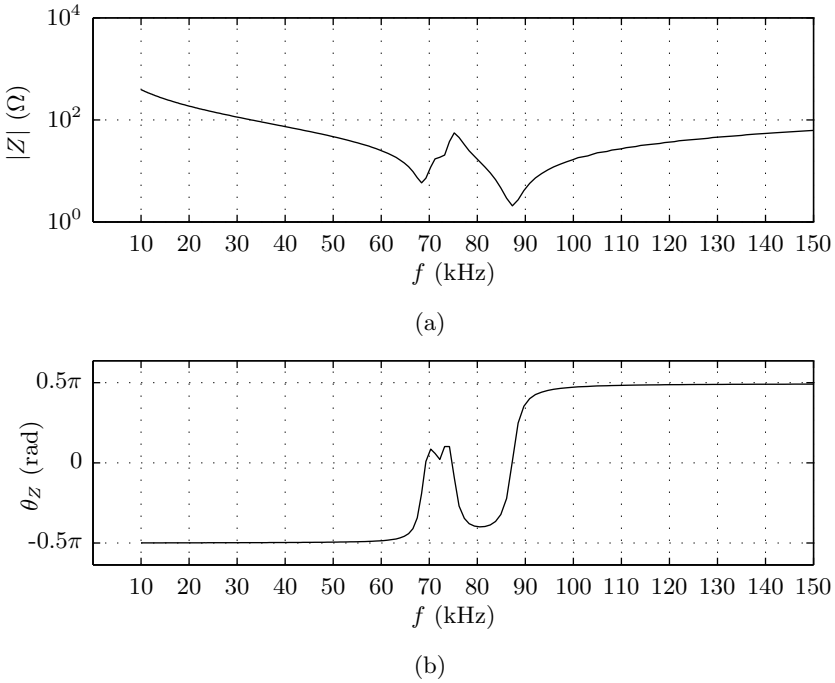

Figure 6.11: Impedance of a single secondary coil and three adjacent primary coils seen from the secondary side: (a) absolute value, and (b) angle.

6.3 Output power of the contactless energy transfer system

The output power of a CET system is obtained by measuring the voltage across the resistive load of the CET system. In this section, first, the output power values, measured on CET Systems A, B and C, are shown and compared to each other. Second, the output power values measured on the integrated CET system is presented for a single, two and four secondary coils for different velocities of the translator, respectively.

Table 6.1: Variation in output power for a diagonal movement along a quarter of a primary coil in System B.

frequency (kHz)	ΔP_{out} (%)
84.5	21.2
85.0	19.1
85.5	15.7
86.0	14.0
86.5	12.1
87.0	13.2
87.5	18.2
90.0	43.5

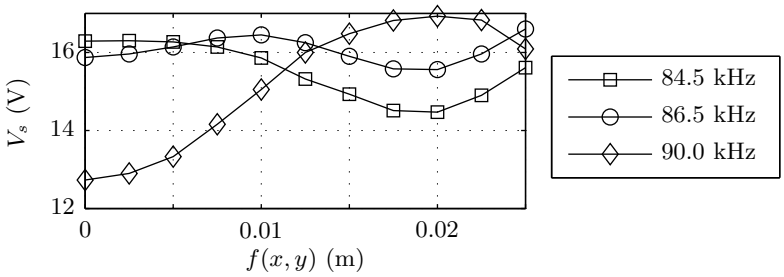

Figure 6.12: Output voltage for a diagonal movement, $f(x, y)$ as indicated in Fig. 6.9, along of a primary coil for an input voltage of 50 V and a load resistance of 9.8 Ω measured at the setup with eight primary coils for System B.

6.3.1 Output power of a single secondary coil

To minimize the variation in output power of a single secondary coil, the resonance frequency is modified with respect to the variation in realized and designed values of the resonance capacitors and the self-inductances of the coils. The output voltage of System B is measured for various frequencies of the primary voltage for a diagonal movement, $f(x, y)$, of the center of secondary coil, as indicated by the thick line in Fig. 6.9. The variation in output power for the different frequencies of the primary voltage is shown in Table 6.1. The variation in output power varies 43.5% at a frequency of 90 kHz and 12.1% at a frequency of 86.5 kHz. The measured output voltage along the diagonal movement is shown for three different frequencies in Fig. 6.12. The output voltage related to an operating frequency above resonance, for example, 90 kHz, increases when the center of the secondary coil is moving away from the center of the middle primary coil. A reverse pattern is considered for an operating frequency below the resonance frequency, for example, 84.5 kHz. Based on the obtained results, the remaining measurements are performed with an operating frequency of 86.5 kHz.

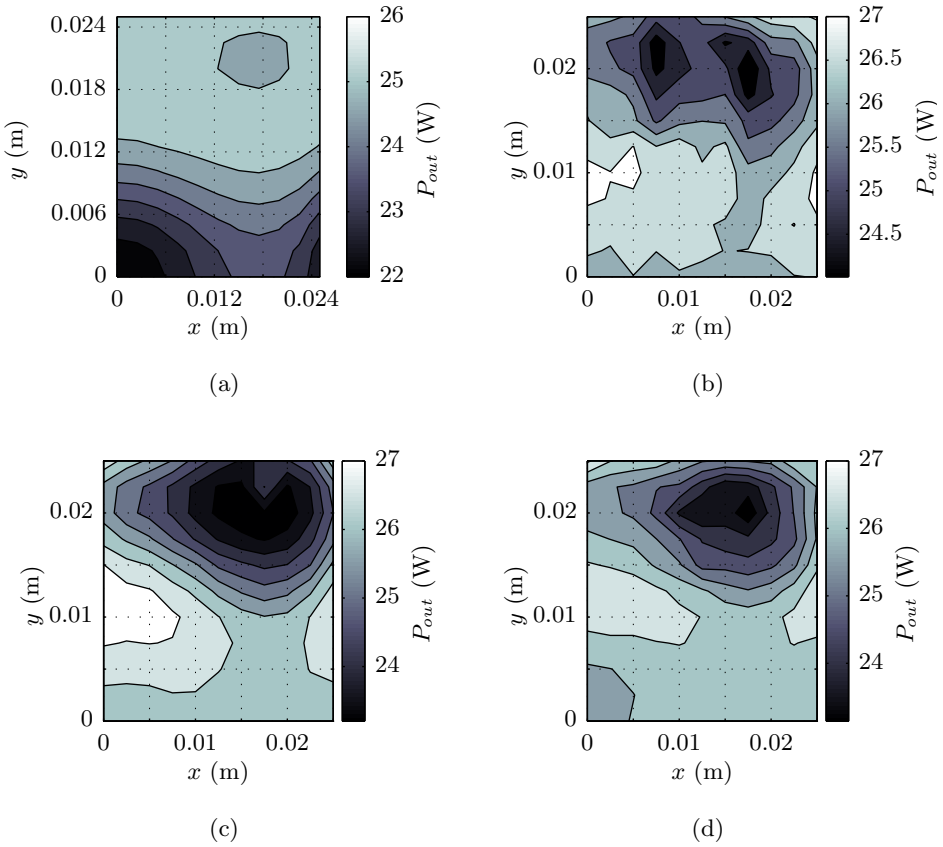

Figure 6.13: Output power of a CET system with three primary coils and a single secondary coil measured along a quarter of a primary coil for an input voltage of 50 V and a load resistance of 9.8 Ω: (a) design, (b) System A, (c) System B, and (d) System C.

The output power of a CET system with three primary and a single secondary coil is measured in Systems A - C, the integrated system, and compared to the designed performance. The measurements are performed with a dc-bus voltage of 50 V, a load resistance of 9.8 Ω, an airgap length equal to 1 mm, and for a displacement of the center of the secondary coil across a quarter of the middle primary coil, i.e. the dashed area in Fig. 6.9. The average output power, variation in output power and efficiency of the CET systems are listed in Table 6.2, and the output power as a function of position of the center of the secondary coil is shown in Figs. 6.13(a)-(d) for the different CET systems. The designed output power is equal to 24.5 W for an input of 50 V. The efficiency of the inductive coupling is predicted to be 91%. Combined with the efficiency of three dc-ac converters and

Table 6.2: Output power for a single secondary coil

	P_{ave} (W)	ΔP_{out} (%)	η_{ave} (%)
Design	24.5	13.1	80.4
System A	26.1	11.6	78.7
System B	25.7	15.4	71.5
System C	25.8	14.5	71.0
Integrated	14.6	13.5	59.4

a single ac-dc converter, which is equal to 88.4%, the efficiency of the designed system is equal to 80.4%.

In System A, an average output power equal to 26.1 W is achieved, which is 1.6 W higher compared to the predicted average output power of 24.5 W. The variation in output power in System A is 1.5 percentage point lower with respect the designed value of 13.1%. An efficiency equal to 78.7% is obtained between the dc-voltage source and the load resistance. Comparing Figs. 6.13(a) and (b) shows that the distribution of the output power differs between predicted and measured values, which is caused by the variation in the values of the resonance capacitors and coils with respect the ones predicted in the design.

In System B, in which the primary coils are mounted on top of the magnet array, an average output of 25.7 W is obtained, which is 0.4 W lower compared to System A. Furthermore, a variation in output power of 15.4% and an average efficiency of 71.5% is measured. Compared to System A, the variation in output power is increased with 3.8% and the efficiency is 7.2% decreased. The lower efficiency is caused by the induced eddy currents in the permanent magnet array.

In System C, a core of a linear motor is located next to the secondary coil. Comparable results with respect to System B are reached in System C. From the measurements it can be concluded that the iron-core of the linear motor does not influence the output power of the CET system, as predicted in Section 5.3.1.

The output power transferred between three primary and a single secondary coil of the CET system integrated in the planar motor is measured for a displacement of the secondary coil across the pitch of the middle of the three adjacent energized coils, and is shown in Fig. 6.14(a). An average output power of 14.6 W is obtained at an airgap of 1.5 mm. The average output power is 43% lower compared to the average output voltage of System C, and the efficiency is decreased to 59.4%. The lower output power and efficiency is caused by the eddy currents induced in the aluminum base-frame of the translator. The decrease in output power is larger than the expected 20% decrease, as modeled in Section 5.3.1. The variation in output power is equal to 13.5%, and, thereby, is similar to the variation in the other measurements and in agreement with the design. In the next section, the energy transfer of the integrated system is discussed in more detail.

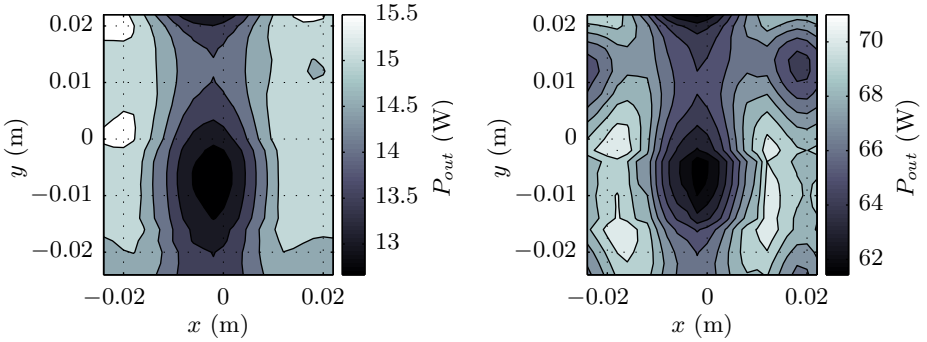

(a) (b)

Figure 6.14: Output power between three primary coils and a single secondary coil for the CET system integrated in the planar motor measured across the area of the middle primary coil for a dc-bus voltage of (a) 50 V and (b) 100 V.

Table 6.3: Output power of the integrated system

secondary coils	R_{load} (Ω)	P_{ave} (W)	ΔP_{out} (%)	η_{ave} (%)
1	9.80	65.7	13.5	65.7
2	19.2	99.9	31.2	63.6
4	39.2	230.3	32.1	71.2

6.3.2 Output power of the integrated contactless energy transfer system

The output power of the integrated CET system is measured for an energy transfer to a single, two and four secondary coils. The dc-bus voltage is set equal to 100 V, and the temperature of a primary coils reaches 50°C. The measured average output power, variation in output power and efficiencies of the different sets are listed in Table 6.3.

The output power of a single secondary coil is measured for a displacement of the center of a secondary coil across the pitch of a primary coil and is shown in Fig. 6.14(b). The average output power is equal to 65.7 W and a variation of 13.5% is obtained in this measurement. The efficiency is equal to 65.7%, and is increased with respect to a dc-bus voltage of 50 V. The output power of a single secondary coil is 21 W lower compared to the designed value of 86.9 W. The lower average output power is caused by the interaction of the magnetic fields of the CET system and the aluminum frame of the translator, as concluded in the previous section.

The output power of the energy transfer to two secondary coils in the planar motor

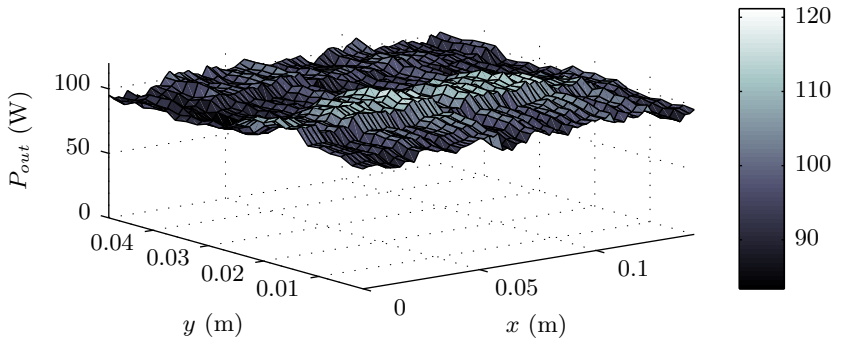

Figure 6.15: Output power of an energy transfer between to two secondary coils in the CET system integrated in the planar motor for an input voltage of 100 V and a load resistance of 19.6 Ω along a transition of the center of a secondary coil across an area of ($6\tau_p$,$2\tau_p$) in the xy-plane.

is measured for a transition of the center of a secondary coil across and area equal to ($6\tau_p$,$2\tau_p$) in the xy-plane. The measured output power is shown in Fig. 6.15. The energy transfer has an average output power of 99.9 W and a variation of 31.2% for an input voltage of 100 V and a load resistance equal to 19.2 Ω. Although a decreased variation in output power is predicted in Section 5.2.2 for two secondary coils, the variation in output power is increased compared to a single secondary coil. The increase is caused by the variation in component values of the resonance capacitors and self-inductances of the coils, which results in a different distribution of the output power compared to the designed one.

The output power of the entire CET system, i.e. four secondary coils, is measured for a transition of the center of a secondary coil across an area equal to ($4\tau_p$,$2\tau_p$) in the xy-plane, and is shown in Fig. 6.16. The output power has an average value of 230.3 W and a variation of 32.1% for an input voltage of 100 V and a load resistance of 39.2 Ω. The variation in output power is caused by the active switching between different sets of three adjacent primary coils and a single secondary coil, where each set has a different ideal resonance frequency due to the variation in component values of the resonance capacitors and self-inductances of the coils. The output voltage of the integrated system has an average value of 93 V and varies by 17.5% along the trajectory of the translator. The efficiency of the integrated CET system is equal to 71.2%.

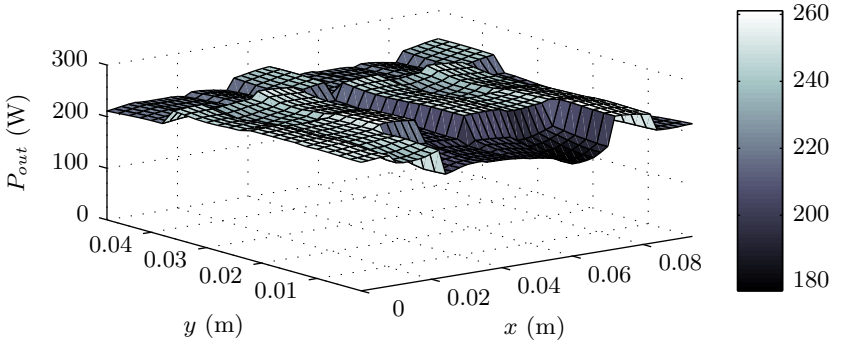

Figure 6.16: Output power of the complete CET system integrated in the planar motor for an input voltage of 100 V and a load resistance of 39.2 Ω along a transition of the center of a secondary coil an area of ($4\tau_p$,$2\tau_p$) in the xy-plane.

6.4 Effects of the system integration

In the previous section the output power of three primary coils and a single secondary coil is measured for various CET systems, in which successive components of the planar motor are added. In this section, the simultaneous operation of the planar motor and the integrated CET system are analyzed for the output power for different velocities of the translator, the primary current of the CET system, and the position error of the planar motor, respectively.

The output power of the CET system integrated in the planar motor is measured for various velocities of the translator for a movement in the x-direction. The measured output power is shown in Fig. 6.17 and is insensitive to the different velocities of the translator. A higher variation in output power is found during this measurement, because of fact that the current path in the de-energized coils is not interrupted by the ac-dc converter. In the previous stationary measurements, the interruption is realized by a physical disconnection of the de-energized coils.

The frequency of the current in the primary coils is an important parameter to establish a resonance in the CET system. Interaction between the primary coils and the magnetic fields of the linear motors could induce an EMF in the primary coils, which modifies the shape of the primary voltage and current. The current in a primary coil is measured for the cases in which the linear motors on the translator are activated and deactivated as is shown in Fig. 6.18. In both cases, an equal primary current is obtained, which alternates at a frequency of 86.5 kHz. From the measurement it can be concluded that the magnetic fields of the planar motor have no interaction with the primary side of the CET system.

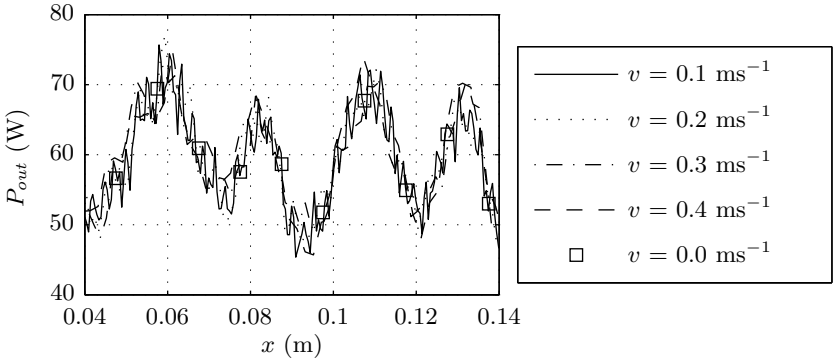

Figure 6.17: Output power of the complete CET system integrated in the planar motor for an input voltage of 100 V and a load resistance of 39.2 Ω for a movement of the translator in x-direction for various speeds of the translator.

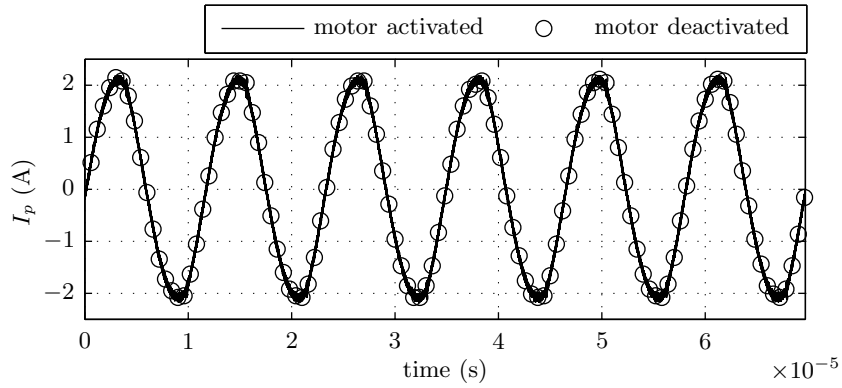

Figure 6.18: Current in a primary coil of the CET system with and without the planar motor activated.

The position accuracy of the planar motor is measured for a diagonal movement with an acceleration equal to 5 ms^{-2}, as shown by the second order motion profile in Fig. 6.19(a). The position error, for the x, y and z-coordinate with and without the CET system activated, is shown in Figs. 6.19(b)-(d), respectively. As follows from the presented results, the embedded CET system did not increase the position error and a similar error is obtained in the two measurements.

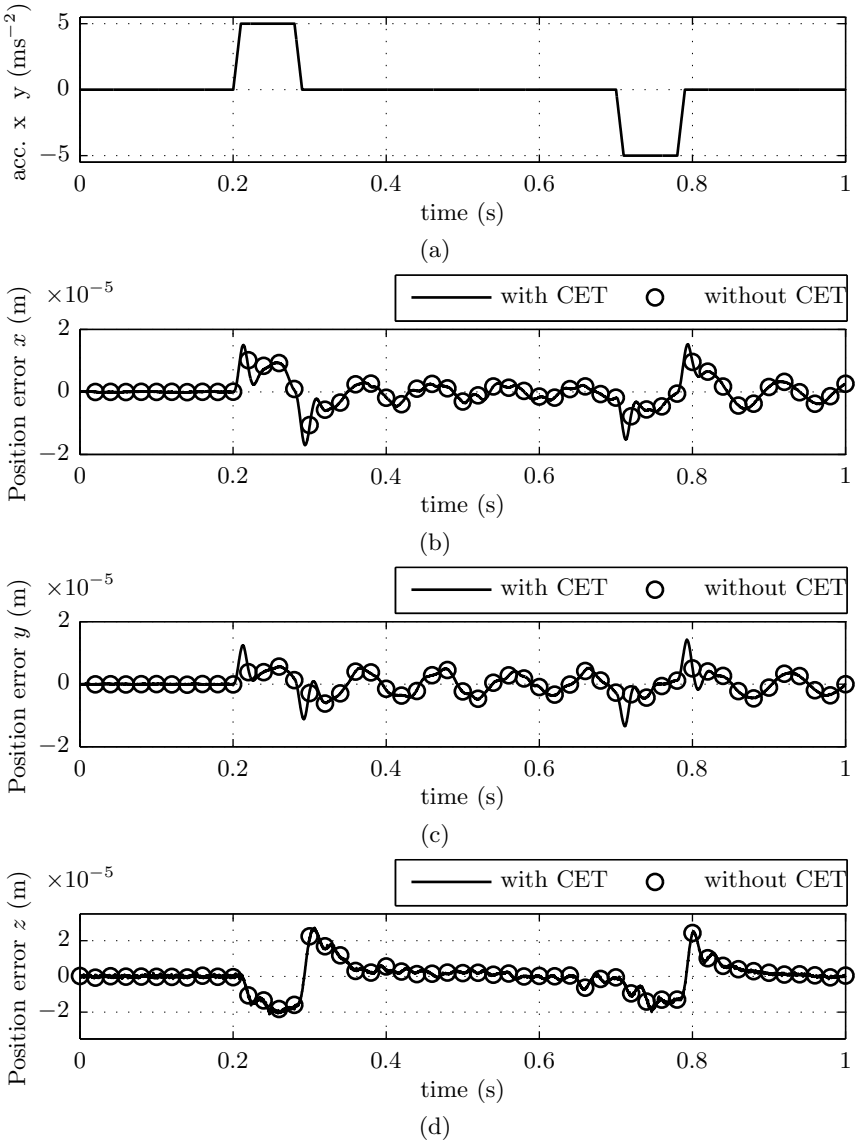

Figure 6.19: Position of the CET system for a diagonal movement: (a) velocity of the translator and position error with and without the CET system activated for (b) x-, (c) y-, and (d) z-direction.

Table 6.4: Output power compared to the initial design

	Predicted (%)	Measured (%)
Coils surrounded by air	100	106
Including segmented magnets	93.7	98.5
Including aluminum base-frame	75.0	63.4

6.5 Summary and conclusions

A prototype of the magnetically suspended planar motor with integrated contactless energy transfer system is manufactured. The primary side of the CET system contains 169 coils which are glued on top of the magnet array. The self-inductance of the primary coils differs by 5% from the designed value, and the resistance of the primary coils is increased by 81% because of the interaction between the magnetic fields of the primary coils and the plastic bonded permanent magnets. The mutual inductance between a single secondary coil and three adjacent primary coils has an average difference of 2% with respect to designed values for a displacement of a secondary coil along a quarter of the middle of the three adjacent primary coils.

The integrated CET system delivers an average output power of 230 W with a variation of 32% along the stroke of the translator for a dc-bus voltage of 100 V. The average output power of the integrated system is lower compared to a similar system with coils surrounded by air. The decrease is caused by the presence of the conducting materials in the neighborhood of the coils. Based on the measurements on the different CET systems with a single secondary coil, it can be concluded that the presence of plastic bonded magnets lowers the output power by 2% and reduces the efficiency by 9%. Furthermore, the linear motors do not influence both the output power and efficiency of the CET system. Finally, as expected in the previous chapter, the aluminum base-frame has a major influence on the performance of the CET system and decreases the output power by another 36%. Overall, as presented in Table 6.4, the measured average output power of the integrated system is 37% lower as the value of an identical CET system with coils surrounded by air.

The variation in output power of a single secondary coil is equal to 13.5%, and is similar to the designed value. However, the variation in the integrated CET system with four secondary coils is increased to 32%. This rise is caused by variation in component values of the resonance capacitors and self-inductances of the coils, which results in a different resonance frequency for each combination of three primary and a single secondary coils. As a result, the distribution of the output voltage as a function of the position of each secondary coil becomes different with respect to the designed distribution, and the resulting variation in output power of the CET system with four secondary coils increases.

The CET system has an average efficiency of 71% along the stroke of the moving translator. Furthermore, the energy transfer is independent of the velocity of the translator, and the position error of the planar motor is not influenced by the CET system.

7

Conclusions and recommendations

This thesis concerns the three-dimensional modeling, analysis, design and realization of a position-independent Contactless Energy Transfer (CET) system for the transfer of energy to an object with a planar movement. The presented three-dimensional analytical model of a CET system embeds a magnetic, electrical and thermal model, and is able to predict the performances of a CET system based on the geometrical parameters and physical variables of the system. To include the three-dimensional geometry of the coils in the magnetic model, the harmonic modeling technique has been extended. The position-independency of the CET system is realized in the magnetic domain, where a low variation in mutual inductance as function of the position of the moving object has been obtained by optimizing the dimensions of the primary and secondary coils. A CET system with a constant mutual inductance remains operating at resonance, and, therefore, an equal amount of energy is transferred at every position of the moving object. The theoretical analysis has been experimentally validated by measuring the performances of the designed and realized position-independent CET system integrated in a magnetically suspended planar motor.

This chapter summarizes the conclusions related to research objectives, as stated in Section 1.3. Furthermore, the scientific contributions of this thesis are addressed, and recommendations for future research are given.

7.1 Conclusions

7.1.1 Modeling framework

An accurate and fast electromagnetic field prediction is required to analyze the interaction between coils, permanent magnets, materials and their properties in electromagnetic devices. Various modeling methods have been discussed, and it has been found that the harmonic modeling technique is a suitable method to describe the magnetic fields and the interactions between coils, such as, for example, in an inductive coupling. The harmonic modeling technique is widely used to describe the magnetic fields in two-dimensional coordinate systems. However, as has been found in literature, the three-dimensional models based on the magnetic scalar potential are limited to permanent magnets as the sources of the magnetic fields. In this thesis, the three-dimensional harmonic modeling technique has been extended by formulating the three-dimensional magnetic vector potential, which allowed to include current-carrying coils as sources in the model, and, thereby, can be applied to an expanded range of electromagnetic problems.

The discussed harmonic model divides the three-dimensional magnetic problem into horizontal regions, which differ with respect to sources, materials properties and periodicity. For each type of region, an expression of the magnetic vector potential has been formulated, by solving the Poisson and Laplace equation using the method of separation of variables. Both the static and quasi-static field theories are taken into account. In this way, both regions with electrical conductive materials and the eddy-current reaction field have been included in the model. A solution for the magnetic flux density distribution has been obtained by solving the boundary conditions between the different regions. An equal number of unknown variables and boundary conditions has been obtained by reformulating the tangential boundary conditions of the magnetic field strength in terms of the magnetic scalar potential. Furthermore, the mode-matching technique has been formulated for a double Fourier series. The mode-matching technique has been applied to correlate the harmonic components of the three-dimensional magnetic fields among regions with different periodicities, which allowed to include slots and cavities in the geometry of the problems. The three-dimensional magnetic field model has been validated with various examples and is able to predict the magnetic flux density distribution around a coil with a maximum difference of 7%.

A coil is modeled by four current-carrying bars and the current density distribution of a coil has been expressed in a similar form as the magnetic vector potential. Three different configurations (overlapping rectangular bars, non-overlapping rectangular bars and trapezoidal bars, respectively) to position these current-carrying bars have been presented and validated with respect to the self-inductance of various coils. The validation of the electromagnetic parameters predicted by the harmonic model allows to select both configurations with four overlapping rectan-

gular bars and four trapezoidal bars as the best representative geometries of a coil. The unique combination of the formulation of the magnetic vector potential, the inclusion of electrical conductive material properties and structures with different periodicities, and the novel description of the current density distribution of a coil, allow to use the harmonic model to establish the relationship between self- and mutual inductance and the geometries of coils.

In addition, the magnetic model has been coupled with an electrical and thermal one in a modeling framework allowing to analyze a CET system in each of these domains. The developed modeling framework is adaptive to different ferromagnetic structures around a coil and various configurations of the primary coil array, such as numbers of energized primary coils and single or multi-layer coil arrays. Furthermore, both a linear and a planar displacement of the coils with respect to each other can be taken into account.

The three-dimensional magnetic field model, which has been derived in this thesis, is not limited to the calculation of inductances in CET systems only, and can be applied to an extensive class of three-dimensional electromagnetic problems.

7.1.2 Position-independent contactless energy transfer system

Contactless energy transfer (CET) systems, by means of an inductive coupling, are the solution to overcome the limitations of moving cables for the supply of electrical energy to objects with a planar movement. However, the relative movement of the primary and secondary coils with respect to each other, results in a varying mutual inductance, and, consequently, a position dependent output power. As a CET system replaces the moving cables, the position dependency of the output power should be minimized to obtain similar performance indexes as the wired energy transfer.

The CET system, as considered in this thesis, consists of a primary coil array with a limited height and a single or multiple secondary coil(s) with a planar movement across the primary side. The position dependency of such a CET system has been analyzed by comparing various topologies with respect to the variation in mutual inductance and average output power along the stroke of the moving secondary coil. The comparison of topologies has resulted in a set of design considerations for a position-independent CET system, which can be summarized as:

- A low variation in mutual inductance can be obtained if the dimensions of the secondary coil envelope the active set of primary coils.
- A ferromagnetic plate behind the primary and or secondary coil of the CET system increases the average output power of the system compared to coils

surrounded by air. Furthermore, the ferromagnetic plate has no influence on the variation in mutual inductance. Salient ferromagnetic structures create a predefined path for the magnetic flux which increases the variation in mutual inductance and, therefore, should be avoided.

- A comparison between different numbers of active primary coils has shown that the combination of a low variation in mutual inductance and a high output power density can be obtained in a system, in which energy is transferred between multiple adjacent energized primary coils and a single secondary coil.

- A single-layer primary coil array is beneficial for both the average output power and variation in mutual inductance. The height of a coil hardly influences the variation in mutual inductance, however a larger coil volume increases the amount of transferred energy.

- The phase angle of the primary current in sets of multiple adjacent energized primary coils has to be equal to each other. In this way, the secondary coil exhibits the largest variation in flux linkage and, as a result, the highest average output power can be obtained.

7.1.3 Design and realization of a contactless energy transfer system in a planar motor

The design and realization of a position-independent CET system, integrated in a magnetically suspended planar motor, have been presented in this thesis. The translator of the planar motor consists of four iron-cored linear motors, which suspend and propel the translator underneath a stationary checkerboard permanent magnet array [79]. The integrated CET system transfers energy between the stationary and the moving part of the planar motor. It can also supply a sufficient amount of energy to the linear motors and to the additional electronic devices on the translator.

The primary coil array of the CET system has been integrated in the airgap of the planar motor and mounted on the permanent magnet array. The coil array has a height equal to 1.5 mm, such that a mechanical clearance of 1 mm remains present in the airgap of the planar motor. Two geometrical topologies for the secondary side of the CET system have been analyzed, and a final design has been made consisting of four secondary coils. The secondary coils receive energy from four sets of three adjacent energized primary coils, where each primary coil is individually energized depending on the position of the translator. The dimensions of the coils, electrical parameters of the CET system, and the distance between the secondary coils have been optimized for a low variation in output power. The optimized design has an average output power equal to 363 W and a variation

of 5.6% along the stroke of the translator. Furthermore, for a proper integration of the CET system in the planar motor, additional attention has been given to electrical conductive materials in the neighborhood of the coils of the CET system. The presence of these materials has been reduced and, if possible, replaced by non-ferromagnetic and non-electrical conductive ones.

A prototype of the magnetically suspended planar motor with integrated CET system has been manufactured, and an output power of 230 W has been obtained which varies by 32% during dynamic operation of the translator. Although the electrical conductivity of the plastic bonded permanent magnets is low, the high-frequency magnetic fields of the primary coils introduce eddy-currents in the magnets which results in an increase of the primary coil resistance. As a result of the higher conduction losses and the applied electrical conductive materials in the construction of the translator, the obtained average output power is 37% lower compared to the design, and a system efficiency equal to 71% has been measured. Furthermore, a higher variation in output power has occurred which is caused by the variation in values of the resonance capacitors and self-inductances of the coils.

The CET system has been designed such that cross coupling between the planar motor and the energy transfer system has been avoided. The energy transfer is independent of the velocity of the translator. Furthermore, the simultaneous operation of the CET system and the planar motor has not increased the position error of the translator. Overall, the conducted research has succeeded in a unique system in which both a planar motor and a CET system are integrated with each other and operate simultaneously without physical interference.

7.2 Thesis contributions

The main contributions and accomplishments of the thesis can be summarized as

- *The extension of the three-dimensional harmonic modeling technique for the description of the magnetic fields around coils.* The ability to model three-dimensional magnetic fields around coils, including the presence of soft magnetic materials and complex geometrical structures, increases the functionality of the harmonic modeling technique.

- *The investigation of the position dependency of a contactless energy transfer system with a physical airgap between the stationary primary side and secondary side with a linear and a planar movement.* Various configurations of CET systems with a limited height have been compared to investigate the effect of the system parameters, and layout with respect to the variation in mutual inductance as a function of a relative displacement between the

primary and secondary coils. The analysis has resulted in a set of design considerations for a CET system with a low position dependency.

- *The design, realization and experimental validation of a position-independent contactless energy transfer system integrated in a magnetically suspended planar motor.* The research has resulted in a unique design and prototype in which both a planar motor and a CET system with a low variation in output power are integrated in each other. The CET system consists of a planar primary coil array with a limited height and four secondary coils. The planar motor and the CET system operate simultaneously without interfering each other.

7.3 Recommendations for future work

7.3.1 Modeling of the magnetic fields of coils wound around ferromagnetic teeth

The three-dimensional magnetic field model, presented in this thesis, does not allow to model coils which are wound around ferromagnetic teeth. This is not possible because the presented model is not able to correlate the spatial frequencies of different adjacent areas in a single region with each other. The mode-matching technique originates from the wave guide technique [87], in which it is possible to model both a T-junction and a rectangular cross junction [48]. If this technique could be translated to the harmonic modeling method and applied to model the magnetic fields of adjacent areas in a single region with different periodicities, the range of electromagnetic problems which can be solved increases and, as a result, improves the strength of the method.

7.3.2 Modeling of the eddy-current reaction field of segmented of conductive materials

The three-dimensional magnetic field model does not allow to include regions with segmented conductive material and to model the eddy-current reaction fields of these regions. In the presented harmonic model regions with electrical conductive materials have to be continuous, however in practice, the conductive material is often segmented, as for example, the checkerboard magnet array of the presented planar motor. Existing modeling approaches are either able to include the segmentation of the conductive material but neglect the eddy-current reaction field, or approach the electrical conductivity of the segmented structure as a value for a continuous structure while taking the eddy-current reaction field into account.

Summarized, the two approaches are not ideal since the segmentation decreases the path of the eddy-currents and modifies the eddy-current reaction field. If both the segmentation of the conductive material and the eddy-current reaction field are included in the magnetic model the accuracy of the prediction of the impedance of the coils is improved.

7.3.3 Dc-ac converter with self-tuning resonance frequency

This research has been focussed to the magnetic design of the CET system, and conventional power converters are applied at the primary and secondary side of the CET system. The experimental verification has shown that the position independency of the output power is sensitive for variations in the value of the resonance capacitors and self-inductances of the coils. These variations cause a shift in resonance frequency for each combination of three adjacent primary coils and a single secondary coil. A power converter with the ability of a self-tuning resonance frequency would assure that every combination of three primary coils and a secondary coil operates at magnetic resonance, which improves the position independency of the CET system.

7.3.4 Planar motor with multiple, wireless translators

The prototype of the magnetically suspended planar motor includes a single translator, while a complete wireless operation of the translator gives the opportunity to create a system in which multiple translators operate underneath a single stationary platform. To obtain a system with multiple translators, the position measurement system needs to be moved from the stationary part to the moving part, and both the ac-dc converters and the drivers of the motor has to be integrated on the translator. Furthermore, to avoid collisions, wireless communication with the translators should be obtained. A planar motor with multiple translators would result in a system in which translators can freely move around each other and travel at different velocities. Such a system can, for example, be used in the next generation of pick-and-place machines.

A

Circuit components of the power converters

The circuit components of the dc-ac converter, Fig. A.1, and the ac-dc converter, Fig. A.2, are listed in Table A.1 and A.2, respectively.

Table A.1: Circuit components of the half-bridge unipolar converter (Fig. A.1)

component	value	description
R_1, R_2, R_3, R_4	10 Ω	resistance
D_1, D_2	BAT48	small signal Schottky diode, $V_{RRM} = 40$ V
D_3	BAV21	small signal diode, $V_{RRM} = 250$ V
M_1, M_2	IRF640	fast switching power MOSFET
IC_1	IR2014	half-bridge MOSFET driver
C_1	220 μF	200 V aluminum electrolytic capacitor
C_2,C_4	100 nF	100 V metallized polyester film capacitor
C_3,C_5	1 μF	50 V metallized plastic film capacitor
C_7,C_8	33 nF	630 V polypropylene film capcacitor

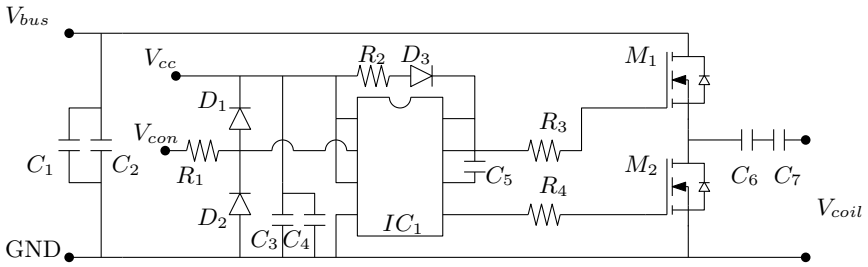

Figure A.1: Electric circuit of the half-bridge unipolar converter including primary series resonance capacitors.

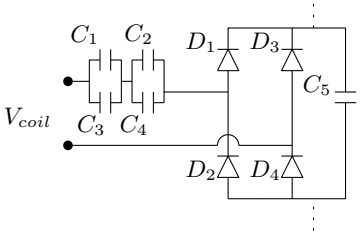

Figure A.2: Electric circuit of the ac-dc converter including the secondary resonance capacitors.

Table A.2: Circuit components of the dc-ac converter (Fig. A.2)

component	value	description
D_1-D_4	MBR10150	Schottky diode, V_{RRM} = 150 V
C_1-C_2	47 nF	1000 V polypropylene film capacitor
C_3-C_4	33 nF	1000 V polypropylene film capacitor
C_5	100 μF	100 V aluminum electrolytic capacitor

Bibliography

[1] Abdolkhani, A., Hu, A. P., Covic, G. A. and Moridnejad, M. [2013], 'Contactless slipring system based on rotating magnetic field principle for rotary applications', *Proc. IEEE Energy Conversion Congress and Exposition,* pp. 2566–2573.

[2] Adachi, S.-I., Sato, F. and Kikuchi, S. [1999], 'Consideration of contactless power station with selective excitation to moving robot', *IEEE Transactions on Magnetics* **35**(5), pp. 3583–3585.

[3] Akyel, C., Babic, S. I. and Mahmoudi, M.-M. [2009], 'Mutual inductance calculation for non-coaxial circular air coils with parallel axes', *PIER, Progress In Electromagnetics Research* **91**, pp. 287–301.

[4] Amrhein, M. and Krein, P. T. [2010], 'Induction machine modeling approach based on 3-D magnetic equivalent circuit framework', *IEEE Transactions on Energy Conversion* **25**(2), pp. 339–347.

[5] Appunn, R., Riemer, B. and Hameyer, K. [2011], 'Combination of a contactless power supply with an electromagnetic guiding for a vertical transportation system', *Proc. Int. Symp. on Linear Drives for Industrial Applications,* pp. 1–6.

[6] Babic, S. I. and Akyel, C. [2008], 'Calculating mutual inductance between circular coils with inclined axes in air', *IEEE Transactions on Magnetics* **44**(7), pp. 1743–1750.

[7] Barnard, J. M., Ferreira, J. A. and v. Wyk, J. D. [1995], 'Optimising sliding transformers for contactless power transmission systems', *Proc. IEEE Power Electronics Specialists Conference,* pp. 245–251.

[8] Barnard, J. M., Ferreira, J. A. and v. Wyk, J. D. [1997], 'Sliding transformers for linear contactless power delivery', *IEEE Transactions on Industrial Electronics* **44**(6), pp. 774–779.

[9] Barrire, O. d. l., Hlioui, S., Ben Ahmed, H., Gabsi, M. and LoBue, M. [2010], 'Three-dimensional analytical modeling of a permanent-magnet linear actuator with circular magnets', *IEEE Transactions on Magnetics* **46**(9), pp. 3608–3616.

[10] Binns, K. J., Lawrenson, P. J. and Trowbridge, C. W. [1992], *The Analytical and Numerical Solution of Electric and Magnetic Fields*, John Wiley & Sons, INC.

[11] Boeij, J. d., Lomonova, E. A., Duarte, J. and Vandenput, A. J. A. [2006], 'Contactless energy transfer to a moving actuator', *Proc. Industry Applications Conference,* pp. 2020–2025.

[12] Boeij, J. d., Lomonova, E. A., Duarte, J. and Vandenput, A. J. A. [2006], 'Contactless energy transfer to a moving load part II: Simulation of electrical and mechanical transient', *Proc. IEEE International Symposion of Industrial Electronics,* pp. 745–750.

[13] Boeij, J. d., Lomonova, E. A. and Vandenput, A. J. A. [2008], 'Contactless planar actuator with manipulator: a motion system without cables and physical contact between the mover and the fixed world', *Proc. IEEE IAS Annual Meeting,* pp. 1–8.

[14] Boroujeni, S. T., Milimonfared, J. and Ashabani, M. [2009], 'Design, prototyping, and analysis of a novel tubular permanent-magnet linear machine', *IEEE Transactions on Magnetics* **45**(12), pp. 5405–5413.

[15] Boys, J. T., Covic, G. A. and Green, A. W. [2000], 'Stability and control of inductively coupled power transfer systems', *IEE Proceedings Electric Power Applications* **147**(1), pp. 37–43.

[16] Brown, W. C. [1984], 'The history of power transmission by radio waves', *IEEE Transactions on Microwave Theory and Techniques* **MTT-32**(9), pp. 1230–1242.

[17] Budhia, M., Covic, G. A. and Boys, J. T. [2009], 'Design and optimisation of magnetic structures for lumped inductive power transfer systems', *Proc. IEEE Energy Conversion Congress and Exposition,* pp. 2081–2088.

[18] Budhia, M., Covic, G. A. and Boys, J. T. [2010], 'Magnetic design of a three-phase inductive power transfer system for roadway powered electric vehicles', *Proc. IEEE Vehicle Power and Propulsion Conference,* pp. 1–6.

[19] Casanova, J. J., Low, Z. N. and Lin, J. [2009], 'A loosely coupled planar wireless power system for multiple receivers', *IEEE Transactions on Industrial Electronics* **56**(8), pp. 3060–3068.

[20] Cathey, J. J. [2001], *Electric Machines, Analysis and Design Applying MATLAB*, 1st edn, McGrawHill.

[21] Chen, L., Liu, S., Zhou, Y. C. and Cui, T. J. [2013], 'An optimizable circuit structure for high-efficiency wireless power transfer', *IEEE Transactions on Industrial Electronics* **60**(1), pp. 339–349.

[22] Cho, H. S., Im, C. H. and Jung, H. K. [2001], 'Magnetic field analysis of 2d permanent-magnet planar motors', *IEEE Transactions on Magnetics* **37**(56), pp. 3762–3766.

[23] Dickinson, R. M. [2003], 'Wireless power transmission technology state of the art the first bill brown lecture', *Acta Astronautica* **53**(4), pp. 561–570.

[24] Elliott, G. A. J., Raabe, S., Covic, G. A. and Boys, J. T. [2010], 'Multiphase pickups for large lateral tolerance contactless power-transfer systems', *IEEE Transactions on Industrial Electronics* **57**(5), pp. 1590–1598.

[25] Fernandez, C., Prieto, R., Garcia, O. and Cobos, J. A. [2005], 'Coreless magnetic transformer design procedure', *Proc. Power Electronics Specialists Conference,* pp. 1–7.

[26] Fernandez, C., Zumel, P., Lazaro, A. and Barrado, A. [2007], 'A simple approach to design a contact-less power supply for a moving load', *Proc. Applied Power Electronics Conference,* pp. 1607–1612.

[27] Fotopoulou, K. and Flynn, B. W. [2011], 'Wireless power transfer in loosely coupled links: Coil misalignment model', *IEEE Transaction on Magnetics* **47**(2), pp. 416–430.

[28] Furlani, E. P. [2001], *Permanent Magnet and Electromechanical Devices*, Academic Press.

[29] Germano, P. and Jufer, M. [1997], 'Contactless power transmission: Frequency tuning by a maximum power tracking method', *Proc. European Conference on Power Electronics and Applications,* pp. 4.693–4.697.

[30] Gerrits, T., Krop, D. C. J., Encica, L. and Lomonova, E. A. [2011], 'Development of a linear position independent inductive energy transfer system', *Proc. International Machine and Drive Conference,* pp. 1–5.

[31] Gysen, B. L. J. [2011], Generalized Harmonic Modeling Technique for 2D Electromagnetic Problems, PhD thesis, Eindhoven University of Technology.

[32] Gysen, B. L. J., Meessen, K. J., Paulides, J. J. H. and Lomonova, E. A. [2010], 'General formulation of the electromagnetic field distribution in machines and devices using fourier analysis', *IEEE Transactions on Magnetics* **46**(1), pp. 39–52.

[33] Hague, B. [1929], *Electromagnetic Problems in Electrical Engineering*, Oxford University Press.

[34] Hahne, P., Dietz, R., Rieth, B. and Weiland, T. [1996], 'Determination of anisotropic equivalent conductivity of laminated cores for numerical computation', *IEEE Transactions on Magnetics* **12**(3), pp. 1184–1187.

[35] Hewitt, E. and Hewitt, R. E. [1979], 'The gibbs- wilbraham phenomenon: An episode in fourier analysis', *Archive for History of Exact Sciences* **21**(2), pp. 129–160.

[36] Ho, S. L., Wang, J., Fu, W. N. and Sun, M. [2011], 'A comparative study between novel witricity and traditional inductive magnetic coupling in wireless charging', *IEEE Transactions on Magnetics* **47**(5), pp. 1522–1525.

[37] Holman, J. P. [1986], *Heat Transfer*, McGraw-Hill Book Company.

[38] Horck, F. B. M. v. [2006], *A Treatise on Magnetics and Power Electronics*, Eindhoven University of Technology.

[39] Howey, D. A., Childs, P. R. N. and Holmes, A. S. [2012], 'Airgap convection in rotating electrical machines', *IEEE Transactions on Industrial Electronics* **59**(3), pp. 1367–1375.

[40] Huang, Y., Ge, B., Dong, J., Lin, H., Zhu, J. and Guo, Y. [2012], '3-D analytical modeling of no-load magnetic field of ironless axial flux permanent magnet machine', *IEEE Transactions on Magnetics* **48**(11), pp. 2929–2932.

[41] Hughes, A. L. [1934], 'Fundamental laws of photoelectricity', *Transactions of the American Institute of Electrical Engineers* **53**(8), pp. 1149–1153.

[42] Huh, J., Lee, S. W., Lee, W. Y., Cho, G. H. and Rim, C. T. [2011], 'Narrow-width inductive power transfer system for online electrical vehicles', *IEEE Transactions on Power Electronics* **26**(12), pp. 3666–3679.

[43] Hui, S. Y. R. and Ho, W. W. C. [2005], 'A new generation of universal contactless battery charging platform for portable consumer electronic equipment', *IEEE Transactions on Power Electronics* **20**(3), pp. 620–627.

[44] Im, C.-Y., Lim, J., Lee, D., Lee, S. and Jung, S.-Y. [2011], 'Analysis and design of contactless power transformer for high-speed maglev train', *Proc. Int. Symp. on Linear Drives for Industrial Applications,* pp. 1–4.

[45] Jackson, J. D. [1999], *Classical Electrodynamics*, John Wiley & Sons, INC.

[46] Jansen, J. W., Lierop, C. M. M. v., Lomonova, E. A. and Vandenput, A. J. A. [2007], 'Modeling of magnetically levitated planar actuators with moving magnets', *IEEE Transactions on Magnetics* **43**(1), pp. 15–25.

[47] Jansen, J. W., Smeets, J. P. C., Overboom, T. T., Rovers, J. M. M. and Lomonova, E. A. [2014], 'Overview of analytical models for the design of linear and planar motors', *IEEE Transactions on Magnetics* **50**(11), pp. 1–7.

[48] Jia, H., Yoshitomi, K. and Yasumoto, K. [1998], 'Rigorous analysis of the rectangular waveguide e-h cross junction using fourier transform technique', *Proc. International Conference on Microwave and Millimeter Wave Technology,* pp. 877 – 880.

[49] Jung, K. S. and Baek, Y. S. [2003], 'Precision stage using a non-contact planar actuator based on magnetic suspension technology', *Mechatronics* **13**, pp. 981–999.

[50] Jung, S., Lee, H., Song, C. S., Han, J.-H., Han, W.-K. and Jang, G. [2013], 'Optimal operation plan of the online electric vehicle system through establishment of a dc distribution system', *IEEE Transactions on Power Electronics* **28**(12), pp. 5878–5889.

[51] Kalhor, H. A. [1990], 'The degree of intelligence of the law of biot-savart', *IEEE Transactions on Education* **33**(4), pp. 365–366.

[52] Kano, Y., Kosaka, T. and Matsui, N. [2010], 'A simple nonlinear magnetic analysis for axial-flux permanent-magnet machines', *IEEE Transactions on Industrial Electronics* **57**(6), pp. 2124–2133.

[53] Kazmierkowski, M. P., Moradewicz, A., Duarte, J. L., Lomonowa, E. A. and Sonntag, C. L. W. [2011], *The Industrial Electronics Handbook - Power electronics and motor drives*, in [132], chapter Contactless Energy Transfer.

[54] Kazmierkowski, M. P. and Moradewicz, A. J. [2012], 'Contactless enery tranfer (CET) systems - a review', *Proc. 15th International Power Electronics and Motion Control Conference,* pp. Session 3–1 – Session 3–6.

[55] Kirtley, J. L., Tolikas, M., Lang, J. H., Ng, C. W. and Roche, R. [1998], 'Rotor loss models for high speed PM motor-generators', *Proc. International Conference on Electrical Machines,* pp. 1832–1837.

[56] Kissin, M. L. G., Boys, J. T. and Covic, G. A. [2009], 'Interphase mutual inductance in polyphase inductive power transfer systems', *IEEE Transactions on Industrial Electronics* **56**(7), pp. 2393–2400.

[57] Kline, M., Izyumin, I., Boser, B. and Sanders, S. [2011], 'Capacitive power transfer for contactless charging', *Proc. 26th Annual IEEE Applied Power Electronics Conference and Exposition,* pp. 1398–1404.

[58] Krop, D. C. J., Jansen, J. W. and Lomonova, E. A. [2011], 'Analysis and design of a tubular linear pm motor with integrated contactless energy transfer', *Proc. 37th Annual Conference on IEEE Industrial Electronics Society,* pp. 1752–1757.

[59] Krop, D. C. J., Jansen, J. W. and Lomonova, E. A. [2013], 'Decoupled modeling in a multifrequency domain: Integration of actuation and power transfer in one device', *IEEE Transactions on Magnetics* **49**(6), pp. 3009–3019.

[60] Krop, D. C. J., Lomonova, E. A., Jansen, J. W. and Paulides, J. J. H. [2009], 'A study on the integration of contactless energy transfer in the end teeth of a pm synchronous linear motor', *Journal of Applied Physics* **105**(7), pp. 07F115–1/3.

[61] Lastowiecki, J. and Staszewski, P. [2006], 'Sliding transformer with long magnetic circuit for contactless electrical energy delivery to mobile receivers', *IEEE Transaction on Industrial Electronics* **53**(6), pp. 1943–1948.

[62] Lee, J. Y., Lee, I. J., Kim, J. W., Chang, J. H., Kang, D. H., Chung, S. U. and Hong, J. P. [2007], 'Contactless power transfer system combined with linear electric machine', *Proc. Int. Conf. on Electrical Machines and Systems,* pp. 1544–1548.

[63] Lee, K., Pantic, Z. and Lukic, S. [2014], 'Reflexive field containment in dynamic inductive power transfer systems', *IEEE Transactions on Power Electronics* **29**(9), pp. 4592–4602.

[64] Lenders, W. L. L. [1961/62], 'The orthocyclic method of coil winding', *Philips Technical Review* **23**(12), pp. 365–379.

[65] Liu, Z. J. and Li, J. T. [2007], 'Analytical solution of air-gap field in permanent-magnet motors taking into account the effect of pole transition over slots', *IEEE Transactions on Magnetics* **43**(10), pp. 3872–3883.

[66] Lotfi, A. W. and Lee, F. C. [1993], 'A high frequency model for litz wire for switchmode magnetics', *Proc. IEEE Industry Applications Society Annual Meeting* **2**, pp. 1169–1175.

[67] Lui, X. and Hui, S. Y. [2008], 'Optimal design of a hybrid winding structure for planar contactless battery charching platform', *IEEE Transactions on Power Electronics* **23**(1), pp. 455–463.

[68] Matsumoto, H., Neba, Y., Ishizaka, K. and Itoh, R. [2011], 'Model for a three-phase contactless power transfer system', *IEEE Transactions on Power Electronics* **26**(9), pp. 2676–2686.

[69] Matsumoto, H., Neba, Y., Ishizaka, K. and Itoh, R. [2012], 'Comparison of characteristics on planar contactless power transfer systems', *IEEE Transactions on Power Electronics* **27**(6), pp. 2980–2993.

[70] McSpadden, J. O. and Mankins, J. C. [2002], 'Space solar power programms and microwave wireless power transmission technology', *IEEE microwave magazine,* pp. 46–57.

[71] Mecke, R. [2001], 'Contactless inductive energy transmission systems with large air gap', *Proc. European Conference on Power Electronics and Applications,* pp. 1–10.

[72] Meessen, K. J. [2012], Electromagnetic fields and interactions in 3D cylindrical structures: modeling and application, PhD thesis, Eindhoven University of Technology.

[73] Meessen, K. J., Gysen, B. L. J., Paulides, J. J. H. and Lomonova, E. A. [2010], 'Three-dimensional magnetic field modeling of a cylindrical halbach array', *IEEE Transactions on Magnetics* **46**(6), pp. 1733–1736.

[74] Mellor, P. H., Roberts, D. and Turner, D. R. [1991], 'Lumped parameter thermal model for electrical machines of tefc design', *IEE Proceedings-B* **138**(5), pp. 205–218.

[75] Mirzaei, M., Binder, A. and Deak, C. [2010], '3D analysis of circumferential and axial segmentation effect on magnet eddy current losses in permanent magnet synchronous machines with concentrated windings', *Proc. XIX International Conference on Electrical Machines,* pp. 1–6.

[76] Moradewicz, A. J. [2008], Contactless Energy Transmission System with Rotatable Transformer - Modeling, Analyze and Design, PhD thesis, Electrotechnical Institute, Warsaw, Poland.

[77] Moradewicz, A. J. and Kazmierkowski, M. P. [2010], 'Contactless energy transfer system with FPGA-controlled resonant converter', *IEEE Transactions on Industrial Electronics* **57**(9), pp. 3181–3190.

[78] Neto, T. R. F. and Mutschler, P. [2011], 'Short primary linear synchronous motor drive with an ultracapacitor regenerative braking system for material handling and processing', *Proc. Int. Symp. on Linear Drives for Industrial Applications,* pp. 1–6.

[79] Overboom, T. T. [2015], Electromagnetic levitation and propulsion, PhD thesis, Eindhoven University of Technology.

[80] Overboom, T. T., Smeets, J. P. C., Jansen, J. W. and Lomonova, E. A. [2011], 'Topology comparison for a magnetically suspended ceiling actuator', *Proc. IEEE International Electric Machine & Drives Conference,* pp. 289–294.

[81] Overboom, T. T., Smeets, J. P. C., Jansen, J. W. and Lomonova, E. A. [2012], 'Design and operating principles of a magnetically suspended ceiling actuator with fail-safe operation', *Proc. 12th International Conference of the European Society for Precision Engineering and Nanotechnology,* pp. 539–542.

[82] Overboom, T. T., Smeets, J. P. C., Jansen, J. W. and Lomonova, E. A. [2012], 'Semi-analytical calculation of the torque in a linear permanent magnet motor with finite stator length', *Proc. IEEE International Magnetics Conference,* pp. 1–1.

[83] Overboom, T. T., Smeets, J. P. C., Jansen, J. W. and Lomonova, E. A. [2012], 'Semianalytical calculation of the torque in a linear permanent-magnet motor with finite yoke length', *IEEE Transactions on Magnetics* **48**(11), pp. 3575–3578.

[84] Overboom, T. T., Smeets, J. P. C., Jansen, J. W. and Lomonova, E. A. [2012], 'Torque decomposition and control in an iron core linear permanent magnet motor', *Proc. IEEE Energy Conversion Congress and Exposition,* pp. 2662–2669.

[85] Overboom, T. T., Smeets, J. P. C., Jansen, J. W. and Lomonova, E. A. [2013], 'Design and control of a magnetically suspended ceiling actuator with infinite planar stroke', *Applied Mechanics and Materials* **416-417**, pp. 492–502.

[86] Paris, D. T. and Hund, F. K. [1969], *Basic Electromagnetic Theory*, McGraw-Hill Book Company, INC.

[87] Park, K. H., and Eom, H. J. [1993], 'An analytic series solution for h-plane waveguide t-junction', *IEEE Microwave and Guided Wave Letters* **3**(4), pp. 104–106.

[88] Pijl, F. A. v. d., Castilla, M. and Bauer, P. [2013], 'Adaptive sliding-mode control for a multiple-user inductive power transfer system without need for communication', *IEEE Transactions on Industrial Electronics* **60**(1), pp. 271–279.

[89] Pramanik, A. [1975], 'Extension of roth's method to three-dimensional multi-region eddy current problems', *IEEE Transactions on Magnetics* **11**(5), pp. 1526–1528.

[90] Raible, D. E., Taysir, D. D. and Nayfeh, H. [2011], 'Optical frequency optimization of a high intensity laser power beaming system utilizing vmj photovoltaic cells', *Proc. International Conference on Space Optical Systems and Applications,* pp. 232–238.

[91] Reece, A. B. J. and Preston, T. W. [2000], *Finite Element Methods in Electrical Power Engineering*, Oxford University Press.

[92] Robertson, B. L. and Terry, I. A. [1929], 'Analytical determincation of magnetic fields, simple cases of conductors in slots', *Transactions of the American Institute of Electrical Engineers* **48**(4), pp. 1242–1259.

[93] Roes, M. G. L., Duarte, J. L., Hendrix, M. A. M. and Lomonova, E. A. [2013], 'Acoustic energy tranfer: A review', *IEEE Transactions on Industrial Electronics* **60**(1), pp. 242–248.

[94] Roters, H. C. [1955], *Electromagnetic Devices*, 6th edn, Wiley, Chichester.

[95] Ruehli, A. E. [1972], 'Inductance calculations in a complex integrated circuit enviroment', *IBM Journal of Research and Development* **16**(5), pp. 470–481.

[96] Ruviaro, M., Rncos, F., Sadowski, N. and Borges, I. M. [2012], 'Analysis and test results of a brushless doubly fed induction machine with rotary transformer', *IEEE Transactions on Industrial Electronics* **59**(6), pp. 2670–2677.

[97] Sahai, A. and Graham, D. [2011], 'Optical wireless power transmission at long wavelengths', *Proc. International Conference on Space Optical Systems and Applications,* pp. 164–170.

[98] Sallan, J., Villa, J. L. and and. J. F. Sanz, A. L. [2009], 'Optimal design of ICPT systems applied to electric vehicle battery charge', *IEEE Transactions on Industrial Electronics* **56**(6), pp. 2140–2148.

[99] Sato, F., Murakami, J., Matsuki, H., Kikuchi, S., Harakawa, K. and Satoh, T. [1996], 'Stable energy transmission to moving oads utilizing new CLPS', *IEEE Transactions on Magnetics* **32**(5), pp. 5034–5036.

[100] Schneider, D. [2010], 'Electrons unplugged', *IEEE Spectrum,* pp. 35–39.

[101] Sergeant, P. and Van den Bossche, A. [2008], 'Inductive coupler for contactless power transmission', *IET Electric Power Applications* **2**(1), pp. 1–7.

[102] Sikora, R., Purczunski, J., Lipinski, W. and Gramz, M. [1978], 'Use of variational methods to the eddy currents calculation in thin conducting plates', *IEEE Transactions on Magnetics* **MAG-14**(5), pp. 383–385.

[103] Sinha, D., Sadhu, P. K., Pal, N. and Bandyopadhyay, A. [2010], 'Computation of the inductance and ac resistance of a twisted litzwire for high frequency induction cooker', *Proc. International Conference on Industrial Electronics, Control and Robotics,* pp. 85–90.

[104] Smeets, J. P. C., Krop, D. C. J., Jansen, J. W., Hendrix, M. A. M. and Lomonova, E. A. [2010], 'Optimal design of a pot core rotating transformer.', *Proc. IEEE Energy Conversion Congress and Exposition,* pp. 4390–4397.

[105] Smeets, J. P. C., Overboom, T. T., Jansen, J. W. and Lomonova, E. A. [2011], 'Three-dimensional magnetic field modeling for coupling calculation between air-cored rectangular coils', *IEEE Transactions on Magnetics* **47**(10), pp. 2935–2938.

[106] Smeets, J. P. C., Overboom, T. T., Jansen, J. W. and Lomonova, E. A. [2011], 'Three-dimensional magnetic field modeling for coupling calculation between air-cored rectangular coils', *Proc. of the INTERMAG 2011 Conference,* pp. 1–1.

[107] Smeets, J. P. C., Overboom, T. T., Jansen, J. W. and Lomonova, E. A. [2012], 'Integration of an inductive position sensor and a contactless energy transfer system', *Proc. of the 2012 XXth International Conference on Electrical Machines,* pp. 1749–1753.

[108] Smeets, J. P. C., Overboom, T. T., Jansen, J. W. and Lomonova, E. A. [2012], 'Mode-matching technique applied to three-dimensional magnetic field modeling', *IEEE Transactions on Magnetics* **48**(11), pp. 3383–3386.

[109] Smeets, J. P. C., Overboom, T. T., Jansen, J. W. and Lomonova, E. A. [2012], 'Three-dimensional mode-matching applied to three-dimensional magnetic field modeling', *Proc. of the INTERMAG 2012 Conference,* pp. 1–1.

[110] Smeets, J. P. C., Overboom, T. T., Jansen, J. W. and Lomonova, E. A. [2013], 'Comparison of position independent contactless energy transfer systems', *IEEE Transactions on Power Electronics* **28**(4), pp. 2059–2067.

[111] Smeets, J. P. C., Overboom, T. T., Jansen, J. W. and Lomonova, E. A. [2013], 'Modeling framework for contactless energy transfer systems for linear actuators', *IEEE Transactions on Industrial Electronics* **60**(1), pp. 391–399.

[112] Smeets, J. P. C., Overboom, T. T., Jansen, J. W. and Lomonova, E. A. [2013], 'Three-dimensional analytical modeling technique of electromagnetic fields of air-cored coils surrounded by different ferromagnetic boundaries', *IEEE Transactions on Magnetics* **49**(12), pp. 5698–5708.

[113] Smeets, J. P. C., Overboom, T. T., Jansen, J. W. and Lomonova, E. A. [2014], 'Inductance calculation nearby conducting material', *IEEE Transactions on Magnetics* **50**(11), pp. 1–4.

[114] Smeets, J. P. C., Overboom, T. T., Jansen, J. W. and Lomonova, E. A. [2014], 'Inductance modeling nearby conducting material', *Proc. of the INTERMAG 2014 Conference,* pp. 1–1.

[115] Smeets, J. P. C., Soulard, J. and Lomonova, E. A. [2010], 'Thermal analysis of a winding turn-to-turn fault in pm synchronous machine.', *Proc. 19th International Conference on Electrical Machines,* pp. 1–6.

[116] Smythe, W. R. [1968], *Static and Dynamic Electricity*, 3rd edn, McGraw-Hill.

[117] Sonntag, C. L. W. [2010], Contactless Energy Transfer Platform using Air-Cored Planar Inductors, PhD thesis, Eindhoven University of Technology.

[118] Sonntag, C. L. W., Duarte, J. L. and Pemen, A. J. M. [2008], 'Variable-phase contactless energy transfer desktop part I: Design', *Proc. Int. Conf. Electrical Machines and Systems,* pp. 4460–4465.

[119] Tang, X. and Sullivan, C. R. [2004], 'Optimization of stranded-wire windings and comparison with litz wire on the basis of cost and loss', *Proc. IEEE Power Electronics Specialists Conference,* pp. 854–860.

[120] Tesla, N. and Childress, D. H. [1993], *The fantastic inventions of Nikola Tesla*, Adventures Unlimited Press.

[121] Theodoridis, M. P. [2012], 'Effective capacitive power transfer', *IEEE Transactions on Power Electronics* **27**(12), pp. 4906–4913.

[122] Theodoulidis, T. P. and Kriezis, E. E. [2002], 'Impedance evaluation of rectangular coils for eddy current testing of planar media', *NDT&E International* **35**, pp. 407–414.

[123] Urankar, L. K. [1980], 'Vector potential and magnetic field of current-carrying finite arc segment in analytical form, part I: Filament approximation', *IEEE Transactions on Magnetics* **16**(5), pp. 1283–1288.

[124] Urankar, L. K. [1982], 'Vector potential and magnetic field of current-carrying finite arc segment in analytical form, part II: Thin sheet approximation', *IEEE Transactions on Magnetics* **18**(3), pp. 911–917.

[125] Urankar, L. K. [1982], 'Vector potential and magnetic field of current-carrying finite arc segment in analytical form, part III: Exact computation for rectangular cross section', *IEEE Transactions on Magnetics* **18**(6), pp. 1860–1867.

[126] Urankar, L. K. [1984], 'Vector potential and magnetic field of current-carrying finite arc segment in analytical form, part IV: General three-dimensional current density', *IEEE Transactions on Magnetics* **20**(6), pp. 2145–2150.

[127] Valtchev, S. S., Borges, B., Brandisky, K. and Klaassens, J. B. [2009], 'Resonant contactless energy transferwith improved efficiency', *IEEE Transactions on Power Electronics* **24**(3), pp. 685–699.

[128] Valtchev, S. S. and Klaassens, J. B. [1990], 'Efficient resonant power conversion', *IEEE Transactions on Industrial Electronics* **37**(6), pp. 490–495.

[129] Vrijsen, N. H., Jansen, J. W. and Lomonova, E. A. [2014], 'Prediction of magnetic hysteresis in the force of a pre-biased e-core reluctance actuator', *IEEE Transactions on Industry Applications* **50**(4), pp. 2476–2484.

[130] Wang, C.-S., Covic, G. A. and Stielau, O. H. [2004], 'Power transfer capability and bifurcation phenomena of loosly coupled inductive power transfer systems', *IEEE Transactions on Industrial Electronics* **51**(1), pp. 148–157.

[131] Wang, C.-S., Stielau, O. H. and Covic, G. A. [2005], 'Design considerations for a contactless electric vehicle battery charger', *IEEE Transactions on Industrial Electronics* **52**(5), pp. 1308–1313.

[132] Wilamowski, B. M. and Irwin, J. D., eds [2011], *The Industrial Electronics Handbook - Power electronics and motor drives*, Taylor and Francis Group, LLC.

[133] Zakrzewski, K. and Lukaniszyn, M. [1987], '3-D reactance calculation of air-core coils with magnetic screening', *Proc. of an International Symposium on Electromagnetic Fields in Electrical Engineering,* pp. 89–92.

[134] Zhang, Y., Yang, Z., Yu, M., Lu, K., Ye, Y. and Liu, X. [2011], 'Analysis and design of double-sided air core linear servo motor with trapezoidal permanent magnets', *IEEE Transactions on Magnetics* **47**(10), pp. 3236–3239.

[135] Zhong, W. X., Lui, X. and Hui, S. Y. [2010], 'Analysis on a single-layer winding array structure for contactless battery charging systems with free-positioning and localized charhing features', *Proc. IEEE Energy Conversion Congress and Exposition,* pp. 658–665.

[136] Zhu, Z. Q. and Howe, D. [1993], 'Instantaneous magnetic field distribution in brushless permanent magnet dc motors part II: Armature-reaction field', *IEEE Transactions on Magnetics* **29**(1), pp. 136–142.

[137] Zhu, Z. Q., Ng, K., Schofield, N. and Howe, D. [2004], 'Improved analytical modelling of rotor eddy current loss in brushless machines equipped with surface mounted permanent magnets', *IEEE. Proc. Electr. Power Appl.* **151**(6), pp. 641–650.

Samenvatting

Contactless Transfer of Energy

3D Modeling and Design of a Position-Independent
Inductive Coupling Integrated in a Planar Motor

De energievoorziening naar het bewegende deel van een lineaire of planaire motor wordt meestal uitgevoerd door middel meebewegende kabels, die de prestaties van de motor beperken. Om deze beperkingen te overwinnen, kunnen de kabels worden vervangen door een draadloos energieoverdracht systeem, waarbij energie wordt overgedragen door middel van een inductieve koppeling, m.a.w. een transformator met een luchtspleet tussen de primaire en secundaire spoel. Een draadloos energieoverdracht systeem met één of meerdere secundaire spoelen met een planaire beweging, heeft typisch een matrix van primaire spoelen. Alhoewel er langs de gehele slag van de bewegende secondaire spoel(en) energie kan worden overgedragen, is de hoeveelheid overgedragen energie afhankelijk van de positie van de secondaire spoel. De variatie van de mutuele inductie tussen de primaire en secondaire spoel(en) is een maat voor de positie afhankelijkheid van een draadloos energieoverdracht systeem. Dit proefschrift beschrijft de driedimensionale modellering en analyse van een positie-onafhankelijke draadloos energieoverdracht systeem. De kennis is toegepast in het ontwerp en realisatie van een magnetisch gelagerde planaire motor met geïntegreerd draadloos energieoverdracht systeem

Een belangrijke bijdrage in dit werk is de uitbreiding van de harmonische modelleringsmethode door de formulering van de driedimensionale magnetische vectorpotentiaal voor de statische en quasi-statische veldtheorie, waardoor het mogelijk is om de magnetische velden van driedimensionale stroom voerende spoelen te beschrijven. De stroomdichtheid van een spoel wordt gemodelleerd met behulp van vier rechthoekige segmenten. Eigenschappen van elektrische geleidende materialen, de permeabiliteit en het magnetisch veld van wervelstromen zijn opgenomen in het model. Daarnaast is de correlatie techniek tussen magnetische velden met een verschillende periodiciteit uitgebreid waardoor sleuven en holtes in platen met

een oneindige permeabiliteit kunnen worden meegenomen in het model. De verdeling van de magnetische flux dichtheid, zelf en mutuele inducties van spoelen zijn berekend met het harmonische model en deze zijn gevalideerd met de eindige elementen methode en metingen. De verschillen tussen de verschillende methodes zijn kleiner dan 7%.

Het magnetische model is gekoppeld met een elektrisch en thermisch model in een modellerings-raamwerk, die het toelaat om het draadloos energieoverdracht systeem in elk van deze domeinen te analyseren. Het ontwikkelde raamwerk is adaptief voor verschillende ferromagnetische structuren rond de spoelen, en voor verschillende configuraties van de matrix van primaire spoelen, zoals het aantal actieve als het aantal lagen primaire spoelen in de matrix. Verder kan zowel een lineaire als een planaire verplaatsing van de spoelen ten opzichte van elkaar in het modellerings-raamwerk worden meegenomen.

Een tweede belangrijke bijdrage is de analyse van de positie afhankelijkheid van een draadloos energieoverdracht system wat bestaat uit een matrix van vlakke primaire spoelen en één secondaire spoel. De analyse is uitgevoerd door het vergelijken van de variatie in de mutuele inductie en het gemiddelde uitgangsvermogen over de slag van de bewegende secondaire spoel voor verschillende topologieën. Een generieke oplossing voor een draadloos energieoverdracht systeem met een lage variatie in mutuele inductie is verkregen in een systeem met een niet elektrisch geleidende en tandeloze structuur rondom de spoelen, waarbij de dimensies van de secondaire spoel de set van meerdere actieve primaire spoelen omhullen, welke allen energie overdragen en gelegen zijn in een matrix met een enkele laag spoelen. Het gewenste uitgangsvermogen wordt bereikt door het optimaliseren van de elektrische parameters van de inductieve koppeling, en kan gemaximaliseerd worden totdat het thermische limiet van het systeem bereikt wordt.

Het modellerings-raamwerk en het verkregen generieke ontwerp voor een systeem met een lage variatie in mutuele inductie is gebruikt bij het ontwerp van een draadloos energieoverdracht systeem dat volledig geïntegreerd is in een nieuw type planaire motor waarin het bewegende deel magnetische opgehangen wordt onder het statische gedeelte van de motor. De matrix van primaire spoelen bevindt zich in de luchtspleet van de motor en vier secondaire spoelen bevinden zich op het bewegende deel. Elk van deze secondaire spoelen ontvangt energie uit drie aangrenzende primaire spoelen, waarbij de primaire spoelen dynamisch worden geactiveerd afhankelijk van de positie van de secondaire spoelen. Een prototype van dit unieke en complexe system is gebouwd. Het geïntegreerde draadloos energieoverdracht system levert een gemiddeld vermogen van 230 W aan het bewegende deel van de planaire motor. Het uitgangsvermogen heeft een variatie van 32% en een efficiëntie van 71% is gehaald over de slag van de bewegende secondaire spoelen.

Kortom, dit proefschrift presenteert een kant-en-klare theorie, een complete set van vergelijkingen, en een magnetisch, elektrisch en thermisch model, die gebruikt kunnen worden voor onderzoek en ontwikkeling van draadloze energieoverdracht

systemen, zoals bijvoorbeeld voor de vervanging van bewegende kabels in lineaire of planaire motoren.

Dankwoord

In het voorjaar van 2007 maakte ik tijdens mijn bachelor eindproject voor het eerst kennis met de Electromechanics and Power Electronics groep en het principe van draadloze energieoverdracht. Nu, acht jaar later, loopt mijn leerweg binnen deze vakgroep ten einde met het afronden van dit proefschrift.

Allereerst wil ik mijn dank uitspreken aan prof. Elena Lomonova voor het vertrouwen dat ze me heeft gegeven door het aanbieden van een promotie plaats in haar groep. In de afgelopen jaren hebben we regelmatig over de voortgang gesproken en de hieruit voortvloeiende discussies heb ik altijd erg gewaardeerd. De suggesties ter verbetering van mijn publicaties en uiteindelijk ook dit proefschrift heb ik als erg waardevol ervaren. Je bekeek het werk vanuit een andere hoek wat vaak resulteerde in andere woordkeuzes en generalisatie van het werk. Heel veel dank dat ik de afgelopen jaren deel mocht uitmaken van jouw vakgroep, waar naast al het harde werken ook op zijn tijd plaats was voor een borrel en jaarlijks een mooi groepsuitje.

Helm, heel veel dank voor je begeleiding in de afgelopen jaren. Bedankt voor de wekelijkse discussies die ik met je heb mogen voeren over het promotieonderzoek, deze hebben me enorm geholpen bij het bevatten van het complexe probleem. Heel veel dank voor het corrigeren van alle publicaties en, niet te vergeten, dit proefschrift. Naast alles wat je voor mij gedaan hebt, vond ik het fijn om jou te mogen helpen bij het opzetten en begeleiden van het nieuwe studentenproject rondom draadloze energieoverdracht. Dit was voor mij een mooie afleiding van mijn promotieproject.

I would also like to thank my core committee members, prof. Hameyer, prof. Perriard, dr. Soulard, dr. Vermeulen and prof. Baltus. Many thanks for reading my thesis and the valuable input and discussions which helped me to improve the work.

Het promotieproject autonomous ceiling robots ben ik vijf jaar geleden samen met Timo gestart. Allebei hebben we ons in ons eigen onderzoek vastgebeten,

welke langzaam samen zijn gekomen. Dit heeft uiteindelijk geleid tot de realisatie van het gezamenlijk prototype, de magnetisch opgehangen planaire motor met het ingebouwde draadloze energieoverdracht systeem. Timo, bedankt voor je hulp en de prettige samenwerking in de afgelopen jaren. Vooral tijdens het bouwen van het prototype vond ik het erg fijn dat we deze uitdaging samen hebben mogen oppakken.

Het realiseren van het prototype heb ik niet alleen Timo alleen gedaan. Marijn en Rutger, heel veel dank voor jullie hulp tijdens het bouwen van de opstelling, het fabriceren van de vele kleine onderdelen in de werkplaats en niet te vergeten de dagenlange hulp tijdens het handmatig wikkelen van de 200 primaire spoelen. Verder wil ik ook Erwin Dekkers en Patrick de Laat van het Equipment & Prototype Center van de TU/e bedanken. Met jullie hulp zijn de tweedimensionale schetsen omgezet in een driedimensionale opstelling. Bart Gysen van Prodrive Technologies, heel erg bedankt voor de hulp en de mogelijkheden die we hebben gekregen voor het lijmen van de magneten. Daarnaast wil ik Erwin Hofsté van Tecnotion bedanken voor de hulp bij en het leren wikkelen van spoelen.

Uiteraard ook dank aan mijn collegas binnen de vakgroep Electromechanics and Power Electronics. De gezellige momenten van samenzijn zorgden altijd voor een mooie afwisseling. In het bijzonder wil ik mijn (oud)kamergenoten Timo, Esin, Reyhan, Bob, Tom en Mitrofan bedanken voor de gezelligheid die we samen hebben mogen beleven in Impuls 0.12. Maurice, Thomas en Jan bedankt voor jullie raad rondom mijn vele vragen over vermogenselektronica. Het ga jullie allen goed!

Johan, februari 2015

Curriculum Vitae

Johan Smeets was born on November 13$^{\text{th}}$, 1985 in Eindhoven, The Netherlands. After finishing his pre-university education at the Christiaan Huygens College in Eindhoven, he started his study of electrical engineering at the Eindhoven University of Technology in 2004. During his internship at the Royal Institute of Technology, Stockholm, he studied a turn-to-turn failure in a permanent magnet traction motor. In 2009 he graduated within the Electromechanics and Power Electronics group at the Eindhoven University of Technology. His graduation project was performed in cooperation with TNO Netherlands on the modeling and design of a contactless energy transfer system to a high speed rotating disk.

In December 2009 he started as a PhD student in the Electromechanics and Power Electronics group at Eindhoven University of Technology. During his PhD project he has modeled, designed and realized a contactless energy transfer system integrated in a magnetically suspended planar motor by means of an inductive coupling. He is author or co-author of 10 journal publications and 16 conference publications.